

2

FINAL 15 Feb 93 TO 14 Feb 94

Antiproton-induced microfission

F49620-93-1-0144

Professor Gerald Smith

DTIC
ELECTE
MAR 23 1994
S B D

Penn State University
Department of Physics
303 Osmond Laboratory
University Park, PA 16802

AEOSR-TR- 94 0044

AFOSR/NE
110 Duncan Avenue, Suite B1115
Bolling AFB DC 20332-0001

2301/DS

APPROVED FOR PUBLIC RELEASE: DISTRIBUTION IS UNLIMITED

Approved for public release;
distribution unlimited.

During the past year significant progress has been made in preparation for the Phillips Laboratory antiproton-induced microfission experiment to be carried out at the SHIVA Star solid liner imploder facility starting in 1995. Two dimensional MHD calculations compare favorably with data from initial solid liner implosion tests carried out in December, 1993. Antiproton storage measurements at CERN in July, 1993 have been very successful, offering the prospects for storing and transporting up to 10 million antiprotons by the end of 1995. The involves utilization of electron cooling and multiple pulse injection from LEAR during 1994. A design for portable trap has been achieved, and it is planned to proceed with its fabrication starting later in 1994. The RFQ acclerator has been successfully tested. Extraction optics from the trap to the RFQ, and transfer optics from the RFQ to the SHIVA Star target, have been completed and verified by independent studies at Los Alamos National Laboratory.

END

14. SUBJECT TERMS

15. NUMBER OF PAGES

16. SECURITY CLASSIFICATION
UNCLASSIFIED

17. SECURITY CLASSIFICATION
UNCLASSIFIED

18. SECURITY CLASSIFICATION
UNCLASSIFIED

19. LIMITATION OF ABSTRACT
UNLIMITED

AD-A277 283



PENNSSTATE



DEPARTMENT OF PHYSICS

PHYS 480, 94-00

FINAL TECHNICAL REPORT

AFOSR GRANT F49620-92-1-0144
February 15, 1993 - February 14, 1994
SP-1-1994-0144
February 21, 1994

**LABORATORY FOR ELEMENTARY
PARTICLE SCIENCE**

**303 OSMOND LABORATORY
UNIVERSITY PARK, PA 16802**

Approved for public release;
distribution unlimited.

PSU LEPS 94/06

FINAL TECHNICAL REPORT

AFOSR GRANT F49620-93-1-0144
February 15, 1993-February 14, 1994
Gerald A. Smith
February 21, 1994

94-09081


94 3 22 003

Date: February 21, 1994

To: Dr. Ralph Kelley (AFOSR)

From: Gerald A. Smith, Principal Investigator
AFOSR F49620-93-1-0144

Re: Final Technical Report, February 15, 1993-February 14, 1994

SUMMARY

During the past year significant progress has been made in preparation for the Phillips Laboratory antiproton-induced microfission experiment to be carried out at the SHIVA Star solid liner imploder facility starting in 1995. Two dimensional MHD calculations compare favorably with data from initial solid liner implosion tests carried out in December, 1993. Antiproton storage measurements at CERN in July, 1993 have been very successful, offering the prospects for storing and transporting up to 10 million antiprotons by the end of 1995. The involves utilization of electron cooling and multiple pulse injection from LEAR during 1994. A design for a portable trap has been achieved, and it is planned to proceed with its fabrication starting later in 1994. The RFQ accelerator has been successfully tested. Extraction optics from the trap to the RFQ, and transfer optics from the RFQ to the SHIVA Star target, have been designed. Finally, neutron yield calculations have been completed and verified by independent studies at Los Alamos National Laboratory.

RESEARCH OBJECTIVES

The overall objective of this research is to prepare for an experiment to demonstrate antiproton-induced microfission at the SHIVA Star solid liner implosion facility, Phillips Laboratory, Kirtland AFB, NM, starting in 1995. Specific research objectives include solid liner compression simulations and tests, antiproton storage and transport in a portable trap, extraction of antiprotons from the trap, and acceleration and focusing of antiprotons onto the SHIVA Star microfission target. The following reports elaborate in detail on progress made on these objectives during the past year.

Progress reported here is due to the combined efforts of Drs. P-R. Chiang, R.A. Lewis, T. Otto and G.A. Smith, graduate students S. Chakrabarti, M. Chiaverini, J. Dailey, C. Gazze, K. Higman, R. Newton, and W.L. Werthman, and technician J. Rochet.

For	<input type="checkbox"/>
ed	<input type="checkbox"/>
ion	<input type="checkbox"/>

Availability Codes	
Dist	
A-1	Special

RESULTS OF RESEARCH

OVERVIEW: When this multi-year research program was approved by AFOSR in 1991, the Phillips Laboratory/Penn State groups submitted a timetable for activities to take place during the initial 3 years of activity (Figure 1). The research program is organized in terms of tasks, which are described in detail below. The current plan layout for the experiment is shown in Figure 2. It is suggested that the reader refer to this figure when appropriate.

(1)TASK 1: Studies of ANTIPROTON PHYSICS are supported under a separate AFOSR grant, and will be completed June 14, 1994. A discussion of recent results may be found in TECHNICAL REPORT, AFOSR GRANT F49620-92-J-0374, June 15, 1992-June 14, 1993, Gerald A. Smith, July 14, 1993.

(2)TASK 2: Studies of the FEASIBILITY OF ANTIPROTON ICF are largely completed, the result of work done by Lt.Col.Denis Beller, Air Force Institute of Technology, Wright-Patterson AFB, Dr.Bruce Wienke, Los Alamos National Laboratory, and Dr.Gerald A. Smith, Principal Investigator. The most recent results of work done by Drs.Wienke and Smith were reported at the Advanced Technology Weapons Symposium, Kirtland AFB, NM, April 6-7, 1993 and discussed at the Workshop Executive Working Group Meetings, Kirtland AFB, NM, April 27-29, 1993. A classified report, prepared under the direction of Dr.Joe Howard of Los Alamos National Laboratory, has been prepared. Dr. Wienke's most recent published work is found in Nuc.Sci.& Eng., 113, 86-92, 1993. Both Drs.Wienke and Smith maintain a low, but constant, level of activity in this area.

Specific to the SHIVA Star experiment, the Penn State group submitted in October, 1993 two papers for publication in Nuc.Sci.& Eng on the subject of subcritical neutron yields expected in that experiment. The papers discuss primary neutron production from antiproton annihilation on a compressed target (Appendix I) and secondary neutron production by charged pions produced in the antiproton annihilation (Appendix II). Reviewer's comments on these two papers have not yet been received.

(3)TASK 3: EXPERIMENTAL PLAN & TARGET DESIGN is on-going, and encompasses all facets of experimental plan and design, including responsibilities assigned to the Phillips Laboratory and Penn State, which are discussed in detail in the following sections. Enclosed with this report in Appendix III is the M.S.thesis of Martin Chiaverini, which describes in detail the plan for extraction of antiprotons from the portable trap onto the target. The following discussion draws on this material in part.

Antiproton Catalyzed μ -Fission Schedule

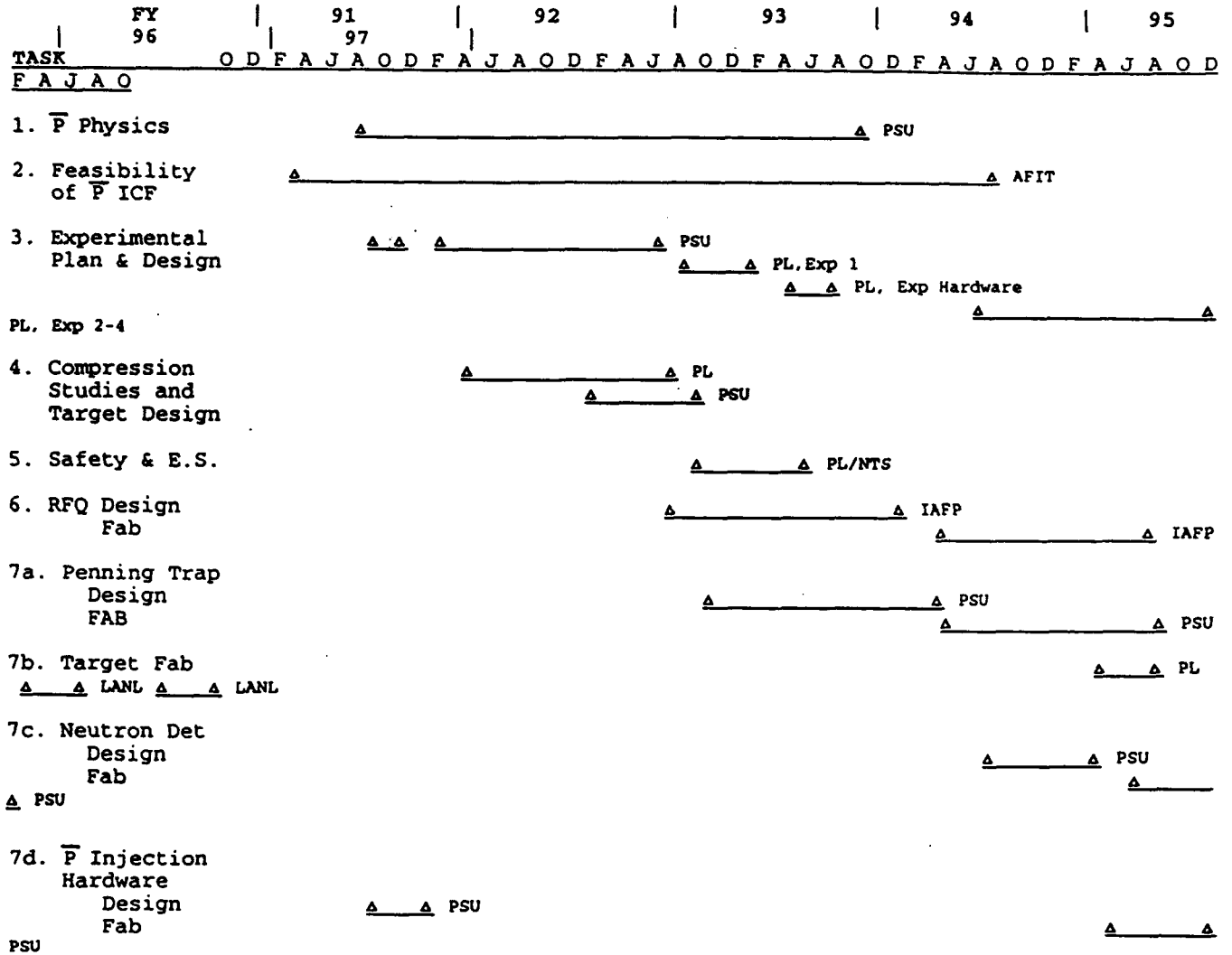
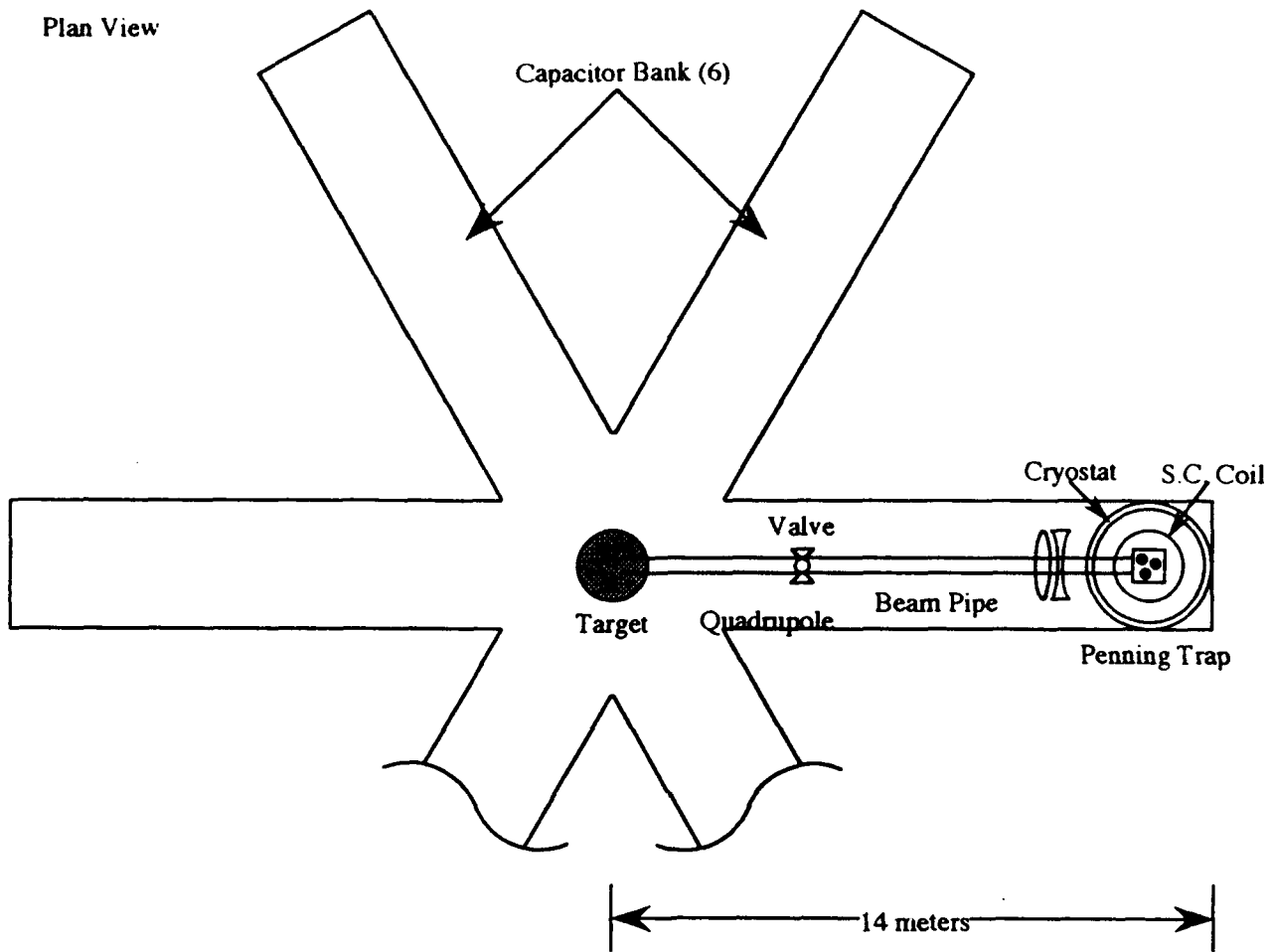


Figure 1

Plan View



Elevation View

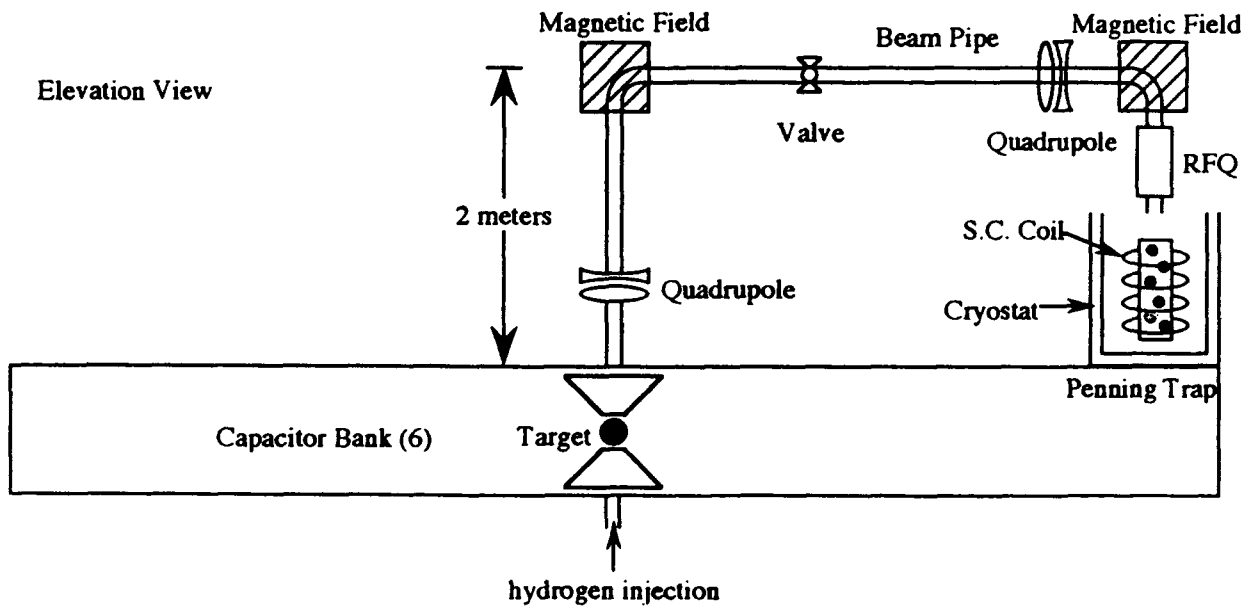


Figure 2

(4)TASK 4: COMPRESSION STUDIES AND TARGET DESIGN have been successfully completed, involving a collaboration among four members of the High Energy Plasma Division, Phillips Laboratory, Kirtland AFB, and Penn State University. A paper was submitted to the Journal of Applied Physics (Appendix IV) in Oct.1993, which describes 1D and 2D computations and simulations of target compression for the SHIVA Star experiment. The paper is presently being revised according to referee's suggestions, and should appear in print in the next few months.

Solid liner implosion tests carried out at SHIVA Star in December, 1993 were highly successful. These were the first in a series of tests intended to prepare for antiproton experiments in 1995, and at this time did not include a target load. Radiographs (Appendix V) of the liner during implosion are consistent with predictions from the 2D MHD code CALE, acquired from LLNL, and run at the Phillips Laboratory and Penn State. Tests including a target load will be carried out later in 1994.

(5)TASK 5: EH&S for the experiment is the responsibility of the Phillips Laboratory, and was not supported by this grant.

(6)TASK 6: In 1992 responsibility for RFQ DESIGN AND FABRICATION was assumed by the Penn State group. During G.A. Smith's sabbatical leave at the Phillips Laboratory, July 1, 1992-June 30, 1993, he worked actively on this problem, and identified an existing Phillips Laboratory RFQ which met all required specifications for the experiment. This RFQ had been fabricated at SAIC, San Diego, in the late 1980's as part of a neutral beams activity at the Phillips Laboratory. Using Penn State AFOSR equipment funds, a contract was prepared with SAIC to refurbish and test the RFQ with the antiproton experiment requirements in mind, i.e. 1.2 MeV output energy and antiproton currents as low as 0.1 microamps. G.A. Smith and R.A. Lewis of Penn State visited SAIC on June 13 and Aug.29-30, 1993 to consult with SAIC staff and participate in test measurements. SAIC and Penn State concur that the tests are now completed and considered successful. A full report on the performance of the RFQ is found in Appendix VI.

(7a)TASK 7a: PENNING TRAP DESIGN AND FABRICATION has two distinct parts: (1) trapping studies for antiprotons in the Los Alamos National Laboratory (LANL) "catcher" trap, located at the Low Energy Antiproton Ring (LEAR), CERN, Geneva, Switzerland, and (2) design and fabrication of a "portable" trap, followed by transfer and holding of antiprotons from the "catcher" trap to the "portable" trap. The following summarizes progress to date in these two areas.

(1) Catcher Trap Studies (in collaboration with LANL): During July, 1993, we successfully trapped up to 780,000 antiprotons in the "catcher" trap from single beam pulses injected from LEAR. Data are provided in Figures 3c,d which illustrate this successful activity. This is a record number, and permits further studies of multipulse stacking of antiprotons, scheduled for early in 1994. For this purpose, the vacuum has been improved, and electron cooling apparatus has been installed. During scheduled beam periods in May-June and September-October, 1994, we expect to trap a number approaching 10 million antiprotons. Assuming most of these can be transferred to the "portable" trap, our goal of 100,000 antiprotons for the Phillips Laboratory microfission experiment should be easily met.

(2) Portable Trap Design and Fabrication (in collaboration with LANL): A preliminary design has been completed (Figures 4a,b), and a schedule for fabrication with completion by mid-1995 has been established. The single largest component of the trap is the magnet, currently planned to be a superconducting coil which provides a 1-2 T confining field and which must be "portabilized", i.e. able to withstand modest acceleration forces and insulated to maintain coil operation for up to 30 days during transport. We are also considering the possibility of using a permanent magnet, although a cryosystem will still be needed to maintain vacuum. Electrode, vacuum, voltage feedthrough, pulsing circuitry, and control electronics will be fabricated by LANL.

(7b) TASK 7b: TARGET FABRICATION is the responsibility of the Phillips Laboratory/LANL and has not been supported under this grant.

(7c) TASK 7c: NEUTRON DETECTOR DESIGN AND FABRICATION is the responsibility of the Penn State group and will be addressed in 1994-5. No funds were provided in the present grant for this work.

(7d) TASK 7d: ANTIPROTON INJECTION HARDWARE: DESIGN AND FABRICATION has several important facets:

(1) Extraction of Antiprotons from the Portable Trap: We have completed the design (Figure 5) of a three element einzel lens required to focus antiprotons accelerated out of the trap into the 3 mm aperture of the RFQ. The code EGUN from the Stanford Linear Accelerator Center was used for this purpose. The central element of the lens operates at -15KV relative to ground potential. Strong focusing by this lens is required to overcome defocusing of antiprotons as they travel through the diverging magnetic field at the exit end of the superconducting coil.

Antiproton Trapping and Transport Studies
Penn State University

Jan 19, 1994

In 1993 Penn State and Los Alamos physicists trapped antiprotons at the Low Energy Antiproton Ring (LEAR) at CERN, Geneva, Switzerland in record numbers. The 2m long Penning (Catcher) Trap is shown in (a). Five MeV antiprotons were injected axially and degraded in SF6 gas and Al foils, and subsequently trapped in the central electrode trap structure by confining electrostatic (axial) and magnetic (transverse) forces. In 1994 antiprotons will be transferred from the Catcher Trap to a smaller Portable Trap (b) using electrostatic einzel lenses (L1,L2). During 1993 antiprotons were extracted from the Catcher Trap over a 600 ms period (c) and made to annihilate on the MCP seen in (a). The resultant pions were detected in scintillators 1-8. Many successful fills of the trap were achieved, including a maximum and record fill of 721.5 thousand (d).

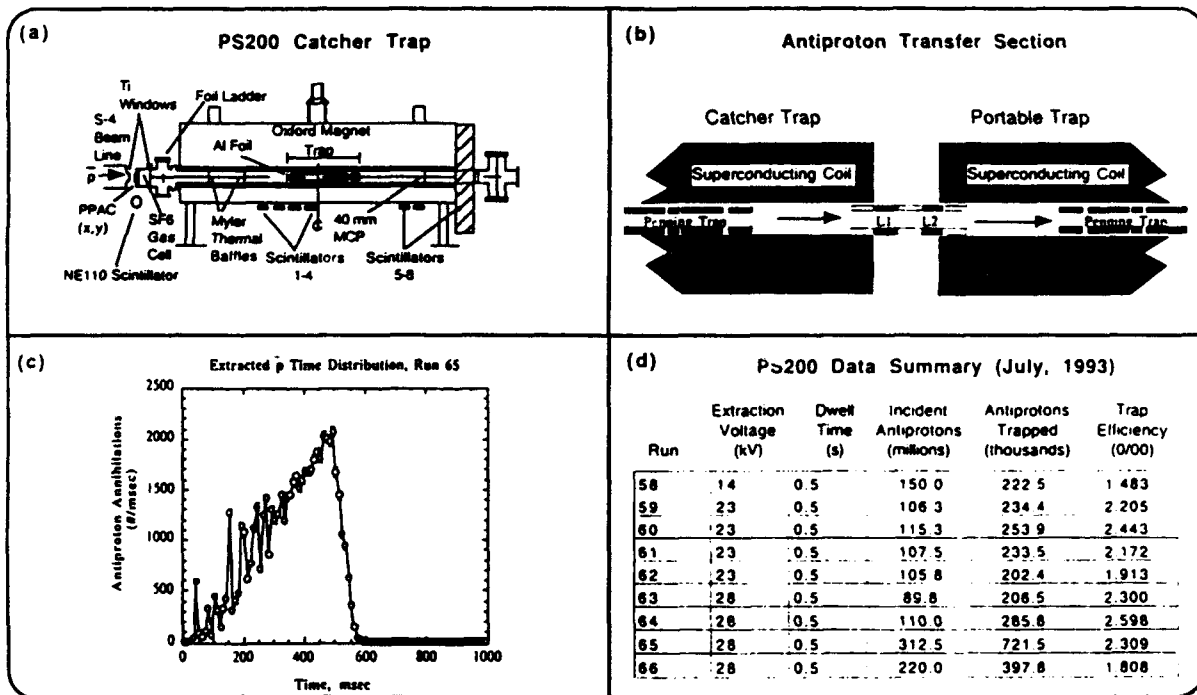


Figure 3

Portable Antiproton Trap

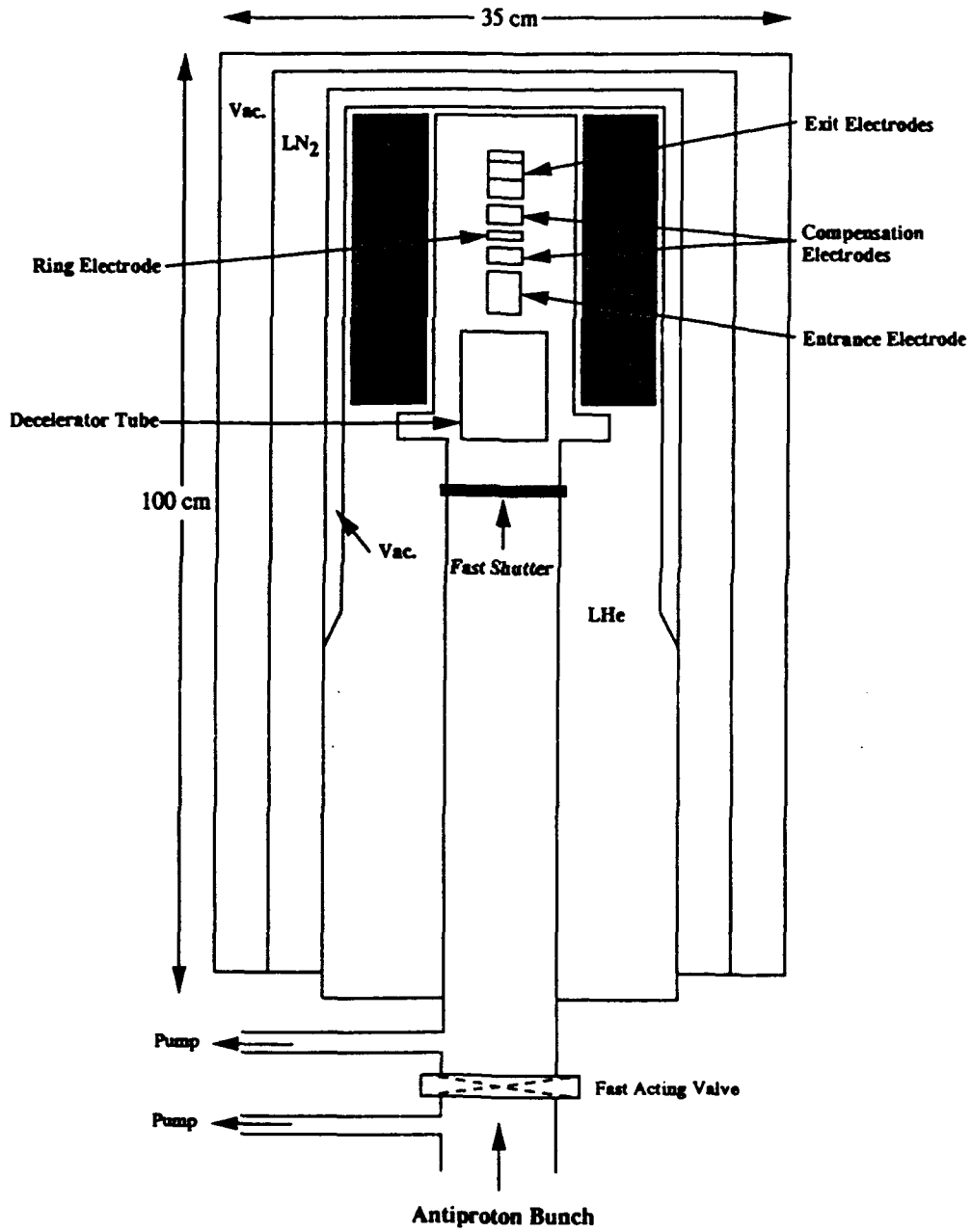


Figure 4a

Portable Trap Electrode Structure

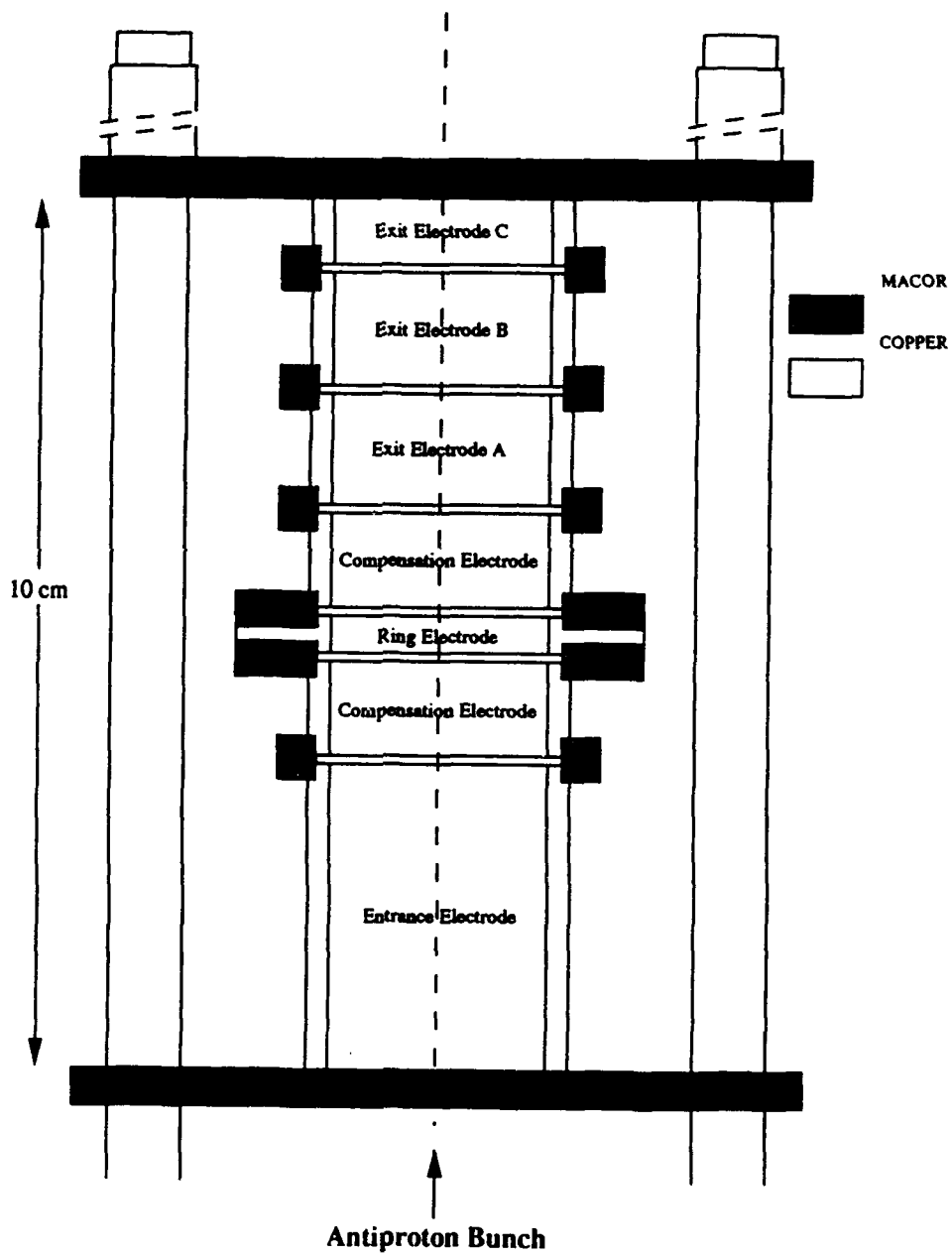


Figure 4b

Antiproton Extraction Optics

Portable Trap to RFQ: Magnetron Radius = 0.12 cm, Lens Pot. = -15kV

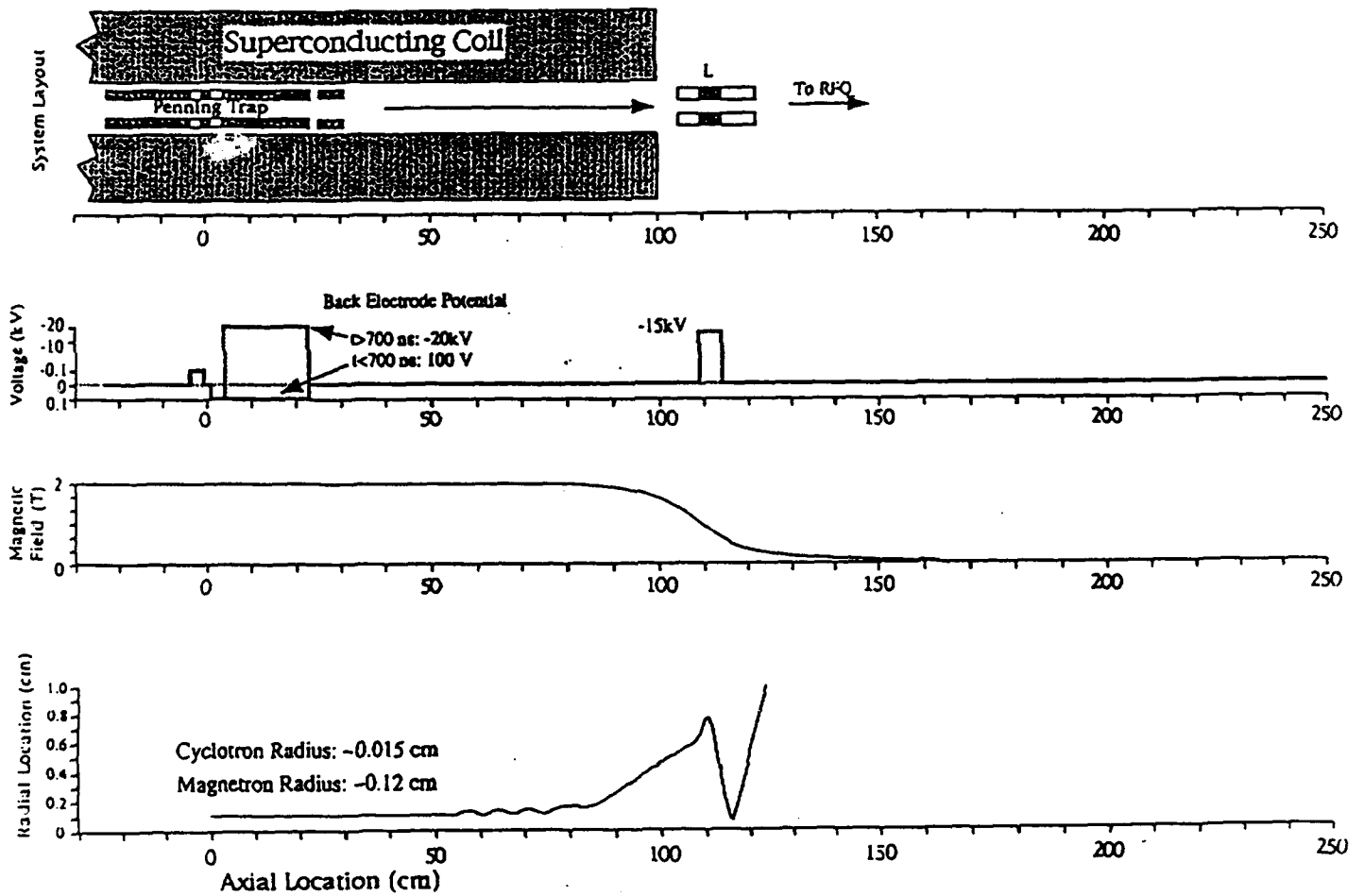


Figure 5

Motion of the antiprotons is initiated by a small +100V pulse on the central trap electrode, followed 700 ns later by application of -20KV on the last electrode at the exit end of the trap. Figure 6 shows the calculated (and recently measured) input emittance of the RFQ (ellipsoidal outline), with one hundred antiprotons tracked by EGUN through these fields. It can be seen that focusing of antiprotons within the boundaries permitted by the RFQ is achieved.

Tests of extraction concepts and hardware are planned for March, 1994 at LANL, using the launcher trap originally built for the LANL gravity experiment. The electrode structure and magnet closely resemble those of the planned portable trap, so successful extraction of protons from this trap is seen as a reliable method for predicting success of the antiproton system.

(2) Transport Optics from the RFQ to Target: Referring to Figure 2, having been accelerated to 1.2 MeV by the RFQ, antiprotons are magnetically bent through two 90 degree turns and focused over a 17m path onto the SHIVA Star target. Figure 7 shows vertical and horizontal ray traces from the TRANSPORT code. This is achieved with two bending magnets (D1,D2) and two quadrupoles (Q1,Q2). Vacuum requirements over the line from trap to target are typically a few microtorr of pressure, achieved with ion vacuum or turbomolecular pumps. Special care must be given to the design of the fast acting valve shown in Figure 4a, which couples this vacuum to the ultra-high vacuum of the trap itself. Final image sizes at the entrance to the working fluid meet the 2 mm diameter tolerance imposed by window and target sizes. Designs for the magnetic dipole and quadrupole lenses are in progress, and acquisition of these structures is planned for 1994.

(3) Transmission of Antiprotons through the Electrode and Working Fluid onto the Target: This subject is discussed extensively in Appendix III. The compression chamber includes a diamond window which allows entry of antiprotons into the compressed working fluid and target after passing through the anode entry channel. Peak compression begins about 12.8 microseconds after discharge of SHIVA Star compressions, lasting for about 300 ns. Thus, arrival of the antiprotons must be timed to be at $12.8 < t < 13.1$ microseconds. A master timing signal is used to control release of the antiprotons from the trap in accordance with this requirement.

When the pressure inside the chamber reaches 200 kbar, the window breaks, blowing plasma and diamond shards up the beam pipe. A fast valve (Figure 2) is closed 2 microseconds later to protect the RFQ and trap from this debris. Antiprotons released at the appropriate time encounter the expanding plasma and shards about 10 cm from the entry window. Detailed calculations show that 1.2 MeV energy is sufficient to range the antiprotons into the target, provided the following considerations are included: (1) a tapered expansion volume just outside the window to provide significant dilution of

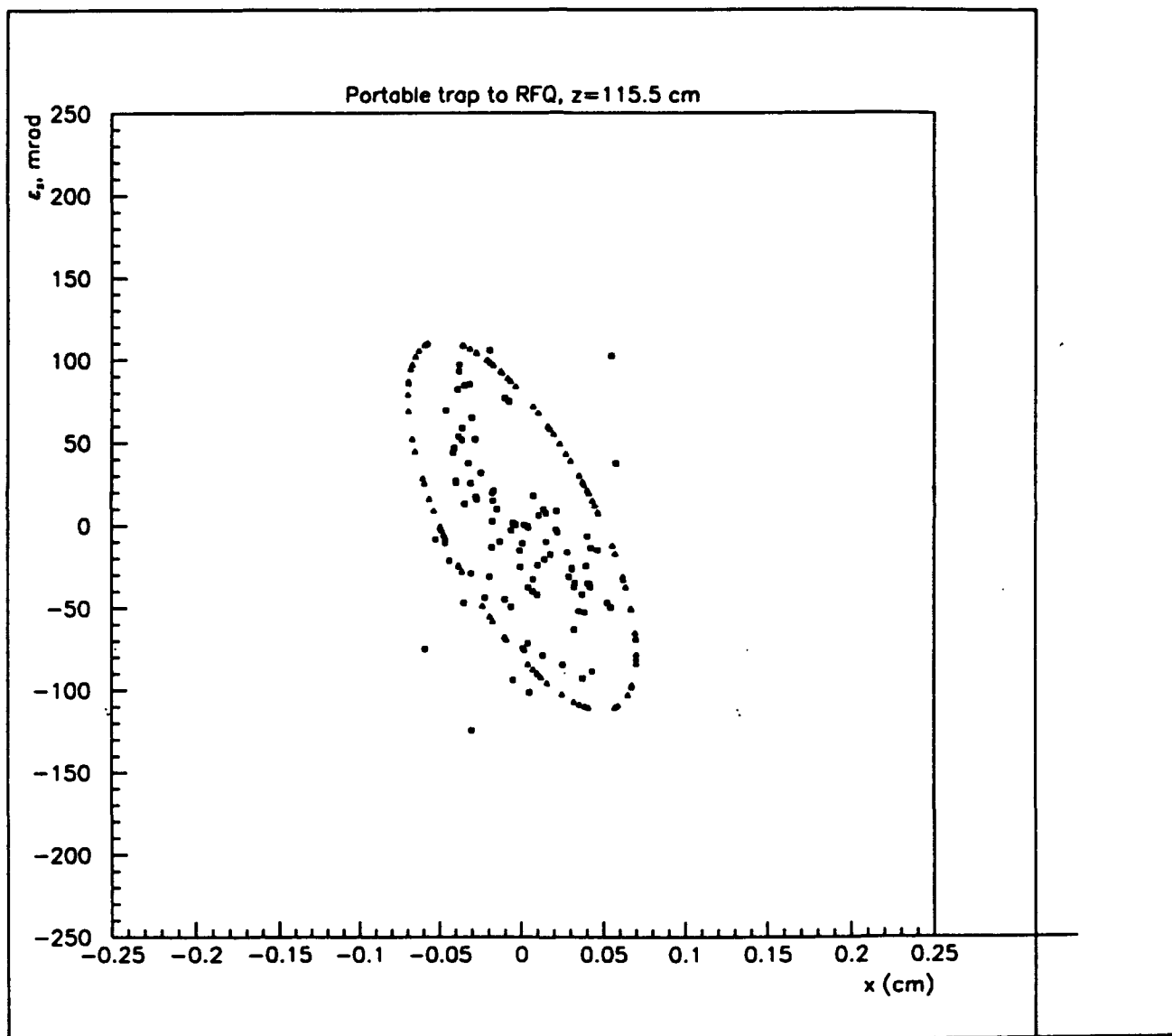
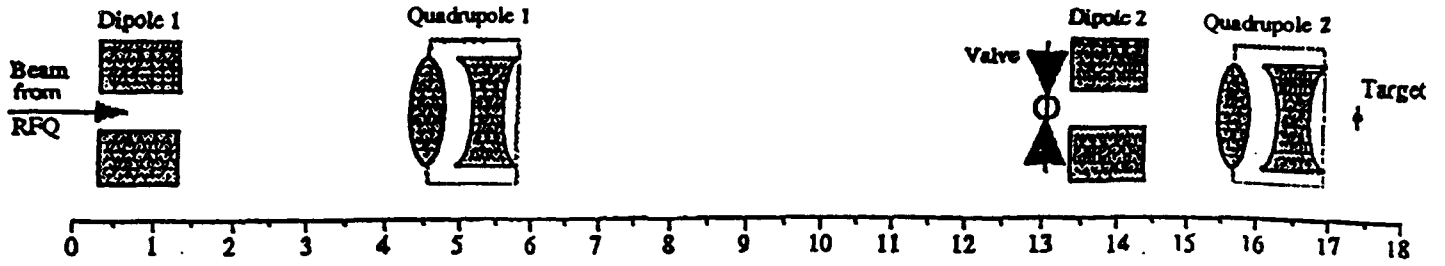


Figure 6

Antiproton Transport Optics



D1, D2: Boundary of dipoles
Q1x, Q2x: Boundary of x-focusing segment of quadrupoles
Q1y, Q2y: Boundary of y-focusing segment of quadrupoles

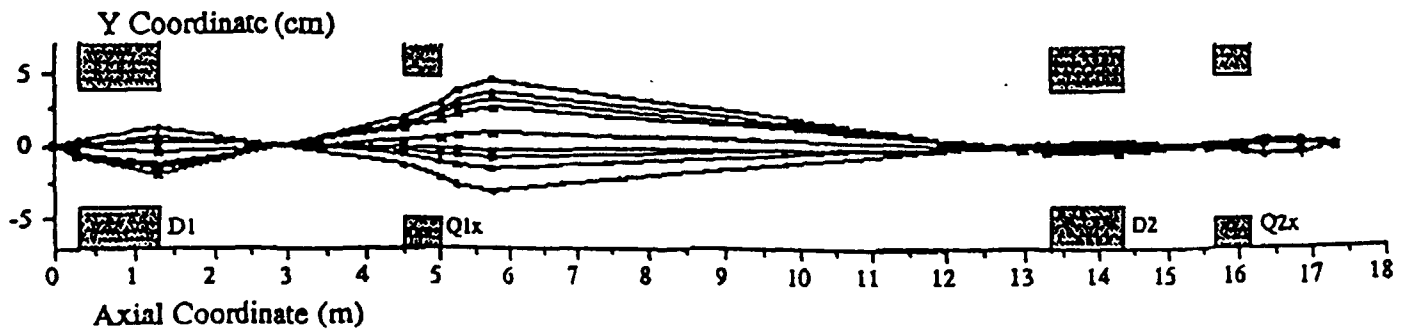
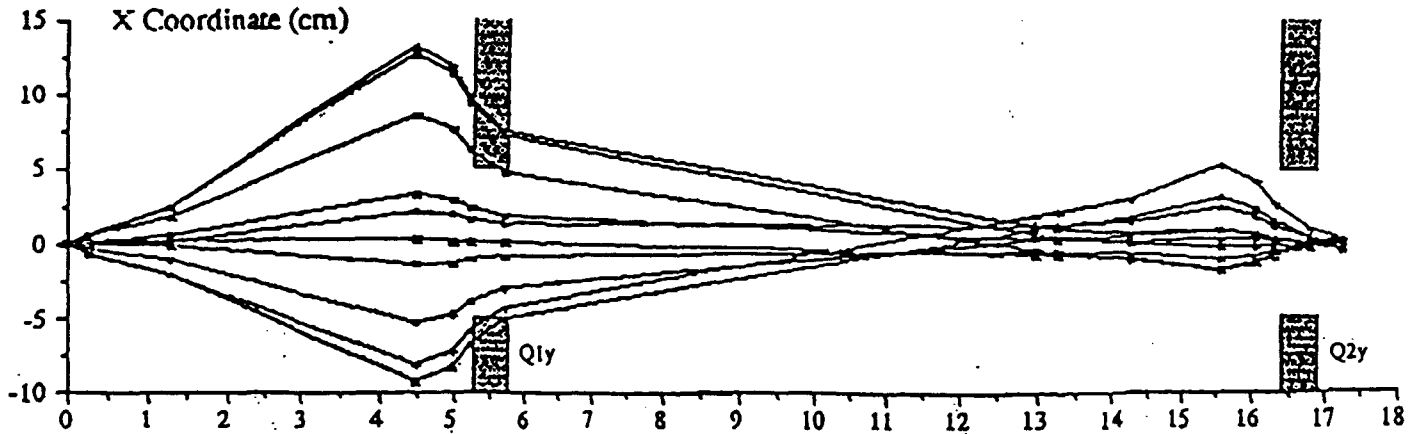


Figure 7

plasma and shards (2) a target design which (partially) maintains vacuum behind the entry window (3) adsorption of hydrogen plasma on the electrode walls and (4) energy loss by collisions of antiprotons with the plasma.

PUBLICATIONS

1.G.A.Smith, Applications of Trapped Antiprotons, Hyperfine Interactions 81, 180 (1993).

2.G.A.Smith, An Antiproton Driver for ICF Propulsion, Proc. 5th. Annual Symposium, Pennsylvania State University Engineering Research Center, University Park, PA, Sept.8-9, 1993, p.195

3.C.Gazze et al, Neutron Yields for Antiproton Microfission Experiments, Nucl.Sci.& Eng. (submitted)

4.K.Higman et al, Containment and Neutron Production by Charged Pions in Antiproton Microfission Experiments, Nuc.Sci.& Eng. (submitted)

5.P-R.Chiang et al, Target Compression by Working Fluids Driven with Solid Liner Implosions, Journal of Applied Physics (submitted)

PARTICIPATING PROFESSIONALS

P-R.Chiang, Ph.D. 1991, Pennsylvania State University, "The Effects of Velocity-Space Particle Loss in Field-Reversed Configurations"

R.A.Lewis, Ph.D. 1966, MIT, "Pion Photoproduction Angular Distributions"

T.Otto, Ph.D. 1994, Johannes Gutenberg Universitat, Mainz, Germany, "Penningfallen-Massenspektrometrie an neutronenarmen Rubidium- und Strontium-Isotopen"

G.A.Smith, Ph.D. 1961, Yale University, "Proton-Proton Interactions at 2.85 BeV"

COUPLING ACTIVITIES

a) COLLOQUIA, LECTURES AND SEMINARS

1.G.A.Smith, INVITED PAPER, Workshop on Traps for Antimatter and Radioactive Nuclei, TRIUMF, Vancouver, British Columbia, Canada, 1993

2.G.A.Smith, SEMINAR, Dept.of Chem.and Nucl. Eng., University of New Mexico, 1993

3.G.A.Smith, INVITED PAPER, NASA Symposium on Advanced Propulsion, Jet Propulsion Laboratory, Pasadena, CA, 1993

4.G.A.Smith, INVITED PAPER, 5th Annual Symposium, Pennsylvania State University Propulsion Engineering Research Center, University Park, PA, 1993

5.G.A.Smith, INVITED PAPER, Advanced Weapon Technology Symposium, Phillips Laboratory, Kirtland AFB, NM, April 6-7, 1993

b) CONSULTING

1. IPA appointee, Phillips Laboratory, Kirtland AFB, NM, Oct.1, 1992-Sept.30, 1993; contact, Dr.James Degnan

2. P-15 Division, Los Alamos National Laboratory, Oct.1, 1991-July 30, 1994; contact, Dr. Nicholas King

APPENDIX I

NEUTRON YIELDS FOR ANTIPROTON MICROFISSION EXPERIMENTS*

Christopher E. Gazze, Richard J. Newton

Department of Nuclear Engineering

and

Raymond A. Lewis, Pi-Ren Chiang, and Gerald A. Smith

Laboratory for Elementary Particle Science, Department of Physics

Pennsylvania State University

University Park, PA 16802

ABSTRACT

Neutrons produced following antiproton annihilation on uranium nuclei are transported through compressed targets by the SCATTER Monte Carlo code in support of antiproton microfission experiments. The SCATTER code and necessary input data are described. Results show that the high energy (>20 MeV) component of the source is responsible for the majority of the neutron yield. Results for a wide range of uniformly compressed targets are presented for moderation levels of (H:U) 0:1, 3:1, and 9:1 in U-235 targets and U-238. Moderation is found to increase neutron yields at a given ρr . Uniformly compressed unmoderated U-238 targets demonstrate 9-16% lower yields than U-235. Four targets under different, non-uniform compression conditions are considered. The average yield in these cases is about 21.8 ± 0.2 neutrons per source antiproton, an increase of 34% over the 16.3 primary neutrons per antiproton. The average yield of the non-uniform compression cases agrees within error with uniformly compressed targets.

[Submitted to Nuclear Science and Engineering]

*Work supported in part by the Air Force Office of Scientific Research and Jet Propulsion Laboratory (NASA).

I. INTRODUCTION

Practical, non-destructive uses of nuclear systems are limited by the inability to safely harness the resulting large energy yields. In microfission, these energy yields are reduced by burning as little fissile material as possible while still maintaining a net energy gain. The concept, first introduced in 1973 by Askar'Yan *et al.* [1] and Winterberg [2], involves starting a chain reaction in a small, compressed, fissile target.

It has been proposed [3] to use antiprotons annihilating on the surface of fissionable nuclei as the initiator for the chain reaction. Recent experiments [4] at the Low Energy Antiproton Ring (LEAR) at CERN, in Geneva, Switzerland have demonstrated that large numbers of highly energetic neutrons are released following such annihilations. These neutrons could be used to bypass the slow, early stages of the chain reaction, increasing the number of fissions which can occur during the confinement time.

A Monte Carlo study was performed to examine moderated and unmoderated neutron reactions induced by the annihilation of antiprotons in fissionable nuclei. This study was done in support of a larger effort to demonstrate the feasibility and potential applications of antiproton catalyzed microfission at the SHIVA Star facility [5]. Other studies address reactions induced by pions released during the annihilation of antiprotons [6], and the trapping and delivery of the antiproton beam [7].

The goal of the SHIVA Star experiment is to demonstrate that significant subcritical neutron yields can be observed under moderate levels of compression following antiproton annihilation on fissionable targets. SHIVA Star is a solid liner imploder capable of providing 10-40 Mbars of pressure to compress a small (tens of grams) uranium target. The apparatus is shown schematically in Figure 1. The system operates by discharging a 5.3 MJ capacitor bank through a thin liner connecting the anode and cathode. The resulting 10 Mamp average current induces large inwardly directed magnetic pressures. The liner then collapses, applying pressure on the working fluid inside, a hydrogen plasma. This produces a uniform pressure field in the plasma which can uniformly and adiabatically compress the spherical target located in the center of the system.

The one dimensional radiative Lagrangian hydrodynamics code HYDRAD [5] and the two dimensional (2D) magnetohydrodynamics (MHD) code CALE [8] have been used to model the compression process in the SHIVA apparatus. CALE is a finite difference code that provides the time dependent density profile during the compression. The information provided by the computer codes is then used directly in the neutronics calculation.

II. Description of Neutronics

To accurately model neutron reactions initiated by antiproton annihilation, it is necessary to characterize neutron cross sections within an energy regime that extends up to 750 MeV. Although existing data libraries focus on the energy regime below 20 MeV, our work has shown that neutrons in the higher energy regime are important.

The kinetic energy spectrum of neutrons from the antiproton annihilation is shown in Figure 2 [4]. The spectrum extends to 747 MeV, which is the highest kinetic energy listed in the literature for fission related reactions in uranium. The released neutrons are distributed isotropically in the laboratory frame and total 16.3 [4].

The Monte Carlo code SCATTER was written to study the neutronics of the SHIVA Star experiment [9]. The code requires a variety of input data. The energy spectrum of annihilation neutrons has been used to model the source. Total and partial neutron cross sections have been taken from the literature (from 0 to 1000 MeV). A time dependent density profile has been taken from CALE and been applied to the model. Anisotropic elastic scattering probability distributions have been used to propagate neutrons through the target. Finally, energy dependent multiplicity data and fission and other inelastic energy spectra have been applied to create secondary neutrons with the appropriate energies [4,10-11].

Cross sections and nuclear reaction data in the lower energy regions (below 100 MeV for hydrogen and below 20 MeV for uranium) have been taken from the ENDF-B/VI database, compiled by Brookhaven National Laboratory [12]. Data for the higher energy regions were gathered from a variety of sources in the literature [9,13-14]. High energy cross section data used by the SCATTER program are shown in Figure 3 for hydrogen and

in Figures 4 and 5 for U-235 and U-238, respectively. The neutron production cross section ($n \rightarrow xn$) is defined as the total cross section minus the elastic and inelastic ($n \rightarrow n$) cross sections. Multiplicity data are presented in Figure 6 for uranium. The difference between U-235 and U-238 below 125 MeV results from the larger fission cross section in U-235.

Spectra for neutrons released from high energy reactions at 20 MeV [neutrons, 12], 155 MeV [protons, 11], 300 MeV [protons, 10], and 455 MeV [antiprotons, 15] are shown in Figure 7. The 455 MeV curve is based on an energy transfer measurement for antiprotons at rest. In terms of equivalent laboratory bombarding energy, the curve would likely be represented at a higher energy.

The SCATTER code has been extensively tested. Predictions for more conventional neutron experiments (i.e. those occurring below 20 MeV) have been compared with the results of the MCNP (Monte Carlo Neutron Photon) code [16]. The results produced by the two codes agree very well.

III. Results for Uniformly Compressed Targets

While the most probable energy for primary neutrons is 2 MeV [4], the average energy of neutrons selected from the energy spectrum is just over 50 MeV. Neutron multiplying interactions involving very high energy neutrons are important because of their high multiplicities and high energy secondary neutrons they can produce. The SCATTER code was run with the primary neutron spectrum (Figure 2) terminated at 20 MeV. Results from these tests have shown that the primary neutron population above 20 MeV is responsible for over half of the yield in a typical SHIVA Star target.

A. U-235

Before analyzing targets specific to the SHIVA Star experiment, the SCATTER code was used to examine simple, one-region, spherical targets of uniform density. Such targets have been described by the product of their density and radius, ρr . The purpose of this study is to examine the behavior of the neutron population over a wide range of

compression conditions and levels of moderation. Cases have been run for ρr from 10 to 40 gm/cm², and at moderation levels (molar ratio) of H:U = 0:1 (unmoderated), 3:1, and 9:1. Each case has used a 27 gram target, typical of a SHIVA Star targets. Examination of the figure of merit's (fom's) for each case indicates the results are stable.

Neutron yields for uniformly compressed cases using U-235 are presented in Figure 8. The neutron yield is defined as the number of neutrons escaping the target per source antiproton. The neutron yield increases monotonically with ρr at all levels of moderation. This dependence can be expressed by a power series in ρr of the form,

$$Y = c_0 + c_1(\rho r) + c_2(\rho r)^2 + c_3(\rho r)^3 + \dots \quad (1)$$

where Y is the yield of escaping neutrons in neutrons per antiproton and c_i , shown in Table I for these fits, are the coefficients of the expansion. It is evident that the effect of adding moderation is to increase yield.

Figure 9 shows how average energies of the primary neutron population depend on ρr and moderation ratio in U-235 targets. The statistical accuracy of these measurements is typically 10%. For all levels of moderation, the average energy at which primary neutrons escape is approximately equal to the average energy at which they are created for all values of ρr . For the 0:1 and 3:1 moderated cases, the average energy of absorbed neutrons is significantly higher than that of the rest of the population due to the larger neutron production cross section ($n \rightarrow xn$) above 8 MeV (see Figure 4).

In the 3:1 moderated case, the behavior of the average absorption energy at low ρr is the same as that observed for the unmoderated case. The effect of the hydrogen is not yet felt on the absorption average, since the average path length of a neutron is relatively large at small values of ρr . As ρr increases, however, it becomes more likely that a neutron

will be absorbed after a scattering collision. Such events lower the average energy of absorption. The 9:1 moderated case is different; at low ρr values there is significant moderation which results in a lower average absorption energy. As in the 3:1 case, the average energy of absorption falls off rapidly with ρr .

Our study has shown that in the presence of a moderator, the average absorption energy of primary and secondary (not shown) neutrons remains well above 100 keV, thus not accessing regions of substantially higher cross section. However, the addition of a moderator aids in confining neutrons within the target. The probability of a neutron producing event occurring increases the longer neutrons are confined, resulting in larger yields.

B. U-238

Uniformly compressed unmoderated U-238 targets were also studied. The yield of escaping neutrons is smaller than the yield from U-235 for all values of ρr . This is due to the lower neutron producing U-238 cross section ($n \rightarrow xn$) and multiplicity below 10 MeV (see Figures 4-6). Unmoderated U-238 coefficients for equation (1) are listed in Table II. At 20 gm/cm², the number of escaping neutrons from a U-238 target is 18.9 neutrons per antiproton (compared to 20.8 neutrons for U-235). At 40 gm/cm², the numbers of escaping neutrons per antiproton are 21.5 and 25.7 for U-238 and U-235 respectively. We see that the neutron yield of a U-238 target is lower by 9-16% than the yield of the corresponding U-235 target, depending on ρr .

As in the case of U-235, the addition of a moderator to the U-238 targets could improve the yield of escaping neutrons. The effect of moderation has been shown to improve confinement, and not to significantly degrade the neutron energy distribution. Using the yields from the U-235 targets as a representative case, at 40 gm/cm² one can expect an increase in the yields from U-238 targets between 8% (H:U=3:1) and 50% (H:U=9:1).

IV. Expected Yields from the SHIVA Star Experiment

The CALE code is used to model the compression of a 27 gram U-235 target. Four cases are considered with varying initial plasma conditions resulting in different density profiles at peak compression [5]. The code calculates density conditions throughout the target and reports the density profile every 10 ns. Antiprotons are injected at peak compression. Moderated cases were evaluated using the same density profiles, although it is recognized that SHIVA Star will not be able to compress a moderated target as well as a pure uranium target.

CALE and HYDRAD have demonstrated that there is little evaporation of the target around the point of peak compression. At this point, the target's density profile changes slowly with respect to the speed at which the neutron reaction rate proceeds. The changes in the density profile over 10ns are small and only slightly effects the evolution of neutron production within the target.

Results for the unmoderated and moderated (H:U = 3:1) CALE cases are shown in Tables III and IV respectively. Initial conditions of the working fluid listed in Tables III and IV are discussed in reference 5. The comparison of CALE results with results for uniformly compressed targets (Figure 8) shows good agreement. Yields from uniformly compressed targets are similar to the yields of the CALE cases at similar ρr .

Currently, the SCATTER code is modeling neutrons which arise directly from the intranuclear cascade (INC). However, at SHIVA Star neutrons will also be produced when high energy pions from INC interact in the target and the aluminum liner. Calculation of neutron yields produced by these pions is found in another paper [6]. These mechanisms represent a significant additional source of neutrons.

Wienke *et al.* [17] have described how a multigroup microfission calculation using the antiproton source might be done with transport theory. Specifically, they set up thirty energy groups, dedicating eight to the region below 1 KeV and one to the region above 15

MeV. In the most moderated case considered in this study only 0.02% of the total neutron population dropped below 1 KeV. Therefore, without modification this method seems inappropriate for this application.

V. CONCLUSIONS

This study has explored the behavior of neutron reactions initiated by antiproton annihilations on microfission targets. In particular, special effort has been directed toward predicting neutron yields for the SHIVA Star antiproton experiment.

Results for uniformly compressed U-235 targets show that neutron yields are described by a power series in ρr . Furthermore, adding a hydrogen moderator increased yields at all compression levels due to enhanced confinement of neutrons. This increase is small at low ρr , but increases with higher ρr . Studies of average energy and interaction profiles for primary and secondary neutron populations indicate that the effect of moderation is to confine the neutrons in the target, rather than degrading them into regions of higher cross section.

Modeling of unmoderated U-238 targets has demonstrated 9-16% lower yields of escaping neutrons than yields from U-235 targets. The yield of escaping neutrons from moderated U-238 targets are expected to increase analogously with the yields from the moderated U-235 targets.

Four SHIVA Star moderated (H:U=3:1) and unmoderated U-235 targets with differing initial plasma density and temperature conditions were evaluated. Results for the cases, which had average ρr values of about 21 gm/cm², differ only slightly. The SCATTER code predicts an average yield per antiproton for these targets of 21.8 ± 0.2 , which is in good agreement with uniformly compressed cases of similar ρr .

REFERENCES

- [1] G.A. Askar'Yan *et al.*, JETP Letters 17, 424 (1973).
- [2] F. Winterberg, Z. Naturforsch. 28a, 900 (1973); Letters al Nuovo Cimento 6, 407 (1973); Nature 241, 449 (1973).
- [3] R.A. Lewis *et al.*, "Antiproton Boosted Microfission," Nucl. Sci. Eng. 109, 411 (1991); Fusion Tech., 20, No. 4, Part 2, 1046 (1991).
- [4] B. Chen *et al.*, Phys. Rev. C45, 2332 (1992).
- [5] P-R. Chiang *et al.*, "Target Compression by Working Fluids Driven with Solid Liner Implosions", submitted to J. Appl. Phys.
- [6] K.I. Higman *et al.*, "Containment and Neutron Production by Charged Pions in Antiproton Microfission Experiments", submitted to Nucl. Sci. Eng.
- [7] G.A. Smith, "Applications of Trapped Antiprotons", to appear in Hyperfine Interactions.
- [8] CALE users manual, July 1, 1991, R. Tipton, Lawrence Livermore National Laboratory, Mail Stop L-35, P.O. Box 808, Livermore, CA 94550.
- [9] C.E. Gazze, "Neutron Yields for the SHIVA Star Antiproton Microfission Experiment," M.S. thesis, The Pennsylvania State University, 1993.
- [10] F.S. Alsmiller *et al.*, Nucl. Sci. Eng. 79, 147 (1981).
- [11] E. Cheifitz *et al.*, Phys. Rev. C2, 256 (1970).
- [12] ENDF-102 Data Formats and Procedures for the Evaluated Nuclear Data File ENDF-6, Brookhaven National Laboratory, BNL-NCS-44945, (1990).
- [13] J. Franz *et al.*, Nucl. Phys. A490, 667 (1988).
- [14] W. Schimmerling *et al.*, Phys. Rev. C7, 248 (1973).

- [15] E.D. Minor, et al., *Z. Phys.*, **A336**, 447 (1990).
- [16] CCC-200/MCNP, Version 3A Code (1986). Code is distributed through RSIC, Oak Ridge National Laboratory.
- [17] B.R. Wienke, R.E. Seamon, and D.G. Madland, *Nucl. Sci. Eng.*, **113**, 86 (1993).

Table I. Coefficients for the fitted curves in Figure 8.

	H:U = 0:1	H:U = 3:1	H:U = 9:1
c₀ Neutrons/Antiproton	1.6300e+1	1.6300e+1	1.6300e+1
c₁ Neutrons/Antiproton-gm/cm ²	2.1120e-1	1.7110e-1	2.1040e-1
c₂ Neutrons/Antiproton-gm ² /cm ⁴	6.0850e-4	3.0000e-3	2.0000e-3
c₃ Neutrons/Antiproton-gm ³ /cm ⁶	0.0000e+0	0.0000e+0	0.0000e+0
c₄ Neutrons/Antiproton-gm ⁴ /cm ⁸	0.0000e+0	0.0000e+0	4.6660e-6

Table II. Coefficients for the uranium-238 escaped neutron yield.

	H:U = 0:1
c₀ Neutrons/Antiproton	1.6300e+1
c₁ Neutrons/Antiproton-gm/cm²	1.3030e-1
c₂ Neutrons/Antiproton-gm²/cm⁴	0.0000e+0
c₃ Neutrons/Antiproton-gm³/cm⁶	0.0000e+0

Table III. Neutron yields for unmoderated uranium-235 CALE cases.

	Case 1 ^a	Case 2 ^b	Case 3 ^c	Case 4 ^d
Average pr , (gm/cm ²)	21.4	21.6	21.0	19.3
Neutron Yield per Antiproton	21.56 ± 0.16	21.69 ± 0.16	21.50 ± 0.21	21.50 ± 0.21

^a Initial plasma temperature 2.0 eV, initial density 1×10^{19} ions/cm³.

^b Initial plasma temperature 2.0 eV, initial density 6×10^{19} ions/cm³.

^c Initial plasma temperature 5.0 eV, initial density 1×10^{19} ions/cm³.

^d Initial plasma temperature 5.0 eV, initial density 6×10^{19} ions/cm³.

Table IV. Neutron yields for moderated (H:U=3:1) uranium-235 CALE cases.

	Case 1 ^a	Case 2 ^b	Case 3 ^c	Case 4 ^d
Average pr , (gm/cm ²)	21.4	21.6	21.0	19.3
Neutron Yield per Antiproton	21.71 ± 0.21	21.87 ± 0.16	21.72 ± 0.21	21.92 ± 0.21

- a** Initial plasma temperature 2.0 eV, initial density 1×10^{19} ions/cm³.
- b** Initial plasma temperature 2.0 eV, initial density 6×10^{19} ions/cm³.
- c** Initial plasma temperature 5.0 eV, initial density 1×10^{19} ions/cm³.
- d** Initial plasma temperature 5.0 eV, initial density 6×10^{19} ions/cm³.

List of Figures

Figure 1. Schematic diagram of the SHIVA Star apparatus.

Figure 2. Neutron energy spectrum resulting from antiproton annihilation in uranium.

Figure 3. Neutron elastic cross section in hydrogen.

Figure 4. Neutron cross sections for uranium-235. Total cross section solid line (—), neutron producing cross section ($n \rightarrow xn$) dashed line (- - -), elastic dotted line (.....), inelastic ($n \rightarrow n'$) dot-dashed line (·-·-·-·).

Figure 5. Neutron cross sections for uranium-238. Total cross section solid line (—), neutron producing cross section ($n \rightarrow xn$) dashed line (- - -), elastic dotted line (.....), inelastic ($n \rightarrow n'$) dot-dashed line (·-·-·-·).

Figure 6. Neutron multiplicity from neutron induced reactions in uranium. Uranium-235 solid line (—), uranium-238 dashed line (- - -).

Figure 7. Secondary neutron energy distributions normalized to absolute yields. 20 MeV solid line (—), 155 MeV dashed line (- - -), 300 MeV dotted line (.....), and 455 MeV dot-dashed line (·-·-·-·).

Figure 8. Yields of neutrons escaping uniformly compressed uranium-235 targets for three levels of moderation.

Figure 9. Average energy of primary neutrons in uranium-235. Escaping neutrons solid line (—) and absorbed neutrons dotted line (.....).

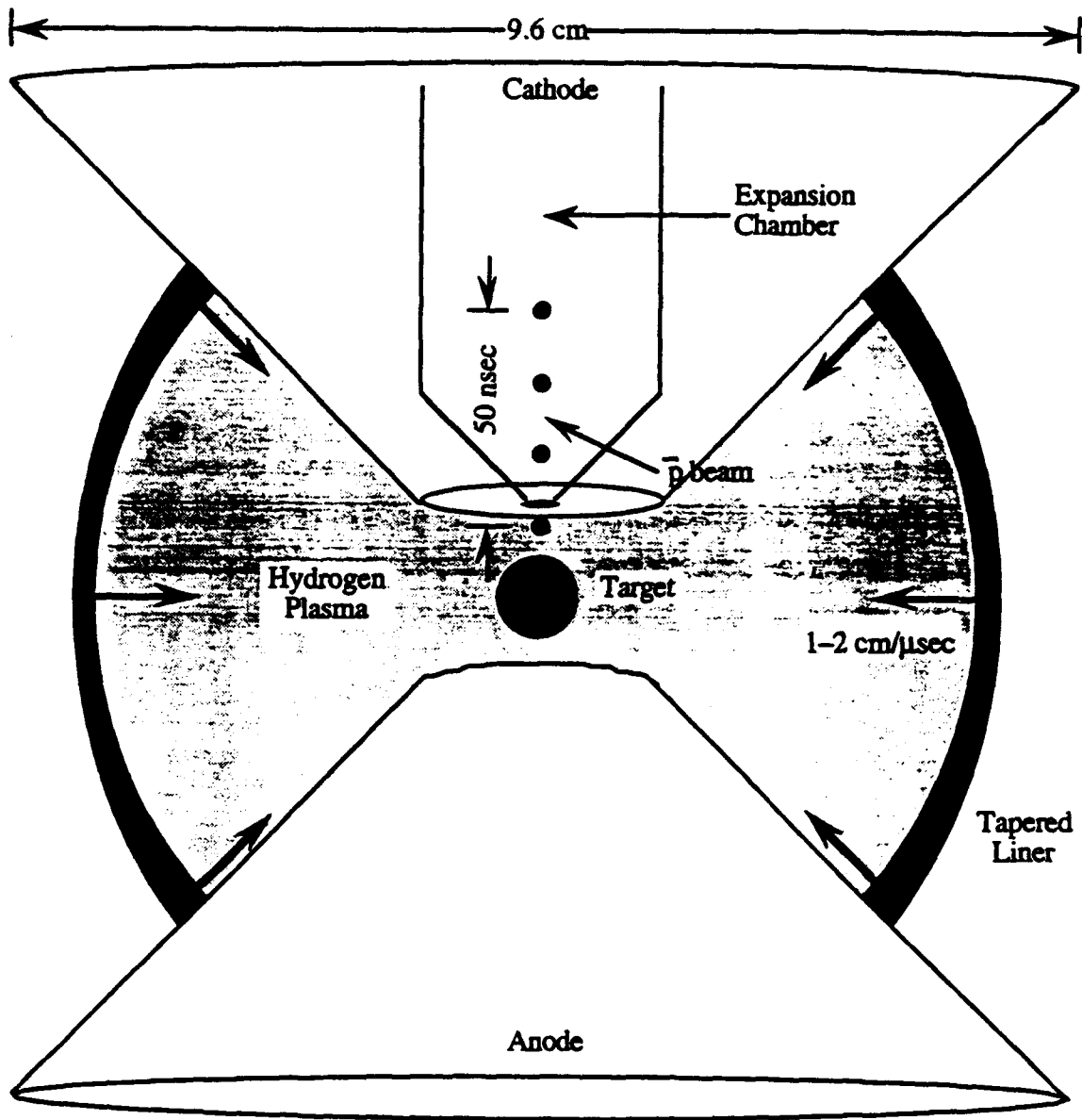


Figure 1

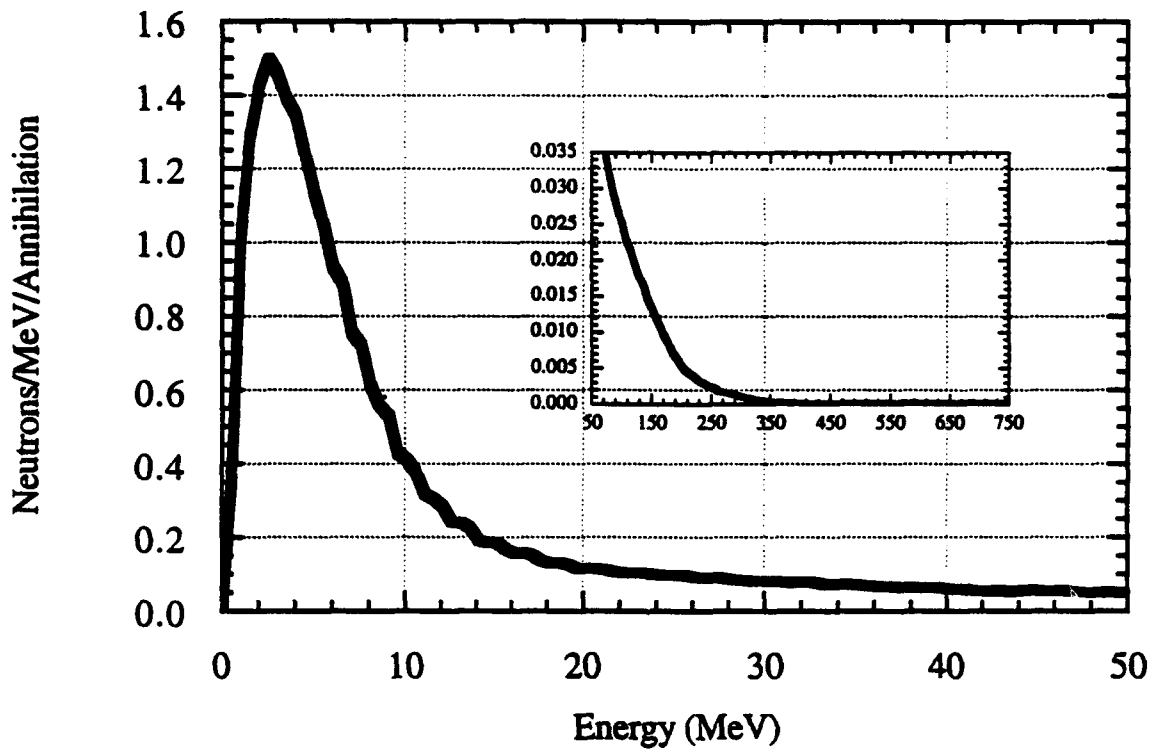


Figure 2

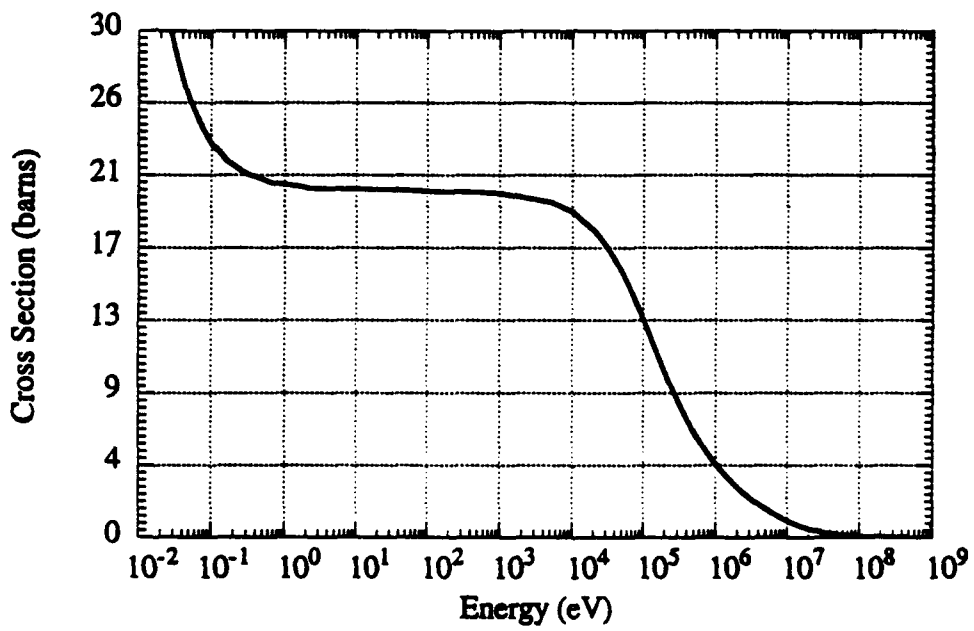


Figure 3

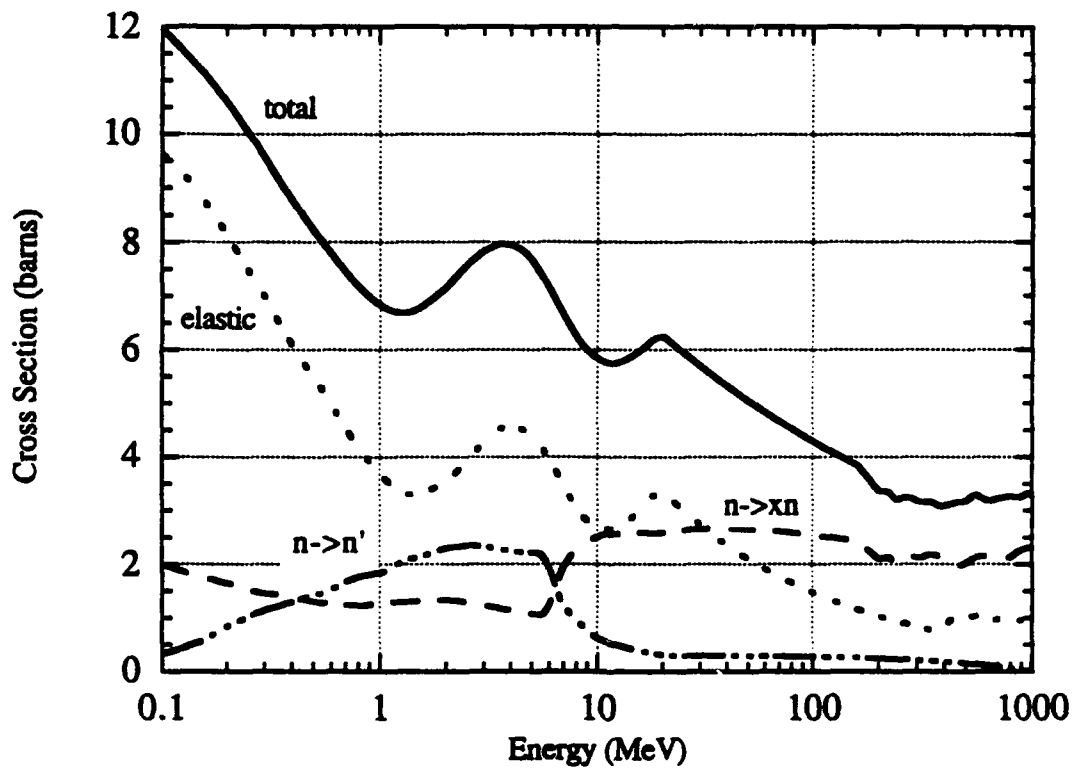


Figure 4

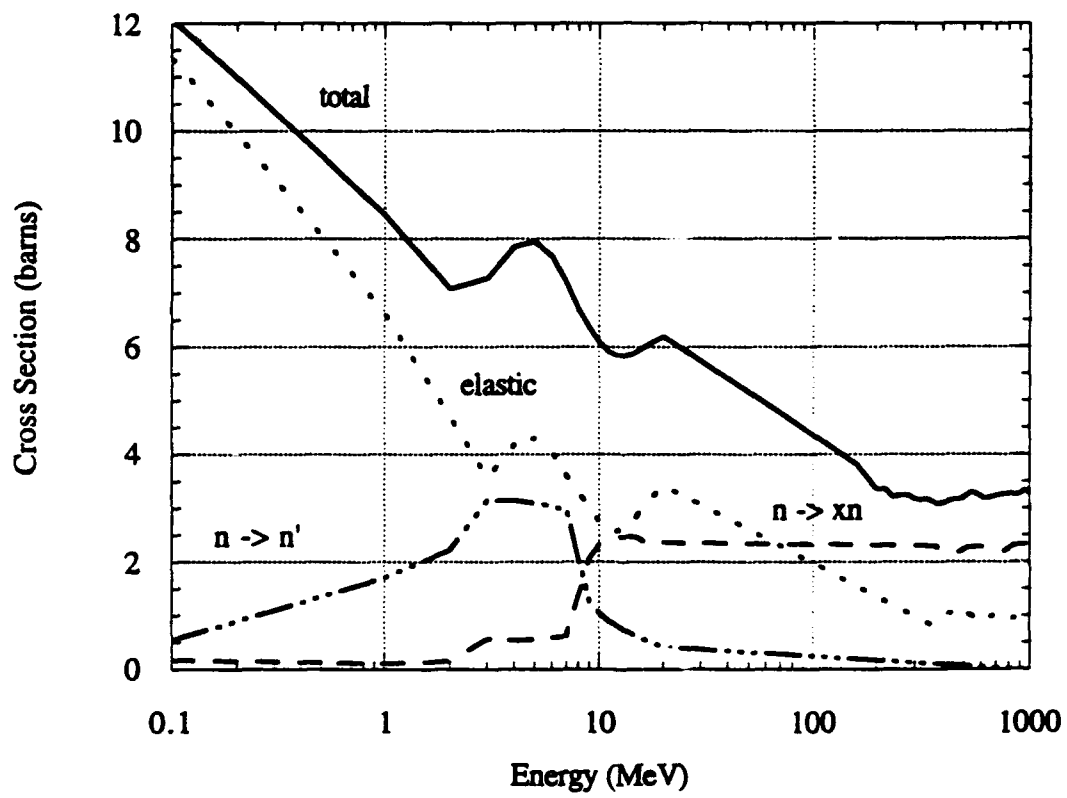


Figure 5

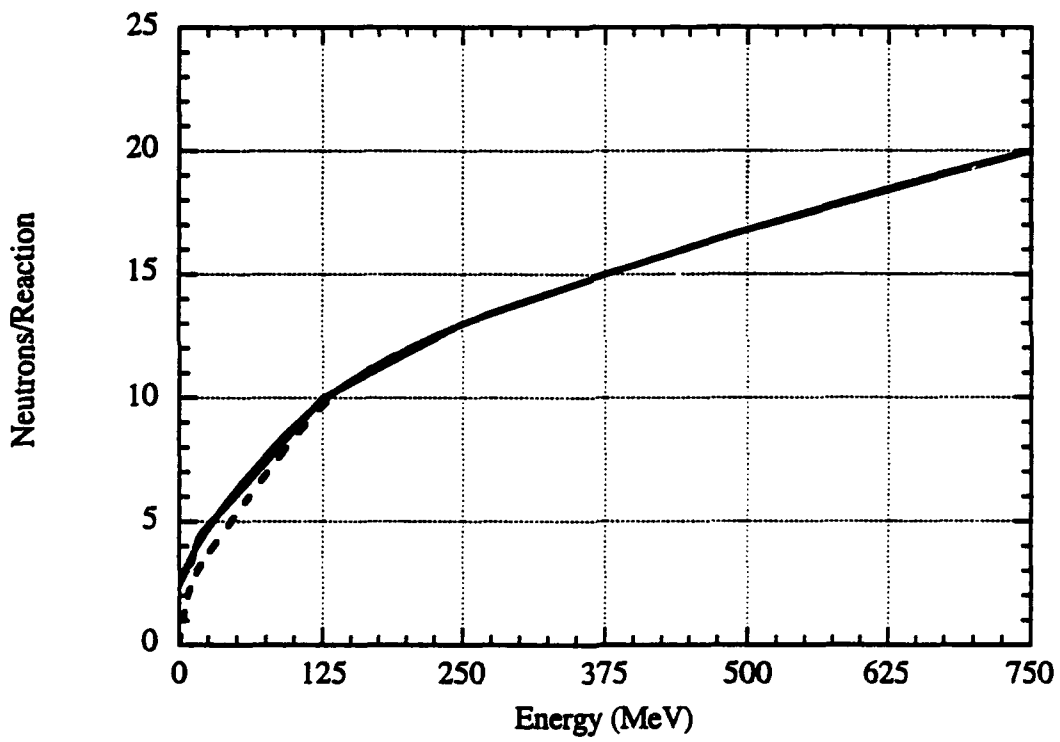


Figure 6

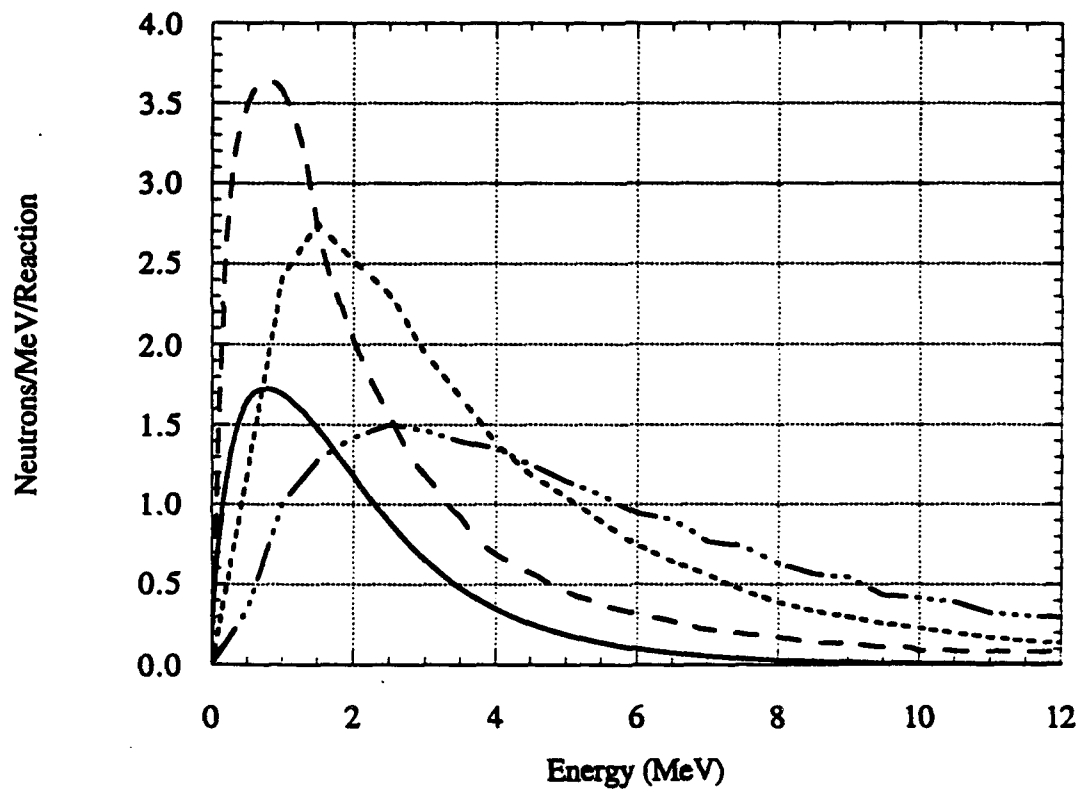


Figure 7

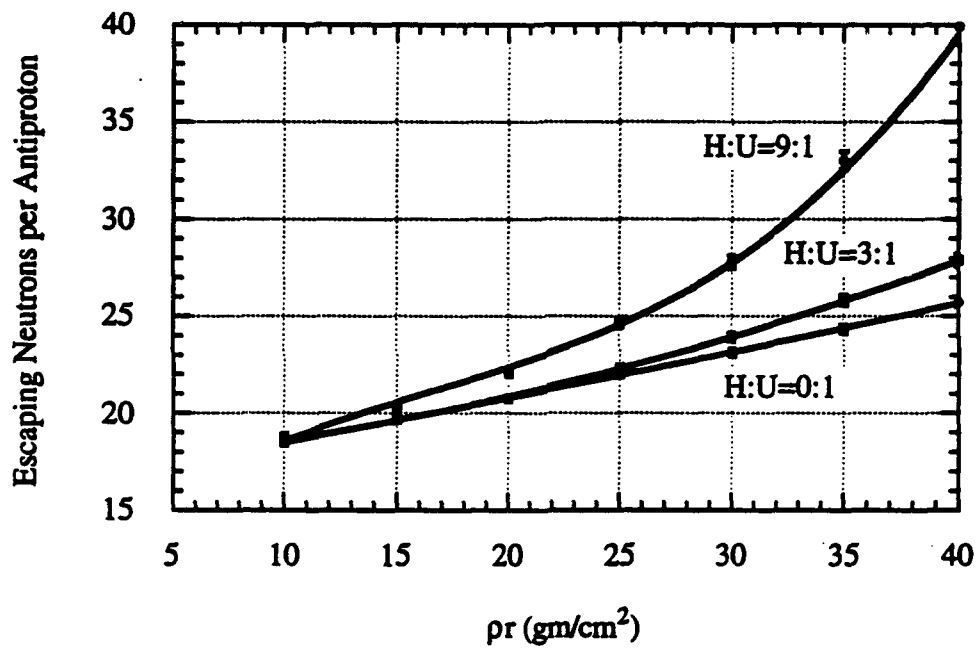


Figure 8

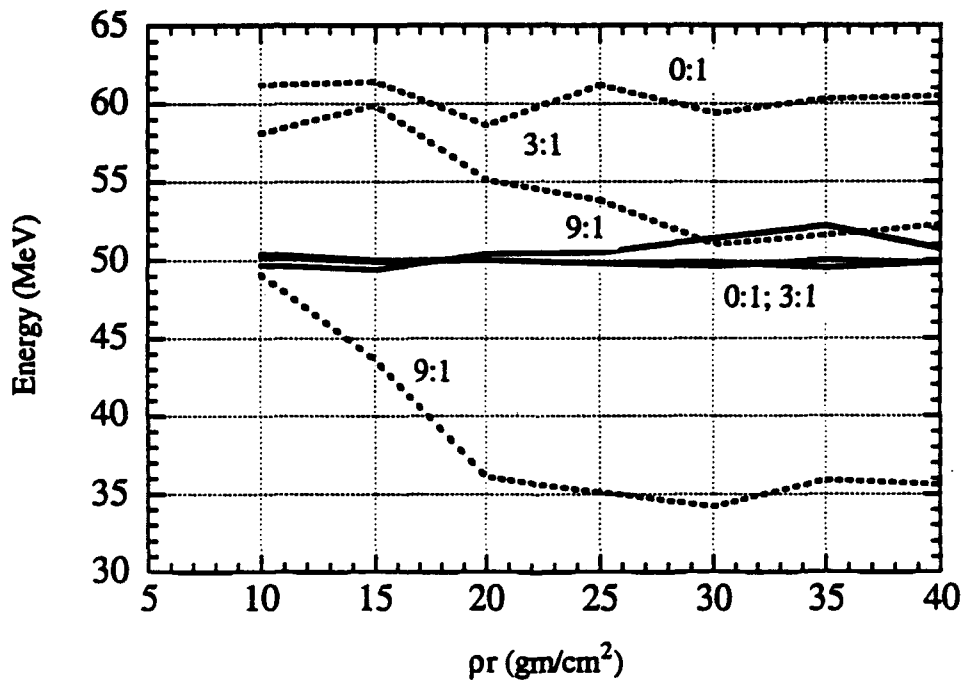


Figure 9

APPENDIX II

Containment and Neutron Production by Charged Pions in Antiproton Microfission Experiments*

Kumiko I. Higman and Richard J. Newton
Department of Nuclear Engineering

Raymond A. Lewis, Pi-Ren Chiang, and Gerald A. Smith
Laboratory for Elementary Particle Science, Department of Physics
The Pennsylvania State University
University Park, PA. 16802

ABSTRACT

Containment and interaction of charged pions in a solid liner implosion system are simulated. Pions are generated from annihilation of antiprotons at the surface of a compressed target. A three-dimensional Monte Carlo code has been developed to simulate the interaction of charged pions with the system. Neutron yields are presented for several 27 gram uranium targets compressed under different initial plasma conditions. Effects on neutron yields from the diffused magnetic field and density profiles at peak compression are discussed. Results show that the magnetic field at peak compression significantly increases overall neutron yields.

[Submitted to Nuclear Science and Engineering]

* Work supported in part by the Air Force Office of Scientific Research and the Jet Propulsion Laboratory (NASA).

I. INTRODUCTION

Antiproton annihilation has been shown to be a strong source of neutrons¹ and charged pions.² Under conditions of high density, the neutrons, and neutrons produced by charged pions, enable a significant reduction in the burn time and hence, size of fissile targets. The concept of antiproton microfission will be tested by compressing a small fissile target with an electromagnetically imploded solid liner.³ A subcritical test is possible at this time using presently limited numbers of antiprotons available. The experiment employs hydrogen plasma as a working fluid to compress the target and will be conducted at the SHIVA Star facility, located at the Phillips Laboratory, Kirtland AFB, NM. The solid liner implosion system is suitable due to its relatively high efficiency of energy conversion and capability of compressing high Z materials.

Pions from antiproton annihilation have a mass of about one-seventh of a nucleon mass, and are produced in three charge states. On the average 1.48 π^- , 1.36 π^0 and 0.99 π^+ are produced per annihilation in uranium (U), with an average kinetic energy of 232 MeV per pion. The π^0 's decay into two gamma-rays with a lifetime of 8.4×10^{-17} seconds, and contribute little to secondary interactions. The 26 nanosecond lifetime of charged pions is long compared to 1-2 nanoseconds required for a pion to escape or stop in the target. The π^- can stop in nuclear targets and produce secondary interactions at-rest, whereas π^+ can interact only in-flight due to their repulsion from positively charged nuclei.

In the absence of pion interactions, the experiment will yield a $\approx 20\%$ increase in neutrons relative to the primary source of neutrons 16.3.¹ The actual neutron yield will consist of primary neutrons and secondary neutrons induced by antiprotons, plus neutrons created by charged pions. Since path lengths for charged pions are increased due to the magnetic field diffused around the target, neutron multiplicities from charged pions are expected to be enhanced.

A three-dimensional Monte-Carlo code, PICALÉ, has been developed to simulate containment and interactions of charged pions in the apparatus at peak compression.⁴ PICALÉ is described in section II. Results obtained from PICALÉ for different initial plasma conditions in SHIVA Star are presented, and effects on neutron yields from magnetic field and density profiles at peak compression are discussed in section III. Results are summarized in section IV.

II. PION-CONTAINMENT MODEL

A. Simulation of Pion Motion and Interactions

PICALÉ tracks the motion of charged pions in a magnetic field, and simulates interactions of pions with the target (U) and aluminum (Al) liner (see Fig. 1), using the Monte Carlo method. Given the initial position and momentum of a pion born on the upper surface of the target, the code updates the pion's position at every time step by integrating the equations-of-motion. Magnetic field and density profiles in the simulations are calculated by a two-dimensional magnetohydrodynamics code, CALE.⁵ Because the time scale (≈ 1 -2 nanoseconds) for pion interactions is much shorter than the dwell time³ (≈ 400 nanoseconds) of peak compression, the magnetic field and density are assumed to be constant throughout the simulations. The Lorentz force due to the magnetic field is 240 MeV/cm, three orders magnitude larger than the force due to the electric field (≈ 90 KeV/cm). Therefore, effects on pion motion from both the static electric field and that induced by the time-dependent magnetic field are neglected.

Because most of pion's path length occurs at momenta above 100 MeV/c,² charged pions are assumed to lose energy at a constant rate of 1.09 MeV/gm-cm² due to collisions with atomic electrons.⁶ Interactions of pions with a nucleus include elastic scattering, inelastic scattering, and absorption. Elastic scattering at high energies shows strong forward diffraction scattering, and energy loss is assumed negligible in collisions with nuclei.

In an inelastic scattering, a pion may undergo charge exchange. However, experiments^{7,8} show that the fraction of charge exchange in the total reaction cross section is small (less than 1 %). The inelastic scattering angle and energy distributions of charged pions on nuclei are assumed to be uniform in the center-of-mass and laboratory frames, respectively.^{7,8}

The energy range of measured neutron yields and cross sections from pions is limited to low momenta.⁷⁻⁹ Since the momentum cut-off of pion spectra from antiproton annihilation is $1000 \text{ MeV}/c$,² it is necessary to further model neutron yields and cross sections due to pions up to this energy.

B. Energy-dependent Neutron Yields

Figure 2 shows neutron yields versus energy deposited in U and Al nuclei for different projectiles. The solid curve is a characterization of the yield in U, drawn through points at 455 MeV (antiprotons at-rest,²), 140 MeV (π^- at-rest,¹⁰) and 20-50 MeV (protons in-flight,¹¹). Based on the smooth energy dependence, it is concluded that neutron yields do not depend on the incident particle, but rather on the amount of energy deposited into a nucleus. Production of neutrons in U can be induced by absorption and inelastic scattering of charged pions, and the two mechanisms are treated separately in the simulation.

Due to lack of data, neutron yields for Al are scaled from U. A correlation between the average number of ejectiles from annihilation of an antiproton and the atomic mass number of the target is¹²

$$N_{\text{eject}} \propto A^{0.43}. \quad (1)$$

Assuming that the number of emitted neutrons is proportional to N_{eject} , energy-dependent neutron yields for Al are scaled from those for U. As seen in Fig. 2, data from Madey et al.¹³ agree with the scaled curve for Al (dotted curve).

C. Energy-Dependent Cross Sections

Cross sections from Ashery et al.⁸ for absorption and inelastic scattering of π^+ and π^- in Al are used. Although data for U are not available, those for Bi can be used to infer cross sections for U. Absorption and inelastic scattering cross sections for U can be scaled using⁸

$$\sigma_m \propto A^{q_m(E)}, \quad (2)$$

where $q_m(E)$ is an energy-dependent exponent, A is the target atomic mass, and the subscript m indicates the reaction, i.e., "absorption", "inelastic scattering", etc.

Exponents $q_m(E)$ of π^+ for various types of interactions and effective number N_{eff} of nucleons participating in the process are obtained from Ashery et al.⁸ For π^- , data for $q_m(E)$ are available only at 125 and 165 MeV,¹⁴ and are not sufficient to establish scaling. Therefore, the same $q_m(E)$ for π^+ is used for π^- as an approximation. Using Eq.(2), cross sections for U are scaled as

$$\sigma_{m,U}(E) = \sigma_{m,Bi}(E) \left[\frac{238}{209} \right]^{q_m(E)}. \quad (3)$$

Cross sections for interactions between charged pions and U at energies above 315 MeV are not available in the literature. However, it is reasonable to infer them from data from other projectiles. Reaction cross sections for U with proton incident energies up to 3 GeV,¹⁵ total and reaction cross sections for U and Al with neutron incident energies of 0.9-2.6 GeV,¹⁶ and total cross sections for U and Al at intermediate incident neutron energies (160-575 MeV),¹⁷ are used to infer cross sections for charged pions.

For an opaque nucleus, the geometric limit, $2\pi R^2$, for the total cross section, is the sum of cross sections due to absorption and diffractive processes, and both cross sections approach the geometric limit asymptotically.¹⁷ Therefore, it is reasonable to assume that both absorption and inelastic scattering cross sections are approximately constant at high

energies. Both the reaction and absorption cross sections of π^+ and π^- for U and Al for energies above 400 MeV are interpolated between data at energies below 315 MeV and values at higher energies.

To model absorption cross sections at low energies, data obtained by Navon et al.¹⁸ at 50 MeV are used. The data do not include U and Al. However, a correlation between absorption cross sections and atomic mass number at 50 MeV is given, and cross sections for U and Al are deduced using this correlation.

For cross sections at energies below 50 MeV, the following features¹⁹ are included:

- a) The absorption cross section of π^- increases to infinity as the pion energy approaches zero;
- b) The absorption cross section of π^+ drops to zero around 20 MeV for U and 4 MeV for Al, energies required to penetrate the Coulomb barrier;
- c) The inelastic scattering cross sections of π^+ and π^- become very small at low energies and rapidly drop to zero at a threshold value.

Gathering together all of the measurements and features discussed above, energy-dependent cross sections for π^- and π^+ interactions with U and Al nuclei are shown in Figs. 3 and 4 (U), and Figs. 5 and 6 (Al), respectively.

III. RESULTS AND DISCUSSION

A. Effects of Magnetic Field and Density Profile

The preferred direction of antiproton injection is opposite to the direction of current (see Fig. 1). This preference results from the charge asymmetry and relative cross sections of pions. With such an arrangement, a π^- turns toward the target and a π^+ turns away from the target. Since a π^- produces more neutrons than a π^+ , neutron yields will be enhanced

by choosing this direction for antiproton injection. In addition, as discussed later, the magnetic field direction also helps focus the antiproton beam.

CALE results for the compression of a 27 gram target with initial plasma conditions of 2 eV and $1 \times 10^{19} \text{ cm}^{-3}$ are used for the simulations.³ At peak compression, the target has density fluctuations up to 90 g/cm^3 , and magnetic fields of several hundred Tesla. Results of simulations with/without target compression and/or magnetic field are summarized in Table I. Case A is the baseline simulation, wherein the antiprotons are injected before compression. At peak compression with magnetic field (case B), the neutron yield increases by a factor of 3.6 due to the combination of compression and magnetic field. For case C, with magnetic field ignored in the simulation, the neutron yield increases by only a factor of 2.0, implying that the magnetic field accounts for a factor of 1.8 increase in yield.

Orbits of three typical charged pions in the magnetic field are shown in Fig. 7 (elevation view as shown in Fig. 1) and Fig. 8 (top view). Path lengths of charged pions, especially in the liner, increase due to the magnetic field as seen in Table I. Comparing cases B and C in Table I, the magnetic field increases the path lengths of charged pions, especially π^- , by factors ranging from 1.04 to 1.94. The percentage of stopped π^- is also increased by nearly a factor of 4.

B. Neutron Yields

In this section neutron yields for four CALE cases are presented. These results, and their corresponding initial plasma conditions, are summarized in Table II. For comparison, case A discussed in the previous section is also listed.

Case 2 gives the largest yield of 4.574 ± 0.042 neutrons from the target. The average target density for case 2 is largest among all cases, thus increasing interactions between pions and the target. The magnetic field also increases path lengths of π^- and π^+ ; therefore, the neutron yield is further enhanced. Effects from the magnetic field can be seen in the

difference in π^- and π^+ path lengths. Since the magnetic field direction increases the path length of π^- more than that of π^+ , a stronger magnetic field results in a greater difference in the path lengths. As seen in Table II, the differences in path lengths of π^- and π^+ in case 2 are the largest among the four cases. Therefore, the magnetic field enhances the neutron yield the most in case 2.

Azimuthal magnetic field contours for case 2 are shown in Fig. 9. A large magnetic field of ≈ 1 MGauss is predicted within 0.1 cm of the beam axis ($r = 0$). By Ampere's law, the magnetic field must decrease to zero on the axis. An antiproton moving off the beamline will be deflected radially inward by the Lorentz force. Taking into account energy loss per unit length, dE/ds , due to antiproton interactions with electrons, we numerically ray-trace antiproton trajectories in this field. Typical trajectories inside the compression chamber are shown in Fig. 10. As seen, a beam with a maximum spread of 0.9 mm from $r = 0$ and initial energy of 4 MeV hits the target surface within a 0.2 mm radius from $r = 0$. In other words, the chosen magnetic field direction focuses the antiproton beam onto the target.

Neutron yields from the liner are greatly enhanced (factor of 40 to 60), compared with those for case A, for all four cases. As seen in Fig. 9, this is because the magnetic field is much stronger in the liner than in the target, and the liner thickness is greatly increased under compression; hence, the average path length of pions is dramatically larger in the liner under compression.

The magnetic field profile at peak compression differs somewhat for different initial plasma conditions. As a consequence, neutron yields induced by charged pions are more sensitive to initial plasma conditions than those induced by primary neutrons generated by annihilation of antiprotons. To illustrate, the gain in neutron yields¹ from the compressed target induced by parent neutrons is enhanced by a factor of ≈ 1.8 compared to the

uncompressed target case A, whereas the factor varies between 1.95 and 3.43 for neutron yields induced by charged pions.

The version of CALE used in these simulations does not include radiation and thermal conduction. Including thermal radiation, we find that the target density at peak compression is relatively unchanged for cases 1-3, and increases by 10 % for case 4.³ Therefore, neutron yields at peak compression including radiation and thermal conduction should be similar to the results in Table II.

IV. SUMMARY

Containment of charged pions generated at annihilation of an antiproton have been simulated. Neutron yields resulting from interactions between charged pions and the target and liner are obtained. The results are summarized as follows:

- a) The magnetic field at peak compression increases neutron yields induced by charged pions by a factor of $\approx 2.4 - 4.1$ over yields with an uncompressed target without magnetic field;
- b) Neutron yields induced by charged pions are sensitive to initial plasma conditions used for compression, since different initial plasma conditions significantly change the magnetic field profile at peak compression;
- c) The highest neutron yields induced by charged pions per antiproton are 4.6 from the target and 1.0 from the liner. Including 16.3 primary neutrons, 3.0 neutrons induced by parent neutrons,¹ and 5.6 neutrons induced by pions, approximately 25 neutrons are produced from the target and liner at annihilation. This represents a gain of a factor of 1.3 over an uncompressed target .

REFERENCES

1. C. E. Gazze et al., "Neutron Yields for Antiproton Microfission Experiments," submitted to Nucl. Sci and Eng.
2. E. D. Minor *et al.*, *Z. Phys. A* **336**, 461 (1990).
3. P-R. Chiang et al., "Target Compression by Working Fluids Driven with Solid Liner Implosions," submitted to J. Appl. Phys.
4. K. I. Higman, "Compression and Pion Recirculation in Antiproton-Induced Microfission", Ph.D. thesis, The Pennsylvania State University, 1993.
5. CALE users manual, July 1, 1991, Robert Tipton, Lawrence Livermore National Laboratory, Mail Stop L-35, P.O. Box 808 Livermore, LA 94550.
6. *Particle Properties Data Booklet*, extracted from the Review of Particle Properties, Phys. Rev. **D45**, part 2 (June 1992).
7. J. P. Schiffer, Nucl. Phys. **A335**, 339 (1980).
8. D. Ashery et al., Phys. Rev C **23**, 2173 (1981)
9. K. Nakai et al., Phys. Rev. Lett. **44**, 1446 (1980).
10. H. P. Isaak et al., Nucl. Phys. A **392**, 368 (1983).
11. H. Baba et al., Nucl. Phys. **A159**, 625 (1970).
12. J. Cugnon et al., Nucl. Phys. **A470**, 558 (1987).
13. R. Madey et al., Phys. Rev. C **25**, 3050 (1982).
14. D. Ashery and J. P. Schiffer, Ann. Rev. Nucl. Part. Sci. **36**, 207 (1986).
15. F. S. Alsmiller et al., Nucl. Sci. Eng. **79**, 147 (1981).
16. W. Schimmerling et al., Phys. Rev. C **7**, 248 (1973).
17. J Franz et al., Nucl. Phys. **A490**, 667 (1988).
18. I. Navon et al., Phys. Rev. C **28**, 2548 (1983).
19. E. Segre, *Nuclei and Particles - An Introduction to Nuclear and Subnuclear Physics*, 2nd edition, (Benjamin Publishing, Reading, Mass., 1977).

Table I. Average pathlengths of pions in target and liner, fraction of stopped π^- in target, and resultant neutron yields for 27 gram target, 2 eV and $1 \times 10^{19} \text{ cm}^{-3}$ initial working fluid conditions.

Items	Case A	Case B	Case C
Avg l_{path} of π^- in target (mm)	3.179 ± 0.027	3.435 ± 0.025	2.604 ± 0.020
Avg l_{path} of π^+ in target (mm)	3.233 ± 0.019	2.825 ± 0.017	2.709 ± 0.015
Avg l_{path} of π^- in liner (mm)	0.439 ± 0.003	15.181 ± 0.123	7.828 ± 0.048
Avg l_{path} of π^+ in liner (mm)	0.445 ± 0.002	9.725 ± 0.062	8.133 ± 0.036
% of stopped π^- in target (%)	0.46	4.73	1.19
Neutron yield from target per \bar{p}	1.335 ± 0.022	3.810 ± 0.038	2.151 ± 0.028
Neutron yield from liner per \bar{p}	0.016 ± 0.001	1.001 ± 0.012	0.557 ± 0.009
Total neutron yield per \bar{p}	1.351 ± 0.022	4.811 ± 0.040	2.708 ± 0.029

Case A: Uncompressed target

Case B: CALE density profiles and magnetic field

Case C: CALE density profiles without magnetic field

Table II. Average pathlengths of pions in target and liner, fraction of stopped π^- in target, and resultant neutron yields for 27 gram target and four cases (1-4) of initial working fluid conditions. Case A from Table I is repeated for comparison.

Items	Case A	Case 1 (2 eV, $1 \times 10^{19} \text{cm}^{-3}$)	Case 2 (2 eV, $6 \times 10^{19} \text{cm}^{-3}$)	Case 3 (5 eV, $1 \times 10^{19} \text{cm}^{-3}$)	Case 4 (5 eV, $6 \times 10^{19} \text{cm}^{-3}$)
Avg lpath of π^- in target (mm)	3.179±0.027	3.435±0.025	4.041±0.029	3.334±0.024	3.111±0.024
Avg lpath of π^+ in target (mm)	3.233±0.019	2.825±0.017	2.834±0.018	2.960±0.018	3.180±0.019
Avg lpath of π^- in liner (mm)	0.439±0.003	15.181±0.123	15.675±0.124	13.326±0.114	10.955±0.085
Avg lpath of π^+ in liner (mm)	0.445±0.002	9.725±0.062	9.102±0.056	9.829±0.067	10.273±0.066
% of stopped π^- in target (%)	0.46	4.73	5.18	3.60	3.13
Neutron yield from target per \bar{p}	1.335±0.022	3.810±0.038	4.574±0.042	3.365±0.035	2.609±0.031
Neutron yield from liner per \bar{p}	0.016±0.001	1.001±0.012	0.987±0.012	0.824±0.011	0.666±0.010
Neutron yield from target and liner per \bar{p}	1.351±0.022	4.811±0.040	5.561±0.044	4.189±0.037	3.275±0.033
Neutron yield from target induced by parent neutrons (Ref. 1)	1.63±0.03	2.94±0.04	3.02±0.04	2.91±0.05	2.91±0.05
Total neutron yield per \bar{p} *	19.28	24.05	24.88	23.40	22.49

*Includes primary neutron yield of 16.3 neutrons per \bar{p} .

Figure Legend

- Fig. 1 Schematic of spherical solid liner implosion system with working fluid shown at peak compression.
- Fig. 2 Neutron yields versus energy deposited into the nucleus for U (solid curve) and Al (dashed curve). Data are taken from Refs. 2 (solid circle), 10 (solid square), 12 (open circles), and 13 (solid triangle).
- Fig. 3 Energy-dependent neutron producing cross sections for π^- interactions with U: inelastic (dashed curve), absorption (dot-dashed curve).
- Fig. 4 Energy-dependent neutron producing cross sections for π^+ interactions with U: inelastic (dashed curve), absorption (dot-dashed curve).
- Fig. 5 Energy-dependent neutron producing cross sections for π^- interactions with Al: inelastic (dashed curve), absorption (dot-dashed curve).
- Fig. 6 Energy-dependent neutron producing cross sections for π^+ interactions with Al: inelastic (dashed curve), absorption (dot-dashed curve).
- Fig. 7 Three typical pion orbits seen in the elevation view.
- Fig. 8 Three typical pion orbits from Fig. 7 seen in the top view.
- Fig. 9 Magnetic field profiles at peak compression for case 2 (Table II).
- Fig. 10 Enlarged view of target, working fluid region showing focusing of antiproton beam rays (solid lines).

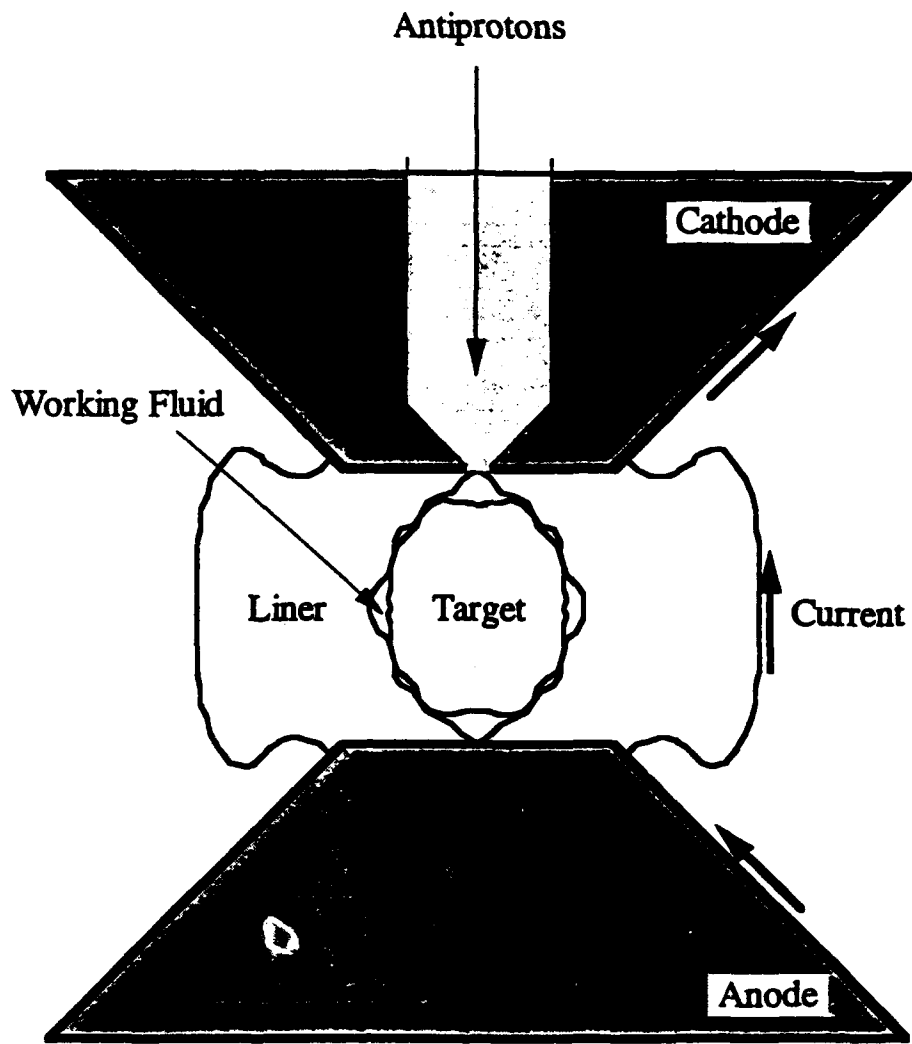


Fig. 1

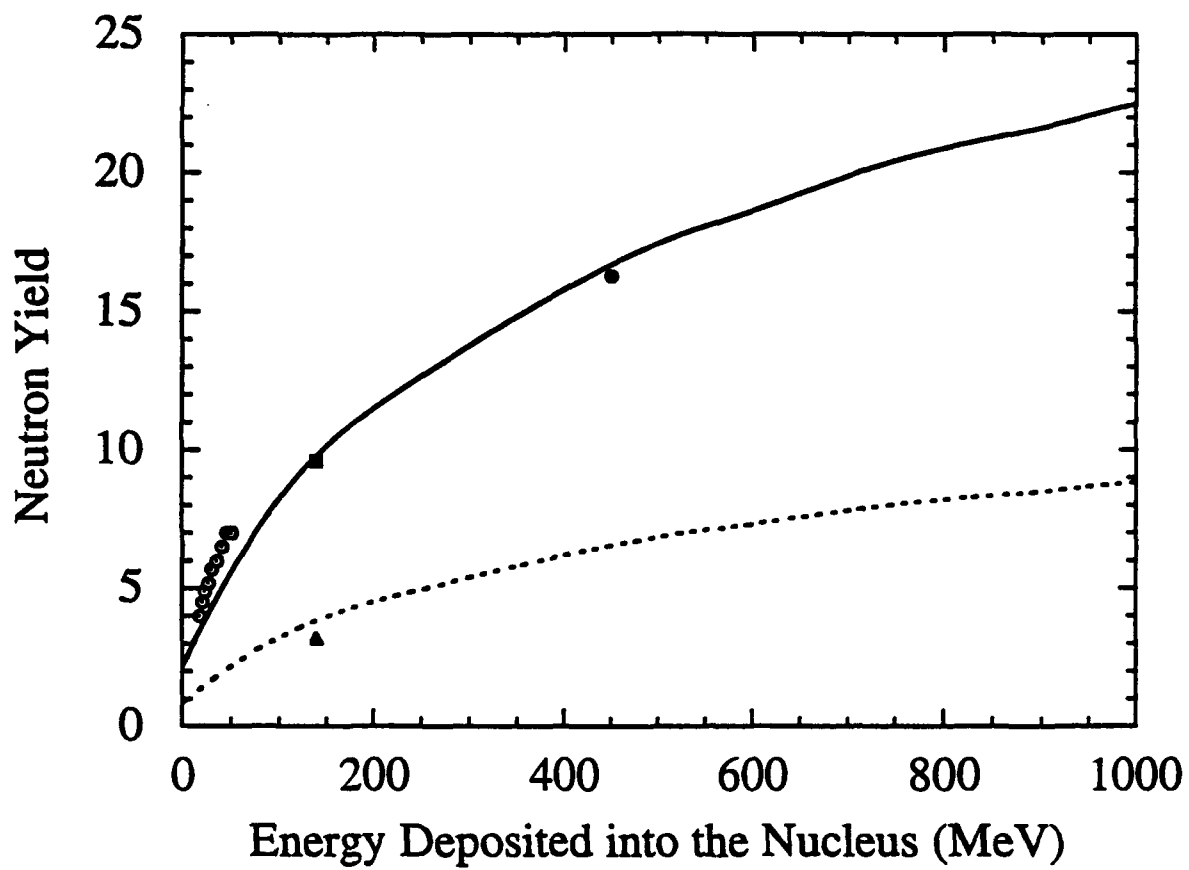


Fig. 2

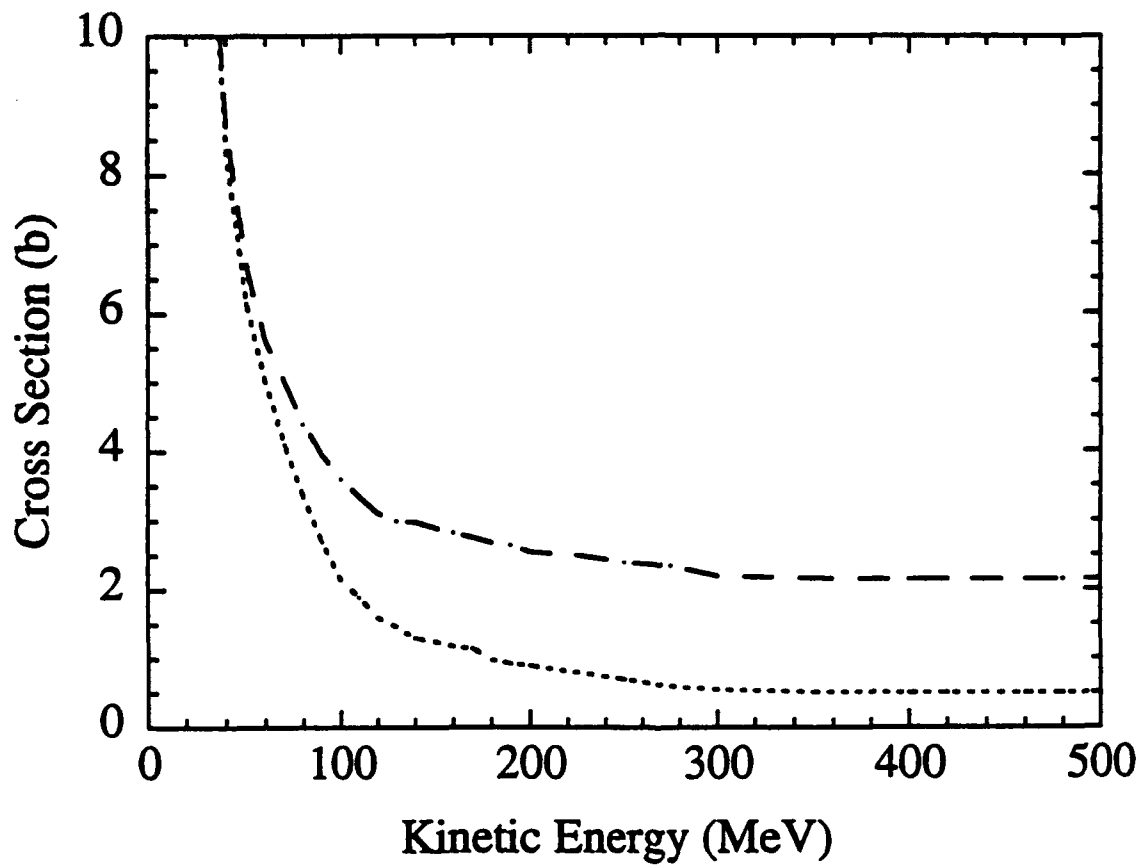


Fig. 3

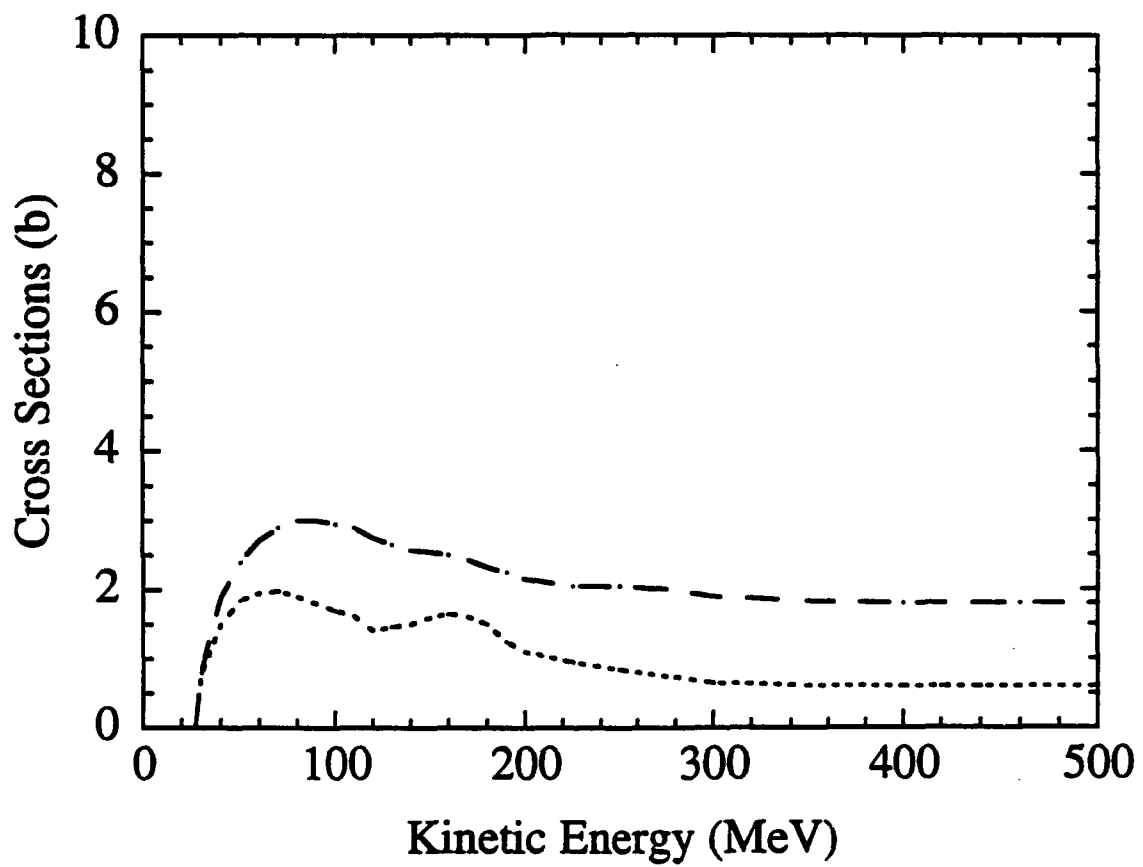


Fig. 4

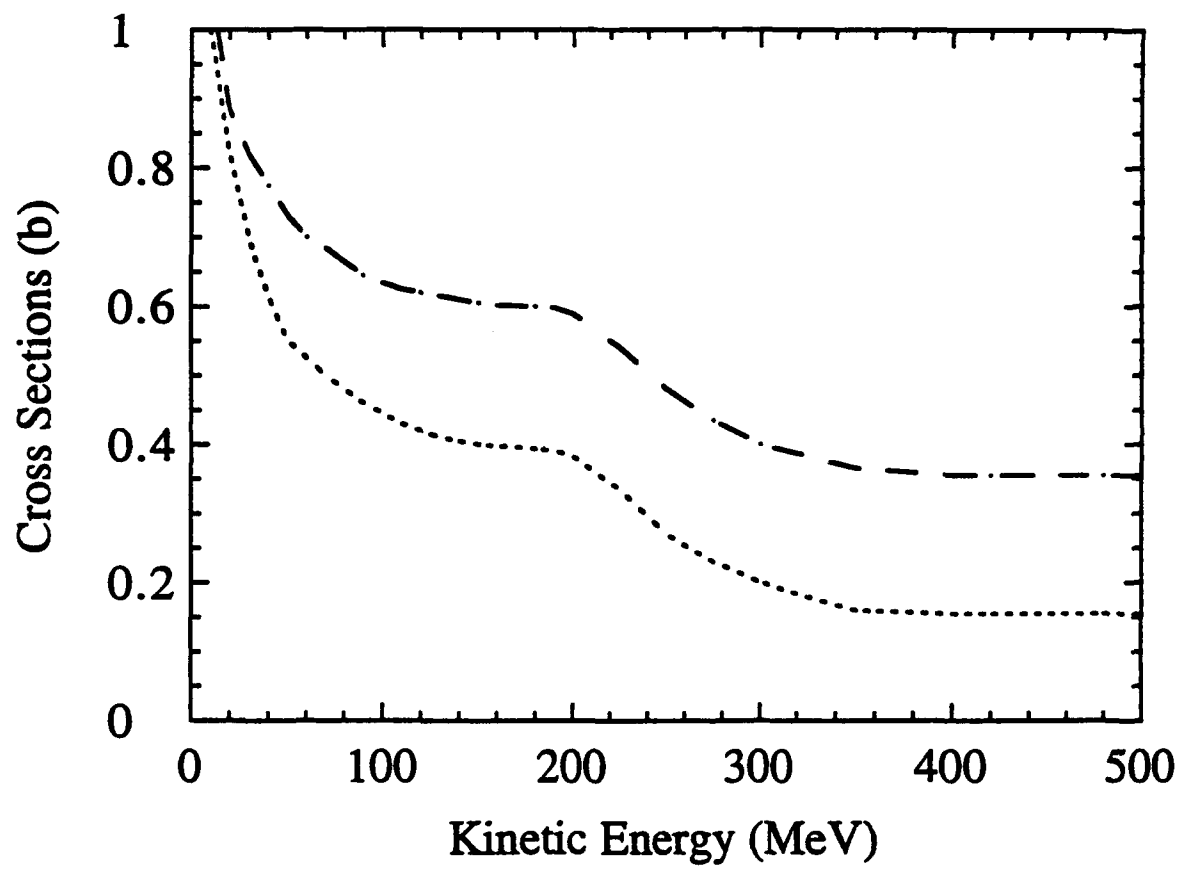


Fig. 5

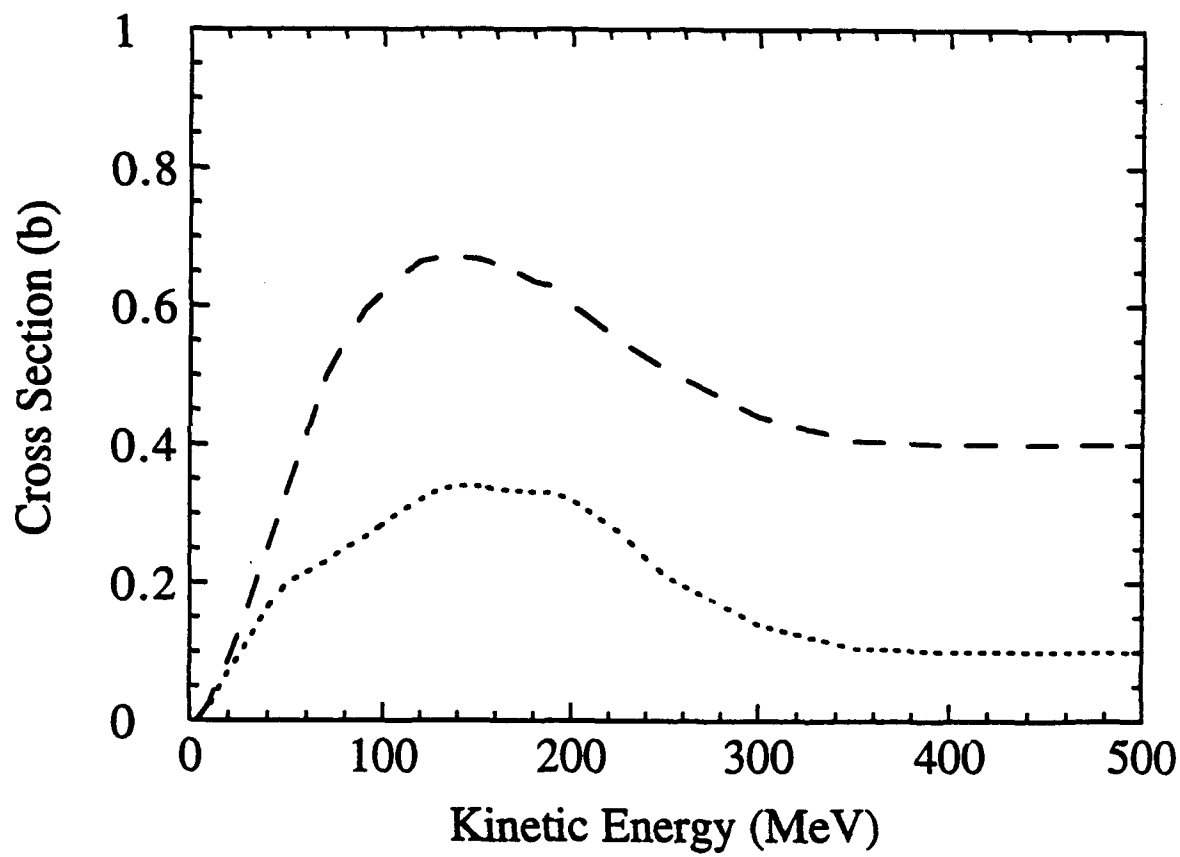


Fig. 6

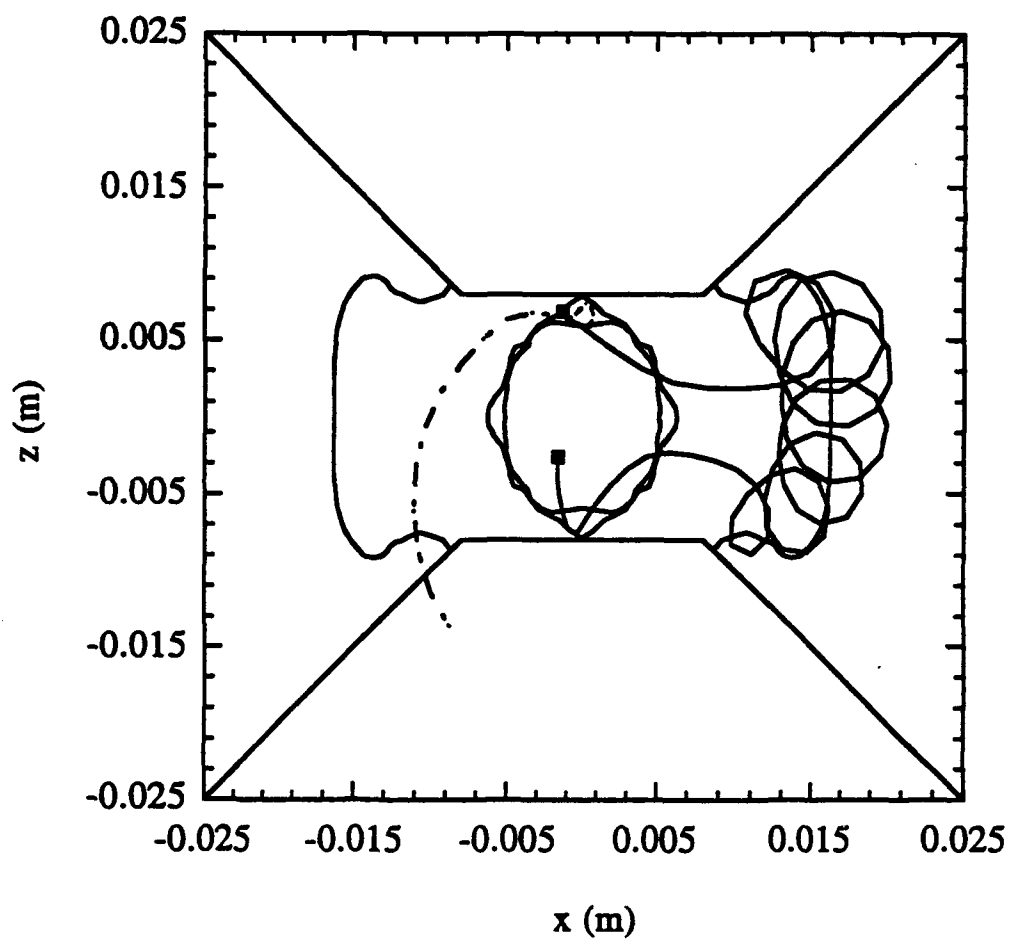


Fig. 7

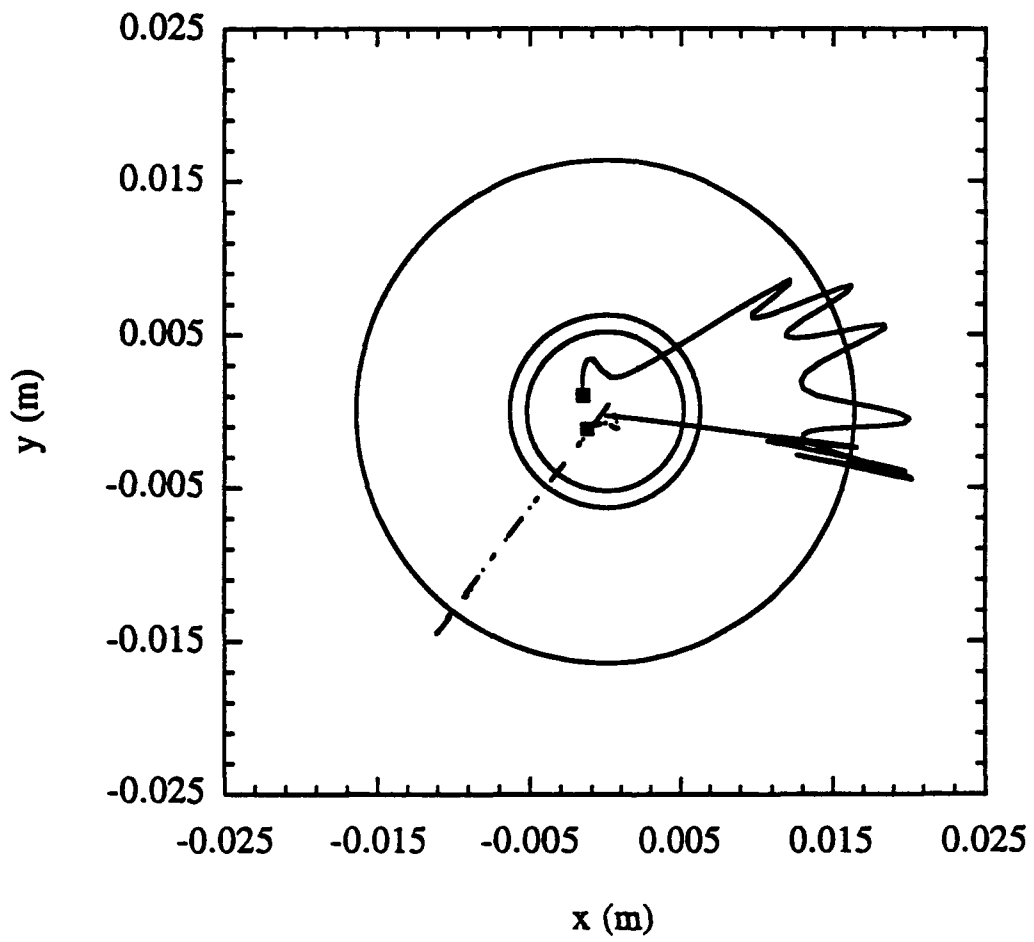


Fig. 8

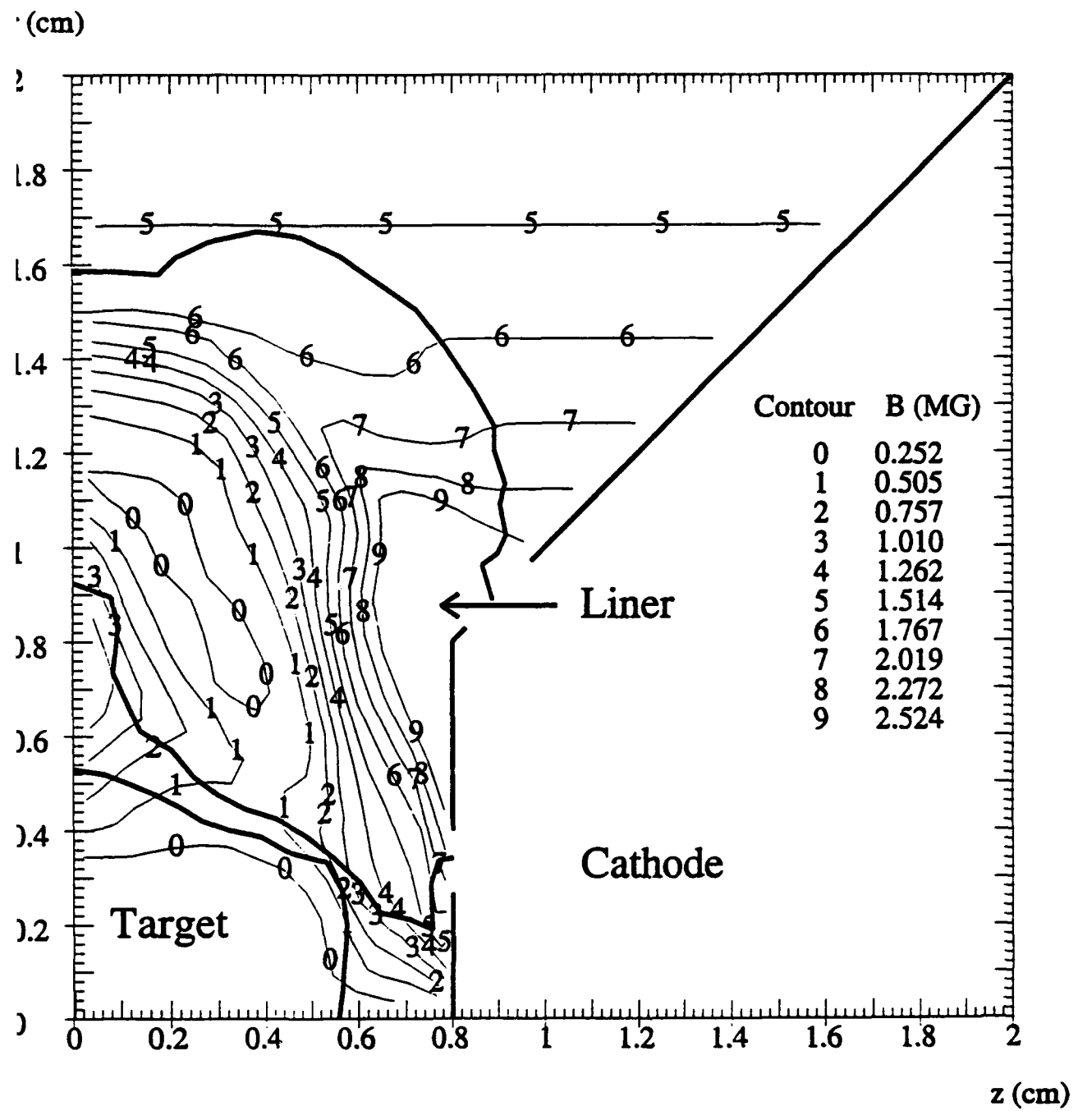


Fig. 9

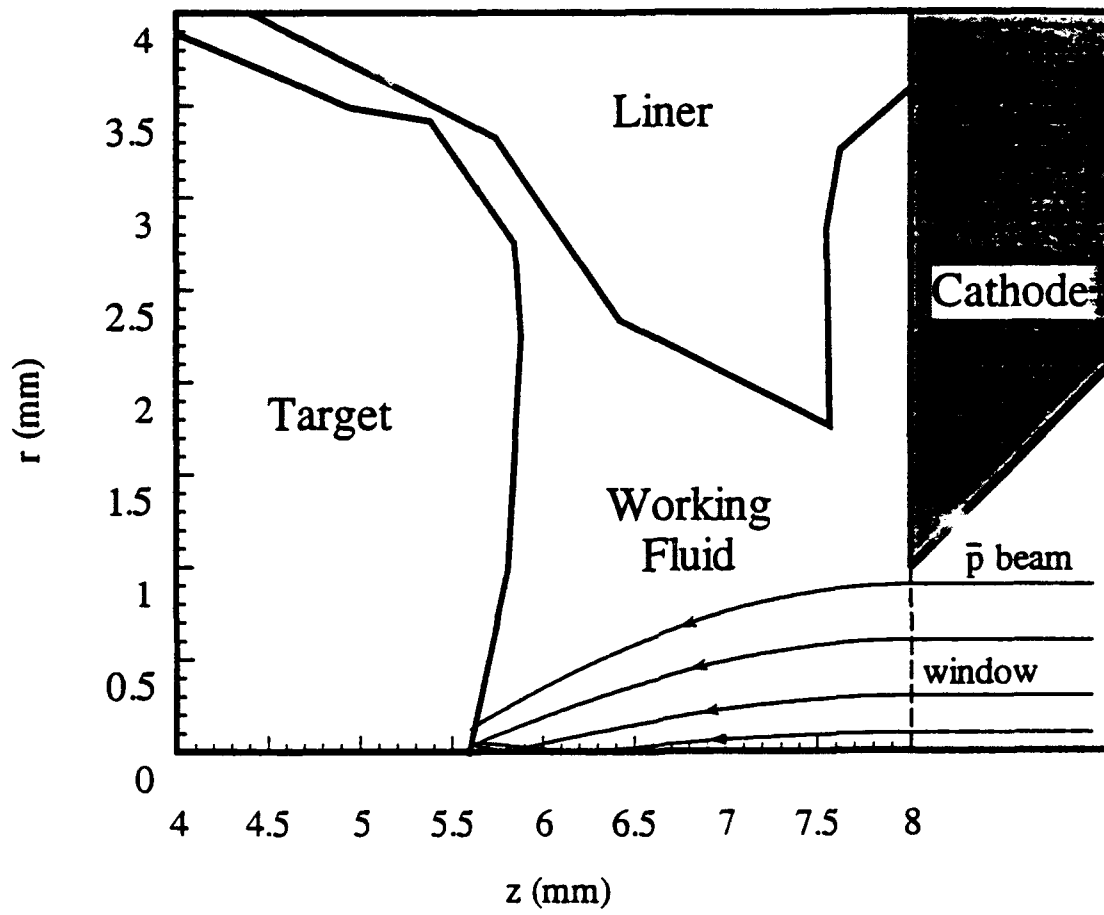


Fig. 10

APPENDIX III

The Pennsylvania State University
The Graduate School

ANTIPROTON BEAM-HYDROGEN PLASMA INTERACTIONS
IN THE SHIVA STAR MICROFISSION EXPERIMENT

A Thesis in
Aerospace Engineering

by
Martin J. Chiaverini

Submitted in Partial Fulfillment
of the Requirements
for the Degree of

Master of Science

December 1993

ABSTRACT

Antiproton annihilation on uranium nuclei is used to initiate microfission during the SHIVA Star experiment. A 17 meter long, evacuated injection pipe transports the antiprotons from a Penning storage trap to the target region. In order to reach the uranium target, the antiproton beam must penetrate the dense, hydrogen working fluid which surrounds the target and contaminates a portion of the injection pipe. While travelling through the fully ionized hydrogen plasma, the antiprotons lose energy to the plasma electrons, undergo deflection from the plasma protons, and may also annihilate with the protons. As a result of these collisions, the antiprotons may either lose all their energy in the plasma, and not reach the target, or may undergo deflection into the pipe wall. To ensure that a high percentage (at least 80%) of the antiprotons in the beam reach the target and initiate a microfission, one must determine the beam energy necessary to overcome these loss mechanisms.

The antiproton energy loss, deflection, and annihilation all depend on the plasma density profile in the injection pipe at the time of beam injection. The density profile, in turn, depends on the beampipe geometry and the state of the plasma as it streams from the target chamber into the beampipe entrance. The two-dimensional, magneto-hydrodynamics program CALE provides plasma properties at the entrance to the beampipe, while the magnetic pressure (a by-product of the target compression process) exerted on the beampipe governs its geometry. Using the CALE data and specified beampipe geometry, program BLAST57 determines the plasma density profile in the beam pipe. Next, program SWMXC2 uses this density profile to determine the antiproton energy loss, deflection, and annihilation.

Eight cases, determined by initial plasma conditions and target shape, were studied. Results indicate that electronic energy loss governs the necessary beam energy for the cases with a spherical target, while antiproton deflection influences the required energy for the cylindrical target cases. The necessary beam energy for the spherical target cases ranged from 3.0 MeV to 4.6 MeV. The antiprotons underwent an rms scattering distance of about 0.2 mm from the beam centerline in these cases. All cylindrical target cases required an energy of 1.2 MeV, and had rms scattering lengths of about 0.5 to 0.6 mm. Proton-antiproton annihilation does not represent a serious problem in either scenerio. The cylindrical target displayed two major advantages over the spherical target: lower required beam energy and smaller plasma leakage into the injection pipe.

CONTENTS

LIST OF FIGURES	. vii
LIST OF TABLES	. ix
ACKNOWLEDGMENTS	. x
Chapter 1 INTRODUCTION	. 1
Chapter 2 THE PLASMA EXPANSION	. 8
2.1 Introduction	. 8
2.2 The Diamond Window	. 8
2.3 Window Fragmentation	. 14
2.4 Magnetic Pressure on Cathode	. 16
2.5 Ohmic Heating	. 21
2.6 Plasma Considerations	. 23
2.7 Determining the Plasma Density Profile	. 33
Chapter 3 ANTIPROTON ENERGY LOSS IN FULLY IONIZED PLASMAS	. 39
3.1 Introduction	. 39
3.2 Binary Coloumb Collisions	. 39
3.3 Debye Shielding and Plasma Frequency	. 42
3.4 Energy Loss through Multiple Coloumb Collisions	. 45
3.5 Antiproton Range	. 51
3.6 Comparison with Experimental Results	. 55

Chapter 4 ANTIPROTON DEFLECTION IN FULLY IONIZED PLASMAS 57
4.1 Introduction 57
4.2 Binary Antiproton-Ion Collisions 57
4.3 The Rutherford Scattering Cross Section 61
4.4 Multiple Scatters 64
4.5 Sample Results 68
Chapter 5 ANTIPROTON ANNIHILATION 72
5.1 Introduction 72
5.2 Nuclear Cross Sections 73
5.3 Sample Results 75
5.4 Corrections for a Hot Plasma 80
Chapter 6 RESULTS 85
6.1 Case 1 88
6.2 Case 2 88
6.3 Case 3 90
6.4 Case 4 92
6.5 Cylindrical Target 94
6.6 Case 5 101
6.7 Cases 6, 7, and 8 104
Chapter 7 CONCLUSIONS 105
REFERENCES 108
Appendix CALE DATA 110

LIST OF FIGURES

Figure 1.1	Schematic Diagram of Shiva Star Apparatus	6
Figure 1.2	Expanded View of Target Region	7
Figure 2.1	Diamond Window Geometry	11
Figure 2.2	Beampipe Magnetic Optics	13
Figure 2.3	Design of the Anode	16
Figure 2.4	Time for Stress Waves to Reach Beampipe	19
Figure 2.5	Stress on Beampipe	20
Figure 2.6	Variation of Sticking Coefficient with Energy	32
Figure 2.7	A Maxwellian Velocity Distribution	34
Figure 2.8	A Sample Plasma Density Profile	36
Figure 3.1	Coloumb Collision between an Ion and Electron	40
Figure 3.2	Illustration of Debye Shielding	43
Figure 3.3	The Plasma Volume Element	46
Figure 3.4	Antiproton Energy Loss Profile for Case 1	53
Figure 4.1	Binary Collision Between two Ions	59
Figure 4.2	Illustration of Elastic Scattering Cross Section	62
Figure 4.3	Beam Scattering Results for Case 1	71
Figure 5.1	Illustration of Nuclear Cross Section	73
Figure 5.2	Annihilation Cross Section for Limiting Cases	83
Figure 5.3	Percent Difference in Annihilation Probability	84
Figure 6.1	Flowchart of Procedure Used to Obtain Initial Beam Energy	87
Figure 6.2.1	Energy Loss Profile for Case 2	89
Figure 6.2.2	Scattering Results for Case 2	90

Figure 6.3.1	Energy Loss Profile for Case 391
Figure 6.3.2	Scattering Results for Case 392
Figure 6.4.1	Energy Loss Profile for Case 493
Figure 6.4.2	Scattering Results for Case 494
Figure 6.5.1	The Hollow Target Prior to Compression96
Figure 6.5.2	The Hollow Target at Peak Compression97
Figure 6.5.3	Scattering Results for Ideal Hollow Target99
Figure 6.5.4	Variation of RMS Scattering Angle with Vacuum Pressure100
Figure 6.5.5	Variation of RMS Scattering Length with Vacuum Pressure100
Figure 6.6.1	Energy Loss Profile for Case 5103
Figure 6.6.2	Scattering Results for Case 5104

LIST OF TABLES

Table 1.1	Theoretical Specific Energies of Various Reactions	2
Table 2.1	Ultimate Strengths of Various Materials	9
Table 2.2	Characteristic Debye Lengths	27
Table 2.3	Number of Recombination Reactions	29
Table 3.1	Various Coupling Term Values	51
Table 3.2	Obtaining the Proper Beam Energy for Case 1	54
Table 3.3	Comparison of Numerical and Experimental Results	56
Table 5.1	Representative Annihilation Probabilities	79
Table 6.1	The Plasma/Antiproton Beam Cases	85
Table 6.2	Initial Plasma Properties at Beampipe Inlet	86
Table 6.3	Mass of Plasma Leakage for Hollow Target Cases	102
Table 7.1	Summary of Major Results for Cases 1-4	105
Table 7.2	Summary of Major Results for Cases 5-8	107

ACKNOWLEDGEMENTS

I would like to extend my appreciation to Dr. Edward Klevans for teaching me introductory plasma physics on an individual basis. Plasma physics plays a central role in this work. I would also like to thank Dr. Raymond Lewis for his technical advice on a wide variety of subjects. His day-to-day advice was a great help in completing this thesis. I am indebted to Dr. Gerald Smith, my thesis advisor, for giving me the chance to work on the SHIVA Star project and for the many long hours he spent helping me refine this work. I would like to thank my fellow graduate students and the other members of the Laboratory for Elementary Particle Science for their various contributions which helped to further this effort. Finally, I owe my deepest and heartfelt appreciation to my patient and caring fiancé, Jennifer Neidenbach, who provided the emotional support needed to complete this endeavor.

Chapter 1

INTRODUCTION

In recent years, possible manned missions to Mars and new exploration of the outer planets have renewed the scientific community's and the general public's interest in the space program. Traditionally, chemically powered rockets have been used for human space travel. Chemical rockets provide high thrust to weight ratios, but prove relatively inefficient, able to obtain maximum specific impulses of only four or five hundred seconds [1]. The specific impulse is a measure of a rocket engine's ability to convert the energy of the propellant into usable thrust energy, and is equal to thrust divided by weight flow rate, in units of seconds. Chemical propellants, such as mixtures of liquid hydrogen (LH₂) and liquid oxygen (LO₂), are limited in specific impulse by the strength of their chemical bonds. For high energy missions, such as "fast" (a few months) transits to and from Mars, one must find more efficient energy sources.

Electric and nuclear propulsion concepts represent more efficient alternatives to the chemical rocket. The electrostatic thruster achieves the highest specific impulse of all classes of electric rockets. In order to obtain thrust, the electrostatic motor accelerates a stream of heavy ions across a large electric potential. Using this scheme, Isp's of about 7000 seconds are possible. Nuclear thermal rockets derive thrust by expanding a light propellant, such as hydrogen, through a hot nuclear reactor core, either solid, liquid, or gas. Specific impulses of approximately 3000 to 7000 seconds may be achieved using gas core nuclear thermal rockets.

Nuclear pulsed propulsion works by exploding nuclear bombs some distance behind a spacecraft. A large pusher plate and shock absorbing system mounted on the rear of the ship catch a fraction of the energy released by the sequential explosions, and the craft accelerates under this force.

Though nuclear thermal and electric propulsion may have much higher I_{sp} 's than chemical propulsion, other systems may prove even more efficient. Matter-antimatter reactions release enormous amounts of energy, mostly in the form of charged pions and gamma ray radiation. Table 1.1 compares the theoretical specific energy of several nuclear reactions, including fission, fusion, and matter-antimatter annihilation, to that of H_2+O_2 combustion.

Table 1.1 Theoretical specific energies of various reactions.

System	e_{th} J/kg
Chemical H_2+O_2	1.3×10^7
Fission U235	8.2×10^{13}
Fusion DD	7.9×10^{13}
DT	3.4×10^{14}
Antimatter Annihilation pbar+p	9.0×10^{16}

The energy released in the annihilation of a few milligrams of antimatter approximately equals the energy released by tens of tons of chemical propellant [1]. Though a theoretical antimatter rocket would prove highly efficient, achieving a specific impulse of nearly 3×10^7 seconds [1], it would require much more antimatter than possible using modern means of production, making this type of propulsion unfeasible at the time of this writing. However, antimatter may be utilized in other ways, specifically: Ion Compressed Antimatter Nuclear (ICAN) propulsion. This scheme utilizes antiprotons to initiate microfission: fast burns of small, dense fissile targets. According to Lewis et al [2], the concept of microfission was introduced nearly twenty years ago. The goal of microfission is to initiate self-propagating fission reactions in the smallest possible amount of material.

Microfission works by compressing a material to high density. While the fission proceeds, the material's inertia maintains the high density. Antiprotons may be used to start the reaction quickly, thus eliminating the time consuming early stages of the fission. Theoretically, the energy released from the nuclear reaction could be harnessed and converted to usable thrust via magnetic nozzles or, more probably, by using a variation on the pulsed propulsion system discussed above. Such a system could conceivably achieve thrusts on the order of tens of kilonewtons and specific impulses greater than 20 or 25 thousand seconds [3]. The combination of relatively high thrust and efficiency makes this system very attractive for fast interplanetary manned or unmanned missions.

Fast interplanetary missions (about 300 days or less) are desirable because prolonged exposure to interstellar radiation may prove harmful to both spaceship crews and cargo [1]. In traveling to Mars, an astronaut would receive about 0.12 rem per day, assuming a 2 g/cm² aluminum spacecraft radiation shield [4]. During a year-long round trip, the space traveller receives a 45 rem dose. In comparison, the general populace receives about 0.17 rem a year from cosmic background radiation, radioactive elements in rocks, soil, and wood, and other inescapable sources in food and water [5]. The U.S. government recommends that the general population receive a maximum dose of 0.5 rem/year, though workers in occupations involving higher radiation exposure may safely receive up to 5 rem/year. A radiation dose of 400 to 500 rem results in a human mortality rate of about 50% [6].

In addition to radiation hazards, space flight also subjects astronauts to periods of weightlessness. According to [7], long-term (i.e., more than two weeks) effects of weightlessness include 10% decrease in lung capacity, loss of bodily fluids, loss of protein, and calcium excretion in urine.

Recently, a group working at the Low Energy Antiproton Ring (LEAR) at CERN in Geneva, Switzerland observed antiproton-induced fission in a uranium (U²³⁸) target for the first time [2]. They concluded that fission in the target occurred nearly 100% of the

time, suggesting the possibility of ICAN propulsion [2]. In order to test the theory of ICAN, Smith et al proposed a proof-of-principle experiment to take place at the SHIVA Star facility at Kirtland Air Force Base, New Mexico. Figure 1.1 shows a schematic of the SHIVA Star apparatus, a solid liner imploder, while Figure 1.2 shows an expanded view of the target region. The target is surrounded by a staging fluid, such as hydrogen, which is in turn encased in a thin, solid aluminum shell. Two electrodes, an anode and cathode, face the target. This apparatus can compress a fissile target to high density, making it suitable for a microfission experiment.

A capacitor bank discharges a large amount of energy (5.2 MJ) through the cathode-cathode structure. The resulting multi-megamp current flows across the surface of the solid liner and creates a powerful magnetic field about the shell. This magnetic field causes the liner to collapse into the staging fluid. The compressed staging fluid in turn compresses the spherical target, increasing its density. When the fissile target reaches peak compression, antiprotons are released from their storage container, called a Penning trap. A radiofrequency quadrupole focuses and accelerates the antiproton beam, which travels along an injection pipe to the target. The antiprotons impact on the compressed target and initiate microfission. Streak photography, neutron and photonics diagnostics measure the compression and yields from the experiment.

The transport of the antiprotons from the Penning trap to the target represents one of the greatest challenges to the success of the experiment. The antiproton beam must be able to penetrate the hot, dense working fluid which escapes down the injection pipe once the compression cycle reaches a certain point. The end of the injection pipe, which terminates on the inside face of the cathode, is capped by a diamond window. The window is designed to prevent the working fluid from flowing into the pipe and along the antiproton injection system for as long as possible while the liner collapses toward the target. Diamond was chosen for the window material because it has high ultimate strength of about 75 kbar (in tension and compression) and relatively high melting temperature, about 3300

K [8]. However, compression work increases the temperature, density, and pressure of the working fluid. Soon, the fluid temperature becomes so high that a fully ionized plasma develops. Eventually, the diamond window will shatter from the extreme temperature and pressure of the plasma. Though the target may not yet have reached peak compression, the hot, dense plasma streams into the injection pipe. The antiproton beam must have enough energy to pass through this plasma and reach the target.

This work will examine the details of the plasma flow process as well as the obstacles the antiproton beam encounters as it passes through this plasma. Specifically, the antiprotons undergo energy loss through multiple binary collisions with plasma electrons and collective plasma excitations, as well as scattering to large angles from close encounters with plasma ions and annihilation with plasma ions in direct collisions.

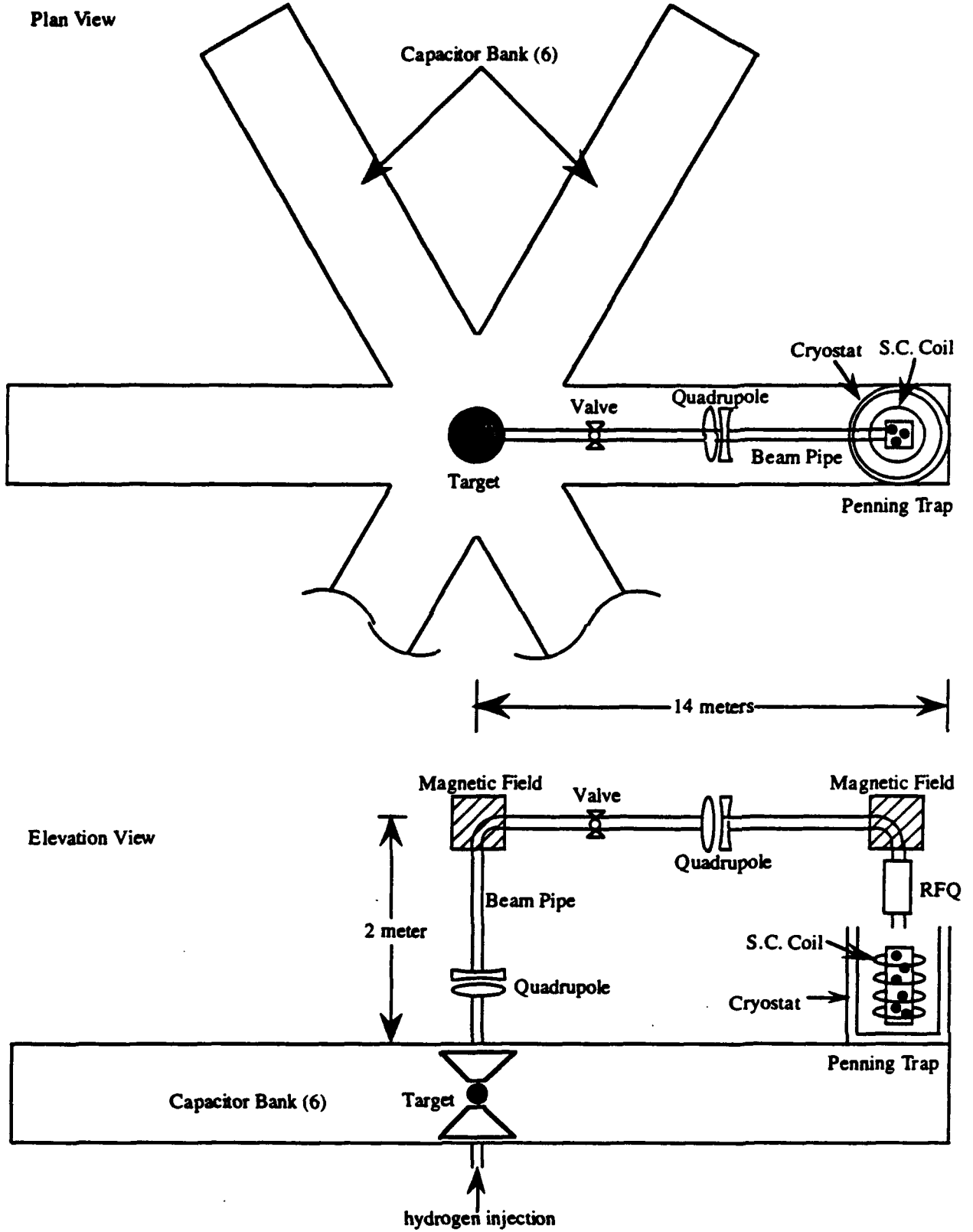


Figure 1.1 SHIVA Star Antiproton Injection System schematic (not to scale).

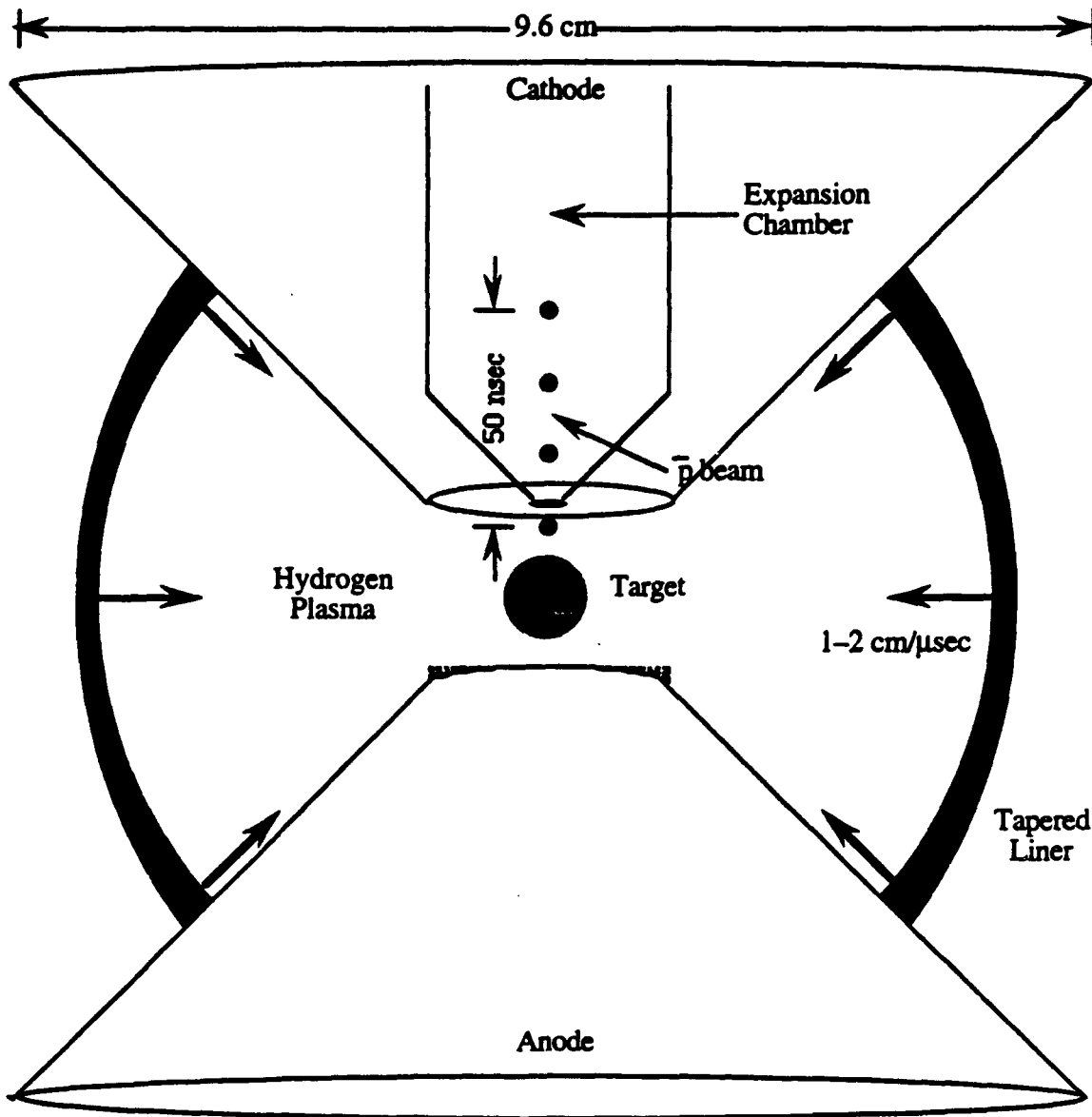


Figure 1.2 Expanded view of SHIVA Star target region (to scale).

Chapter 2

THE PLASMA EXPANSION

2.1 Introduction

In order to initiate antiproton–boosted microfission by annihilating on the target surface, the ion beam must overcome three major loss mechanisms (electronic energy loss, Rutherford scattering, and annihilation) as it traverses the plasma expanding up the injection pipe. All of these loss mechanisms depend, in some fashion or another, on the hydrogen plasma density. Obtaining an accurate time– and space–varying plasma density profile in the expansion chamber is important for determining the necessary antiproton injection energy. Before describing the expansion model, however, we examine the retaining window and expansion chamber geometry more closely.

2.2 The Diamond Window

When the 10 Mamp average current passes between the electrodes, a large magnetic field squeezes the aluminum liner, which in turn compresses the hydrogen plasma around the target. As the liner collapses radially inward, the plasma density, pressure, and temperature continue to increase until the target reaches peak compression. At this time, the antiproton beam travels about 1 meter from the Penning trap to the RFQ at a velocity of about 1.96×10^6 m/s (0.0065c), then flies approximately 16 meters from the RFQ to the target at 1.52×10^7 m/s (0.050c), giving a total flight time of approximately 1560 nsec. Time $t=0$ corresponds to the time the antiprotons leave the Penning trap.

From the standpoint of antiproton injection, an orifice must exist in the cathode for the antiproton beam to pass through. This orifice also provides an exit for the hydrogen plasma and window debris. An *ideal* system would allow antiprotons to reach the target while still containing all the plasma surrounding the fissile for the following reasons: First,

any plasma escaping from the liner will tend to reduce the maximum target compression; second, plasma streaming down the injection pipe will impede antiprotons on their way to the target.

The diamond retaining window (see Figure 2.1) represents a partial solution to this problem. Capping the end of the cathode, the window keeps the hydrogen plasma from streaming down the pipe during the compression. As Table 2.1 shows, diamond has a high ultimate strength, and therefore represents a good choice for the window material.

Table 2.1 Strength of diamond compared to strength of other materials.

Material	Ultimate Strength (tension)
Diamond	360.0 kbar
Aluminum	2.2 kbar
0.6% Carbon Steel	6.9 kbar
Tungsten carbide	50.0 kbar
Carbon fiber	30.0 kbar

The value of 360 kbar given above is based on the following equation [8]:

$$\sigma_f = m \left(\frac{\gamma E}{c} \right), \quad (2.1)$$

where σ_f is the fracture stress, E is the elastic modulus, γ is the fracture surface energy, and c is the crack length. For diamond, $E=10.5 \times 10^{11}$ Pa, and $\gamma=5.3$ J/m². The factor m represents a dimensionless number based on geometry and the particular stress situation (e.g. plain strain), and always has a magnitude on the order of unity. Inserting a crack length of 10 nm into Eq. (2.1) gives a fracture stress of about 360 kbar in tension. The value of 10 nm represents a reasonable crack length [8]. Scaling 360 kbar by a factor of 1.57 (the ratio of 1.9 Mbar/1.2 Mbar, or the theoretical tension to shear strength ratio)

gives 230 kbar for the fracture stress, in shear. When the internal pressure exceeds this value, the diamond window breaks and plasma starts flowing up the injection line.

In order to determine antiproton beam energy loss and deflection, we must characterize the plasma density and temperature profiles along the injection pipe, so we must know when the diamond window breaks and the hydrogen plasma enters the beampipe. Following Stanek [9], one may derive the following equations for the principal, or total, stresses on a volume element of the window (see Figure 2.1):

$$\sigma_r = 0.375p \frac{b^2}{h^2} [(3 + \mu)X^2 - (1 + \mu)], \quad (2.2)$$

$$\sigma_\theta = 0.375p \frac{b^2}{h^2} [(3\mu + 1)X^2 - (1 + \mu)], \quad (2.3)$$

$$\tau = \frac{pb}{2h}, \quad (2.4)$$

and $X=r/b,$ (2.5)

where p represents the plasma pressure, b is the window radius, h the window thickness, r the radial coordinate, and μ is Poisson's ratio. For an isotropic material, μ is a constant between 0 and 1.0, independent of the orientation of the material. Though diamond has an anisotropic crystalline structure, it is nearly isotropic [8], so we take $\mu_{\text{Diamond}}=0.2$, regardless of the crystalline orientation.

Eq. (2.4) gives the average shear stress developed in any type of beam, plate, or shell with rectangular cross section [10]. Figure 2.1 shows the geometry of the window, with a radius $b=1$ mm and a thickness $h=1$ mm, and the stresses, σ and τ , on a volume element. Though the window is circular, a slice made in the z direction has a rectangular cross section. It is assumed that the window has a fixed outer edge.

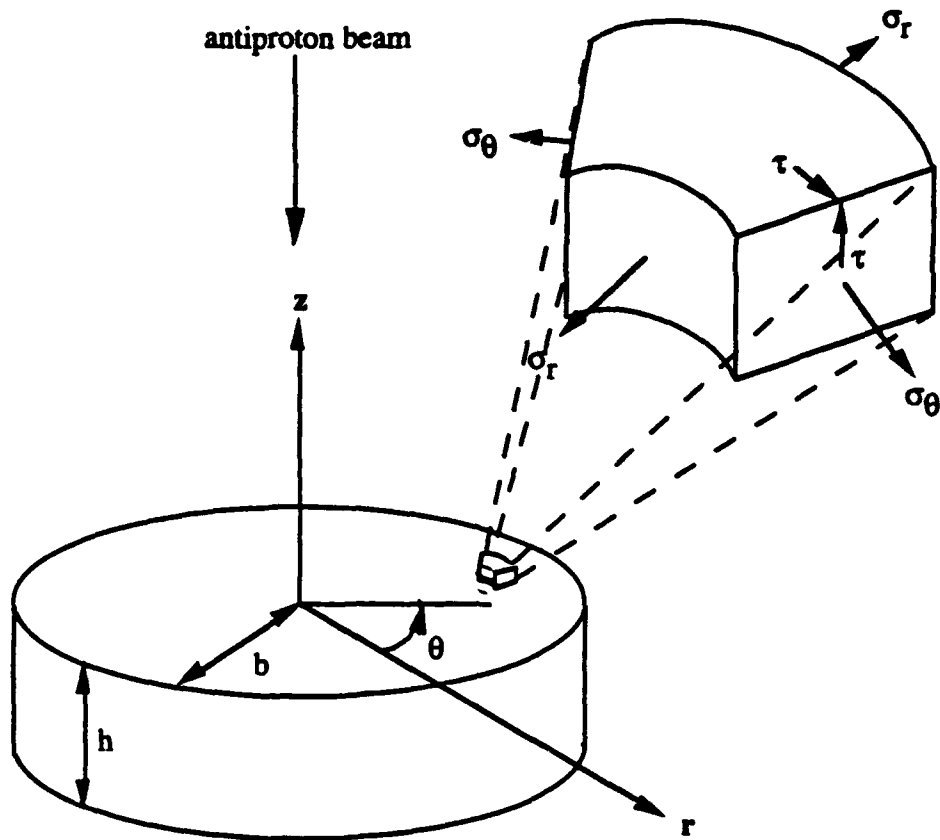


Figure 2.1 Diamond window geometry.

Since the parameter X in Eq. (2.2), (2.3), and (2.5) varies between 1 and 0, the maximum normal stress in the r direction occurs at the edge of the window, where $X=1$, while the maximum normal stress in the θ direction occurs in the center of the window, where $X=0$. The factor b/h appears in all three stress equations, and represents the thickness to radius ratio of the window. The normal stress varies quadratically with b/h , while the shear stress varies linearly with this factor.

In order to determine when the window fails, one must first choose a diameter to thickness ratio. The theory behind Eqs. (2.2)—(2.4) breaks down if b/h becomes smaller than about 1.0, and this value represents the upper limit on the window thickness. One can

invert Eqs. (2.2)—(2.5) and solve for the maximum plasma pressure the window can withstand, knowing σ_r and σ_θ both equal 360 kbar in Eq. (2.2) and (2.3), while τ is 230 kbar in Eq. (2.5).

Since diamond is weaker in shear than in tension or compression, Eq. (2.5) governs the practical limit on the plasma pressure the window can withstand. When the plasma pressure on the window exceeds 200 kbar, the normal stress in the θ -direction causes the window to rupture, and plasma streams into the beampipe.

Figure 2.2 shows the magnetic optics in the bend plane from the RFQ to the target [11]. The radius of the antiproton beam at the window is 1mm. Therefore, we choose a diamond window with a 1 mm radius, to insure that the beam passes through the cathode orifice, and a thickness of 1mm. This configuration employs the maximum h/b ratio. Since diamond has a density of 3520 kg/m^3 , the window has a mass of $1.1 \times 10^{-5} \text{ kg}$.

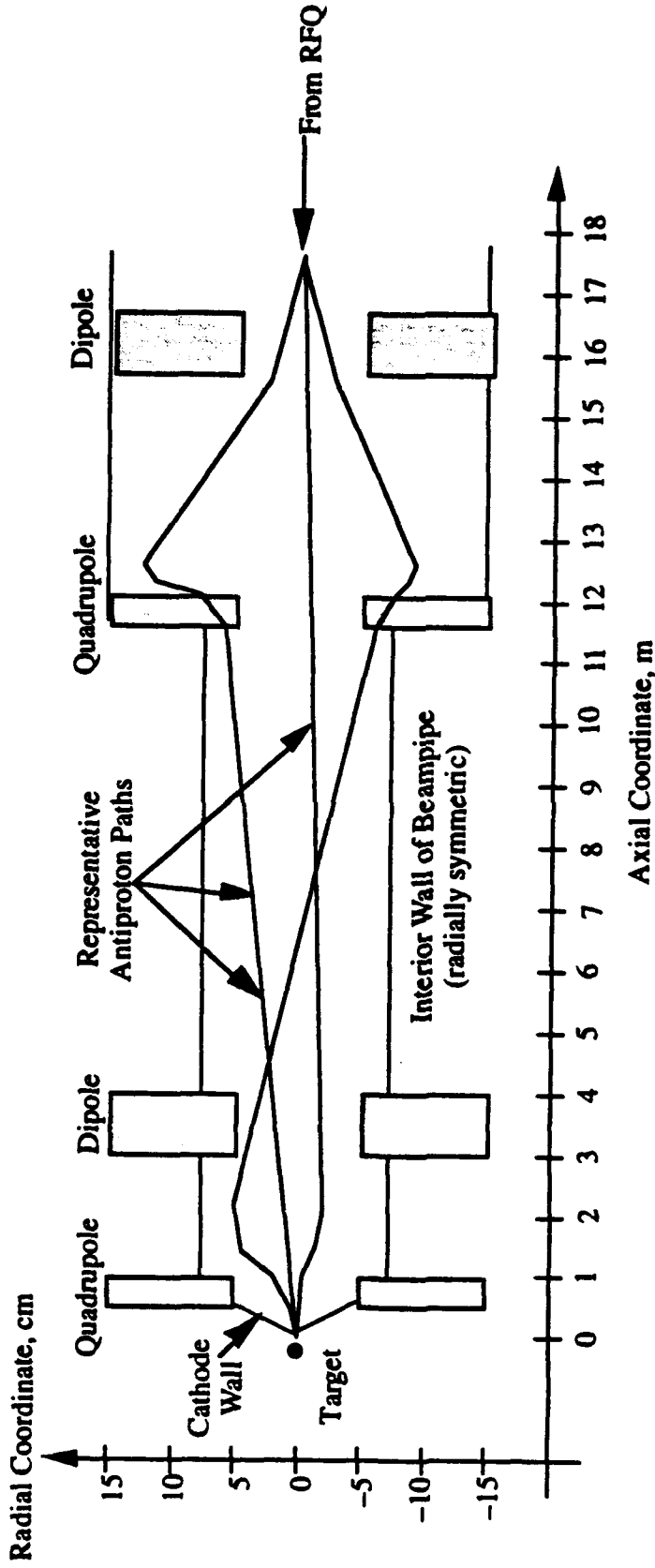


Figure 2.2 Schematic drawing of beam pipe showing magnetic optics which guide the antiproton beam from the RFQ to the target.

2.3 Window Fragmentation

Both electrodes in the SHIVA Star experiment are made of tungsten and have a truncated cone geometry. They have a 45° half angle, a minor radius of 8 mm, a major radius of 4.8 cm, and a length of 4 cm. Though the anode is solid, an orifice runs along the centerline of the cathode to accommodate antiproton beam delivery to the target. Several competing factors influence the overall design of this orifice.

On one hand, we would like a large orifice inside the cathode to give the plasma and window fragments as much expansion room as possible before the antiproton beam passes through. On the other hand, we would like to make the cathode wall as thick as possible to provide mechanical support for the magnetic pressure caused by the 10 Megamp current flowing along the cathode surface. Since this current also heats the cathode, a thick wall acts as a heat sink to prevent thermal damage.

In order to determine an appropriate geometry for the interior cathode wall, we consider first diamond fragments traveling up the beampipe. Regardless of the number of fragments we may determine the approximate fragment velocity by equating the work done on the window to its resulting kinetic energy:

$$W = F\Delta x = mv^2/2 \quad (2.6)$$

where F is the force exerted on the window by the plasma and Δx is the distance the plasma displaces the window. Since the circular window fails at a plasma pressure of 200 kbar and has a radius of 1 mm, $F=62,832$ N. Furthermore, the window is 1 mm thick, so the plasma must push the window this distance before it breaks free. Inserting these values into Eq. (2.6) give $W=62.8$ J. Also, diamond has a density of about 3520 kg/m³, so the window mass is 1.1×10^{-5} kg. Solving for the velocity, one obtains $v=3380$ m/s. Since

about 1 μ sec elapses before peak compression, the window fragments travel 3.4 mm up the beampipe before encountering the antiproton beam.

We would like to determine the fraction of antiprotons which will annihilate by colliding with the window fragments. This fraction is given by

$$f = \frac{\pi b^2}{0.586\pi(z + b)^2}, \quad (2.7)$$

where it is assumed that the fragments expand uniformly into a cone of half-angle 45° . With $b=1$ mm and $z=3.4$ mm, $f=0.088$, or 8.8%. Figure 2.3 illustrates the cathode and orifice geometry.

The above arguments assume that the window fragments before vaporizing. A calculation of the heat flow rate from an inner temperature of 22,300 K (2 eV) to an outer temperature of 300 K across the window gives 72 kW. The energy required to vaporize the window is found to be 68 J. Therefore, vaporization occurs on a time scale of milliseconds, allowing complete fragmentation.

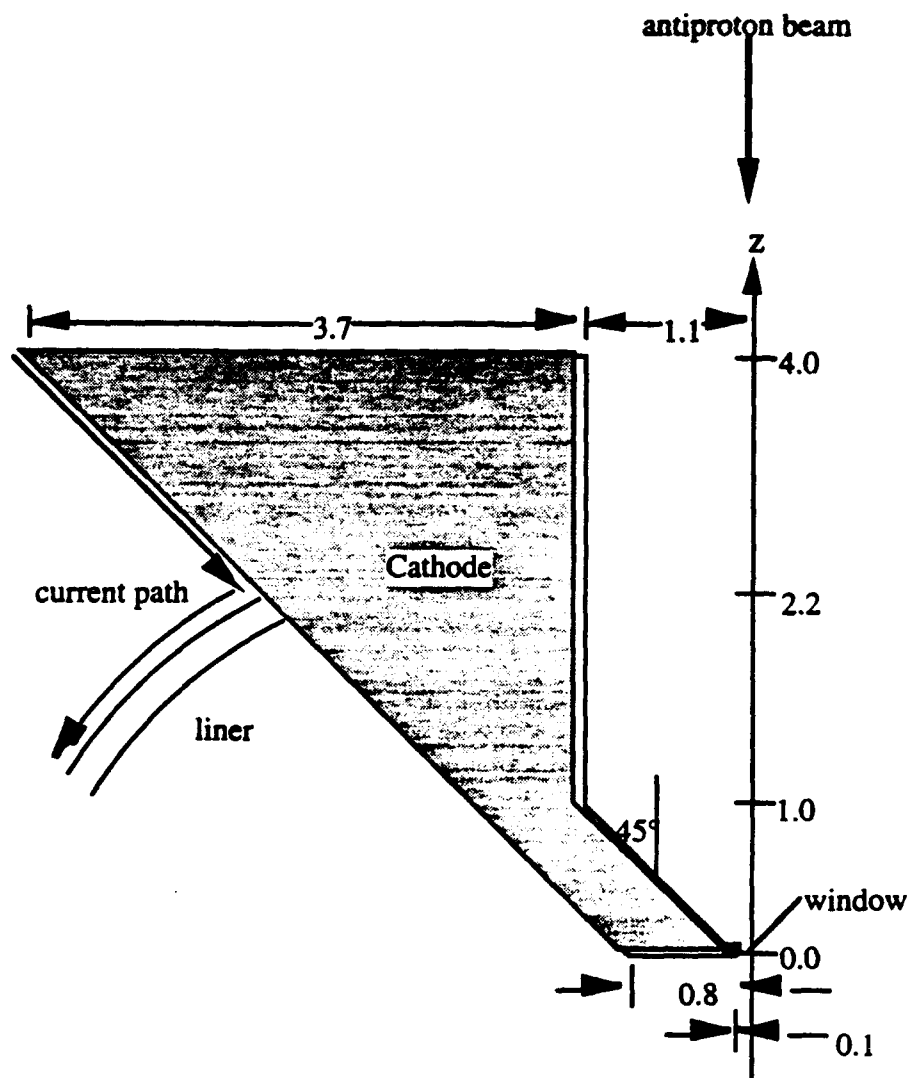


Figure 2.3 A cross sectional view of the cathode, shown to scale. All dimensions are given in units of centimeters.

2.4 Magnetic Pressure on Cathode

With the geometry of the cathode defined, we now determine the stress in the tungsten due to magnetic pressure generated on the exterior surface by the current. At the beginning of the compression cycle, the outside edge of the liner rests on the cathode surface at $z=2.2$ cm (see Figure 1.2).

The current generates an azimuthal magnetic field, which in turn creates magnetic pressure that compresses the liner and cathode. As time progresses, the liner moves toward the end of the cathode, creating an extended current path on the cathode. Thus, the stress generated in the cathode wall by the external pressure has a time dependence.

The magnetic field and corresponding pressure may be found from:

$$B_{\theta} = \frac{\mu_0 I}{2\pi b} \quad (2.8)$$

and

$$P = \frac{B_{\theta}^2}{2\mu}, \quad (2.9)$$

where I is the current, μ is the permeability of the cathode equals $4\pi \times 10^{-7}$ (N/A²), and b and θ are measured in a plane perpendicular to z . The relationship between b and z is

$$b = z + 0.8 \text{ cm.} \quad (2.10)$$

Ref [12] gives the following equations for the principal stresses in a thick-walled, radially-symmetric pressure vessel:

$$\sigma_r = -\frac{Pb^2}{b^2 - a^2} \left(1 - \frac{a^2}{r^2} \right) \quad (2.11)$$

and

$$\sigma_{\theta} = -\frac{Pb^2}{b^2 - a^2} \left(1 + \frac{a^2}{r^2} \right), \quad (2.12)$$

where a is the radius of the interior surface. Note that the maximum circumferential stress occurs on the inner surface (where $r=a$), while the radial stress at this location vanishes. In order to determine when the magnetic pressure causes the cathode to collapse, we compute

Eq. (2.12) at various times. Tungsten has a yield point stress of about 40.7 kbar. After the stress in the cathode reaches this level, the interior wall stretches beyond the elastic limit.

Stress waves in the cathode propagate at the speed of sound in tungsten. According to Serway [6], the equation

$$c = \sqrt{\frac{B}{\rho}} \quad (2.13)$$

gives the speed of sound in a solid, where c represents the acoustic speed, B the bulk modulus, and ρ the solid's density. Since tungsten has a bulk modulus of 20×10^{10} Pa and a density of $19,300 \text{ kg/m}^3$, c equals 3219 m/s . We can use this speed to determine how long it takes a stress wave to travel through the cathode wall to the interior surface.

The two-dimensional hydrodynamics program CALE [13] provides many details about the liner/plasma/target system during the compression cycle. Specifically, CALE gives the position of the liner/cathode interface as a function of time. Using this information, we may determine the arrival time (since the start of current flow) of the stress wave to reach the interior cathode surface. For the portion of the cathode between 2.2 cm and 4.0 cm, the arrival time of the stress wave is

$$\tau = \frac{b-a}{c}, \quad (2.14)$$

where $b-a$ is the thickness of the cathode wall at a given z location. For $z < 2.2 \text{ cm}$,

$$\tau = \frac{b-a}{c} + \frac{(2.2-z)}{0.707 v_{\text{liner}}} \quad (2.15)$$

represents the stress wave arrival time. The liner velocity, $v(t)_{\text{liner}}$, is taken from CALE.

Figure 2.4 shows the time required for stress waves to reach the inner surface as a function of z . Figure 2.5 shows σ_{θ} at the time of the arrival of the stress waves versus z . From 2.2 cm to 4 cm, the cathode has sufficient thickness so that the stress on the interior surface does not exceed the yield point of tungsten. Between 0.4 and 0.7 cm, though, the magnetic pressure causes the stress on the interior surface to exceed the yield point at or after peak compression (see in Fig. 2.3). For the region $0.7 < z < 2.2$ cm, the yield stress point is reached before peak compression.

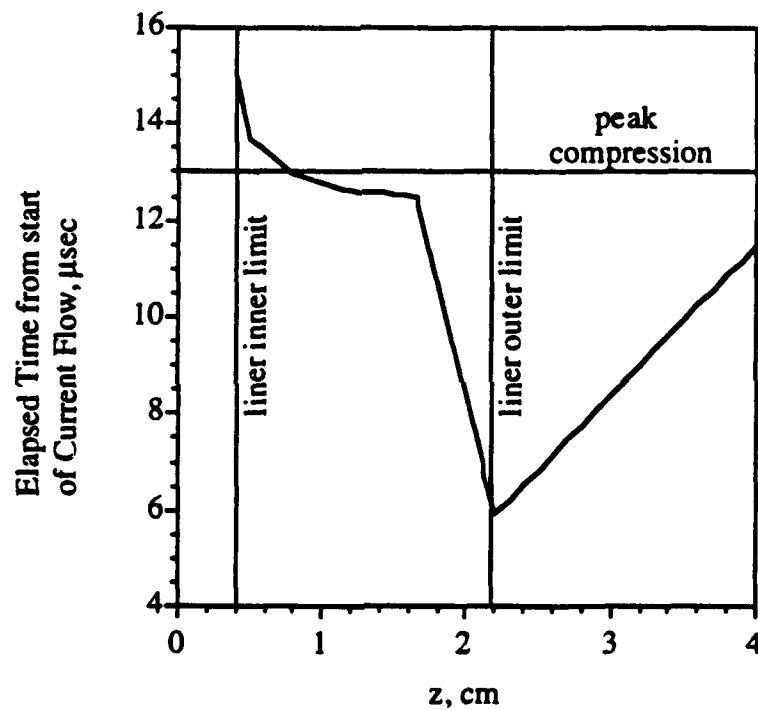


Figure 2.4 Time for stress waves to reach inner surface of anode.

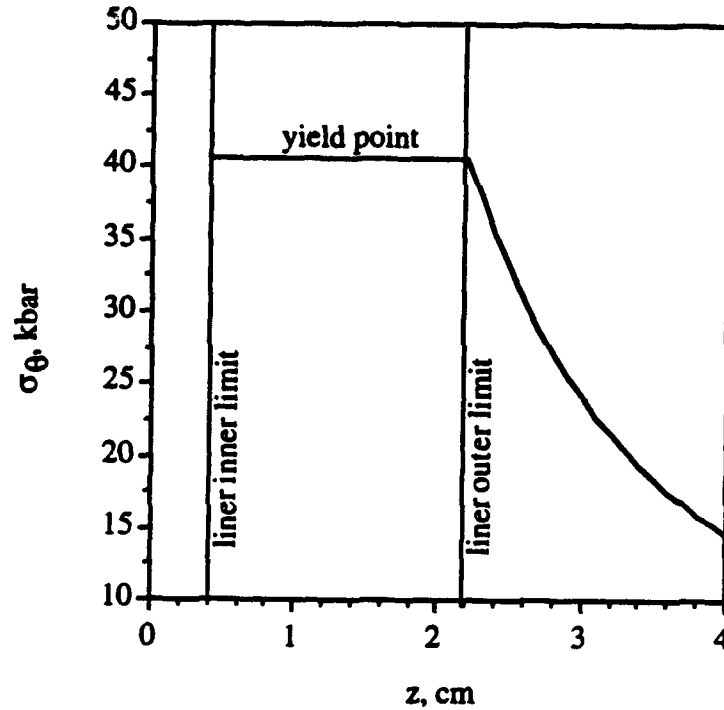


Figure 2.5 Stress on inner surface of the anode.

According to [14], tungsten has a body centered cubic (bcc) crystal lattice and therefore fails in a brittle mode at relatively low temperatures (i.e., about room temperature). Since all real materials contain microcracks as a result of manufacturing and use, we would expect the cathode to develop macroscopic cracks as a result of the applied pressure, and then fail catastrophically. The size of a microscopic crack that will cause failure may be found from

$$l = \pi^{-1}(K_{Ic})^2(\sigma)^{-2}, \quad (2.16)$$

where l represents the length of a surface crack or half the length of an internal crack, K_{Ic} a material constant representing fracture toughness and σ the stress at the point of interest. Inserting $K_{Ic}=20\text{MPa}/\sqrt{\text{m}}$, $\sigma_{\theta}=\sigma_{\text{yield}}=40.7\text{ Mbar}$ gives $l=8\ \mu\text{m}$. Therefore, if a microscopic crack of length approximately $8\ \mu\text{m}$ exists on the interior surface of the

cathode near the 2.2 cm mark (where the stress wave first reaches the surface), a macroscopic crack will likely develop which will propagate through the cathode and cause it to fail catastrophically. Since cracks propagate at the speed of sound [15], the minimum time required for the crack to propagate through the cathode is equal to the time the stress wave needs to travel from the inner back to the outer surface, which, according to Eq. (2.14) is 6 μsec .

Therefore, the above analysis indicates that 12 μsecs elapse between the start of current flow and the time the cathode fractures. Additional time is required for the magnetic pressure to close the orifice. About 13 μsec after the start of current flow, sufficient stress develops in the region between $z=0.7$ and 2.2 cm to cause fracturing (see Figures 2.4 and 2.5). An average pressure of 29 kbar acts on the outer surface of this portion of the cathode, which has a mass of 0.32 kg. In order to close the orifice between $z=0.7$ and 2.2 cm, the cathode must fill a volume of 5.7 cm^3 . The $p\text{d}V$ work required to close the orifice is therefore 16.5 kJ. Assuming that all this work is converted into kinetic energy, the cathode attains an inward velocity of 324 m/s. The inner surface of the cathode must move 1.1 cm to reach the centerline of the orifice, so an additional 34 μsec elapses between cathode fracture and the time the cathode fully blocks the orifice. This value represents a lower limit, since heat dissipation has been ignored. Thus, we estimate that a total of greater than 46 μsec elapses between the start of current flow and the time when the cathode blocks the orifice. The beampipe therefore remains unobstructed during antiproton beam injection, done approximately 13 μsec into the cycle.

2.5 Ohmic Heating

In addition to generating a magnetic pressure field when it passes between the electrodes, the current also deposits heat energy in the cathode and anode. The amount of energy depends on the magnitude of the current, the cathode resistance, and the total

amount of time the current is applied. The energy deposited at the surface is dissipated through heat conduction into the cathode and radiation to the surroundings.

In order to obtain an estimate of heat damage to the cathode, the following analysis assumes that all heat energy is deposited rapidly (13 μsec) into a volume of tungsten defined by the cathode surface geometry and the current penetration depth.

The depth that the current penetrates into the cathode, Δr , during the compression time may be obtained from

$$\Delta r^2 = \frac{t}{\sigma\mu}, \quad (2.17)$$

where t is approximately 12 μsec , σ , the resistivity of tungsten, equals $1.825 \times 10^7 \Omega^{-1}\text{m}^{-1}$, and μ , the cathode permeability, equals $12.57 \times 10^7 \text{N}^2/\text{A}$. Solving for Δr gives a penetration depth of approximately 0.8 mm.

The cathode resistance may be found from

$$R = \frac{l}{\sigma A}, \quad (2.18)$$

where A is the area that the current passes through as it travels along the cathode, and l represents the length of the current path. Since the cathode has the geometry of a truncated cone, A and l depend on z . The total resistance, found by integrating the differential resistance along z , from 0 to 4 cm, is $4 \times 10^{-5} \Omega$.

The equation

$$Q = I_{\text{avg}}^2 R t \quad (2.19)$$

gives the total energy deposited during the 12 μsec compression time, where the average current, I_{avg} , equals 10 Megamps. Inserting values for R , I_{avg} , and t gives a value of 48

kJ for the energy deposited in the top 0.8 mm of the cathode. The mass of this surface tungsten is 0.11 kg.

The final temperature of the tungsten may be found from

$$Q = mc(T_f - T_i), \quad (2.20)$$

where $Q=48$ kJ. Since tungsten has a specific heat, c , of 134 J/kg°C, and the cathode is assumed to have room temperature initially, the final temperature of the the top 0.8 mm is about 3360 °C. This temperature is slightly less than the melting temperature of tungsten, $T_{\text{melt}}=3380$ °C. Thus, a small fraction of the total cathode mass, corresponding to that wetted by the current, is raised to the melting temperature. Since conduction and radiation most likely dissipate at least some of the deposited energy, ohmic heating of the cathode will not render the cathode impassable to antiprotons.

2.6 Plasma Considerations

The problem of antiproton injection reduces to determining the space varying density profile along the centerline of the expansion chamber at the time of antiproton passage. In general, plasma dynamics represents a difficult and challenging topic because one must consider not only thermo- and fluid-dynamics, but electrodynamics as well, when describing plasma phenomena.

Let us attempt to define a model of the plasma expansion that provides reasonably accurate time- and space-varying density profiles for use in the electronic energy loss, Rutherford scattering, and annihilation equations. To begin with, one can determine the degree of ionization of a gas with the *Saha* equation [16]:

$$\frac{n_i}{n_n} = 2.4 \times 10^{21} \frac{T^{3/2}}{n_i} e^{-U_i/kT}. \quad (2.21)$$

Here, n_i and n_n represents the number density of the ionized atoms and neutral atoms, respectively, T the gas temperature in $^{\circ}\text{K}$, k the Boltzmann constant ($1.38 \times 10^{-23} \text{ J/}^{\circ}\text{K}$) and U_i the ionization energy of the gas. The initial total number density, n_T , where $n_T = n_i + n_n$, is between 1×10^{19} to $6 \times 10^{19} \text{ cm}^{-3}$. The initial plasma temperature expected in the SHIVA Star apparatus is in the 2 to 5 eV range. Taking the lower values, and using an ionization potential of 13.6 eV for hydrogen, we find that the hydrogen ionized at the beginning of the compression cycle is approximately 10%, where $\% \text{ionization} = 100(n_i/n_T)$.

The two-dimensional hydrodynamics code CALE [13] provides details of the compression process. The entire compression cycle can be simulated using this computer program. If the retaining window suffers catastrophic failure when the plasma pressure reaches about 200 kbar, we can find all the pertinent plasma properties from CALE output just as the plasma begins streaming into the expansion chamber. Since the plasma properties at the time of window fracture depend on initial plasma temperature and density, let us restrict the starting values of plasma temperature and density to about 2 to 5 eV and 1×10^{19} to $6 \times 10^{19} \text{ atoms/cm}^3$, respectively. Though the exact values of plasma temperature, pressure, and density depend on the specific initial conditions, as well as location in the plasma, for the range of initial condition listed above the plasma temperature just inside the window right before window fracture will always be greater than 15 eV. Once again using the Saha equation, we obtain a value of $\approx 100\%$ for the percentage of ionization in the plasma at the time of window fracture. Therefore, we may assume that by the time the pressure in the plasma has reached a level high enough to break the window, the plasma has become fully ionized.

Essentially two fluids stream through the window: one fluid composed of light, highly mobile electrons, and a second fluid of much heavier ions. For the case of hydrogen plasma, protons represent the ions. It would seem that two fluids interacting

would greatly complicate matters; however, Chen presents the following equation for the frequency, in s^{-1} , of ion–electron collisions

$$\nu_{ei} = 2 \times 10^{-6} \frac{Z n_e \ln \Lambda}{T^{3/2}}, \quad (2.22)$$

where $Z=1$ for hydrogen, n_e represents the electron number density in cm^{-3} , T the gas temperature in eV, and $\ln \Lambda$ a constant approximately equal to 10. Inserting representative values of 80 eV and $4 \times 10^{21} cm^{-3}$ for the plasma temperature and density during the compression process yields an ion–electron collision frequency of about 10^{14} Hz. In other words, the time between successive collisions with protons for a single electron is about 0.01 picoseconds. In comparison, at least 10 μ sec, or 10^{-5} seconds, elapse between the start of the compression cycle and the time the window fails. Since the time between collisions is about nine orders of magnitude smaller than the compression time, the electron and proton fluid temperatures quickly equilibrate by exchanging energy through many collisions. Therefore, the temperature of the electron fluid, T_e , is equal to the temperature of the proton (ion) fluid, T_p , as the plasma streams into the beampipe.

Furthermore, since we started with pure hydrogen, which contains one electron orbiting a single proton nucleus, and the plasma is fully ionized (i.e., the electron is stripped from its proton) by the time the window breaks, we may also assume that the number density of the electron fluid, n_e , is equal to the number density of the proton fluid, n_p . The *plasma approximation* also assumes equal number densities [16]. The plasma approximation remains valid as long as the bulk fluid motions are slow enough such that both ions and electrons have time to move, so the ions can distribute themselves in such a way as to minimize the electric field. In essence, the plasma remains quasi–neutral throughout the expansion. The plasma approximation provides a fundamental basis for all subsequent analysis in that we will not have to differentiate between the electron and proton densities, since they are the same.

In addition to having the same temperature and density, the proton and electron fluids also move down the beampipe with the same velocity. At first, one might think that the electrons, having 1837 times smaller mass than the protons, would move much faster, since a particle's thermal velocity is linked to its mass and temperature through

$$v_{th} = (3kT/m)^{1/2}. \quad (2.23)$$

In a plasma with equal electron and ion temperatures, the electrons do, on average, have a higher thermal velocity than the ions. However, strong electrostatic restoring forces prevent the electrons from traveling too far ahead of the ions. Suppose, for example, that a mass composed of electrons and protons each with number density n streams through the cathode orifice at time t_0 . Since the two fluids have the same temperature, T , the electrons travel approximately 43 times faster than the protons. According to Clemmow [17], after the electron mass has traveled a distance λ away from the protons, an electric potential of the order $ne^2\lambda^2/\epsilon_0$ develops between the two masses which pulls the electrons back to the protons. The electrons may overshoot and oscillate around the protons as the two fluids travel together down the beampipe. Since λ defines the distance from the ions where the electron kinetic energy is approximately equal to the electrostatic potential energy, one can find an analytic expression for λ by setting these energies equal to each other. Thus,

$$kT = ne^2\lambda^2/\epsilon_0. \quad (2.24)$$

Solving for λ , one obtains

$$\lambda = (\epsilon_0 kT/ne^2)^{1/2}, \quad (2.25)$$

where ϵ_0 represents the permittivity of free space. λ is commonly called the *Debye length*. It has important applications in plasma physics, and will be discussed more thoroughly in Chapter 3.

When electrons try to move further than λ away from the protons, their kinetic energy of thermal agitation succumbs to the more powerful electrostatic potential energy between the two fluids. Since the protons have larger mass and more inertia than the electrons, the proton velocity governs the plasma expansion. Table 2.2 below lists some characteristic Debye lengths for representative plasma densities and temperatures in the beampipe (obtained from the procedure discussed later in this chapter).

Table 2.2 Characteristic Debye lengths for representative plasma densities and temperatures.

Temp, eV	Density, cm^{-3}	λ_D , cm
2	3.0×10^{22}	6.07×10^{-9}
10	3.0×10^{22}	1.36×10^{-8}
50	3.0×10^{22}	3.03×10^{-8}
100	3.0×10^{22}	4.29×10^{-8}
2	3.0×10^{21}	1.92×10^{-8}
10	3.0×10^{21}	4.29×10^{-8}
50	3.0×10^{21}	9.59×10^{-8}
100	3.0×10^{21}	1.36×10^{-7}
2	6.0×10^{20}	4.29×10^{-8}
10	6.0×10^{20}	9.59×10^{-8}
50	6.0×10^{20}	2.14×10^{-7}
100	6.0×10^{20}	3.03×10^{-7}
2	6.0×10^{18}	4.29×10^{-7}
10	6.0×10^{18}	9.59×10^{-7}
50	6.0×10^{18}	2.14×10^{-6}
100	6.0×10^{18}	3.03×10^{-6}
2	6.0×10^{17}	1.36×10^{-6}
10	6.0×10^{17}	3.03×10^{-6}
50	6.0×10^{17}	6.78×10^{-6}
100	6.0×10^{17}	9.59×10^{-6}

2	3.0×10^{16}	6.07×10^{-6}
10	3.0×10^{16}	1.36×10^{-5}
50	3.0×10^{16}	3.03×10^{-5}
100	3.0×10^{16}	4.29×10^{-5}

Since the electrons are never separated from the protons by more than the Debye length, which is very small compared to the length of the beampipe, we may treat the separate species as a single fluid.

As the plasma streams along the injection pipe, an ion and an electron may possibly collide and form a neutral hydrogen atom. This process is known as *radiative recombination*, and can be described by the following reaction:



In the above process, the last term on the right hand side represents the amount of energy released as a photon, where h represents Planck's constant and ν is the photon frequency in Hz. The photon frequency depends on the electron energy both before and after its collision with the proton.

The number of recombinations which take place per unit time depends on the plasma number density as well as the *radiative recombination coefficient*, α . The recombination coefficient depends on the plasma temperature and atomic number of the plasma species. According to Massey [18], α for hydrogen decreases monotonically with increasing temperature. Therefore, to find the maximum number of recombinations that occur, we should employ the recombination coefficient that corresponds to the lowest expected plasma temperature in the beampipe, which, from CALE data, is approximately 5 eV. Table 14.4 of reference [18] gives $\alpha = 10^{-13} \text{ cm}^3/\text{s}$ for this temperature. One may determine the total number of recombinations which have occurred with the following equation:

$$N_{\text{rec}} = \alpha \cdot n \cdot \Delta t, \quad (2.27)$$

where N_{rec} represents the number of recombinations, n the plasma number density in cm^{-3} , and Δt the time, in seconds, under consideration.

The plasma density in the beampipe ranges over five or six orders of magnitude; further, the plasma expansion time of interest varies between approximately 1 and 10 μsec . Therefore, the total number of recombinations taking place in the plasma changes drastically depending on location along the beampipe and elapsed time since the beginning of the expansion. Table 2.3 below shows some representative results for the total number of recombinations occurring during an expansion based on characteristic expansion times and plasma densities.

Table 2.3 Representative values for number of recombinations, N_{rec} , occurring in the H plasma.

$\Delta t, \mu\text{sec}$	$\rho, \text{g/cm}^3$	n, cm^{-3}	N_{rec}
1	5.0×10^{-2}	3.0×10^{22}	3.0×10^3
10	5.0×10^{-2}	3.0×10^{22}	3.0×10^4
1	5.0×10^{-3}	3.0×10^{21}	3.0×10^2
10	5.0×10^{-3}	3.0×10^{21}	3.0×10^3
1	1.0×10^{-3}	6.0×10^{20}	6.0×10^1
10	1.0×10^{-3}	6.0×10^{20}	6.0×10^2
1	1.0×10^{-5}	6.0×10^{18}	6.0×10^{-1}
10	1.0×10^{-5}	6.0×10^{18}	6.0×10^0
1	1.0×10^{-6}	6.0×10^{17}	6.0×10^{-2}
10	1.0×10^{-6}	6.0×10^{17}	6.0×10^{-1}
1	5.0×10^{-8}	3.0×10^{16}	3.0×10^{-3}
10	5.0×10^{-8}	3.0×10^{16}	3.0×10^{-2}

Based on the procedure used to find the plasma density profile along the beampipe given later in this chapter, and from the results presented in Chapter 6, we will see that *at least* 0.01 mg of plasma leaks into the beampipe during the compression process. This mass of plasma contains about 6×10^{18} protons. Compared to this value, even the upper limit of about 30,000 recombinations is insignificant. Therefore, we can safely ignore the effects of electron-proton recombination in all subsequent analysis.

In addition to recombining with electrons, plasma protons may also stick to the interior beampipe wall. Protons that stick to the pipe surface cannot contribute to antiproton scattering. Furthermore, since the movements of the protons and electrons are linked through the electrostatic force, when protons stick to the wall a net negative charge develops in the plasma which causes the electrons to also move toward the wall in order to maintain charge neutrality. Therefore, the electronic stopping power of the plasma is also reduced.

The probability that a particle will stick to a solid surface depends on the particle charge, the surface material, the particle energy, E_0 , and the angle of incidence, α , between the particle path and the surface [19]. Based on a fit to experimental data, Langley et al present the following equation to describe the particle *reflection coefficient*:

$$R_n = \{ [1 + 3.2116(\epsilon \cos \alpha)^{0.34334}]^{1.5} + [1.388(\epsilon \cos \alpha)^{1.5}]^{1.5} \}^{-0.667}, \quad (2.28)$$

where ϵ , in keV, represents a quantity called the *reduced energy*. For hydrogen ions incident on iron (or stainless steel), the major component of the beampipe, ϵ equals $0.3934E_0$, with E_0 in keV, while for hydrogen ions incident on tungsten, ϵ equals $0.1014E_0$. Though the fit given by Eq. (2.28) represents the reflection coefficient for hydrogen or helium ions incident on iron or nickel, according to the data presented in ref. [19] it also gives accurate results for protons on tungsten.

Since the probability that, after a collision, a particle either sticks to the wall or reflects from the wall is unity,

$$S_n = 1 - R_n \quad (2.29)$$

represents the *sticking coefficient*. Figure 2.6 shows the variation of S_n with energy and angle of incidence, where 90° represents normal incidence, on iron(Fe) and tungsten(W) for hydrogen ions. Note that the abscissa has units of eV, not keV. Also note that the curves start at 1 eV since physical phenomena different than those considered in [19] occur at low temperatures. Since S_n may reach about 0.4 on tungsten and 0.5 on iron at high angles of incidence, we must consider plasma interactions with the beampipe wall when calculating the density profile.

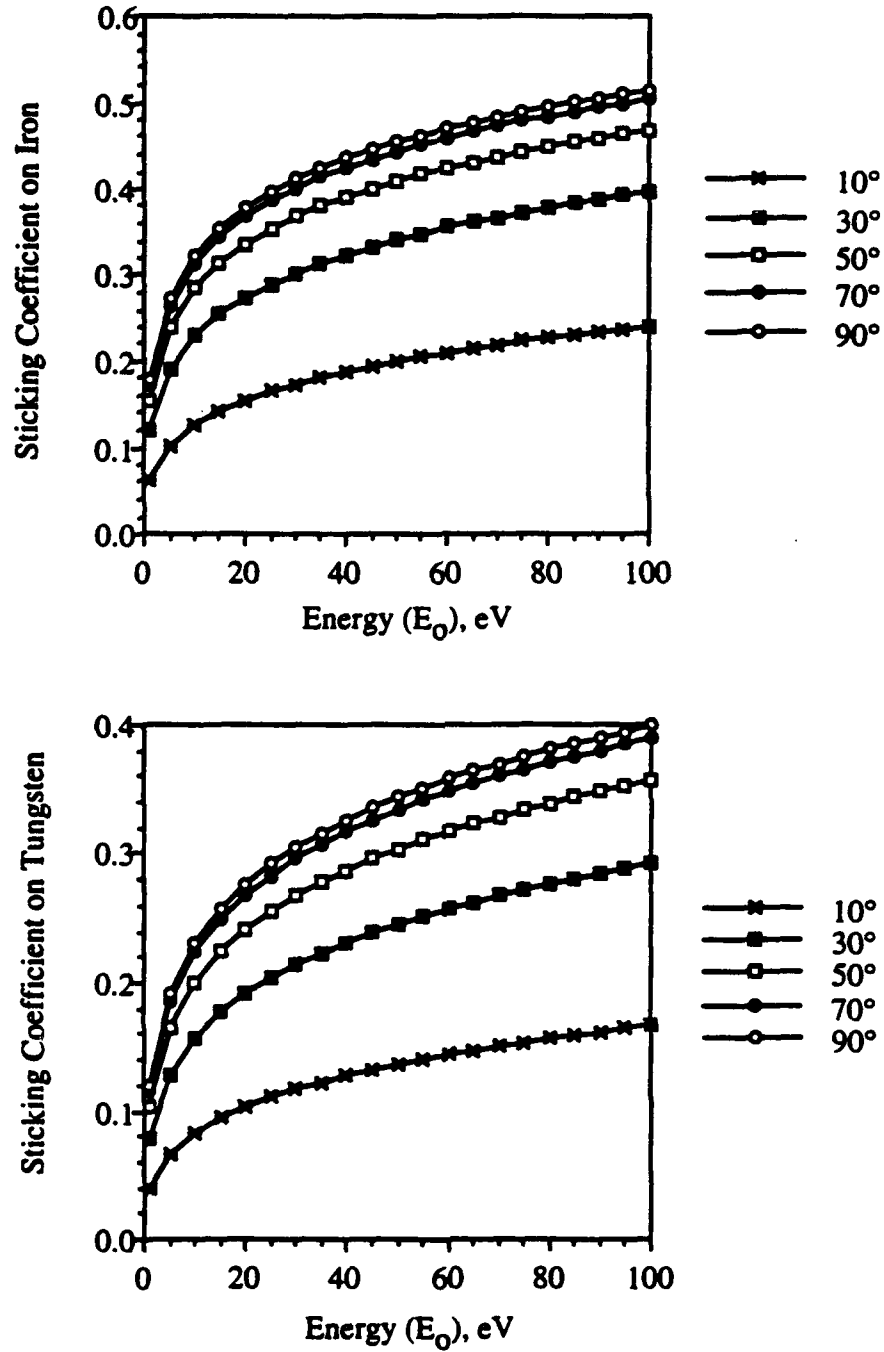


Figure 2.6 Variation of sticking coefficient with particle energy and angle of incidence for hydrogen ions on iron (top graph) and tungsten (lower graph).

2.7 Determining the Plasma Density Profile

The previous discussion has shown that electron and proton fluids which stream down the beampipe have approximately the same temperature, density, and velocity. We must now determine values of these quantities at each longitudinal station along the beampipe. Kinetic theory may be used to find the velocity distribution function, $f(v)$, for the plasma, which will allow us to find the density profile along the beampipe. With the correct density profile in hand, the resulting beam energy loss, scattering, and annihilation may be found using the procedures discussed in Chapters 3, 4, and 5.

The Boltzmann equation represents the fundamental equation of kinetic theory. An important solution to the Boltzmann equation is the Maxwellian velocity distribution function:

$$P(v)dv = 4\pi v^2 \left\{ \frac{m}{2\pi kT} \right\}^{3/2} e^{-(m/2kT)v^2} dv. \quad (2.30)$$

In Eq. (2.30) k is Boltzmann's constant, T the gas temperature, v the molecular speed, and m the mass of the proton. Maxwellian distribution functions apply to gases in thermal equilibrium and generally arise as a result of frequent collisions between the particles in a gas or plasma [16]. The discussion surrounding Eq. (2.22) showed that the plasma near the beampipe entrance is highly collisional, and therefore in thermal equilibrium. We can therefore model the plasma velocity flowing along the beampipe with a Maxwellian distribution.

Figure 2.7 shows the Maxwellian velocity distribution function. The peak of the curve represents the most probable proton velocity,

$$C_{mp} = (2kT/m)^{1/2}. \quad (2.31)$$

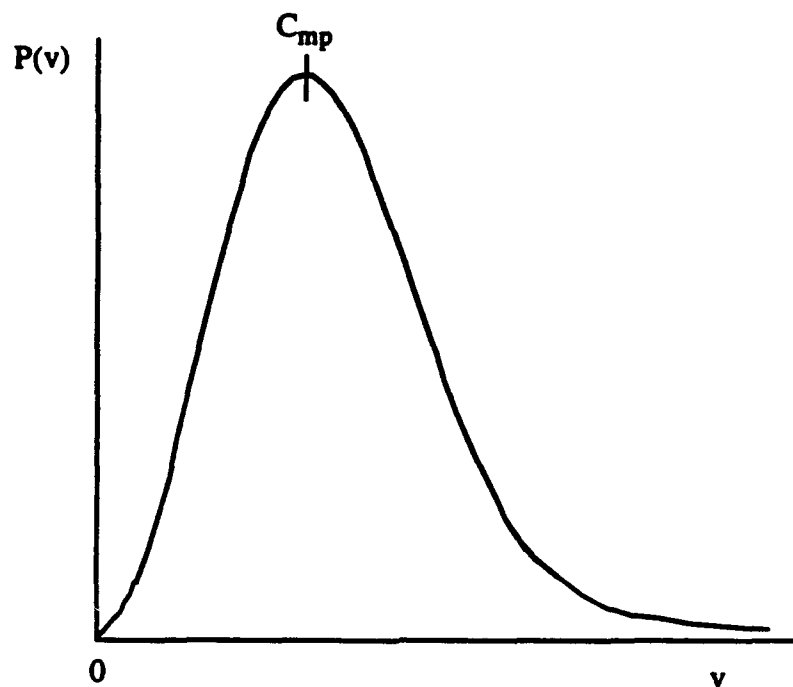


Figure 2.7 Maxwellian velocity distribution.

We can use the following procedure to obtain the density profile at the time of antiproton injection:

1. Using the two-dimensional fluid dynamic computer program CALE, obtain the plasma density, pressure, and temperature time histories during the compression process on the inside face of the cathode. These histories give the state of the plasma streaming into the beam pipe at all times of interest during the compression process.

2. Assume that the diamond window breaks when the plasma pressure on it reaches 200 kbar, then subtract this time from the time of peak compression to determine the time the plasma expands down the pipe.

3. Use the plasma temperature at the first time-step to obtain the Maxwellian velocity distribution for this time-step.

4. Slice up the velocity distribution into a finite number of thin, rectangular subdivisions and determine the number of particles associated with each velocity.

5. Further divide this chunk of plasma into ten pieces, equally divided in $\cos\theta$, where θ is the polar angle. This step accounts for the fact that the plasma, having a three-dimensional Maxwellian velocity distribution, expands isotropically into the beampipe. However, since the beampipe has radial symmetry about the centerline, we need only worry about what happens in a plane of constant Φ , the azimuthal angle around the beampipe.

6. Determine how far along the pipe each of the particles travels by multiplying the velocities of the individual Maxwellian slices by the expansion time and $\cos\theta$. Also determine the number of collisions (N_{coll}) each chunk of plasma makes with the beampipe walls during its expansion.

7. Determine the sticking coefficient of each plasma chunk from Eqs. (2.28) and (2.29).

8. Knowing the plasma mass and beampipe elemental volume, find the density of the plasma chunks at the location they reach by peak compression. Multiply this density by $S_n^{N_{\text{coll}}}$ to account for the plasma which sticks to the beampipe walls. This factor, which arises from the binomial theorem, gives the fraction of plasma from each chunk that *does not* stick to the beampipe wall as a result of collisions, and therefore the fraction of plasma that actually arrives at a particular axial location by the time of beam injection. Note that S_n will vary for each chunk of plasma because it depends on both energy and angle of incidence. Since S_n is always less than unity, note that the sticking phenomenon reduces the density profile below that which would occur if we assumed perfectly reflecting walls.

9. Update the remaining expansion time and temperature and repeat the above procedure until the time of peak compression, which corresponds to the injection time. Each time steps 1 through 8 are repeated, sum the plasma density at each station along the pipe to obtain the total plasma density.

Figure 2.8 shows the results of the above procedure for initial (i.e., just prior to the start of compression) plasma conditions of 2 eV temperature and 10^{19} atoms/cm³ density. Results for both sticking and perfectly reflecting beampipe walls are shown. The origin of the plot corresponds to the surface of the target, represented by the circle centered at -0.3 cm. Both curves drop very rapidly with increasing distance from the target, and change by nearly two orders of magnitude in the first centimeter.

Both curves shown in Figure 2.8 have a peak density of 0.0234 g/cm³ between $z=0$, the target surface, and $z=0.3$, the window. The curves begin to diverge just outside the window because of the sticking effect. Further down the beampipe, the two density profiles separate continuously since more and more plasma sticks to the wall. Ten centimeters down the beampipe, the two curves differ by about an order of magnitude, and the plasma sticking to the beampipe wall accounts for nearly 90% of the total plasma in this region.

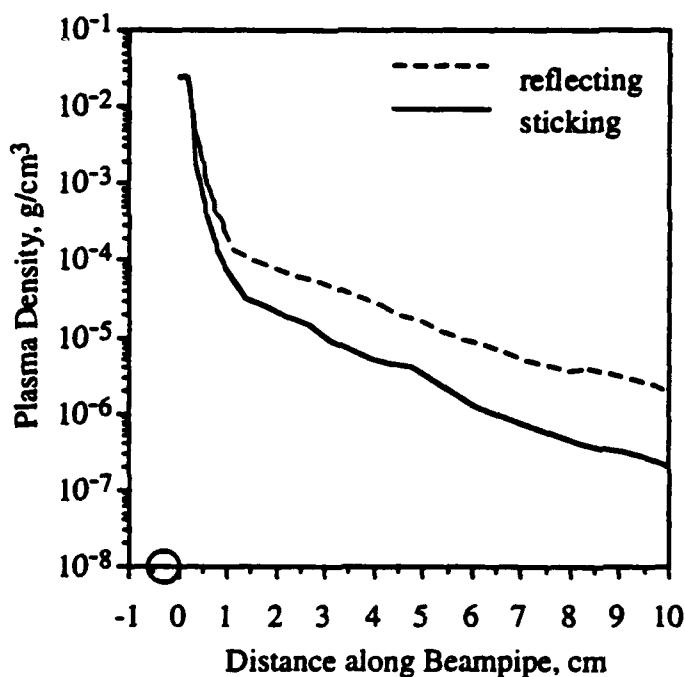


Figure 2.8 Comparison of plasma density profiles for reflecting and sticking walls.

With the initial conditions of 2 eV and 10^{19} atoms/cm³, the diamond window fails about 12.22 μ sec after the start of the compression cycle. The target undergoes peak compression at 12.98 μ sec, giving the plasma approximately 760 nsec to expand down the beampipe before antiproton beam injection. During this time, 1.55 mg of plasma streams into the beampipe. Since the spherical liner contains 3.1 mg of working fluid, the plasma that leaks into the beampipe corresponds to about 50% of the total plasma. The amount of plasma in the beampipe may be obtained by either integrating the reflecting-wall density profile or summing the plasma mass passing through the cathode window at the beginning of each timestep, which can be found from the known CALE data. The one-dimensional, unsteady, continuity equation applied at the cathode window gives the total mass leakage:

$$dm/dt = \rho A_{win} v_{th}/4, \quad (2.32)$$

where A_{win} represents the window area, and equals 3.1416×10^{-6} m² and Eq. (2.23) gives v_{th} . Since the plasma density and temperature are known from CALE at each timestep of interest at the window, the discretized plasma mass passing through the window during each timestep may be found by rearranging Eq. (2.32):

$$\Delta m = \rho A_{win} v_{th} \Delta t / 4, \quad (2.33)$$

where Δt represents the timestep duration. Summing the masses found at each timestep gives the total plasma leakage. Appendix A lists the CALE data used in the mass flow and kinetic theory calculations.

Since the density profile represents the sum of 40 Maxwellian distributions (one corresponding to each timestep of CALE data between window fracture and peak compression) it does not resemble the single, one-dimensional distribution shown in Fig. 2.6. The density decreases monotonically with increasing distance from the target because,

as time progresses, the plasma has less and less time to expand and subsequently piles up near the entrance to the beampipe.

Chapter 3

ANTIPROTON ENERGY LOSS IN FULLY IONIZED PLASMAS

3.1 Introduction

In Chapter 2 we developed a method for determining the space varying plasma density profile along the injection pipe. With this information, we can investigate antiproton beam propagation through the plasma cloud. As the antiprotons move through the fully ionized plasma, they undergo four types of interactions with the plasma particles, namely: electronic energy loss, scattering from plasma ions, annihilation with plasma ions, and charge exchange with plasma ions. The reaction $p + \bar{p} \rightarrow n + \bar{n}$ describes the charge exchange reaction between a proton and antiproton which produces a neutron and an antineutron. Compared to the three other processes, the probability that an individual antiproton will undergo charge exchange for the conditions of the SHIVA Star experiment is extremely small; therefore, we concern ourselves primarily with energy loss, scattering, and annihilation. Chapters 4 and 5 discuss scattering and annihilation, respectively. Here, we address the problem of electronic energy loss in a plasma, which ultimately specifies the necessary initial antiproton beam energy, a major design parameter of the radio frequency quadrupole (RFQ).

3.2 Binary Coulomb Collisions

In order to determine the energy transferred to the electron fluid from the antiproton beam, we must consider the mechanics of a binary (two-particle) Coulomb collision between a swiftly moving incident antiproton and a nearly stationary free electron. We distinguish here between "free" electrons, as in a fully ionized plasma, and "bound" electrons, as in an atom, because some references, such as [20], contain extensive analysis

of the energy loss associated with each type of electron. Since we here deal exclusively with an electron fluid, the bound electron energy loss does not concern us.

Consider the situation shown in Figure 3.1. A fast incident particle of charge Ze , velocity v , and mass M encounters an electron of charge $-e$ and mass m . The distance b , called the "impact parameter", represents the distance of closest approach in the absence of any Coloumb force. For simplicity we assume that the electron is stationary, though strictly speaking it may have some slight thermal motion. From the preceeding discussion, we know that very little momentum transfer occurs between the two particles, so the antiproton travels in essentially a straight line during the collision.

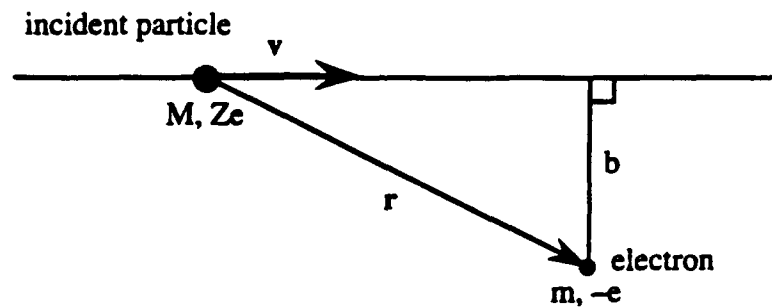


Figure 3.1 Incident particle approaches electron at impact parameter b (after Jackson).

Since both the particles have an electric charge, they need not actually collide in order to interact, but can exchange energy via the Coloumb force between them, given by

$$F_{\text{Coloumb}} = -\frac{(Ze)(ze)}{4\pi\epsilon_0 r^2}, \quad (3.1)$$

where $Z=1$ for an antiproton, $z=1$ for an electron, ϵ_0 represents the permeability of free space, and r is the distance separating the two particles.

As the incident particle passes by the electron, the two particles influence one another via their electric fields. Equation (11.152) of [20] gives the electric fields of the incident particle at the time its position coincides with that of the electron. Only the transverse electric field survives an integration over time, so we get the momentum impulse from

$$\Delta p = \int eE_2(t)dt = 2 \frac{ze^2}{bv} . \quad (3.2)$$

From elementary mechanics we can write the kinetic energy as

$$E = \frac{p^2}{2m}, \quad (3.3)$$

where m is the electron mass. The energy transferred during the encounter may be obtained by substituting Eq (3.2) into Eq (3.3), yielding

$$\Delta E = \frac{\Delta p^2}{2m} = 2 \frac{Z^2 e^4}{mv^2 b^2}. \quad (3.4)$$

where ΔE and Δp represent the energy and momentum, respectively, transferred during the collision. Note that this equation depends on the charge and velocity of the incident particle, but not its mass. Furthermore, the energy transfer varies inversely with the square of the impact parameter, b , so that close encounters involve more energy transferred to the electron than relatively distant collisions.

Equation (3.4) provides the energy transferred from a fast incident particle to a target particle during a single collision. We would like to be able to determine the energy lost as the incident particle passes through a finite thickness of matter and undergoes multiple electron encounters. Before proceeding in this direction, however, we must

review elementary plasma theory. We will find that special properties of the plasma state will greatly affect our subsequent analysis.

3.3 Debye Shielding and Plasma Frequency

One useful definition of a plasma states [16]:

“A plasma is a quasineutral gas of charged and neutral particles which exhibits collective behavior.”

A plasma displays “collective” behavior because the moving charges can cause concentrations and gradients to develop which generate electric fields, currents, and hence, magnetic fields. These fields can affect the behavior of plasma particles large distances away via the long range Coloumb force. Furthermore, plasmas tend toward neutrality when at rest, so that the electron density approximately equals the ion density. However, the equilibrium plasma still displays characteristic electromagnetic phenomena, so that it is not completely neutral, only “quasineutral”. (Of course, the specific hydrogen plasma we consider for the SHIVA Star experiment has no neutral particles, and consists only of totally ionized electron and proton fluids.)

According to Chen: “A fundamental characteristic of the behavior of a plasma is its ability to shield out electric potentials that are applied to it.” Such behavior is called Debye shielding. Suppose we insert two oppositely charged plates (cathode and anode) into an ambient, fully ionized plasma consisting of free electrons and ions, as shown in Fig. 3.2. The electrodes are connected to a simple circuit consisting of a battery somewhere outside the plasma and two perfectly conducting wires. Since the electrodes generate an electric field, they attract particles of the opposite charge. The anode (positive electrode) attracts the positively charged ions, while the cathode (negatively charged electrode) attracts the negatively charged electrons. Almost immediately after placing the electrodes in the plasma, a cloud of particles surrounds each plate and shields out most of the electric potential. The shielding is not perfect, though, because at the edge of the particle cloud,

where the potential is weak, the random thermal motion of the particles may be enough to separate the particle from the cloud, and some of the potential subsequently leaks into the plasma. In other words, particles at the edge of the cloud may have enough kinetic energy to escape from the electrostatic potential well generated by the electrodes. The approximate edge of the cloud occurs where the potential energy of the electrostatic well equals the thermal energy, kT , of the particles, where k is Boltzmann's constant, and T is the particle temperature. If the plasma were "cold" such that the particles had no thermal motion, then the shielding would be complete because the particle clouds would have just as many charges as the corresponding electrode. There would be no electric potential in the plasma outside of the clouds. However, all real plasmas have finite temperature, so Debye shielding is never perfect.

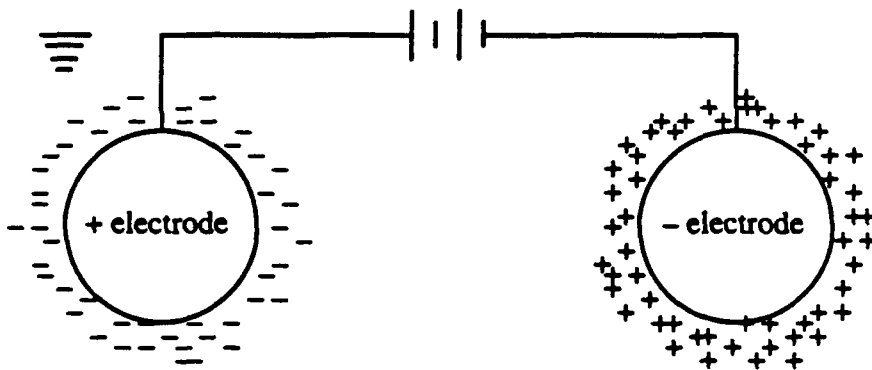


Figure 3.2 Electron and ion clouds surround oppositely charged electrodes in a plasma, illustrating Debye shielding (after Chen).

According to [16], the thickness (radius) of the particle cloud, called the Debye length, may be found from Poisson's equation, and is given by

$$\lambda_D = \sqrt{\frac{\epsilon_0 kT}{ne^2}}. \quad (3.5)$$

where ϵ_0 is the permittivity of free space, n is the plasma number density, and e is the charge on a single electron.

The collective behavior of plasmas represents another fundamental characteristic that will prove useful to discuss. Consider a swift, massive test particle passing through a quiescent, fully ionized plasma. As the test particle passes through the plasma, its electric field interacts with the fields of both the electron and ions. If the test particle has positive charge, then the electrons move toward it; on the other hand, it will repel electrons if it has a negative charge. In either case, the electrons, having much larger thermal velocities than the more massive ions, are displaced from their original positions. Charge and density bunching may occur. Since the ions cannot follow fast enough, electric fields build up between the two species which tend to pull the electrons back to their initial positions. However, because the electrons have nonzero inertia, they tend to overshoot and oscillate about this equilibrium position with a characteristic frequency called the plasma frequency.

One can obtain an expression for the plasma frequency by linearizing via small perturbation analysis the plasma fluid equations and Poisson's equation. Following [16], this procedure yields

$$\omega_p = \sqrt{\frac{n_0 e^2}{\epsilon_0 m}} \text{ rad/sec,} \quad (3.6)$$

where n_0 is the equilibrium plasma density, e the charge on a single electron, m the electron mass, and ϵ_0 the permittivity of free space.

From the discussion of Debye shielding and plasma oscillations, we draw the following conclusions. The length scale of a plasma can be divided into two different regions: first, for dimensions small compared to the Debye length (the thickness of the Debye sphere) we can use the previously discussed binary collision theory to find the electron stopping power; second, for dimensions larger than the Debye length, the

contribution to electron energy loss can be found by considering the collective wave excitation of the plasma. Thus, the Debye length represents the maximum impact parameter, b_{\max} , for binary collision energy loss, but we must also consider energy loss due to collective oscillations. According to Melhorn [21]:

“Simple binary collision theory within a Debye radius coupled with collective plasma wave excitation outside the Debye radius is normally considered to give a sufficiently accurate description of the plasma electron stopping power.”

As a test particle moves through the plasma, it encounters electrons within its Debye sphere. These electrons receive energy from the test particle via binary Coulomb collisions. The Debye sphere shields the test particle from the rest of the plasma so that little direct interaction results, but the passage of the intruder excites electron plasma waves of frequency ω_p , which cause density and charge bunching. The energy responsible for this plasma excitation comes from the test particle. Therefore, both binary collisions inside the Debye sphere and plasma oscillations outside the sphere contribute to the energy loss of the intruder. We must derive equations which account for both types of energy loss, beginning with binary collision energy loss inside the Debye sphere.

3.4 Energy Loss through Multiple Collisions

Recall Eq. (3.4), which gives the energy loss of the test particle per single collision, within the Debye sphere for a plasma. We would like to determine the differential energy loss per unit path length a test particle travels. This differential energy loss includes binary collisions with many electrons, not just one.

Suppose a fast particle travels through a plasma with atom number density N of charge number z . As the particle moves through the plasma, it suffers energy loss to electrons through binary collisions inside its Debye sphere. In a thickness of plasma dx ,

the number of electrons located between impact parameters b and $b+db$, both less than b_{\max} , is given by

$$dn = Nz 2\pi b db dx, \quad (3.7)$$

where $2\pi b db dx$ represents the volume element shown in Figure 3.3.

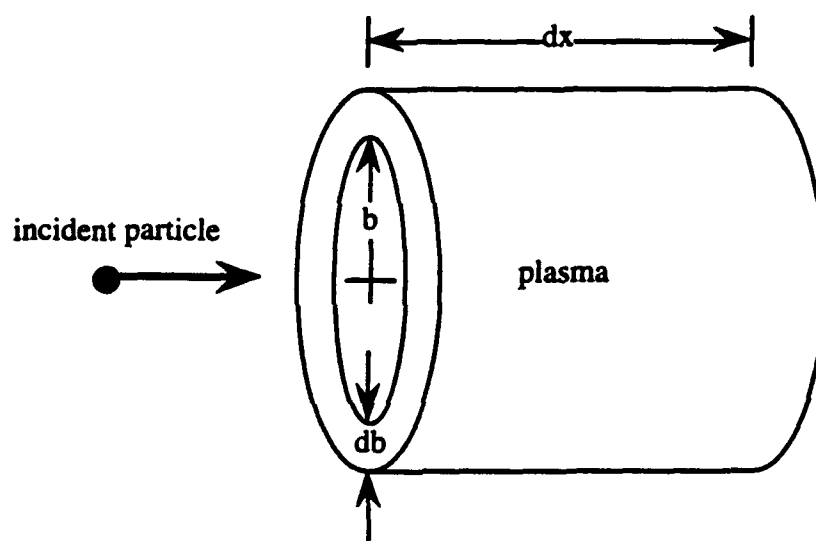


Figure 3.3 Plasma volume element

In order to obtain the differential energy loss, we multiply this equation by the ΔE obtained for one electron encounter, yielding

$$dE = 2\pi Nz b \left(\frac{2Z^2 e^4}{mv^2 b^2} \right) db dx, \quad (3.8)$$

or

$$\frac{dE}{dx} = \left(\frac{4\pi Nz Z^2 e^4}{mv^2 b} \right) db. \quad (3.9)$$

Integrating over all possible impact parameters yields

$$\frac{dE}{dx} = \frac{4\pi N_z Z^2 e^4}{mv^2} \int \frac{1}{b} db, \quad (3.10)$$

where all constants of the integration have been moved outside the integration sign and b_{\max} and b_{\min} represent the limits of integration for the definite integral. Performing the necessary operation yields

$$\frac{dE}{dx} = \frac{4\pi N_z Z^2 e^4}{mv^2} \ln \frac{b_{\max}}{b_{\min}}. \quad (3.11)$$

This expression gives the differential energy loss per unit distance traveled by the incident particle into the matter. However we must still obtain values for the maximum and minimum allowed impact parameters.

The closest possible encounter involves a head-on collision, but, according to [20], the above method of analysis becomes invalid for extremely small impact parameters. The lowest limit on the impact parameter, b_{\min} , may be obtained by considering the maximum transfer of energy during the collision. From [20]

$$\Delta E_{\max} = 2mv^2 \quad (3.12)$$

gives the maximum energy transfer occurring for b_{\min} . Substituting this into eq. (3.4) and solving for b gives b_{\min} :

$$b_{\min} = \frac{Ze^2}{mv^2}. \quad (3.13)$$

If the impact parameter is smaller than this value, then equation (3.6) must be replaced by

$$\Delta E(b) = \frac{2z^2 e^4}{mv^2 (b_{\min}^2 + b^2)}, \quad (3.14)$$

which gives a more accurate result. Note that this equation reduces to the previous equation as b becomes much larger than b_{\min} .

As a result of our previous discussion, we already know the maximum allowed impact parameter. For binary collision electronic energy loss

$$b_{\max} = \lambda_D = \sqrt{\frac{\epsilon_0 kT}{ne^2}}. \quad (3.15)$$

Substituting this value into the differential energy loss equation yields

$$\frac{dE}{dx} = \frac{4\pi NzZ^2 e^4}{mv^2} \ln \frac{\lambda_D}{b_{\min}}. \quad (3.16)$$

We may make one more simplification to this expression. Recall the definition of the plasma frequency, ω_p , given by Eq. (3.6). Since the plasma has atom number density N , and z electrons per atom, the plasma has electron number density Nz , since in a fully ionized plasma all electrons have been stripped from the nuclei. But Nz is simply n_0 , so we may rewrite the plasma frequency as

$$\omega_p = \sqrt{\frac{4\pi Nz e^2}{m}}. \quad (3.17)$$

where $\epsilon_0 = 1/(4\pi)$, in proper units. Substituting this value into the differential energy loss equation yields

$$\frac{dE}{dx} = \frac{Z^2 e^2}{v^2} \omega_p^2 \ln \frac{\lambda_D}{b_{\min}}. \quad (3.18)$$

This equation gives the differential energy loss per unit distance the test particle travels into the plasma for dimensions smaller than the Debye radius. For the same situation, Jackson obtains a very similar result in problem 13.3:

$$\frac{dE}{dx} = \frac{z^2 e^2}{v^2} \omega_p^2 \ln \frac{1}{1.47 k_D b_{\min}}, \quad (3.19)$$

where k_D represents the Debye wave number, simply the reciprocal of λ_D . The slight difference in the argument of the natural logarithm arises from quantum mechanical effects that we have not considered here. Since the logarithm is not sensitive to small differences in its argument, the classical answer is correct to first order.

We have derived an equation which gives the energy loss inside the Debye sphere. Now we must determine the energy loss associated with plasma excitations. According to Jackson, the loss in collective oscillations may be found from Fermi's formula (Jackson 13.67), which ultimately comes from considering a phenomenon known as the *density effect*. This treatment lies beyond the scope of the present work (see Jackson for further details) but we may make use of the results. For energy loss at distances outside the Debye sphere

$$\frac{dE}{dx} = \frac{z^2 e^2}{v^2} \omega_p^2 \ln \frac{1.123 k_D v}{\omega_p}. \quad (3.20)$$

We can combine this with our previous result to obtain the total energy loss of an incident particle in a fully ionized plasma. Thus,

$$\left. \frac{dE}{dx} \right|_{\text{total}} = \left. \frac{dE}{dx} \right|_{b < \lambda_D} + \left. \frac{dE}{dx} \right|_{b > \lambda_D}, \quad (3.21)$$

or

$$\left. \frac{dE}{dx} \right|_{\text{total}} = \frac{Z^2 e^2}{v^2} \omega_p^2 \ln \frac{0.764v}{b_{\min} \omega_p}, \quad (3.22)$$

where equation (3.13) gives b_{\min} . Melhorn presents a slightly different equation (Melhorn, equation 10), which incorporates a dimensionless "coupling factor", symbolized by $G(y)$, to account for a correction due to electron temperature:

$$\left. \frac{dE}{dx} \right|_{\text{total}} = \frac{Z^2 e^2}{v^2} \omega_p^2 G(y) \ln \left[\frac{0.764v}{b_{\min} \omega_p} \right]. \quad (3.23)$$

Mathematically,

$$G(y) = \text{erf}(\sqrt{y}) - 2\sqrt{y/\pi} e^{-y}, \quad (3.24)$$

where

$$y = v_{\text{beam}}/v_e.$$

The function $G(y)$ provides a measure of the Coulomb interaction between a beam ion and a plasma electron, which depends on the relative velocity between the two particles. For most plasma temperature/beam energy combinations that we expect to occur in the SHIVA Star experiment, $G(y)$ is of order unity because the parameter y exceeds 1.0. That is to say, the beam ions travel faster than the plasma electrons. However, when the parameter y becomes smaller (when the plasma electrons have higher average velocity than the beam ions) $G(y)$ decreases, indicating that electron stopping power becomes less effective. Since CALE indicates that the temperature of the plasma streaming through the window varies between about 15 and 125 eV, this situation ($G(y) < 1$) may occur when the ion beam,

having lost most of its energy, approaches the target surrounded by plasma at the upper end of this temperature regime. Table 3.1 shows values of $G(y)$ for different combinations of beam energy and plasma temperature.

Table 3.1 Coupling term values for different beam energy and plasma temperature combinations.

Beam energy	Plasma temp.	y	$G(y)$
1.2 MeV	125 eV	2.30	1.06
1.2 MeV	15 eV	6.57	1.25
0.1 MeV	125 eV	0.66	0.17
0.1 MeV	15 eV	1.90	0.90

Notice that $G(y)$ is near unity for all cases where ion velocity exceeds plasma electron velocity. According to Fig. 14 of [21], when $y=1$, $G(y)=0.43$. Therefore, when the beam ion and plasma electron velocities are equal, the electron stopping power is reduced by about one-half.

3.5 Antiproton Range

Another quantity of interest in the study of an antiproton beam penetrating a hydrogen plasma is the particle path length, or range. We shall define the range as the distance the incident particle has traveled when it loses all of its original energy. Therefore,

$$R = \int_{E_0} \frac{1}{dE/dx} dE, \quad (3.25)$$

where R represents the particle range. Since our ultimate goal is to determine the beam energy necessary for the antiprotons to reach the target, we must calculate the particle range in the plasma.

In our analysis thus far, we have implicitly assumed that the particles incident on the plasma travel in a straight-line trajectory. This assumption is not in general true because the incident particles undergo deflections from their original trajectories via collisions with the plasma ion species, a phenomenon known as range straggling. According to ref [21], the difference between the true particle range and the assumed straight-line range is about 5%. Therefore, we will ignore this effect in the preceding analysis and make sure that the antiprotons always have some small residual energy when they hit the target.

In order to determine the necessary initial antiproton beam energy, we carry out the following procedure:

1. From the analysis presented in Chapter 2, we determine the plasma density and temperature profile at each axial point along the injection pipe. This also gives the distance the plasma wavefront travels down the pipe during the expansion time.
2. We choose a spatial step size to discretize the plasma cloud into a small, but finite number of steps.
3. We make an initial guess as to the antiproton beam energy necessary to penetrate the plasma cloud. Note that we need only choose the overall beam energy and not each individual antiproton's energy since we assume that the passage of one particle does not disturb the plasma enough to affect the passage of the particles following in its wake.
4. Beginning at the plasma wavefront, we determine the energy lost in the first space step using the density and temperature at that point in space.
5. We swim the antiproton through the plasma, summing the energy lost along the way.

6. If the antiproton does not reach the target, we repeat the process with a higher initial energy.
7. If the antiproton reaches the target, we determine its residual energy. If the antiproton has more than 0.2 or 0.3 MeV residual energy, we repeat steps 3 through 6, starting with a lower initial energy. Ultimately, we would like the antiproton beam to impact the target with about 0.1 to 0.2 MeV to account for the difference between the true and assumed path lengths.

Figure 3.4 shows the results of the above procedure for Case I, a scenario with initial plasma conditions of 2 eV and 10^{19} atoms/cm³, which was previously discussed at the end of Chapter 2 (Chapter 6 discusses seven additional Cases). The graph shows the energy profile of an antiproton beam as it travels up the injection pipe to the target. The plasma density profile (including sticking effects), discussed in Chapter 2, is included to illustrate the energy loss dependence on plasma density.

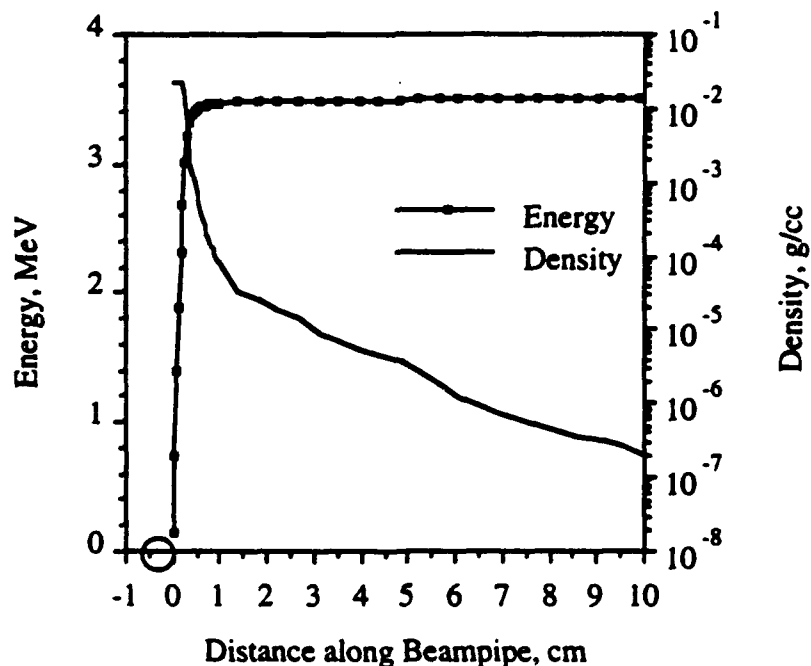


Figure 3.4 Beam energy and plasma density profiles for Case I.

In order to reach the target, the antiproton beam requires an initial energy of 3.5 MeV. Most of its kinetic energy is lost through electronic collisions and plasma wave excitation. On impact, it has a residual energy of about 0.152 MeV. Since the plasma density does not become significant until about 1 cm from the target (located at the origin), the beam loses no appreciable energy over most of its flight. The plasma has a peak density of 0.0234 g/cm^3 in the 3 mm long space between the target surface (located at the origin) and the cathode edge. The antiproton beam loses most of its energy to the plasma in this region.

Table 3.2 shows the iterative procedure used to obtain the proper energy (3.5 MeV) for Case 1. Each attempt refers to a run of the computer code SWMXC2, which incorporates the 7 step recipe discussed above, and outputs the antiproton beam's range through the plasma and final energy at the end of that range. The final column, labelled Δz , refers to the final distance between the target surface and the antiproton beam.

Table 3.2 Obtaining the proper beam energy for Case 1.

Attempt	E_{initial} , MeV	E_{final} , MeV	Δz , cm
1	1.0	0.00	0.33
2	2.0	0.00	0.20
3	3.0	0.00	0.08
4	4.0	1.50	0.00
5	3.5	0.15	0.00

The first three beams do not have enough energy to penetrate the plasma and reach the target. The fourth beam reaches the target, but has excessive residual energy of 1.5 MeV upon impact. We do not require a safety margin of more than about 0.1 to 0.3 MeV. The fifth beam with an energy of 3.5 MeV represents the best choice for Case 1 since it reaches the target with the proper amount of excess energy, about 0.15 MeV.

Table 3.2 also illustrates the affect of the high-density plasma region (between the target surface and the cathode) on antiproton energy loss. The 1.0 MeV beam has sufficient energy to reach the end of the beampipe, located 3 mm from the target. However, an additional 2.5 MeV is required to penetrate the 3 mm of dense plasma between the target surface and the end of the beampipe. The beam loses most of its necessary energy in the 3 mm region between the target surface and the end of the beampipe.

3.6 Comparison with Experimental Results

The physical phenomena and mathematical models described above for the loss of energy from an ion beam and subsequent deposition into a plasma have several applications other than the Shiva Star experiment. Much of the research on ion beam—plasma interactions has been conducted to study plasma heating in tokamaks. The tokamak is an important research tool in the area of thermonuclear fusion which utilizes toroidal and poloidal magnetic fields to contain a plasma [22]. In order to produce thermonuclear power, one must heat a tokamak plasma to a temperature on the order of 10 keV. *Neutral beam injection* represents one method used to heat the plasma. In this process, a beam of neutral atoms, often hydrogen, is injected into the plasma at energies between 10 keV and 1 MeV. As a result of collisions with plasma particles, the beam atoms undergo ionization and acquire a charge. They are then trapped by the tokamak magnetic fields and execute orbital motion. The beam atoms decelerate under the influence of Coulomb collisions, and transfer some of their energy to the plasma particles, heating both plasma ions and electrons [22].

Table 3.3 compares some experimental results presented by Duderstadt and Moses, [23], to results obtained from SWMXC2 for protons traversing a 4 m long, fully ionized, plasma channel with constant electron density $n_e=3.2 \times 10^{17} \text{ cm}^{-3}$.

Table 3.3 Comparison of experimental and computer code results.

Initial Energy	Energy Loss, [23]	Energy Loss (T=1000ev), code
2 MeV	0.160 MeV	0.190 MeV
4 MeV	0.090 MeV	0.096 MeV
10 MeV	0.040 MeV	0.043 MeV

The close correspondence between the experimental and numerical results implies that SWMXC2 gives reasonable and accurate results for the energy loss and range of the antiproton beam in the plasma streaming along the beampipe.

Chapter 4

ANTIPROTON DEFLECTION IN FULLY IONIZED PLASMAS

4.1 Introduction

As stated in Chapter 3, a charged particle moving through matter, whether solid, liquid, gas, or plasma, suffers collisions with both atomic electrons and atomic nuclei. Energy loss arises primarily from electronic collisions, whereas collisions with nuclei cause deflection from the particle's original path. Furthermore, nuclear reactions may occur if the proper conditions are met, and will be considered in the following chapter on antiproton annihilation.

4.2 Binary Antiproton-Ion Collisions

We have previously concerned ourselves with the electronic energy loss of the antiproton beam due to electronic collisions. In the analysis of Chapter 3, the implicit assumption was made that the particles constituting the antiproton beam followed a straight line path in their flight through the expanding plasma cloud to the target. Strictly speaking, this assumption is not true, though it did allow us to obtain an accurate measure of the energy necessary for the beam to penetrate the plasma for various initial plasma conditions. In reality, the plasma will cause not only decelerations of the beam, but deflection of the beam as well.

Let us again consider the passage of the antiproton beam through the plasma cloud, this time examining binary antiproton-ion collisions instead of antiproton-electron collisions. As the antiprotons pass through the plasma, they undergo various collisions with the ion particles. For the special case of a fully ionized hydrogen plasma, the ion fluid consists solely of protons. The proton-antiproton collisions can cause large changes in the momentum of the particles, leading to deflection from the original straight line path. As an

individual antiproton moves through the ion fluid, bouncing from proton to proton, it undergoes a random walk away from its original trajectory. If enough deflection occurs, the particle could miss the target, or more probably, impact on the interior surface of the cathode. Therefore, it becomes necessary to include beam deflection in our analysis to determine how many antiprotons will be lost through scattering before reaching the target. Beam scattering also affects the size of the cathode orifice, since this aperture can be modified to accommodate the passage of the scattered antiprotons. In other words, we can change the diameter of the circular orifice to slightly exceed the (expected) width of the scattered antiproton beam.

In order to understand how a plasma can scatter an ion beam, we must examine the mechanics of a binary coulomb collision. At the outset, we assume that the incident particle moves at nonrelativistic speeds (that is, less than about $0.1c$) so that we may use classical mechanics to analyze the collision. The dynamics of a close encounter between a pair of charged particles are governed by the charges of the incident and target particles, Z_1e and Z_2e , respectively (where the Z 's correspond to the particle charge number, and e is the charge of a single electron), their respective masses, the relative velocity between the two particles, and the impact parameter b , which gives the distance of closest approach if no momentum transfer occurred. Figure 4.1 shows the geometry of the collision. In the illustration, θ indicates the deflection angle of the incident particle. Note that target particle also suffers a change in momentum from the collision, and moves off on a separate path.

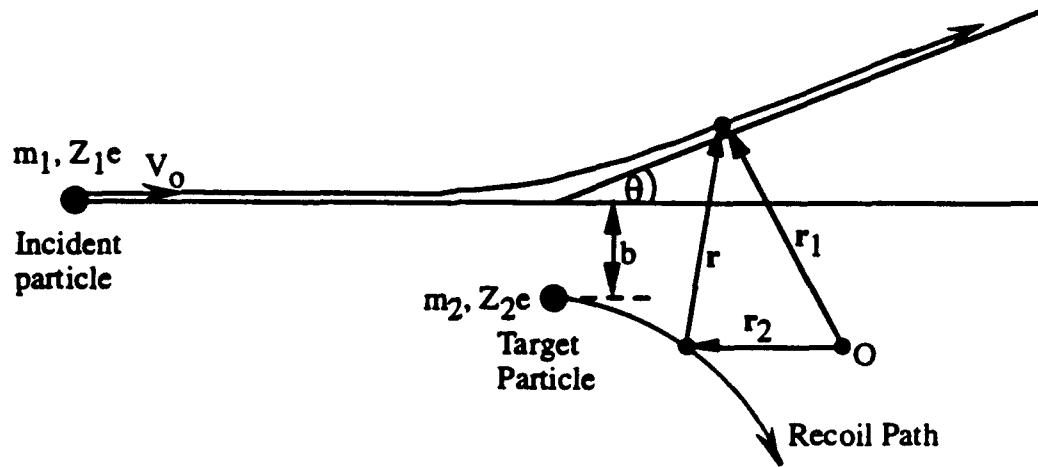


Figure 4.1 Incident particle suffers a deflection of angle θ from its original trajectory due to an encounter with target particle of same charge type (after Krall and Trivelpiece).

Applying Newton's second law to the system gives the following equations of motion for the collision:

$$\frac{m_1 d^2 r_1}{dt^2} = \frac{Z_1 Z_2 e^2 (r_1 - r_2)}{|r_1 - r_2|^3}, \quad (4.1a)$$

$$\frac{m_2 d^2 r_2}{dt^2} = \frac{Z_1 Z_2 e^2 (r_2 - r_1)}{|r_1 - r_2|^3}, \quad (4.1b)$$

where m gives the particle mass, r is the position vector, Z is the atomic number, e represents the charge on a single electron, and subscripts 1 and 2 indicate the particle number. Essentially, these equations indicate that the time rate of change of momentum of the particles is equal to the Coloumb force between them. Note that the above equations closely resemble the classical equations of motion from orbit theory, with the Coloumb force replaced by the gravitational force.

Combining these equations yields:

$$\frac{m_1 d^2 r_1}{dt^2} + \frac{m_2 d^2 r_2}{dt^2} = (m_1 + m_2) \frac{d^2 R}{dt^2} = 0, \quad (4.2a)$$

and

$$\frac{d^2 r_1}{dt^2} - \frac{d^2 r_2}{dt^2} = \frac{d^2 r}{dt^2} = \frac{m_1 + m_2}{m_1 m_2} \frac{Z_1 Z_2 e^2}{|r|^3} r, \quad (4.2b)$$

where

$$R = \frac{m_1 r_1 + m_2 r_2}{m_1 + m_2}, \quad (4.3a)$$

and

$$r = r_1 - r_2. \quad (4.3b)$$

The first of these indicates that the center-of-mass of the system, at R , moves with constant velocity, and the second says that the relative position r changes as if describing the motion of a single particle of mass $m_1 m_2 / (m_1 + m_2)$. This term is called the reduced mass of the system, and is usually denoted by μ .

Following Krall and Trivelpiece [24], Eq. (4.2) can be solved in polar coordinates, using the initial conditions $\theta_0 = \pi$, $r_0 = \infty$, $dr/dt|_0 = -v_0$, $r_0^2 d\theta/dt|_0 = -v_0 b$. After some algebra, there results

$$\tan \frac{\theta}{2} = \frac{Z_1 Z_2 e^2}{\mu v_0^2 b}. \quad (4.4)$$

For small angles, this reduces to

$$\theta = 2 \frac{Z_1 Z_2 e^2}{\mu v_0^2 b}. \quad (4.5)$$

Note from the preceding equation that the deflection angle varies inversely with the impact parameter. In other words, incident particles with small impact parameters suffer large deflections from their original trajectory, while particles with large impact parameters undergo small angle deflections. Furthermore, particles with high inertia (e.g., heavy or

fast particles) undergo smaller deflections than particles with less inertia because their momentum tends to counteract the influence of the Coloumb force.

We have derived an expression for the deflection angle of an incident particle on a second target particle. However, as an ion traverses a plasma cloud, as in the case with the SHIVA Star experiment, it undergoes many such collisions, and we would like to be able to determine the particle's final trajectory as it exits the plasma. As we will see, large angle scatter resulting from a single collision is much less likely to occur than a net large angle deflection resulting from a multitude of large b collisions. In general, the particle executes a random walk away from its original trajectory. Furthermore, as a single particle moves through a fully ionized plasma of number density, n , the deflection from its original path averages to zero, since completely random motion occurs. Any deflection in the (arbitrary) positive direction is just as likely as a deflection in the opposite direction, for the plane perpendicular to the path of the particle. But the root mean square deflection is certainly not zero, since the particle undergoes a random walk away from its initial trajectory.

4.3 The Rutherford Scattering Cross Section

We will return to these ideas soon; however, let us first show that a large angle scatter from a single encounter is much less likely than a large net deflection from many collisions. Suppose we have a very massive target particle that does not recoil from a collision with an incident particle. Further, suppose that we fire a host of particles at this target, each of which has a different impact parameter, b . Each of the incident particles will suffer a deflection according to equation (4.5). Somewhere downstream of the target particle the incident particles hit and adhere to an impenetrable spherical screen. Figure 4.2 illustrates the situation.

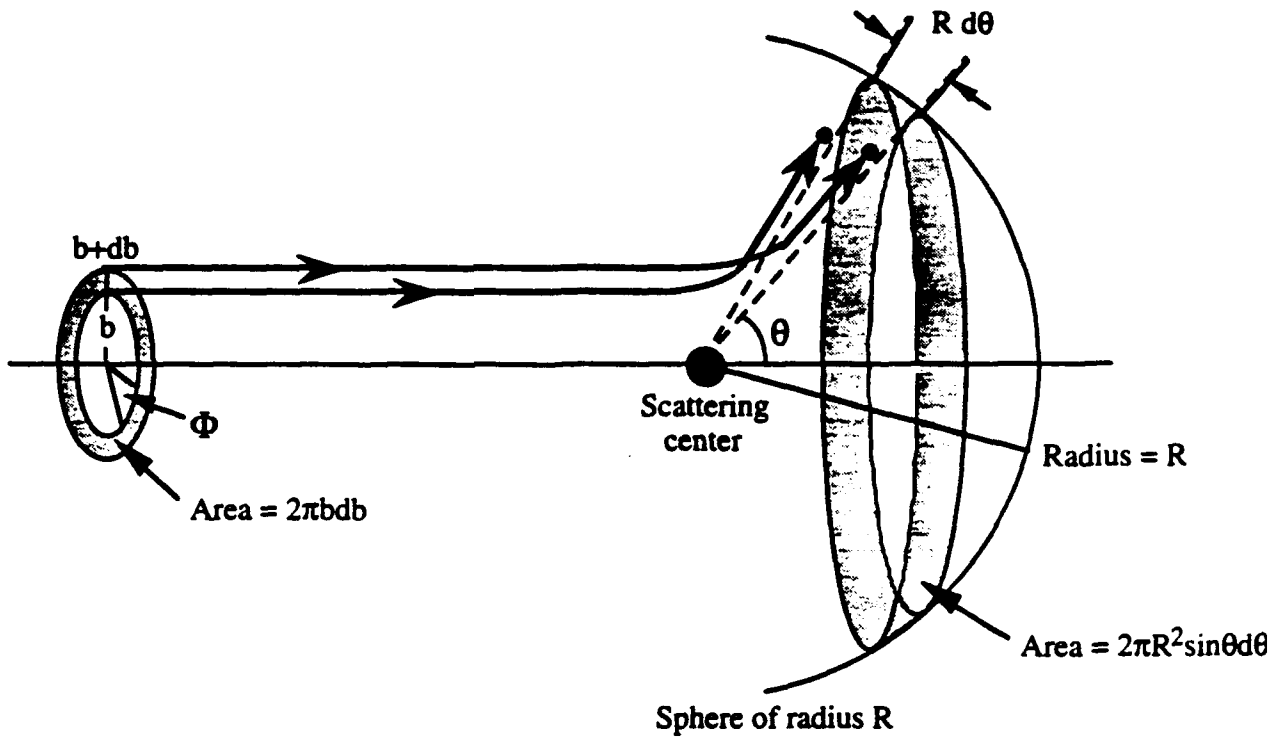


Figure 4.2 A large number of light ions impinging on a massive target particle illustrates the concept of elastic scattering cross section and Rutherford scattering.

All the particles that pass through the annular ring of inner radius b and thickness db are deflected through angles of θ to $\theta+d\theta$. If n represents the number of particles incident on the target per unit area per unit time, we may write

$$N_i = n (b db)(d\Phi), \quad (4.6)$$

where N_i represents the total number of particles incident per unit time at azimuthal angles between Φ and $\Phi+d\Phi$ and impact parameters between b and $b+db$. On the other hand,

$$N_e = n (d\sigma/d\Omega) \sin\theta d\theta d\Phi \quad (4.7)$$

represents the number of particles emerging from the scattering center (the target particle) per unit time in the differential element of solid angle $d\Omega$. But, from conservation of particles, we know that the number of incident particles must equal the number of scattered particles. In other words, $N_i = N_e$, or

$$n (b db)(d\Phi) = n (d\sigma/d\Omega) \sin\theta d\theta d\Phi. \quad (4.8)$$

In this equation $d\sigma/d\Omega$ represents the differential scattering cross section with dimensions of area per unit solid angle. By cancelling common factors, we can write the classical differential scattering cross section as

$$\frac{d\sigma}{d\Omega} = \frac{b}{\sin\theta} \left| \frac{db}{d\theta} \right|. \quad (4.9)$$

The absolute value sign is added since, in general, db and $d\theta$ can have different signs, but by definition, the differential cross section is always positive. Substituting eq. (4.5), we find, after some algebra

$$\sigma(\theta_c) = \left(\frac{Z_1 Z_2 e^2}{2\mu v_0^2 \sin^2\left(\frac{\theta}{2}\right)} \right)^2. \quad (4.10)$$

This equation represents the well known *Rutherford scattering cross section*. In order to compare the probability of a single large angle deflection to the probability of a net large angle scatter, define a close encounter as one that results in a deflection of 90° or more from the original trajectory. Using equation (4.4) with 90° , the impact parameter that results in a close encounter is

$$b_{90^\circ} = \frac{Z_1 Z_2 e^2}{\mu v_0^2}. \quad (4.11)$$

The corresponding cross section may be found using

$$\sigma_{90^\circ} = \pi b_{90^\circ}^2 = \pi \left(\frac{Z_1 Z_2 e^2}{\mu v_0^2} \right)^2. \quad (4.12)$$

For the specific case of antiprotons traversing a fully ionized hydrogen plasma (which consists of free protons and electrons) we have $Z_1 = Z_2 = 1$ and $\mu = 8.365 \times 10^{-28}$ kg, or 469.15 MeV/c². Using these values in the above equation gives a cross section of approximately 2.960×10^{-21} m².

4.4 Multiple Scatters

At this point we must determine the cross section which results from a large number of small angle deflections. Consider a test particle moving through a fully ionized plasma. As the particle traverses the plasma, it undergoes numerous collisions with the plasma ions and undergoes a random walk away from its original trajectory. We would like to determine the mean square angular deflection of the particle along its path. From statistical theory

$$\langle \theta^2 \rangle = \frac{\int \theta^2 \frac{d\sigma}{d\Omega} d\Omega}{\int \frac{d\sigma}{d\Omega} d\Omega} \quad (4.13)$$

gives the mean square angle of scattering. After substituting the previously obtained equations for θ and performing some algebra, there results

$$\langle (\Delta\theta)^2 \rangle = \frac{8\pi n L Z^2 e^4}{m^2 v_o^4} \ln \frac{b_{\max}}{b_{\min}}. \quad (4.14)$$

Notice that this equation becomes pathological at large b_{\max} and small b_{\min} . In other words, when either the maximum impact parameter gets very large, or the minimum impact parameter becomes very small, the argument of the \ln factor goes to infinity, and the equation diverges. Therefore, we must set certain limits on the maximum and minimum impact parameters.

The value for the *maximum* possible impact parameter becomes obvious when one considers the well-known plasma phenomenon of Debye shielding, discussed in Chapter 3. When a test ion enters a plasma the highly mobile electrons surround it and shield out its electric potential from the rest of the plasma, just as they would shield out an anode. Therefore, as the ion traverses the plasma, it does not "see" particles outside of its Debye sphere since the electrons essentially block most of the Coloumb attraction or repulsion between the test ion and the other plasma species. On the other hand, plasma particles which penetrate the test ion's Debye sphere can interact with it via the Coloumb force, and either deflect the ion in the case of large plasma particles, or decelerate it in the case of plasma electrons. From these considerations, we conclude that the Debye length forms the natural maximum possible impact parameter, since plasma particles outside the Debye sphere cannot significantly deflect the test ion. Therefore,

$$b_{\max} = \lambda_D. \quad (4.15)$$

We must keep in mind, though, that the sharp cutoff at the Debye length represents only an approximation since the Debye sphere has no definite edge, and potentials on the order of kT/e may leak through the shielding.

We must now choose a value for the minimum impact parameter. Jackson [20] utilizes the Thomas–Fermi model of the atom to obtain an atomic radius, a . He then equates this value with b_{\min} . Unfortunately, the literature seems unclear on whether this method also applies to a fully ionized hydrogen plasma consisting of only free protons and electrons, and no neutral atoms. Therefore, we turn again to [24] which employs a more direct, if less elegant, technique.

In order to obtain equation (4.5) we assumed that the angle in equation (4.4) was small. Stated another way, $\theta \ll 1$ radian. Setting

$$\Delta\theta_{\max} = 1 \quad (4.16)$$

gives

$$b_{\min} = \frac{Ze^2}{mv_0^2} \approx \frac{Ze^2}{3kT}, \quad (4.17)$$

where the particle kinetic energy relates to its thermal energy. The mean square deflection angle varies only logarithmically with the choice of b_{\max} or b_{\min} , so the results are not sensitive to an exact value of the limiting impact parameters.

We are now in a position to complete the analysis. Using the estimates of b_{\max} and b_{\min} in the mean square angle equation yields:

$$\langle(\Delta\theta)^2\rangle = \frac{8\pi n Z^2 e^4}{m^2 v_0^4} L \ln \Lambda, \quad (4.18)$$

where

$$\Lambda \equiv \frac{3}{2} \left[\frac{(kT)^3}{\pi n} \right]^{1/2} \frac{1}{Ze^3}. \quad (4.19)$$

In this equation, L represents the distance that the test particle has penetrated into the plasma. As one would expect, the mean square deflection angle increases as the particle moves deeper and deeper into the plasma.

Previously, we found the cross section corresponding to a single scatter that resulted in a deflection of 90° . In order to compare the chances of a single large angle scatter to a net large angle scatter, we must now determine the cross section for a net scatter of 90° . According to [24], setting $\langle \theta^2 \rangle = 1$ gives the approximate path length, L , corresponding to a net 90° deflection:

$$L_{90^\circ} = \frac{1}{8\pi n \left(\frac{e^2}{mv_0^4} \right)^2 \ln \Lambda} . \quad (4.20)$$

This allows us to write the cross section corresponding to a 90° net deflection as

$$\sigma_{90^\circ} = \frac{1}{nL_{90^\circ}} = 8\pi n \left(\frac{e^2}{mv_0^4} \right)^2 \ln \Lambda . \quad (4.21)$$

Comparing this to the previous result yields the ratio of the cross section for multiple scattering to the cross section for a single scatter:

$$\frac{\sigma_{\text{multiple}}}{\sigma_{\text{sin gular}}} = 8 \ln \Lambda . \quad (4.22)$$

Since almost all plasmas display a $\ln \Lambda$ of about 10 to 20, we find that, as expected, multiple scattering dominates single scattering in producing a deflection of the test ion. A large angle deflection is orders of magnitude more likely to occur as a result on many small angle scatters than as a result of a single close encounter.

From the preceding analysis, we may draw the following general conclusions. First, Rutherford scattering occurs for very small angles. The maximum deflection angle for any single encounter is much less than a degree. Therefore, a small angle scatter occurs much more often than a large angle scatter. In other words:

“A particle traversing a finite thickness of matter will undergo very many small-angle deflections and will generally emerge at a small angle which is the cumulative statistical superposition of a large number of deflections. Only rarely will the particle have made only one such collision [20].”

This observation allows us to partition the range of possible angular deflections into two specific regions: First, we have a region where many small angle deflections dominate; secondly, we define another region where a few large angle scatters exist. The intermediate region between the two consists of several moderate deflections. This phenomenon is known as plural scattering. As a particle traverses a plasma it suffers many small angle collisions, a few larger deflections, and possible one or two close encounters resulting in a large angle scatter. These successive collisions are strictly independent results and do not depend on one another. Therefore, one may use the central limit theorem of statistical theory to show that the angular distribution for a large number of deflections roughly follows a Gaussian distribution in the forward direction. It is the tail of this Gaussian distribution that contributes to the single, large angle Rutherford scattering.

4.5 Sample Results

Up to this point, we have been concerned with developing the theory of Rutherford (single) and Coloumb (multiple) scattering. Now, we must put the theory to use and develop a method to simulate the scattering of a particle as it traverses a fully ionized plasma. Specifically, we wish to determine the scattering of an antiproton beam as it traverses an expanding, fully ionized, hydrogen plasma. The first problem we encounter relates to the fact that the plasma factors (n and L) in the mean square angle formula, Eq. (4.18), represent constant values, whereas the plasma cloud in the SHIVA Star experiment

has constantly changing parameters. We can determine the pressure, temperature, and density profiles for the expansion from the analysis in Chapter 2 and insert a functional form of the density profile into Eq. (4.18). Notice that since the density and temperature change with position along the pipe and time of expansion, the limiting impact parameters vary because the Debye length varies with both n and T .

In order to determine the scattering of a single antiproton as it traverses the expanding hydrogen plasma, we carry out the following procedure:

1. From the analysis presented in Chapter 2, we determine the time and space varying plasma density, pressure, and temperature profiles along the axis of the expansion chamber during the time between window fracture and peak compression. The plasma expansion is now completely defined.
2. The antiproton energy (and corresponding velocity) is known before the particle enters the plasma cloud. Using a fixed space step and the initial antiproton velocity, the particle is advanced the step size distance into the plasma cloud.
3. Following the procedure developed in Chapter 3, we calculate the energy lost by the antiproton during the first step, and determine the new velocity.
4. At the end of the first step, the root mean square deflection angle is calculated using the known temperature and density profiles. Note that this value gives the width of the Gaussian angle distribution.
5. Using the central limit theorem and a random number generator, we choose a deflection angle from the Gaussian distribution defined in the previous step. This angle represents the antiproton deflection angle in space, from which we can calculate the projection of the space angle onto the x and y axis.
6. Moving to the second space step, we find a new temperature and density and a new Gaussian angle distribution. Also, we update the antiproton energy loss and find a new velocity.

7. Using the new antiproton trajectory, we find a new deflection angle, and update the trajectory.
8. This procedure is followed until the antiproton either reaches the target or impacts the on the wall of the cathode, at which point it is lost.
9. We repeat the entire procedure for each antiproton we wish to swim through the plasma.

Figure 4.3 illustrates the results of the above procedure for Case 1. The graph shows the position of 1000 antiprotons in the x - y plane at the end of the beampipe, which has a pressure of $3 \mu\text{Torr}$ prior to window fracture. The beam, which has an initial energy of 3.5 MeV, undergoes a final root-mean-square scattering length of 0.203 mm in the x direction and 0.201 mm in the y direction. The 2 mm wide circle centered at the origin represents the cathode orifice that the beam must pass through to reach the target. For this Case, all beam antiprotons fall inside the circle, and therefore reach the target. A 20% loss of antiprotons to wall impacts is considered acceptable.

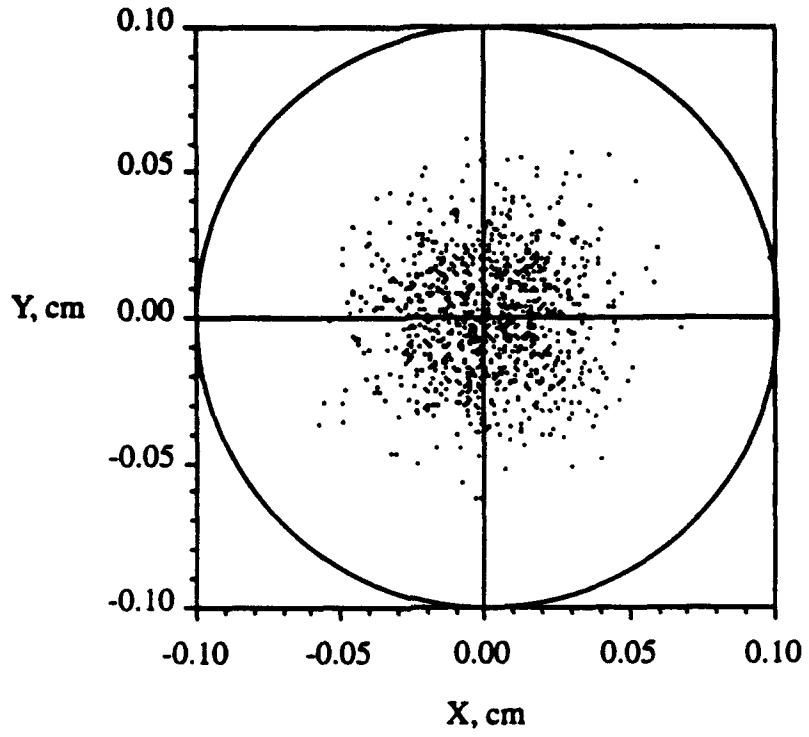


Figure 4.3 Final antiproton positions for Case 1 with a 3.5 MeV beam.

Chapter 5

ANTIPROTON ANNIHILATION

5.1 Introduction

In Chapters 3 and 4 we discussed how electrons inhibit the antiproton beam by decelerating it, and how protons deflect the beam through multiple Coloumb collisions. Now we will discuss one final loss mechanism: antiproton annihilation.

When an antiproton beam interacts with hydrogen plasma, proton–antiproton annihilations may occur. Protons and antiprotons both belong to the baryon family of subatomic particles, and consist of three quarks held together by gluons, the carrier of the strong nuclear force. Two up quarks and one down quark make up proton, while an antiproton consists of two anti–up quarks and an anti–down quark. When an antiproton and a proton react, their constituent quarks recombine to form various mesons. An antiproton–proton annihilation produces, on average, the following by–products:

$$\bar{p} + p \rightarrow 1.527\pi^+ + 1.527\pi^- + 1.96\pi^0 + 0.012K^+ + 0.012K^- + 0.013K^0 + 0.013\bar{K}^0,$$

where the symbol π represents pi mesons (or pions) and the K's symbolize K–mesons (or kaons) [25]. The mesons each consist of one quark and one anti–quark. For instance, a π^+ is made up of one up quark and one anti–down quark. On the other hand, its anti–particle, a π^- , consists of one anti–up quark and one down quark. Since all mesons are unstable, each product particle decays further into other particles.

5.2 Nuclear Cross Sections

In order to determine when an antiproton–proton annihilation will occur, we must explore the concept of the nuclear cross section. Chapter 4 examined this topic briefly, when discussing single large angle deflection versus net large angle deflection.

The concept of nuclear cross section can be described by the following thought experiment, illustrated in Figure 5.1. Suppose a monoenergetic beam of particles strikes an infinitesimally thin (monolayer of atoms) target of surface area S and thickness dx . For simplicity, we assume a circular target and beam. The beam has number density n_b , while the target has number density n_t . Also, all particles of the beam travel at the same velocity, u . From nuclear theory, we define:

$$I = n_b u , \quad (5.1)$$

where I represents the *beam intensity*.

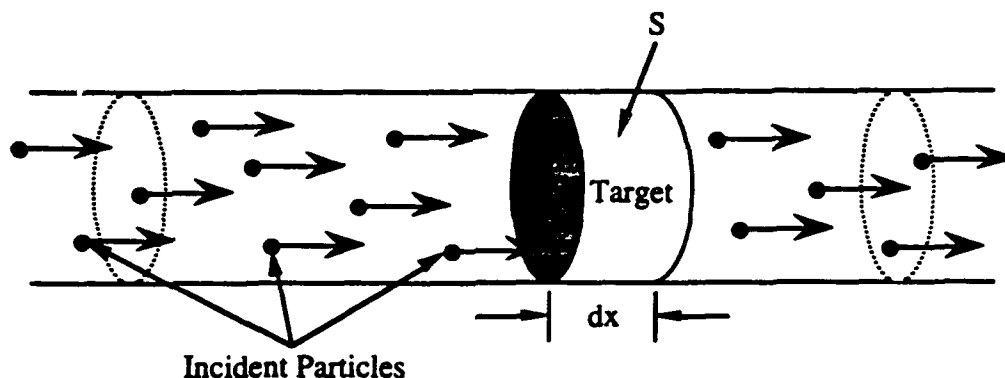


Figure 5.1 Particle beam striking a target illustrates the concept of cross section (after Lamarsh).

In order to obtain an understanding of the cross section, we would like to determine how many of the particles that strike the target actually interact with any of the target nuclei. Since the target is only one atom thick and the size of the nucleus very much smaller than

the size of the atom, most of the incident beam particles pass through the target without any interaction. However, some fraction of the beam particles will, on average, undergo some type of interaction with the target nuclei. Let us now consider the number of particles that strike the target in a certain span of time, for example, in one second. Since the particles all travel at velocity u , they will cover the distance u in one second. Therefore, N particles, where $N = n_b u A$, ahead of the target strike the target in one second. But since $I = n_b u$, we may also write $N = IA$. In terms of unit area, $N/A = IA/A = I$ particles strike the target per unit area per unit time [26].

From a phenomenological standpoint, one might expect that the number of collisions between incident particles and target nuclei would depend on the beam velocity, beam number density, beam cross sectional area, target density, and target thickness, assuming that the target has a larger cross sectional area than the beam. On the other hand, if the beam proved larger in cross sectional area than the target, one would consider the target area rather than the beam area. Thus,

$$\text{number of collisions in target per second} = \sigma (I A n_t dx), \quad (5.2)$$

where σ represents a proportionality constant called the *cross section*. Since I has dimensions of $[L]^{-2} [T]^{-1}$, A has dimensions of $[L]^2$, n_t is in $[L]^{-3}$, and dx is in $[L]$, σ must have dimensions of $[L]^2$, or area. Note that $A n_t dx$ represents the total number of nuclei available to the beam for interactions. Therefore, the number of collisions due to beam interactions in the target per second equals σI . In other words, the cross section, σ , represents the number of collisions with one nucleus per second per unit intensity of the beam.

We may also understand the concept of cross section from the point of view of probability. As noted above, only a certain fraction of the incident beam particles undergo some type of interaction with the target nuclei. Now, IA gives the total number of particles

striking the target per unit time, while $I\sigma$ gives the total number of particles striking the target per unit time. Therefore,

$$\frac{\sigma I}{A I} = \frac{\sigma}{A} \quad (5.3)$$

gives the probability that a certain beam particle will interact with a certain target nuclei. We conclude that σ gives the effective cross-sectional area of the target nucleus, hence the term "cross section" [26].

Nuclear cross sections are generally measured in units of "barns", denoted by b , where 1 barn equals 10^{-24} cm^2 . Another common unit of measurement is the millibarn, mb , equivalent to one thousandth of a barn.

5.3 Sample Results

Particles passing through matter may undergo various types of interactions. In particular, antiprotons traversing a fully ionized hydrogen plasma undergo electronic energy loss (discussed in chapter 3), deflection by the massive protons (discussed in chapter 4) and annihilation with the protons. At higher beam energies that we consider here, other processes such as charge exchange may also occur. Each of these processes may be characterized by a different cross section, as shown by Mutchler, et al [27]. In other words, scattering may be described by a scattering cross section σ_s , etc... The sum of the cross sections for all possible interactions is called the total cross section, σ_T . Mutchler, et al, give a value for $\beta\sigma_a$ of approximately 35 mb.

In order to determine the actual number of beam antiprotons which annihilate while traversing the expanding plasma, we must first find the probability of a single annihilation occurring from the following procedure:

1. Starting from the plasma wavefront and using the same stepping process as described previously, we find the atom density per unit area in each space step from:

$$t_i = \Delta z_i \rho_i N_A , \quad (5.4)$$

where t represents the atom density (atoms/cm²) in a step, Δz is the space step size in cm, ρ represents the plasma mass density (g/cm³) in the step, and N_A symbolizes Avagadro's number, equal to 6.023×10^{23} atoms/g.

2. From the energy loss procedure, we obtain the antiproton velocity in each step, and find b from

$$\beta_i = \frac{v_{\bar{p}_i}}{c} , \quad (5.5)$$

or, more directly,

$$\beta_i = \sqrt{\frac{2E_{\bar{p}_i}}{m_{\bar{p}}}} , \quad (5.6)$$

where $E_{\bar{p}_i}$ (MeV) is the antiproton energy in each step and $m_{\bar{p}}$ (MeV) is the antiproton mass, 938.3 MeV.

3. Using the value of b found above, we determine the annihilation cross section in each step from

$$\sigma_{a_i} = \frac{35}{\beta_i} \text{ mb} . \quad (5.7)$$

4. In order to find the probability of an antiproton–proton annihilation, simply multiply the areal atomic density by the annihilation cross section:

$$P_{\text{ann}i} = \sigma_{\text{ai}} t_i, \quad (5.8)$$

where $P_{\text{ann}i}$ gives the probability of an annihilation occurring in each space step.

5. To determine explicitly whether or not an antiproton annihilates, we compare the probability found above to a random number between 0 and 1. Since the annihilation cross section always lies close to zero compared to unity, we utilize the following logic:

$$\text{If } P_{\text{ann}i} < \text{than Rand}(1)_i: \text{ no annihilation occurs} \quad (5.9a)$$

$$\text{If } P_{\text{ann}i} > \text{than Rand}(1)_i: \text{ antiproton annihilates,} \quad (5.9b)$$

where $\text{Rand}(1)_i$ represents a random number between zero and one, which the computer must generate at each space step through the plasma. If the probability of annihilation exceeds the random number at a particular step, the computer sends up a flag which indicates an annihilation has occurred, then moves on to swim the next antiproton in the beam through the plasma. Note that since the individual annihilations are independent events, one can swim them through the plasma one at a time, without having to keep track of all the antiprotons at once.

Table 5.1 shows some representative annihilation probabilities for characteristic SHIVA Star plasma densities, path lengths, and beam energies. The last column in the Table gives the probability, between 0 and 1, that the antiproton will annihilate. A value of 1 indicates that the antiproton will definitely annihilate, while 0 indicates that no annihilation occurs. A single antiproton has little chance of annihilating for all cases

considered. A low energy antiproton traversing dense plasma undergoes the greatest probability of annihilation.

Table 5.1: Representative annihilation probabilities
for characteristic path lengths and plasma densities.

Energy, MeV	σ , mb	ρ , g/cm ³	Δz , cm	Probability
3	4.377E-25	5.00E-03	0.01	1.313E-05
1	7.581E-25	5.00E-03	0.01	2.274E-05
0.5	1.072E-24	5.00E-03	0.01	3.216E-05
0.1	2.397E-24	5.00E-03	0.01	7.192E-05
3	4.377E-25	5.00E-03	0.1	1.313E-04
1	7.581E-25	5.00E-03	0.1	2.274E-04
0.5	1.072E-24	5.00E-03	0.1	3.216E-04
0.1	2.397E-24	5.00E-03	0.1	7.192E-04
3	4.377E-25	5.00E-03	1	1.313E-03
1	7.581E-25	5.00E-03	1	2.274E-03
0.5	1.072E-24	5.00E-03	1	3.216E-03
0.1	2.397E-24	5.00E-03	1	7.192E-03
3	4.377E-25	1.00E-03	0.01	2.626E-06
1	7.581E-25	1.00E-03	0.01	4.549E-06
0.5	1.072E-24	1.00E-03	0.01	6.433E-06
0.1	2.397E-24	1.00E-03	0.01	1.438E-05
3	4.377E-25	1.00E-03	0.1	2.626E-05
1	7.581E-25	1.00E-03	0.1	4.549E-05
0.5	1.072E-24	1.00E-03	0.1	6.433E-05
0.1	2.397E-24	1.00E-03	0.1	1.438E-04
3	4.377E-25	1.00E-05	0.1	2.626E-07
1	7.581E-25	1.00E-05	0.1	4.549E-07
0.5	1.072E-24	1.00E-05	0.1	6.433E-07
0.1	2.397E-24	1.00E-05	0.1	1.438E-06
3	4.377E-25	1.00E-05	1	2.626E-06
1	7.581E-25	1.00E-05	1	4.549E-06
0.5	1.072E-24	1.00E-05	1	6.433E-06
0.1	2.397E-24	1.00E-05	1	1.438E-05
3	4.377E-25	1.00E-06	0.1	2.626E-08
1	7.581E-25	1.00E-06	0.1	4.549E-08
0.5	1.072E-24	1.00E-06	0.1	6.433E-08
0.1	2.397E-24	1.00E-06	0.1	1.438E-07
3	4.377E-25	1.00E-06	1	2.626E-07
1	7.581E-25	1.00E-06	1	4.549E-07
0.5	1.072E-24	1.00E-06	1	6.433E-07
0.1	2.397E-24	1.00E-06	1	1.438E-06
0.1	2.397E-24	5.00E-08	1	7.192E-08
3	4.377E-25	5.00E-08	1	1.313E-08
1	7.581E-25	5.00E-08	1	2.274E-08
0.5	1.072E-24	5.00E-08	1	3.216E-08

5.4 Corrections for a Hot Plasma

Before leaving the topic of antiproton annihilation, we must address one further concept: hot versus cold plasma. In the above calculations, we have implicitly assumed that the expanding plasma is "cold", i.e., the proton fluid does not move relative to either the electron fluid or the incident ion beam. In reality, though, the proton fluid has some finite temperature, and we must consider this thermal motion in our calculations. In other words, we must examine not just the antiproton velocity, but the *relative* velocity between the colliding proton and antiproton.

From Chen and other sources, we know that the thermal velocity of the proton relates to the proton temperature through

$$v_{th} = \sqrt{\frac{2kT_p}{m_p}}, \quad (5.10)$$

where k , Boltzmann's constant, equals $1.38 \times 10^{-23} \text{ J/}^\circ\text{K}$. Now, the fluid *en masse* moves down the expansion pipe with some macroscopic velocity u , which in general may be a vector, but for the simple case of one dimensional motion reduces to a scalar. To obtain the overall particle velocity, this bulk fluid velocity must be added to the random thermal velocity, so $v = u + v_{th}$.

It is difficult to predict the exact random trajectory of the proton just before collision. But since we expect the antiproton velocity to far exceed the thermal velocity of an individual proton (and the bulk fluid motion, for that matter), let us assume that the relative velocity approximates the antiproton velocity, and show *a posteriori* that this is true. In other words, we assume that the inclusion of the proton thermal velocity in the calculations has little overall effect on the annihilation cross section.

Consider for the relative velocity the following two limiting cases: first, the antiproton and proton velocity vectors are parallel; second, the velocity vectors are

antiparallel. For the first case, the relative approach velocity is less than the antiproton velocity since the proton moves away from the antiproton; for the second case the approach velocity is greater than the antiproton velocity since the two particles move toward each other. For simplicity, we also assume that the proton thermal velocity and the bulk fluid velocity are aligned. These two scenarios, antiproton velocity, proton thermal velocity, and bulk fluid velocity aligned, and antiproton velocity opposite to aligned proton thermal and bulk fluid velocities, represent bracketing cases.

We must now develop an alternate form of the β factor to include the relative velocity between the two particles instead of the antiproton velocity. To this end,

$$\beta = \frac{v_{rel}}{c}, \quad (5.11)$$

or

$$\beta = \frac{v_{\bar{p}} \pm v}{c}, \quad (5.12)$$

where the + sign indicates antiparallel motion, and the - sign indicates parallel motion. As before, $v = u + v_{th}$. Substituting the definitions of the particle and fluid velocities yields

$$\beta = \frac{\sqrt{\frac{2E_{\bar{p}}}{m_{\bar{p}}}}}{c} \pm \left(\frac{\sqrt{\frac{2kT}{m_p}}}{c} + \frac{\sqrt{\frac{8kT}{\pi m_p}}}{c} \right) \quad (5.13)$$

for the hot plasma, where the first term on the right hand side gives the antiproton velocity, the second term represents the proton thermal velocity, and the third term represents the bulk fluid motion. The bracketed term gives the total proton velocity, v .

Consider the following worst case scenario: As the antiprotons impact the target, they have lost nearly all of their initial energy to the electron fluid; meanwhile, the plasma

just outside of the target has been heated to peak temperature by the compression process. This is the situation that the beam encounters just before impact. At this instant, the antiproton and proton velocities are nearer to each other in magnitude than at any other time. From the results of Chapter 2 we know that the antiproton beam generally has some residual energy (usually between 0.1 to 0.5 MeV) at impact. Also, CALE results indicate that the plasma temperature may average about 60 eV during the expansion. Therefore, we substitute these values into Eq (5.13).

Figure 5.2 shows the results of the above calculations for the limiting cases we have been discussing. Note that all three cases (cold plasma, parallel particle velocity vectors, and antiparallel velocity vectors) yield a decreasing cross section with increasing antiproton energy. We expect this since the annihilation cross section varies inversely with β . However, note further that all three lines of the graph are nearly indistinguishable from one another, except arbitrarily close to zero. Thus, it appears that including the effects of a hot plasma in the calculations do not significantly change the results.

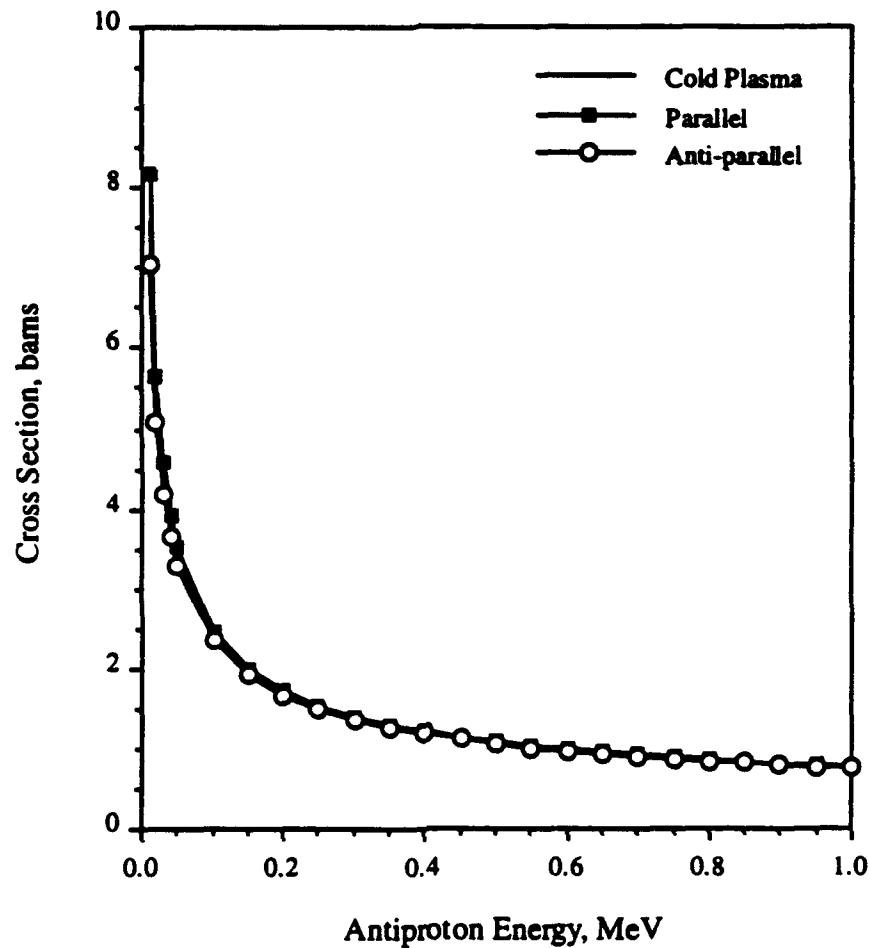


Figure 5.2 Comparison of limiting case annihilator cross sections vs antiproton energy.

Figure 5.3 confirms this observation by showing that the percent difference between the hot and cold plasma calculations for probability of annihilation differ by less than 8% even when the residual antiproton energy becomes very small. Therefore, we shall not concern ourselves further with the hot plasma calculation for antiproton annihilation. We will utilize the original definition of β , and make sure that the antiproton beam always reaches the target with some finite residual energy (at least 0.05 MeV, depending upon the initial plasma conditions) in the energy loss and range calculations.

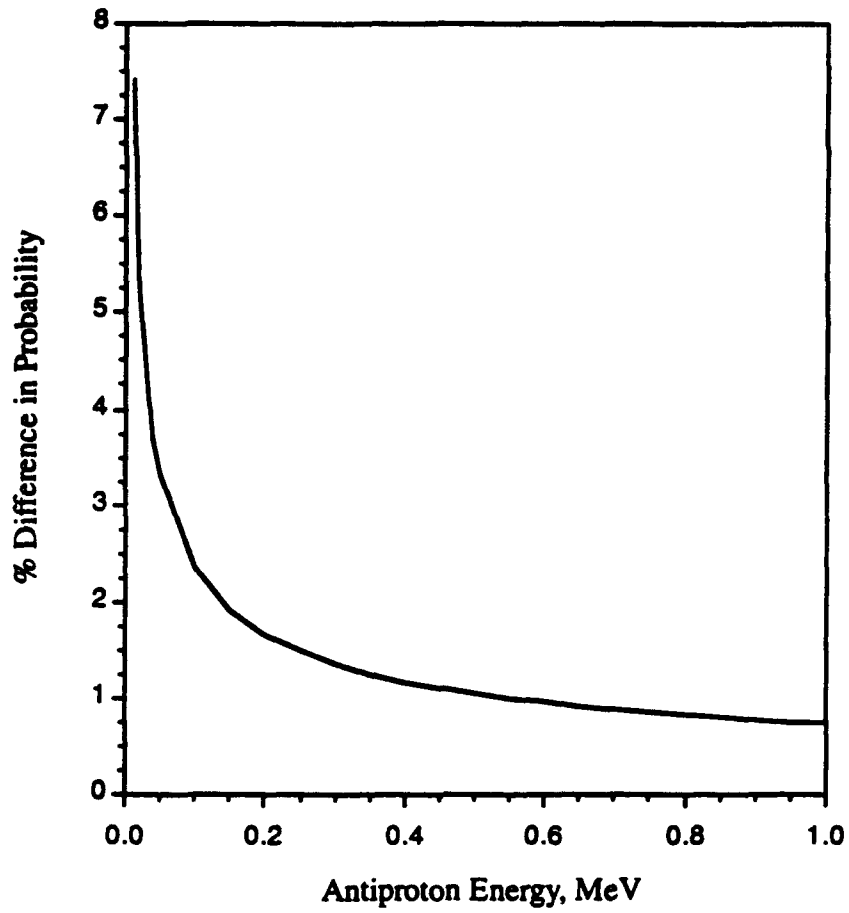


Figure 5.3 Percent difference in probability of annihilation between hot and cold plasmas vs antiproton energy.

Chapter 6
RESULTS

The theory and techniques discussed in Chapters 2—5 were implemented to analyze several different plasma/antiproton beam cases, defined by initial plasma conditions and target geometry. The term 'initial conditions' applies to the density and temperature of the plasma *prior* to the start of the compression cycle. Table 6.1 lists the various initial conditions and target geometry combinations.

Table 6.1 The plasma/antiproton beam cases.

Case	ρ_0 , atoms/cm ³	T_0 , eV	Target Geometry
1	1.0×10^{19}	2.0	spherical
2	6.0×10^{19}	2.0	spherical
3	1.0×10^{19}	5.0	spherical
4	6.0×10^{19}	5.0	spherical
5	1.0×10^{19}	2.0	cylindrical
6	6.0×10^{19}	2.0	cylindrical
7	1.0×10^{19}	5.0	cylindrical
8	6.0×10^{19}	5.0	cylindrical

Recall that CALE provides details of the time dependent state of the plasma *inside* the aluminum liner, but cannot describe the time and space varying density and temperature profiles along the injection pipe. Using CALE, we can easily find approximate window failure times by examining the plasma pressure time history on the interior face of the cathode. When the pressure reaches about 200 kbar, the window fails catastrophically and plasma streams into the beampipe, as explained in Chapter 2. The plasma density, pressure, and temperature are known at the beam pipe *inlet* at all times of interest from

CALE. These plasma properties correspond to those calculated by CALE on the interior face of the cathode. Table 6.2 shows the properties of the plasma, calculated by CALE, which streams into the injection pipe *as the window breaks* for each spherical listed in Table 6.1. The second column corresponds to the elapsed time since the start of the compression cycle.

Table 6.2 *Initial plasma properties at beampipe inlet.*

Case	time, μsec	T, eV	p, kbar	ρ , mg/cm^3
1	12.222	37.649	207.000	2.850
2	11.989	14.927	202.000	7.025
3	12.014	50.082	204.000	2.113
4	12.000	26.403	201.000	3.945

Using the CALE data at each time step, the state of the plasma at the time of beam injection can be found using the kinetic theory code described in Chapter 2. The resulting plasma density and temperature profile along the beampipe is read into the energy loss, scattering, and annihilation code to determine the antiproton losses and necessary initial beam energy required for successful antiproton injection. Figure 6.1 describes this procedure symbolically with a flowchart. This procedure was followed for each case shown above in Table 6.1.

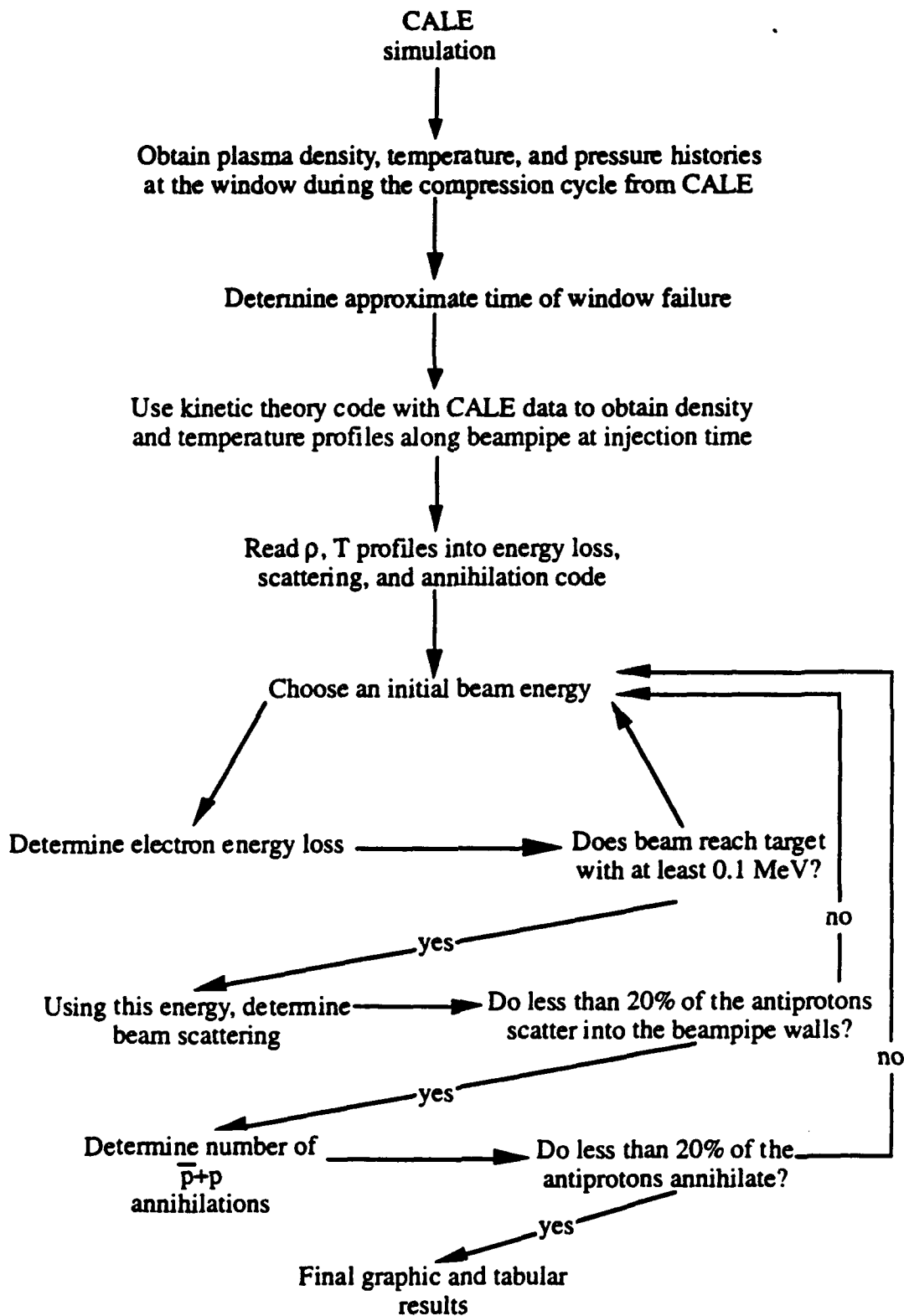


Figure 6.1 Flowchart illustrating the procedure used to determine necessary beam energy to overcome electronic energy loss, antiproton deflection into beampipe walls, and annihilation with protons. The same procedure was followed for each case listed in Table 6.1.

6.1 Case 1

The results of this Case have already been discussed as illustrative examples in Chapters 2, 3, 4, and 5. In summary, 50%, or 1.55 mg, of plasma leaks into the beampipe between the time of window fracture and peak compression. Residual air, at a pressure of 3×10^{-6} Torr, remains during the experiment. The scattering from residual air is included. The antiproton beam requires an initial (i.e., upon leaving the RFQ) energy of 3.5 MeV to reach the target. Just before impact, the beam has a residual energy of 0.152 MeV. The antiprotons also displayed a root-mean-square scattering distance from beam centerline of 0.203 mm in the x (lateral) direction, and 0.201 mm in the y (vertical) direction. No antiprotons undergo annihilation with either the beampipe wall or with plasma protons; therefore, 100% of the antiprotons reach the target.

6.2 Case 2

Increasing the initial density to 6×10^{19} atoms/cm³ causes the window to break about 11.99 μ sec after the start of the compression cycle. The target reaches peak compression 13.06 μ sec after the compression cycle starts. During this time, about 3.22 mg of plasma leaks into the beampipe. Since the working fluid has a total mass of 18.6 mg for this case, about 17.3 % leaks into the beampipe.

As in the previous case, the antiproton beam loses no appreciable energy until it reaches the beginning of the high density region about 1 cm from the target surface, located at the origin in Figure 6.2.1. Here, the plasma density is about 10^{-4} g/cm³. At this point, the beam loses energy rapidly, and impacts the target with a residual energy of 0.322 MeV. The antiproton beam requires an initial energy of 4.6 MeV to reach the target. Since the initial plasma density is higher than in the previous case, the beam must travel through more matter, and thus requires a higher initial energy to overcome electronic energy and plasma oscillation losses.

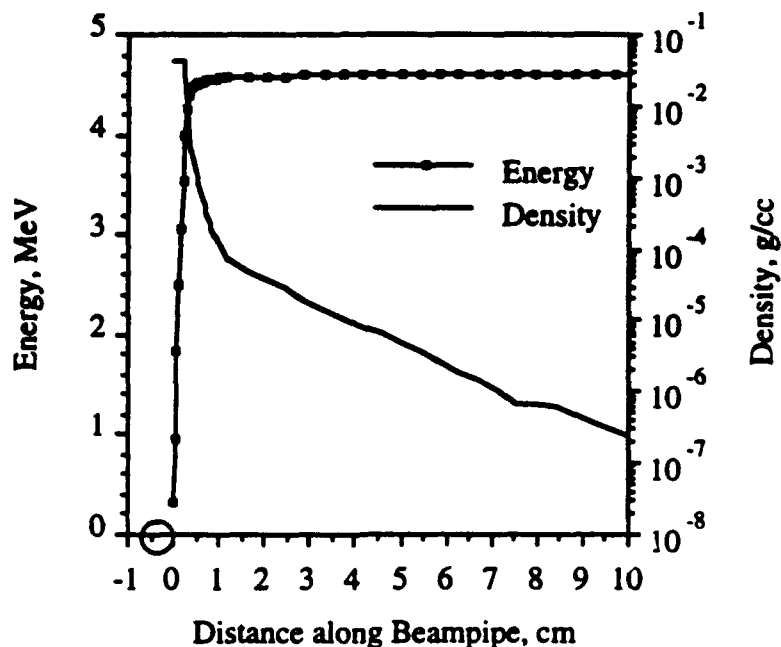


Figure 6.2.1 Beam energy and plasma density profiles for Case 2.

The plasma reaches a peak density of $4.12 \times 10^{-2} \text{ g/cm}^3$ just inside the cathode. Since the initial density in this case is higher than the previous case, the peak density and density where significant energy loss begins are also higher.

Figure 6.2.2 shows the final position of the 4.6 MeV beam antiprotons at the target end of the beampipe. The antiproton beam underwent a 0.153 mm rms deflection in the x direction, and a 0.155 mm deflection in the y direction. As before, these rms lengths correspond to the mean scattering distance from the centerline at the cathode window. The plasma deflects no antiprotons into the pipe walls for this case, but 1 antiproton underwent an annihilation with a plasma proton.

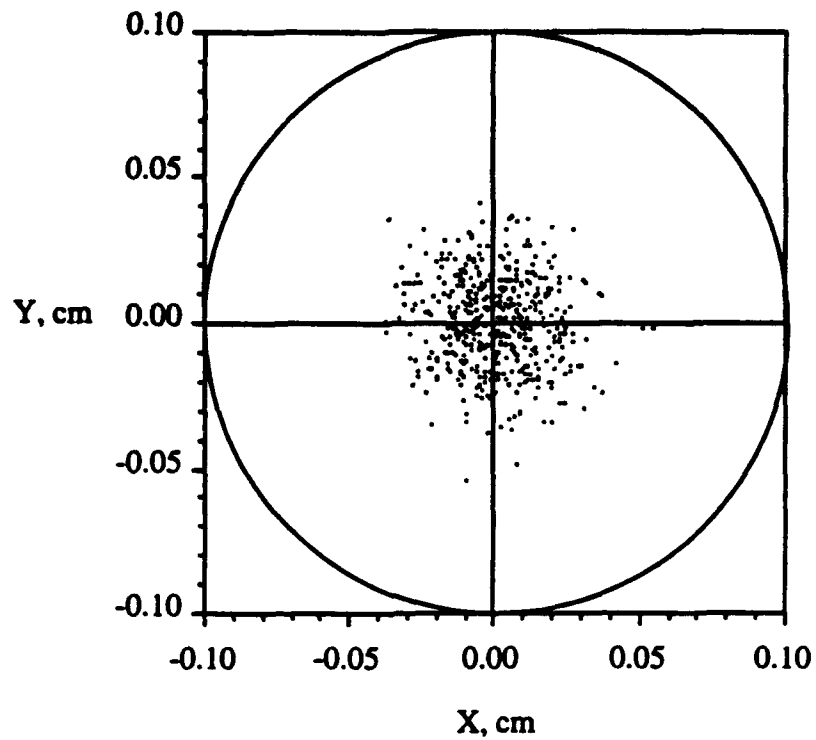


Figure 6.2.2 Final antiproton positions for Case 2 with a 4.6 MeV beam.

6.3 Case 3

In this case, the diamond window again fractures about 12.01 μsec after the start of the compression cycle. Peak target compression occurs at 12.97 μsec , after 1.08 mg, or 34.8 % of the working fluid, leaks into the beampipe. The 3.0 MeV antiproton beam has 0.285 MeV upon impact, as shown in Figure 6.3.1.

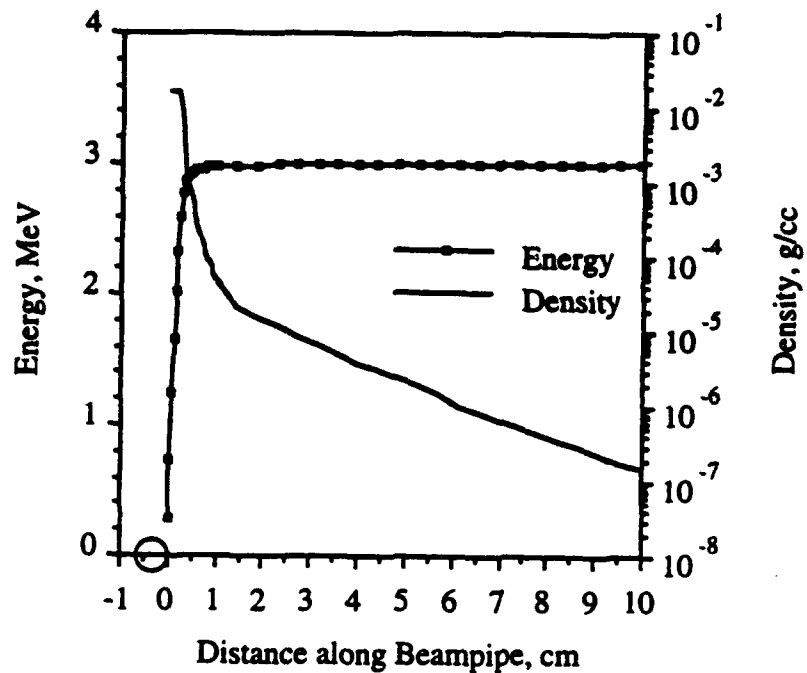


Figure 6.3.1 Beam energy and plasma density profiles for Case 3.

As in the previous cases, the beam begins to lose significant energy about 1 cm from the target. The plasma has a peak density just inside the cathode of $1.68 \times 10^{-2} \text{ g/cm}^3$.

Figure 6.3.2 shows 1000 antiprotons passing through the cathode orifice. No antiprotons undergo scattering into the beampipe wall. The resultant rms scattering length is 0.156 mm in the x direction and 0.147 mm in the y direction. No proton-antiproton annihilations occurred for this Case.

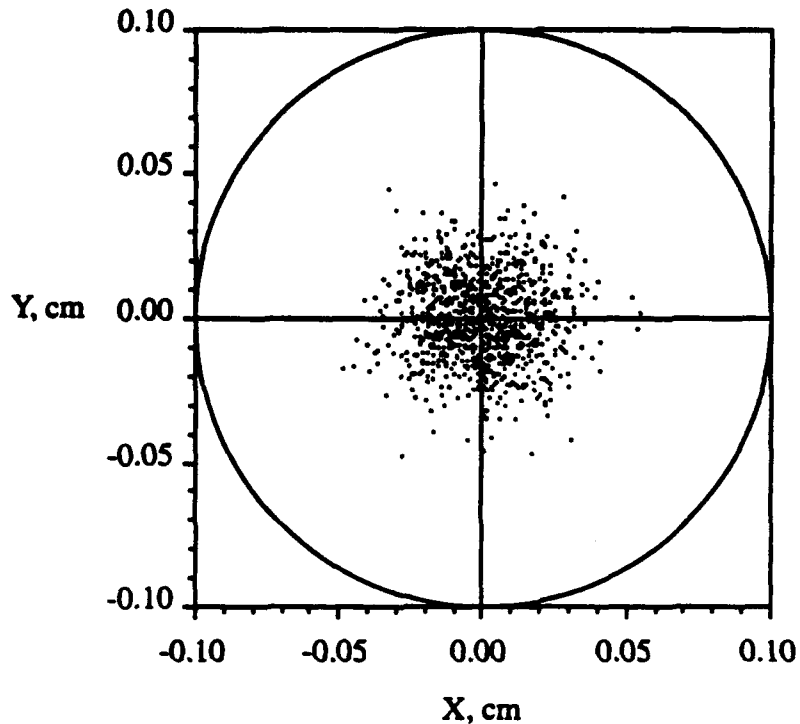


Figure 6.3.2 Final antiproton positions for Case 3 with a 3.0 MeV beam.

6.4 Case 4

Between window fracture at 12 μsec and peak compression at 13.367 μsec , the plasma develops a peak density of $2.06 \times 10^{-2} \text{ g/cm}^3$ in the gap between the edge of the cathode and the target surface. Meanwhile, 1.97 mg, or 10.6 %, of the plasma streams through the cathode orifice into the beampipe. As shown in Figure 6.4.1, the antiproton beam energy loss becomes significant at about 1 cm from the target. The antiproton beam requires an initial energy of 3.3 MeV to reach the target, and has an impact energy of 0.235 MeV.

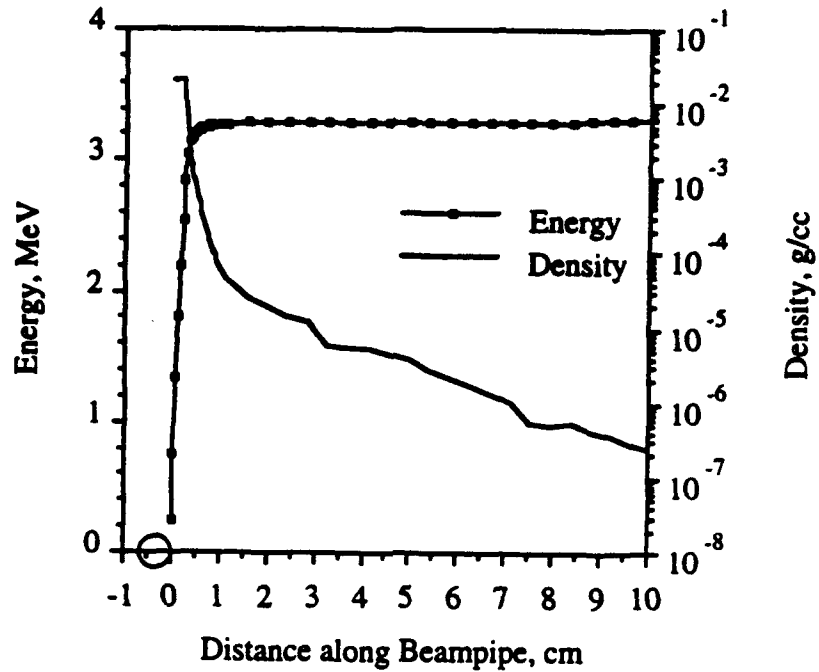


Figure 6.4.1 Beam energy and plasma density profiles for Case 4.

Figure 6.4.2 shows the final antiproton positions of the 3.3 MeV beam. The rms scattering length for this Case was 0.221 mm in the x direction and 0.205 mm in the y direction. No annihilations with either the beampipe wall or with plasma protons occurred for Case 4.

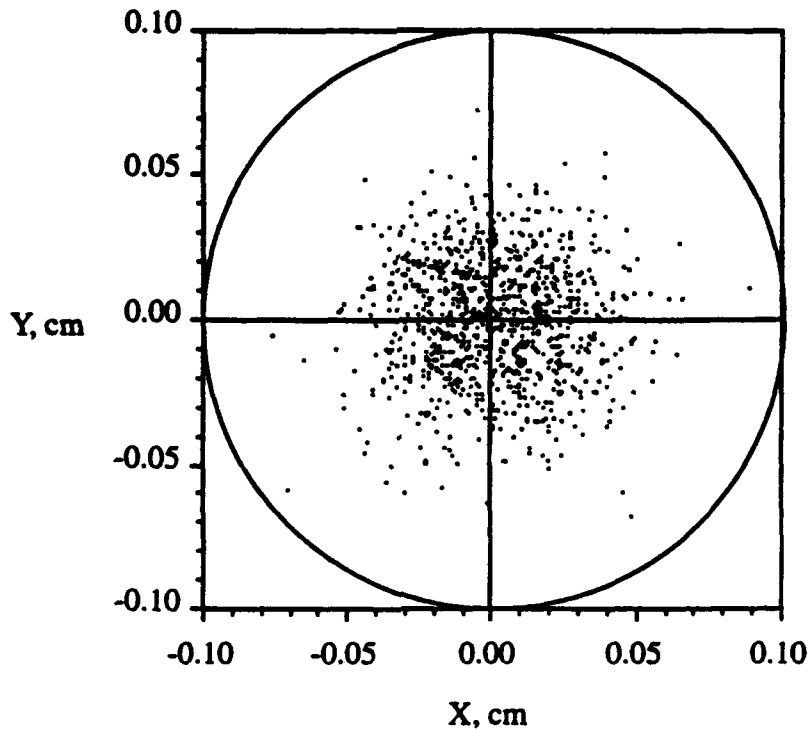


Figure 6.4.2 Final antiproton positions for Case 4 with a 3.3 MeV beam.

6.5 Cylindrical Target

Here, we briefly consider the performance of a hollow, cylindrical target that forms a perfect seal with the cathode. Figure 6.5.1 shows the target prior to the start of the compression cycle. The target stretches between the two electrodes and is axisymmetric about the longitudinal electrode axis.

Figure 6.5.2, reproduced from CALE output, shows the same target an instant before peak compression, at the time of antiproton injection. Note that although the target has undergone cylindrical compression, the top and bottom surfaces of the target remain flush with the cathode surface, preventing any plasma from reaching the entrance to the beampipe. In other words, the target itself acts as a dam to the working fluid, preventing any plasma from flowing into the beampipe.

Since plasma does not contaminate the beampipe during the compression cycle, the next most important obstacle to antiproton transmission is residual air. (The scattering from this residual air was also considered when determining the antiproton deflection in Cases 1 through 4.) Assuming constant density air of 4.72×10^{-12} g/cm³ at a standard temperature of 20° C, the electronic energy loss procedure reveals that a 1.2 MeV antiproton beam retains about 99.9 % of its energy after traversing the 17 m of vacuum between the RFQ and the target. This beam energy provides the baseline consideration for the design of the RFQ. Electronic energy loss does not represent a significant problem for the cylindrical, hollow target scenario.

Beam scattering, however, does deserve careful consideration. Recall that our previous scattering analysis involved Coloumb forces and Debye shielding between charged particles. In this case, though, the medium is a cold, neutral *gas*, not a plasma, so the Moliere equation

$$\theta_{\text{rms}} = \frac{13.6 \text{MeV}}{2E_{\bar{p}}} Z \sqrt{\frac{\rho L}{X_0}} \quad (6.5.1)$$

describes the resultant root mean square scattering angle of antiprotons as they reach the target [28]. Eq. (6.5.1) is the cold gas analog of eq (4.18), which was derived for hot plasmas. In the equation, $E_{\bar{p}}$ is the beam

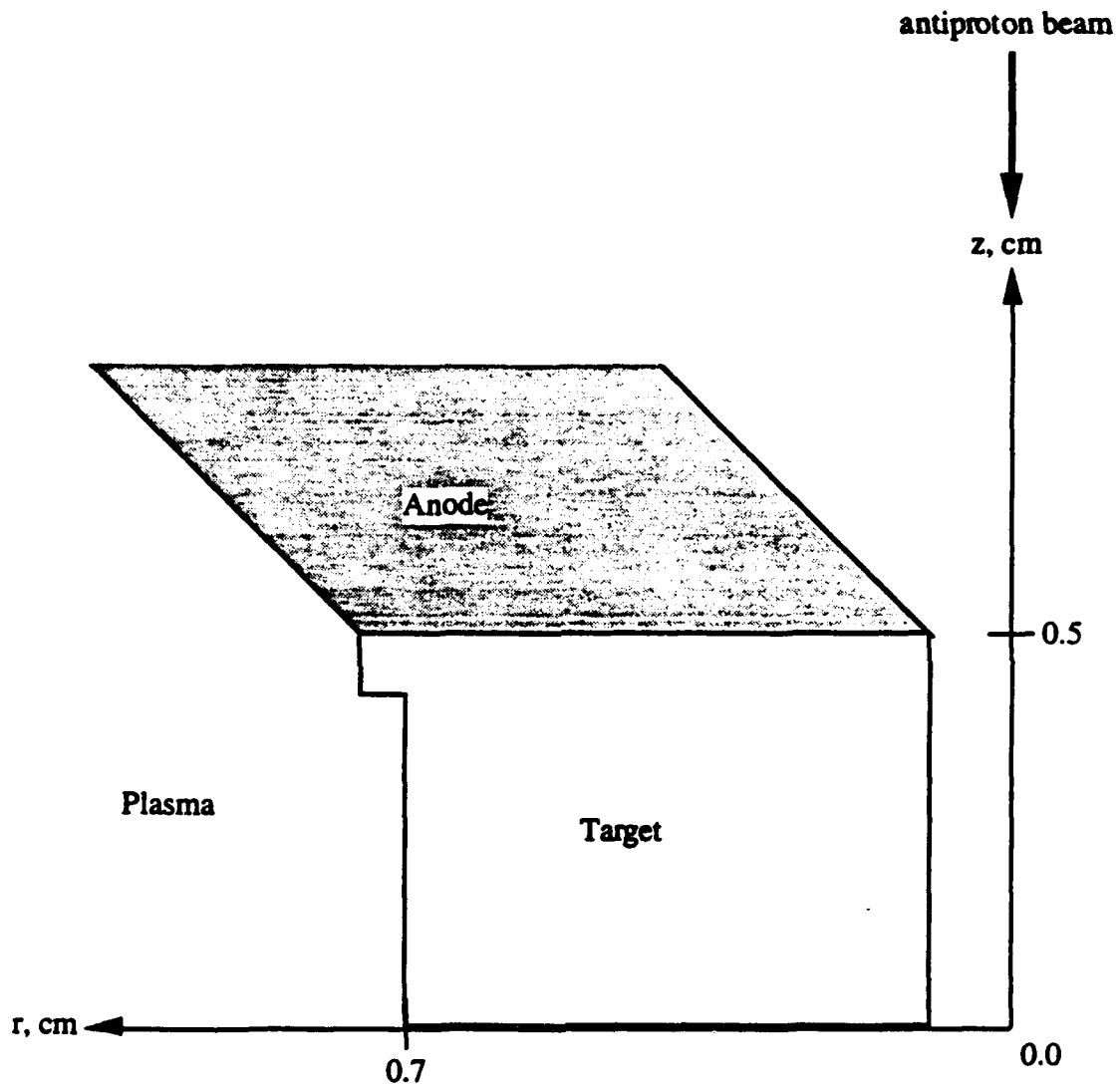


Figure 6.5.1 Cylindrical target, cathode, and hydrogen working fluid prior to the start of the compression cycle. The figure represents one quadrant of the system, which is symmetric about the origin.

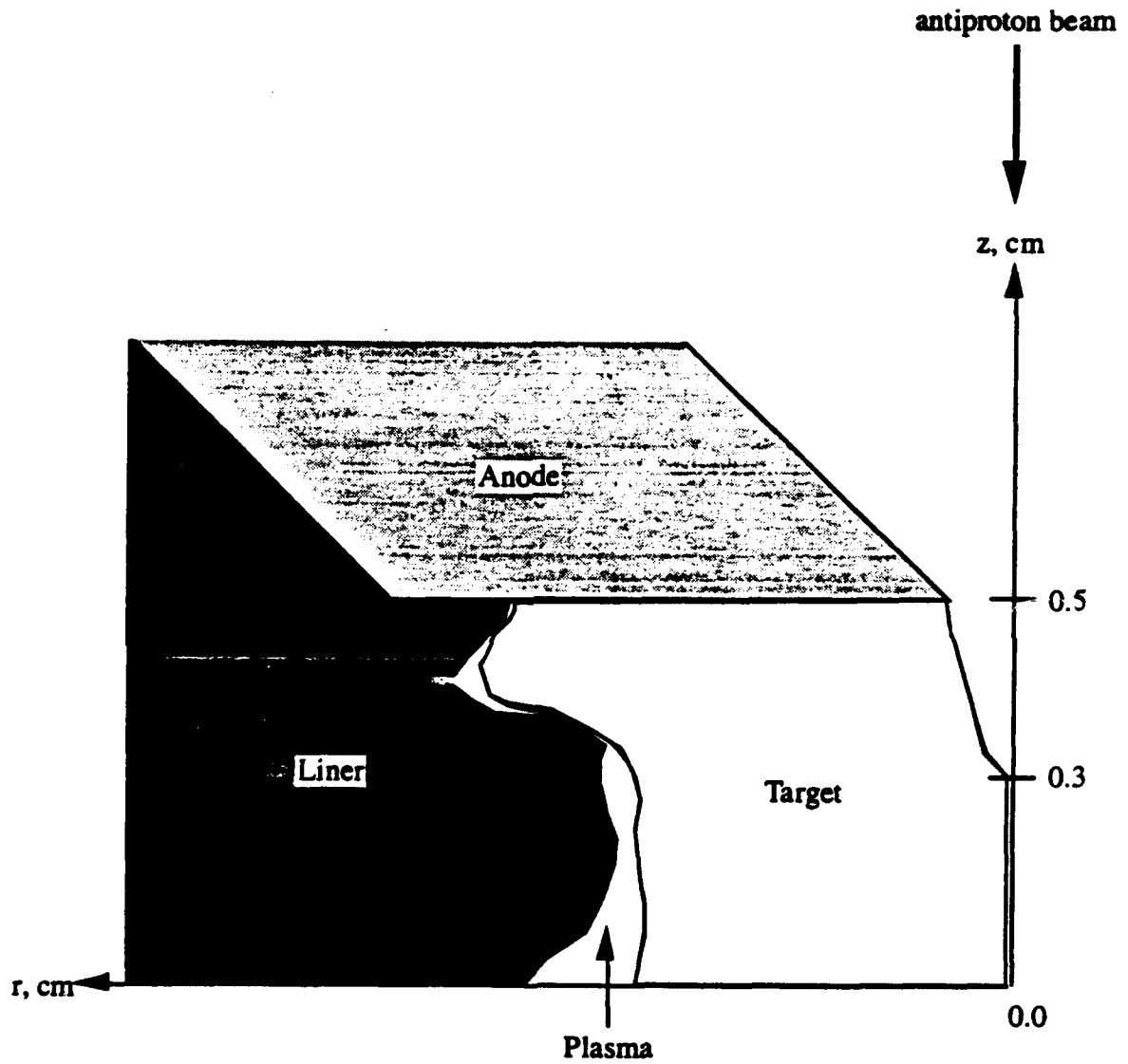


Figure 6.5.2 A view of the cylindrical, hollow target at peak compression. Note that the liner, not shown in Figure 6.5.1, has moved into the target region at this time.

energy (1.2 MeV), Z is the particle charge number (1 for an antiproton), ρ is the density of the medium, L is the distance travelled, and X_0 is a constant called the *radiation length* of the medium. The radiation length is defined as the mean distance over which a high-energy electron loses all but $1/e$ of its energy through bremsstrahlung radiation. The equation

$$X_0 = 716.4 \frac{A}{Z(Z+1) \ln\left(\frac{287}{\sqrt{Z}}\right)} \text{ g/cm}^2, \quad (6.5.2)$$

where Z and A represent the atomic number and weight of the medium, gives an approximate value for X_0 . For air, X_0 equals 36.66 g/cm². Since the beam has constant energy over the length travelled, we may take L to be 17 m. (If the beam lost significant energy during the transmission, the above equation would have to be integrated over the flight path.)

In order to determine the rms scattering length from the pipe centerline, we use

$$y_{\text{rms}} = \frac{1}{\sqrt{3}} L \theta_{\text{rms}}, \quad (6.5.3)$$

where the square root term arises because the rms scattering length represents a projection onto a plane.

Note from Figure 6.5.2 that a small crater, about 1 mm in radius, develops near the beampipe entrance just prior to injection. We would like to focus the antiproton beam onto this crater in order to sample the interior, high-density regions of the target. Therefore, we seek a combination of beam energy and vacuum pressure that will keep the maximum particle scattering to within about 1 mm.

Figure 6.5.3 shows the position of one thousand antiprotons at the end of the beamline (containing only air of density $4.72 \times 10^{-12} \text{ g/cm}^3$) for a 1.2 MeV beam. The rms scattering lengths correspond to $x_{\text{rms}}=0.584 \text{ mm}$ and $y_{\text{rms}}=0.572 \text{ mm}$. The small circle in the center of the graph represents the perimeter of the aforementioned crater. The beam loses 92 antiprotons, or 9.2%, to impacts with the beampipe wall.

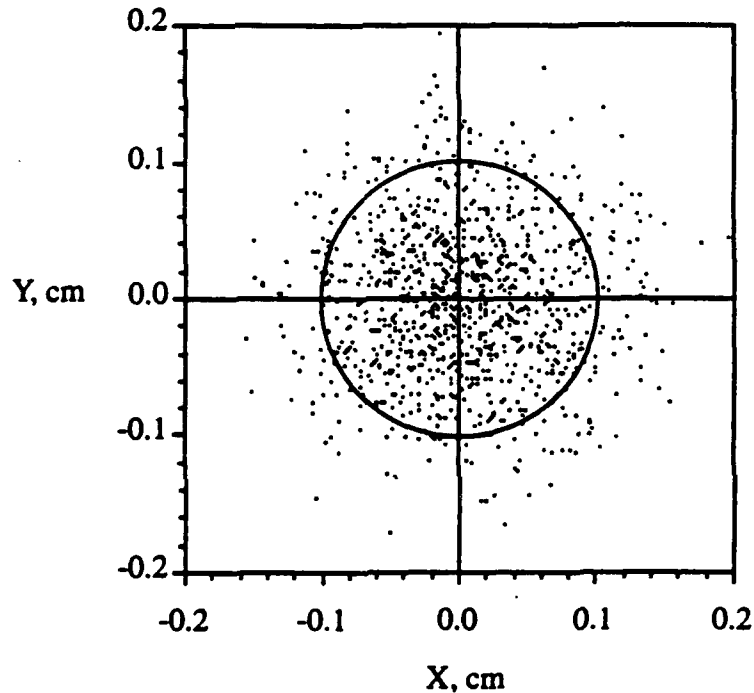


Figure 6.5.3 Final antiproton positions for 3×10^{-6} Torr beampipe air pressure.

The above vacuum pressure/beam energy pair represents only one of the infinite possible combinations available to achieve the 1 mm rms constraint. Figures 6.5.4 and 6.5.5 show the results of a parametric study, illustrating, respectively, the rms scattering angle and rms scattering displacement vs vacuum pressure for a variety of beam energies. Equations (6.5.1) and (6.5.3) were used to obtain the plots. By choosing a beam energy and vacuum pressure, one may quickly determine the rms scattering length from the centerline.

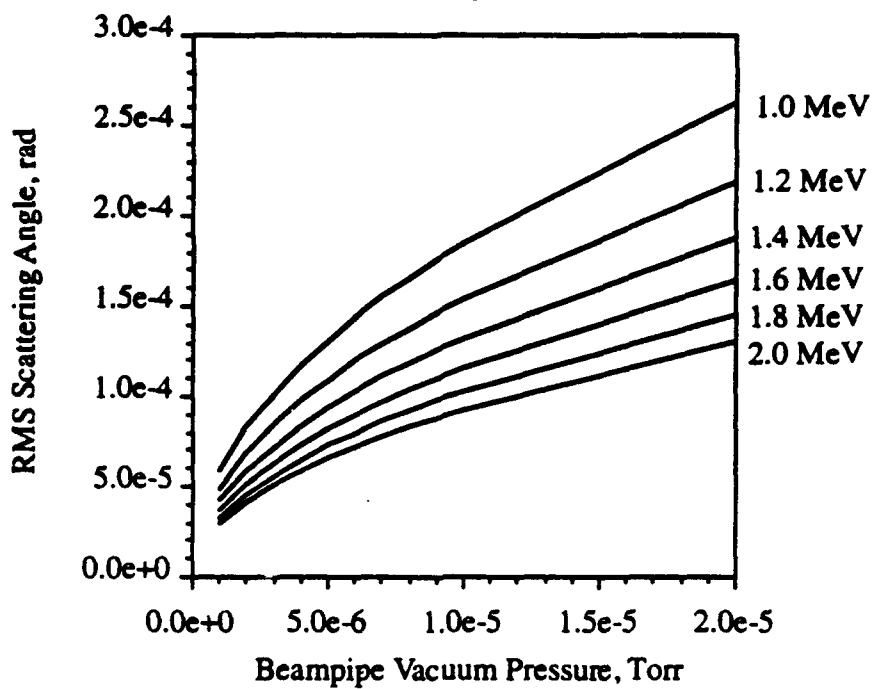


Figure 6.5.4 Antiproton scattering angle vs beampipe pressure for various beam energies.

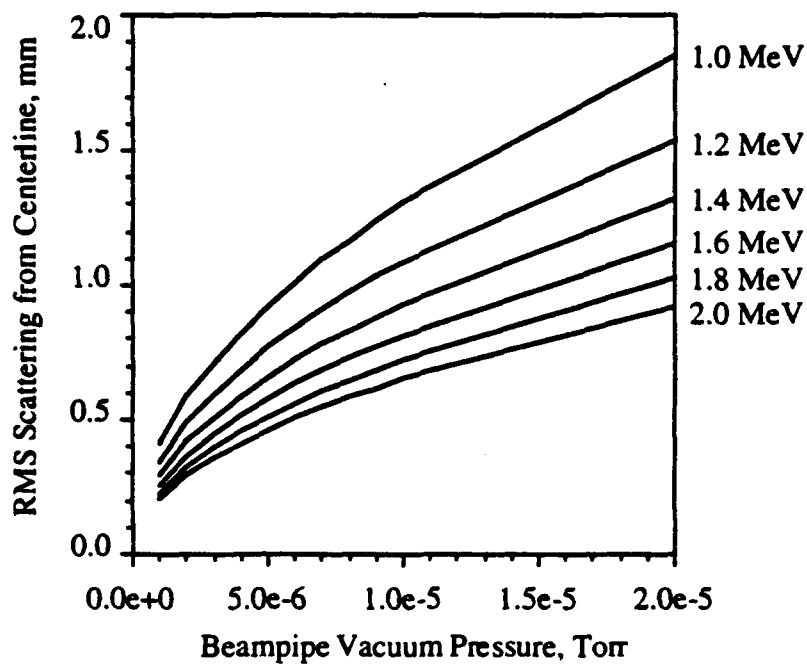


Figure 6.5.5 Antiproton displacement vs beampipe pressure for various beam energies

We now consider the more realistic scenario of the target shown in Figure 6.5.1 forming an imperfect seal with the cathode. During the compression process, a specific amount of plasma for each case leaks into the beampipe. Also, the diamond retaining window is not needed for the imperfect seal cases.

6.6 Case 5

This section presents the results for a cylindrical target that forms an imperfect seal with the electrodes. Here, the plasma has initial conditions of 2 eV and 10^{19} atoms/cm³. The imperfect seal, cylindrical target case represents a plasma leakage situation midway between the complete leakage of the spherical target case and the complete blockage of the perfect seal cylindrical target case.

The following scenario provides a useful order-of-magnitude approach for determining approximate antiproton beam/plasma interaction results. When the plasma fills the aluminum liner prior to the start of the compression cycle, some of it leaks into the target cavity through the imperfect seal between the electrodes and target. During the compression cycle, this plasma diffuses into the beam pipe, but it is not forced in by the compression process since the target does not undergo significant compression until near the end of the process. Meanwhile, increasing plasma pressure closes the seal between the electrodes and target, and the target then effectively shields the beampipe from the working fluid during the rest of the compression process. Since no diamond window exists to cap the cathode orifice in this scenario, the plasma trapped inside the target begins to diffuse down the beampipe at the start of the compression cycle. Therefore, the plasma must be tracked down the pipe during the entire compression cycle.

The above scenario incorporates the following assumptions:

1. Plasma fills the target an instant before the start of the compression cycle.

2. As soon as the target is filled, the exterior plasma pressure squeezes the target just enough to close the gap with the cathode.

3. The plasma diffuses freely into the beampipe and remains unaffected by the imploding target during the compression cycle.

We use the amount of plasma that can fit into the hollow region of the cylindrical target as a benchmark plasma mass that leaks into the beampipe. Table 6.3 lists the plasma mass that leaks into the beampipe, and the total mass of the working fluid, for each case. Multiplying the volume of the hollow region of the cylindrical target by the initial plasma mass density gives the mass of the plasma that leaks into the target and subsequently expands into the beampipe.

Table 6.3 Mass of plasma leakage into beampipe.

Case	Leakage mass	Total plasma mass
5	5.236×10^{-4} mg	3.1 mg
6	3.142×10^{-3} mg	18.6 mg
7	5.236×10^{-4} mg	3.1 mg
8	3.142×10^{-3} mg	18.6 mg

Note that in each case only 0.017 % of the total plasma mass leaks into the beampipe.

Figure 6.6.1 shows the beam energy loss and plasma density along the last 10 cm of the beampipe for the imperfect hollow target with initial conditions of 2 eV and 1×10^{19} atoms/cm³. In the figure, the target is located at the origin. The plasma density in the beampipe is several orders of magnitude lower for this case than for the corresponding spherical target case, Case 1. This difference represents the major advantage of the hollow,

cylindrical target over the spherical target. Since the plasma density for this case is low, 1.2 MeV antiprotons can easily reach the target with no significant energy loss.

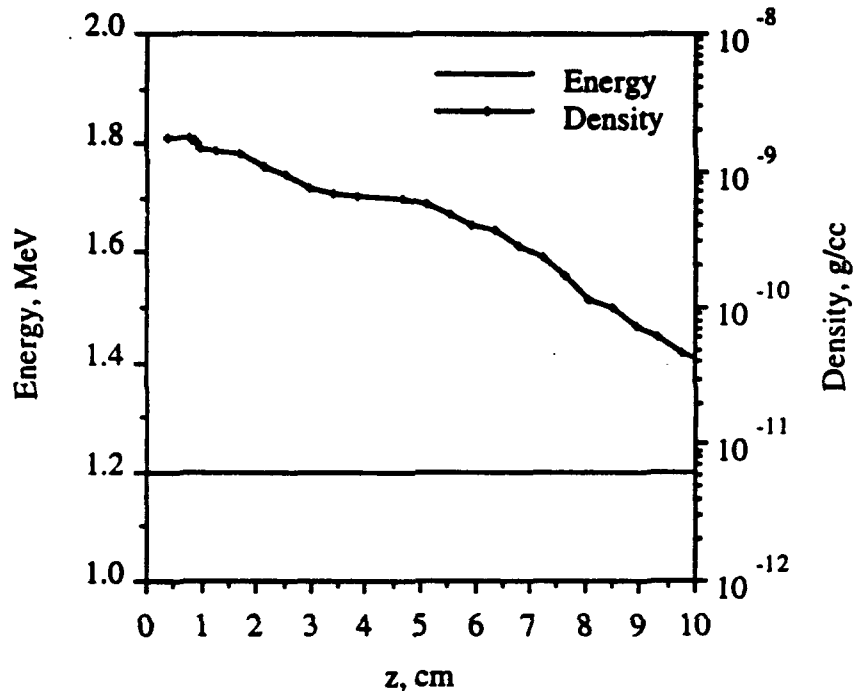


Figure 6.6.1 Beam energy and plasma density profiles for Case 5.

In order to calculate the particle's various scattering angles along the beampipe, Eq. (6.5.1) was used to determine the rms scattering angle in air, while Eqs. (4.18) and (4.19) gave the rms scattering angle in the portion of the beam contaminated by hydrogen plasma. A random number generator was used to predict the individual scattering angle at each space step down the pipe.

Figure 6.6.2 shows the position of beam antiprotons at the end of the beampipe in the x-y plane for a 1.2 MeV beam. The beam has rms scattering values of 0.58 and 0.57 mm in the x and y directions, respectively. Out of the original 1000 antiprotons, 191 fall outside of the circle and thus strike the interior wall of the cathode, corresponding to a 19.1% loss. Less than one antiproton out of a 1000 annihilated.

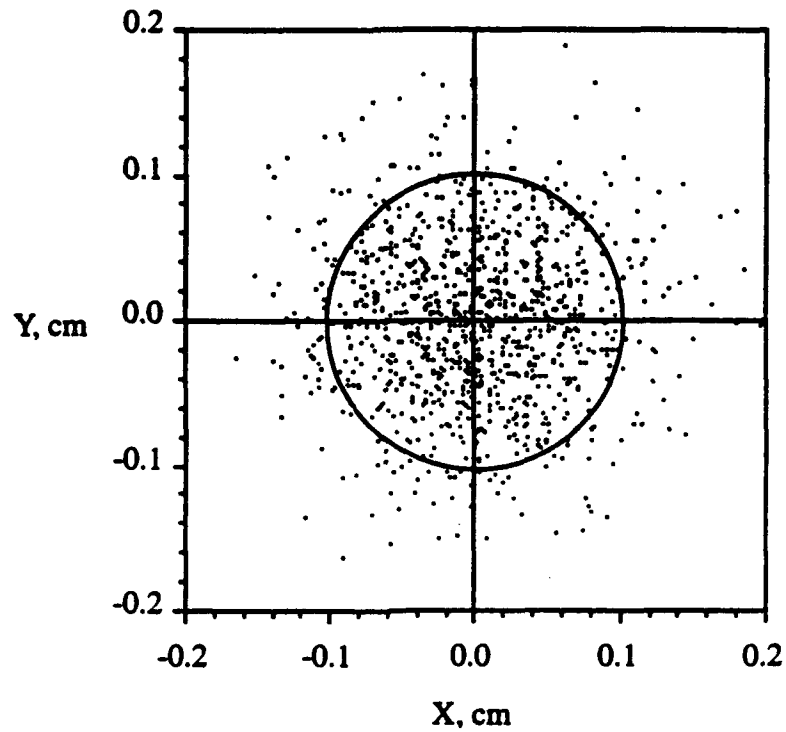


Figure 6.6.2 Final antiproton positions for Case 5 with a 1.2 MeV beam.

6.7 Cases 6, 7, and 8

Since only a small amount of plasma (0.017 % of the total working fluid) leaks into the beampipe for the hollow target scenarios, the antiproton energy loss and scattering for Cases 6, 7, and 8 are similar to those of Case 5. For each Case, a 1.2 MeV antiproton penetrates the plasma with no significant energy loss. Table 7.2 summarizes the major results for the hollow target Cases.

Chapter 7

CONCLUSIONS

Based on the results presented in Chapter 6, we can draw significant conclusions about antiproton beam/hydrogen plasma interactions for the SHIVA Star microfission experiment. First, antiproton-proton annihilations do not represent significant problems for either the spherical target or hollow, cylindrical target scenarios. Since the factor $\sigma\beta$ is relatively small (35 mbarns) for this type of interaction, only one antiproton-proton annihilation occurred for the spherical target cases (Case 2) during the computer simulations of 4000 (total) antiprotons. No antiproton-proton annihilations occurred for the hollow target cases.

Secondly, electronic energy loss represents the major loss mechanism for the spherical target cases, and governs the choice of the necessary initial beam energy. All the spherical target cases required beam energies in excess of 3 MeV. Table 7.1 summarizes the major results for the spherical target cases.

Table 7.1 Summary of beam/plasma results for Cases 1-4.

Case	Required Energy (MeV)	X_{rms} (mm)	Y_{rms} (mm)	Annihilations per 1000 antiprotons with Beampipe Wall
1	3.5	0.203	0.201	0
2	4.6	0.153	0.155	0
3	3.0	0.156	0.147	0
4	3.3	0.221	0.205	0

For each case listed above, the antiproton beam loses most of its energy in the 3 mm space between the target surface and the end of the beampipe. For Case 1, the beam loses only

0.25 MeV between the RFQ exit and the end of the beampipe. It then loses 3.1 MeV in the high-density space, and impacts the target with 0.15 MeV. The 4.6 MeV beam for Case 2 reaches the end of the beampipe with 4.3 MeV, then loses nearly 4 MeV before hitting the target. Similarly, the antiproton beams for Cases 3 and 4 lose only 0.2 and 0.22 MeV, respectively, when travelling between the RFQ and the end of the beampipe.

Rutherford scattering from plasma protons does not represent a significant problem for Cases 1 through 4. During the computer simulations, none of the beam antiprotons were deflected into the beampipe wall as a result of collisions with air molecules and plasma protons. The beampipe had an air pressure of 3×10^{-6} Torr. The energy necessary to overcome collisions with electrons provides the antiprotons with enough momentum to also overcome significant scattering from plasma protons.

In addition to requiring higher energies, the spherical target cases have a second disadvantage in that during computer simulations a significant portion of the plasma working fluid leaks into the beampipe through the cathode window. As discussed in Chapter 2, this plasma leakage will tend to decrease compression of the fissile target. Furthermore, significant plasma leakage also tends to invalidate the density profiles determined by the kinetic theory procedure discussed in Chapter 2.

Because plasma leakage into the beampipe is much smaller for the hollow target cases, the antiproton beams undergo no significant energy loss. Antiproton deflection to the beampipe wall represents the major loss mechanism for Cases 5 through 8. Table 7.2 summarizes the major results for these Cases.

Table 7.2 Summary of beam/plasma results for Cases 5-8.

Case	Required Energy (MeV)	X _{rms} (mm)	Y _{rms} (mm)	Annihilations per 1000 antiprotons with Beampipe Wall
5	1.2	0.584	0.570	191
6	1.2	0.588	0.579	202
7	1.2	0.577	0.570	183
8	1.2	0.614	0.597	234

Notice that the rms deflections do not vary much with the different plasma conditions. Therefore, we conclude that residual air, and not the plasma, contributes to most of the antiproton deflection. A vacuum on the order of 10^{-7} Torr would further reduce antiproton losses for the SHIVA Star experiment.

With its ability to protect the beampipe from plasma contamination, thus minimizing antiproton beam energy loss and necessary beam energy, the cylindrical target represents a better choice for the SHIVA Star microfission experiment than the spherical target.

REFERENCES

- [1] Mallove, Eugene F. and Gregory L. Matloff: *The Starflight Handbook*, John Wiley & Sons, Inc., New York, 1989.
- [2] Lewis, R. A., et al: "Antiproton Boosted Microfission," *Nuclear Science and Engineering* vol. 109, pp. 411, 1991; *Fusion Technology*, vol. 20, no. 4, part 2, pp. 1046, 1991.
- [3] Chiang, P.-R., et al: "An Antiproton Driver for Inertial Confinement Fusion Propulsion," paper presented at Nuclear Technologies for Space Exploration meeting, Jackson, WY, August 1992.
- [4] Fry, Michael R. J., et al: *Guidance on Radiation Received in Space Activities*, NCRP Report No. 98, July 1989.
- [5] Tascione, Thomas F.: *Introduction to the Space Environment*, Orbit Book Company, Malabar, 1988.
- [6] Serway, Raymond A.: *Physics for Scientists and Engineers*, 2nd ed., Saunders College Publishing, Philadelphia, 1986.
- [7] Nicogossian, Arnauld E. and James F. Parker, Jr.: *Space Physiology and Medicine*, NASA SP-447, 1982.
- [8] Field, J. E.: *The Properties of Diamond*, Academic Press, London, 1979.
- [9] Stanek, Floyd J.: *Stress Analysis of Circular Plates and Cylindrical Shells*, Dorrance and Company, Philadelphia, 1970.
- [10] Popov, E.P.: *Mechanics of Materials*, 2nd ed., Prentice-Hall, Inc., Englewood Cliffs, 1976.
- [11] Personal communication from R. A. Lewis.
- [12] Harvey, John F.: *Theory and Design of Pressure Vessels*, Van Nostrand Reinhold Co. Inc., New York, 1985.
- [13] Program provided courtesy of Dr. Robert Tipton, Lawrence Livermore National Laboratory, Livermore, CA 94550.
- [14] Shackelford, James F.: *Introduction to Materials Science for Engineers*, 2nd ed., Macmillan Publishing Company, New York, 1988.
- [15] Yang, W. H., and D. J. Srolovitz: "Cracklike Surface Instabilities in Stressed Solids," *Physical Review Letters*, vol. 71, no. 10, Sept. 1993, pp. 1593-1596.
- [16] Chen, Francis F.: *Introduction to Plasma Physics and Controlled Fusion*, 2nd ed., Plenum Press, New York.
- [17] Clemmow, P.C. and J.P. Dougherty: *Electrodynamics of Particles and Plasmas*, Addison-Wesley Publishing Co. Inc., Reading, 1969.

- [18] Massey, H. S. W.: *Electronic and Ionic Impact Phenomena*, Vol. II, 2nd ed., Oxford University Press, London, 1969.
- [19] Langley, R.A., et al: *Data Compendium for Plasma-Surface Interactions*, International Atomic Energy Agency, Vienna, 1984.
- [20] Jackson, J.D.: *Classical Electrodynamics*, 2nd ed., Wiley, New York, 1975.
- [21] Melhorn, Thomas A.: "A Finite Material Temperature Model for Ion Energy Deposition in Ion-Driven Inertial Confinement Fusion Targets," *J. Appl. Phys.*, vol. 52, no. 11, Nov. 1981, pp. 6522-6532.
- [22] Golant, V. E. and V. I. Fedorov: *RF Plasma Heating in Toroidal Fusion Devices*, Consultants Bureau, New York, 1989.
- [23] Duderstadt, James J. and Gregory A. Moses: *Inertial Confinement Fusion*, John Wiley & Sons, New York, 1982.
- [24] Krall, Nicholas A. and Alvin W. Trivelpiece: *Principles of Plasma Physics*, McGraw-Hill Book Company, New York, 1973.
- [25] Satori, Shin, Hitoshi Kuninaka, and Kyoichi Kuriki: "Antimatter as Energy Source in Space," *JSTS*, vol. 6, no. 2, 1992, pp. 34-50.
- [26] Lamarsh, J.R.: *Introduction to Nuclear Engineering*, 2nd ed., Addison Wesley Publishing Co. Inc., Reading, 1983.
- [27] Mutchler, G.S., et al: "Measurement of the Imaginary Part of the $l = 1$ NN S -Wave Scattering Length," *Physical Review D*, vol. 38, no. 3, August 1988, pp. 742-753.
- [28] Aguiular-Benitez, M., et al: *Particle Properties Data Booklet*, American Institute of Physics, 1992.

Appendix
CALE DATA

The following tables give the CALE-generated plasma temperature, density and pressure time histories at the beampipe exit for Cases 1 through 4. These data are read into the kinetic theory code discussed in Chapter 2, which determines the plasma density profile along the injection pipe at the time of peak compression. The first entry in the leftmost column corresponds to the time of window fracture, while the last entry gives the time of peak compression. The rightmost column lists the differential mass leaking into the beampipe between two consecutive times. For example, the first entry under Δm gives the plasma mass in grams that leaks into the beampipe between the times corresponding to the first and second entries under the Time column. The last two boldfaced entries in the Δm column indicate the total mass of plasma which leaks into the beampipe by the time of peak compression, and the corresponding percentage of the total mass of the working fluid.

Case 1

Time, μsec	T, eV	ρ , g/cm^3	P, kbar	Δm , g
12.222	37.649	2.850E-03	206.699	1.583E-05
12.290	38.815	3.372E-03	252.000	4.831E-06
12.307	39.927	3.683E-03	283.130	5.352E-06
12.325	41.069	4.023E-03	318.054	5.928E-06
12.342	42.242	4.394E-03	357.228	6.566E-06
12.359	43.446	4.798E-03	401.161	7.271E-06
12.376	44.684	5.238E-03	450.424	8.051E-06
12.394	45.954	5.718E-03	505.655	8.914E-06
12.411	47.259	6.242E-03	567.567	9.867E-06
12.428	48.600	6.813E-03	636.957	1.092E-05
12.445	49.976	7.434E-03	714.717	1.208E-05
12.463	51.389	8.112E-03	801.841	1.337E-05
12.480	52.840	8.850E-03	899.442	1.479E-05
12.497	54.330	9.655E-03	1008.763	1.636E-05
12.515	55.860	1.053E-02	1131.192	1.810E-05
12.532	57.431	1.149E-02	1268.279	2.103E-05
12.550	59.127	1.258E-02	1430.000	2.224E-05
12.567	63.870	1.513E-02	1859.561	2.049E-05
12.580	67.601	1.734E-02	2256.000	3.278E-05

12.597	71.012	1.869E-02	2554.942	3.622E-05
12.615	74.589	2.015E-02	2893.002	4.002E-05
12.632	78.342	2.172E-02	3275.237	4.421E-05
12.649	82.278	2.341E-02	3707.345	4.884E-05
12.666	86.407	2.523E-02	4195.753	5.393E-05
12.684	90.736	2.719E-02	4747.703	5.637E-05
12.700	95.027	2.918E-02	5336.000	6.541E-05
12.717	95.911	2.893E-02	5339.893	6.515E-05
12.735	96.802	2.869E-02	5343.784	6.490E-05
12.752	97.700	2.844E-02	5347.673	6.465E-05
12.769	98.605	2.820E-02	5351.559	6.440E-05
12.786	99.517	2.797E-02	5355.442	6.415E-05
12.804	100.436	2.773E-02	5359.323	6.390E-05
12.821	101.363	2.750E-02	5363.202	6.365E-05
12.838	102.297	2.726E-02	5367.079	6.341E-05
12.855	103.238	2.704E-02	5370.952	8.236E-05
12.878	104.476	2.674E-02	5376.000	6.285E-05
12.895	103.588	2.615E-02	5211.607	6.119E-05
12.913	102.708	2.557E-02	5052.452	5.958E-05
12.930	101.838	2.500E-02	4898.360	5.801E-05
12.947	100.975	2.445E-02	4749.164	5.649E-05
12.964	100.122	2.391E-02	4604.702	5.294E-05
12.981	99.308	2.340E-02	4470.000	0.000E+00
				1.547 g
				49.917 %

Case 2

Time, μsec	T, eV	ρ , g/cm^3	P, kbar	Δm , g
11.989	14.927	7.025E-03	202.394	1.138E-05
12.021	15.658	7.824E-03	236.411	1.298E-05
12.052	16.423	8.711E-03	276.032	1.480E-05
12.084	17.223	9.696E-03	322.163	1.687E-05
12.115	18.060	1.079E-02	375.852	1.922E-05
12.147	18.935	1.200E-02	438.313	2.190E-05
12.178	19.850	1.335E-02	510.951	2.494E-05
12.210	20.806	1.484E-02	595.391	2.838E-05
12.241	21.807	1.650E-02	693.511	3.230E-05
12.273	22.852	1.833E-02	807.486	3.674E-05
12.304	23.945	2.036E-02	939.825	4.178E-05
12.336	25.087	2.262E-02	1093.428	4.750E-05
12.367	26.280	2.511E-02	1271.646	5.398E-05
12.398	27.527	2.788E-02	1478.342	6.132E-05
12.430	28.830	3.093E-02	1717.979	6.964E-05
12.461	30.190	3.432E-02	1995.702	7.907E-05
12.493	31.612	3.807E-02	2317.444	8.974E-05
12.524	33.096	4.221E-02	2690.044	1.018E-04
12.556	34.646	4.679E-02	3121.381	1.155E-04

12.587	36.264	5.186E-02	3620.532	1.309E-04
12.619	37.954	5.746E-02	4197.947	1.484E-04
12.650	39.718	6.365E-02	4865.655	1.682E-04
12.682	41.559	7.049E-02	5637.495	2.299E-04
12.720	43.888	7.970E-02	6730.000	2.214E-04
12.752	42.624	7.480E-02	6135.041	2.048E-04
12.783	41.399	7.021E-02	5593.955	1.894E-04
12.815	40.212	6.592E-02	5101.751	1.975E-04
12.850	38.919	6.140E-02	4600.000	1.606E-04
12.882	37.736	5.678E-02	4124.188	1.462E-04
12.913	36.592	5.252E-02	3698.580	1.332E-04
12.945	35.485	4.858E-02	3317.773	9.823E-05
12.970	34.615	4.562E-02	3039.000	1.125E-04
13.002	34.158	4.403E-02	2894.136	1.079E-04
13.033	33.707	4.250E-02	2756.502	8.867E-05
13.060	33.326	4.123E-02	2644.000	0.000E+00
				3.218 g
				17.300 %

Case 3

Time, μsec	T, eV	ρ , g/cm ³	P, kbar	Δm , g
12.014	50.082	2.115E-03	204.043	1.160E-05
12.072	52.751	2.409E-03	244.768	1.346E-05
12.130	55.509	2.740E-03	293.000	5.706E-06
12.151	56.222	2.826E-03	305.987	5.923E-06
12.172	56.942	2.914E-03	319.526	6.147E-06
12.193	57.670	3.005E-03	333.639	6.380E-06
12.214	58.406	3.099E-03	348.350	6.621E-06
12.235	59.151	3.196E-03	363.682	6.870E-06
12.256	59.903	3.295E-03	379.661	7.129E-06
12.277	60.664	3.397E-03	396.313	7.397E-06
12.298	61.433	3.503E-03	413.665	7.674E-06
12.319	62.210	3.611E-03	431.745	7.961E-06
12.340	62.996	3.722E-03	450.583	1.023E-05
12.366	63.981	3.865E-03	475.000	8.642E-06
12.387	66.203	4.180E-03	531.617	9.507E-06
12.408	68.497	4.520E-03	594.868	1.046E-05
12.429	70.867	4.887E-03	665.519	1.150E-05
12.450	73.315	5.283E-03	744.419	1.264E-05
12.471	75.843	5.710E-03	832.516	1.390E-05
12.492	78.454	6.171E-03	930.864	1.528E-05
12.513	81.150	6.669E-03	1040.635	1.679E-05
12.534	83.934	7.205E-03	1163.133	1.845E-05
12.555	86.809	7.784E-03	1299.808	1.448E-05
12.570	88.919	8.225E-03	1407.000	2.168E-05
12.591	92.723	8.948E-03	1596.243	2.409E-05
12.612	96.683	9.733E-03	1810.558	2.675E-05

12.633	100.806	1.059E-02	2053.218	2.971E-05
12.654	105.097	1.151E-02	2327.913	3.299E-05
12.675	109.563	1.252E-02	2638.810	3.662E-05
12.696	114.211	1.361E-02	2990.607	4.065E-05
12.717	119.047	1.479E-02	3388.604	4.511E-05
12.738	124.081	1.608E-02	3838.775	2.861E-05
12.750	127.048	1.686E-02	4122.000	5.312E-05
12.771	127.116	1.686E-02	4122.769	5.312E-05
12.792	127.183	1.685E-02	4123.537	5.312E-05
12.813	127.251	1.685E-02	4124.303	5.312E-05
12.834	127.319	1.684E-02	4125.069	5.312E-05
12.855	127.386	1.684E-02	4125.833	5.312E-05
12.876	127.454	1.683E-02	4126.597	5.311E-05
12.897	127.521	1.683E-02	4127.359	5.311E-05
12.918	127.588	1.682E-02	4128.120	5.311E-05
12.939	127.656	1.682E-02	4128.880	7.840E-05
12.970	127.755	1.681E-02	4130.000	0.000E+00
				1.077 g
				34.755 %

Case 4

Time, μsec	T, eV	ρ , g/cm ³	P, kbar	Δm , g
12.000	26.397	3.943E-03	200.428	1.053E-05
12.039	27.214	4.220E-03	221.163	1.144E-05
12.078	28.052	4.516E-03	243.965	1.243E-05
12.117	28.914	4.831E-03	269.033	1.350E-05
12.156	29.799	5.167E-03	296.583	1.466E-05
12.195	30.708	5.525E-03	326.852	1.591E-05
12.234	31.642	5.906E-03	360.099	1.727E-05
12.273	32.601	6.313E-03	396.605	1.874E-05
12.312	33.586	6.746E-03	436.678	2.032E-05
12.351	34.598	7.208E-03	480.653	2.204E-05
12.391	35.637	7.699E-03	528.896	2.389E-05
12.430	36.703	8.222E-03	581.807	2.682E-05
12.470	37.838	8.800E-03	642.000	2.814E-05
12.509	39.309	9.662E-03	732.322	3.149E-05
12.548	40.832	1.061E-02	835.009	3.523E-05
12.587	42.410	1.164E-02	951.707	3.939E-05
12.626	44.043	1.277E-02	1084.275	4.404E-05
12.665	45.734	1.400E-02	1234.811	4.922E-05
12.704	47.484	1.535E-02	1405.684	5.498E-05
12.743	49.295	1.683E-02	1599.567	6.141E-05
12.782	51.170	1.844E-02	1819.471	6.855E-05
12.821	53.110	2.020E-02	2068.795	7.651E-05
12.861	55.117	2.212E-02	2351.365	8.536E-05
12.900	57.194	2.422E-02	2671.493	9.520E-05
12.939	59.342	2.651E-02	3034.034	8.535E-05

12.970	61.123	2.850E-02	3360.000	1.158E-04
13.009	60.742	2.760E-02	3232.567	1.118E-04
13.048	60.365	2.673E-02	3110.328	1.079E-04
13.087	59.991	2.589E-02	2993.056	1.042E-04
13.126	59.620	2.507E-02	2880.536	1.006E-04
13.165	59.253	2.429E-02	2772.561	9.718E-05
13.204	58.890	2.353E-02	2668.935	9.386E-05
13.243	58.529	2.280E-02	2569.472	9.066E-05
13.282	58.172	2.209E-02	2473.992	8.758E-05
13.321	57.818	2.141E-02	2382.325	8.470E-05
13.367	57.410	2.064E-02	2280.000	0.000E+00
				1.971 g
				10.596 %

APPENDIX IV

Target Compression by Working Fluids Driven with Solid Liner Implosions*

P-R. Chiang, R. A. Lewis, and G. A. Smith
Laboratory for Elementary Particle Science, Department of Physics,

J. M. Dailey
Department of Aerospace Engineering,

S. Chakrabarti
Department of Mechanical Engineering

K. I. Higman
Department of Nuclear Engineering
The Pennsylvania State University, University Park, PA 16802

D. Bell, J.H. Degnan, T.W. Hussey and B.W. Mullins
High Energy Plasma Division, Phillips Laboratory, Kirtland AFB, NM 87117

ABSTRACT

Compression by a spherical solid liner of a gold target surrounded by a hydrogen plasma is simulated. A one-dimensional numerical code has been developed to study physical processes associated with compression. Calculations were performed using parameters for the SHIVA STAR facility at the Phillips Laboratory. Two-dimensional simulations that treat only a subset of the physics included in the one-dimensional code were performed in an attempt to assess multidimensional effects. Results of pressure, density and energy deposited for different initial plasma conditions are presented and discussed. Results from both one- and two-dimensional codes show that the average target density at peak compression is 39 - 43 gm/cm³, using the SHIVA STAR facility at 90 kV discharge.

(Submitted to J. Applied Physics)

* Work supported in part by the Air Force Office of Scientific Research, Jet Propulsion Laboratory (NASA), National Science Foundation, Penn State Propulsion Engineering Research Center Grant NAGW-1356, #6, and the Rocketdyne Corporation.

I. Introduction

Electromagnetically imploded solid liners have been employed at some laboratories as a means of achieving high energy densities and pressures.¹⁻⁷ Solid liner implosions are essentially hollow shell z-pinch⁸ or θ -pinches in which the mass of the liner is sufficient to prevent vaporization of the liner during the run-in phase of the implosion. At the Phillips Laboratory we are planning to use solid liner implosions to compress a hot hydrogen working fluid which will in turn compress an inner target. The advantages of a working fluid include decoupling of outer implosion non-uniformities from the central implosion and the possibility of transferring non-spherical liner energy onto a spherical target.

One application of this technology is antiproton-catalyzed microfission. Antiproton annihilations have been shown to be a strong source of neutrons⁹ and pions¹⁰ which, under conditions of high density, enable a significant reduction in burn time and hence, size of fissile targets. The concept of antiproton-catalyzed microfission¹¹⁻¹² will be tested by compressing a small fissile target with an electromagnetically imploded solid liner. A subcritical test is possible at this time, with presently limited numbers of antiprotons available. To simulate the compression of a solid target, a one-dimensional (1-D) radiative Lagrangian hydrodynamics code, HYDRAD,¹³ has been developed. 1-D results without radiation and thermal conduction physics for differing initial plasma conditions are compared with two-dimensional (2-D) results from a magnetohydrodynamics (MHD) code, CALE,¹⁴ in order to assess multidimensional effects. 1-D calculations with radiation and thermal conduction are also performed to obtain more realistic results.

The solid liner implosion system is shown schematically in Fig. 1. The quasispherical liner is imploded by a 10 MA average discharge from the Phillips Laboratory SHIVA STAR capacitor bank, which stores 5.3 MJ of energy with 1300 μ F of capacitance at 90 KV. The current which flows through the liner forces it to collapse inwardly. A tapered

spherical aluminum liner (1 mm to 2 mm thick) encloses 45°-angle conical electrodes and a sealed chamber with a 4-cm radius; a gold target (gold is used instead of uranium due to availability of parametric information, e.g., equation of state, opacity, etc.) and a hydrogen plasma used as a working fluid are placed in the chamber. The implosion is designed to result in an isotropic, adiabatic compression intended to avoid generating shock waves in the target, which lead to undesirable high-temperature, low-density conditions. However, there is a trade-off between the requirement that the working fluid temperature, and hence its sound speed, be high enough so that the liner will be compressed adiabatically, and the requirement that thermal losses to the walls be minimized. A hydrogen plasma with a temperature between 1-2 eV and density between 10^{19} - 10^{20} cm^{-3} best satisfies these requirements.^{15,16}

In Section II, HYDRAD is described. In Section III, results with different initial plasma parameters, specifically, $T_0 = 2$ eV, 5 eV and $n_0 = 1 \times 10^{19}$ cm^{-3} , 6×10^{19} cm^{-3} are presented and compared with 2-D results from CALE. In Section IV, results including radiation effects are presented and discussed.

II. Description of HYDRAD and CALE

A. HYDRAD

i) One-Dimensional Hydrodynamics

The model of HYDRAD assumes spherical symmetry and fluid-like solids. The one-dimensional Euler equations in spherical geometry are

$$\frac{\partial v}{\partial t} - \frac{\partial r^2 u}{\partial m} = 0 \quad (\text{continuity}), \quad (1)$$

$$\frac{\partial u}{\partial t} + r^2 \frac{\partial p}{\partial m} = g \quad (\text{momentum}), \quad (2)$$

and

$$\frac{\partial E}{\partial t} + \frac{\partial r^2 u p}{\partial m} = u g - K_{th} + q_{ext} \quad (\text{energy}). \quad (3)$$

Here, $v = 1/\rho$ is the specific volume, u is the fluid velocity in the radial (r) direction, g is the external force, p is the pressure, E is the internal energy, m is the mass coordinate, K_{th} accounts for the rate of energy loss due to thermal radiation conduction and q_{ext} is the rate of change of external energy sources.

We use a radiation thermal conduction model¹⁶ to calculate thermal radiation and conduction loss. Thermal conduction due to electrons and ions is included in the calculation by using the following equations, for both plasma and metallic solids:

$$K_{th} = -\frac{1}{\rho} \nabla \kappa \nabla T, \quad (4)$$

$$\kappa = \kappa_i + \kappa_e + \kappa_r, \quad (5)$$

and

$$\kappa_r = \frac{16\sigma L_R T^3}{3}, \quad (6)$$

where T is the temperature, σ is Stefan-Boltzmann constant, L_R is the Rosseland mean free length, and κ_i and κ_e are, respectively, the ion and electron thermal conductivities.

Since a strong shock wave may be created in the solid target due to its initial low temperature, it is necessary to use a sophisticated numerical scheme to account for large pressure and temperature gradients. Therefore, we adopt the piecewise parabolic method (PPM).¹⁷ The PPM scheme is an extension of Godunov's approach,¹⁸ which has; 1) a Riemann solver to handle wave interactions, 2) higher order interpolation techniques, and 3) special monotonicity constraints and discontinuity detectors. The scheme is one of the most accurate numerical methods for hydrodynamics simulations.¹⁸ The accuracy of the method is second order in time and third order in space. Instead of mixing a Lagrangian step and an Eulerian remap step, a pure Lagrangian scheme is used.

The Crank-Nicholson scheme¹⁹ is used for solving the thermal conduction equation and the free stream flux limiter¹⁹⁻²¹ is imposed on thermal conduction coefficients, κ_r and

κ_e to compensate for the diffusion approximation. The numerical model for radiation calculations in HYDRAD is similar to the model of MEDUSA,²² except that HYDRAD uses one temperature only.

ii) Equation-of-State and Rosseland Mean Free Path

To simulate solids, including the target and liner, under compression a three-term model¹⁷ is used to calculate the equation-of-state (EOS), namely,

$$E = E_c(v) + E_i^T(v, T) + E_e^T(v, T), \quad (7)$$

and

$$P = P_c(v) + P_i^T(v, T) + P_e^T(v, T), \quad (8)$$

where $E_c(v)$ and $P_c(v)$ are, respectively, the energy and pressure of the cold isotherms, and subscripts i and e, respectively, indicate the thermal contributions from ions and electrons. Thermal contributions from ions and electrons are expressed in analytical forms.¹⁷ The cold isotherms are generated from the SESAME EOS library,²³ and have been fit by a polynomial function to improve computation speed. The advantage of using this three-term model is that the temperature can be analytically computed without interpolation. However, the original EOS model is reasonably accurate up to $T = 3$ eV. We have adjusted the EOS to match the SESAME EOS up to $T \approx 20$ eV.

With relatively low initial temperature compared to the temperature required for full ionization, the hydrogen gas may not be fully ionized throughout the compression cycle. We therefore use the Saha equation²⁴ to calculate the EOS for the hydrogen plasma. Although the Saha equation may not be appropriate for hydrogen beyond solid density, the model is well justified as long as the Fermi energy is much smaller than the thermal energy.

The SESAME opacity (defined as $1/(\rho L_R)$) library is used to benchmark the Rosseland mean free path used. We use power-law approximations for calculating the Rosseland mean free path in the solids, i.e.,

$$L_r = A\rho^\alpha T^\beta, \quad (9)$$

where A , α and β are chosen to fit the SESAME opacity curves in the region of $T \leq 10$ eV. Thermal conduction in the solid in this temperature regime is still dominated by electron thermal conduction, because the photon mean free path is much shorter than the electron mean free path. Since most temperatures in solids are below 10 eV, simulation results are not sensitive to this parameterization.

Photon absorption in hydrogen is dominated by shell absorption at temperatures below 10 eV. Since there is no analytical expression for opacity in this temperature regime, we use a Maxwellian distribution function to fit the Rosseland opacity curves for hydrogen in the SESAME opacity library for temperatures under 20 eV. Above 20 eV, we use bremsstrahlung¹⁷ absorption cross sections to calculate the opacity.

iii) Pressure due to Magnetic Field

The system circuit for a solid liner compression can be schematically expressed as a simple RLC circuit shown in Fig. 1. The resistance R is considered to be constant throughout the compression cycle. If the liner inductance is constant in time, the current can be analytically expressed as

$$I(t) = CV_0 \frac{A^2 + B^2}{B} e^{-At} \sin Bt, \quad (10)$$

where V_0 is the initial voltage of the capacitor bank,

$$A = \frac{R}{2L} \quad \text{and} \quad B = \left(\frac{1}{LC} - \frac{R^2}{4L^2} \right)^{1/2}. \quad (11)$$

However, since L is a function of the liner position, the circuit equation is coupled with the equation-of-motion. In the absence of a detailed description of the coupling, we have assumed that the liner inductance is constant in time. The following parameters for a cylindrical implosion experiment⁶ have been used in this calculation: $R = 1$ m Ω , $C = 1300$ μ F, $L = 30$ nH (combined inductance of circuit and liner).

The diffusion time scale for the magnetic field in the liner is

$$\tau_B = \sigma_L \mu_L \Delta r^2, \quad (12)$$

where $\sigma_L = 3 \times 10^7 \text{ ohm}^{-1}\text{m}^{-1}$ is the conductivity, $\mu_L = 4\pi \times 10^{-7}$ is the magnetic permeability of the liner and Δr is the liner thickness. Using the initial thickness of the liner as $\Delta r = 1 \text{ mm}$, the diffusion time scale is $\approx 150 \text{ } \mu\text{sec}$, which is relatively long compared with the compression time scale, ($\pi/B \approx 18 \text{ } \mu\text{sec}$). Therefore, it is reasonable to approximate the spatial current distribution in the liner as a surface current.

The magnetic pressure due to a surface current through the liner is nonuniform along the polar angle direction for the spherical compression, and can be expressed as

$$P_B = \frac{B_\phi^2}{2\mu_0}, \quad (13)$$

where

$$B_\phi = \frac{\mu_0 I}{2\pi r_1 \sin \theta} \quad (14)$$

is the azimuthal component of the magnetic field, I is the time-varying current running through the liner, r_1 is the radial position of the liner outer surface, θ is the polar angle measured around the electrode symmetry axis z , and μ_0 is the magnetic permeability in vacuum. Since HYDRAD is a one-dimensional code, it can only compute a single value for the magnetic pressure. To account for the tapered liner thickness, HYDRAD uses an average thickness for the liner. The average magnetic pressure is

$$P_B = 1.247 \times \frac{B_{\phi 0}^2}{2\mu_0}, \quad (15)$$

where

$$B_\phi = \frac{\mu_0 I}{2\pi r_1}. \quad (16)$$

B. CALE

The version of CALE used for the simulation has the following features:

- 2-D MHD calculation in Eulerian coordinates or Lagrangian coordinates,
- elastic properties of materials,
- Saha equation for the equation-of-state and conductivity of hydrogen,
- polynomial function input for the EOS of solids,
- frictionless contact between liner and electrode,
- and no thermal radiation or conduction in the system.

A fully Eulerian calculation is chosen for the simulations. For solids, we use the EOS from the SESAME library to calculate appropriate coefficients for CALE input.

C. Limit of Energy Deposition

Since the total energy results from the magnetic field, the maximum energy deposited in the liner, plasma and target can be estimated from the work done by the magnetic pressure, i.e.,

$$\Delta U = \int_{r_0}^{r_p} F_B dr = \int_{r_0}^{r_p} \left[-2 \ln \tan \frac{\theta_m}{2} \right] \frac{\mu_0 I^2(t)}{4\pi} dr, \quad (17)$$

where r_0 is the initial position of the outer liner surface, r_p is the radius of the liner outer surface at peak compression, and $\theta_m = \pi/4$ is the electrode angle. Therefore,

$$\Delta U_{\max} (\text{MJ}) \approx 1.8 \times 10^{-3} (r_0 - r_p) I_{\max}^2 (\text{MA}), \quad (18)$$

where I_{\max} is the maximum value of $I(t)$. For example, using $r_0 = 4.15$ cm, $r_p = 1.5$ cm, and $I_{\max} = 16$ MA (90 KV discharge), the maximum energy deposition is 1.2 MJ. This can serve as a quick reference for estimating energy deposition for both codes.

III. Results of Simulations

Initial conditions for 4 cases simulated are listed in Table I. In this section, we show results of both 1-D (HYDRAD) and 2-D (CALE) simulations.

A. Without Radiation

The geometry used in HYDRAD simulations is schematically shown in Fig. 2. Since the liner is tapered (see Fig. 1), we take the average thickness of 1.5 mm as the initial thickness of the liner. This leads to a 1-D liner mass of 59 gm, as compared to the actual mass of 51 gm used by CALE. Figure 1 shows that the liner and the plasma occupy an angle of $\pi/2$ radians in the θ direction, whereas the target subtends an angle of π radians. The target, which subtends an angle from $\pi/4$ to $3\pi/4$ in Fig. 2, contains 71 % of the full target volume. Therefore, the target radius is increased by a factor of 1.12 to simulate a target of the same mass. The target in all HYDRAD simulations has a mass of 27 grams, and a radius of 0.783 cm. The total number of Lagrangian cells in HYDRAD simulations is 40, shown in Fig. 2.

Figure 3 shows target pressure, density and temperature, spatially averaged at peak compression, as a function of the initial plasma pressure from HYDRAD and CALE simulations. The average target densities from HYDRAD simulations range from 38 gm/cm³ to 43 gm/cm³, while from CALE simulations range from 34 gm/cm³ to 40 gm/cm³, as the initial pressure ranges from 71 bar (case A) to 952 bar (case D). At initial plasma pressures below 256 bar (case C), the average target density at peak compression is almost constant (≈ 42 gm/cm³) from 1-D, and ≈ 39 gm/cm³ from 2-D. With the initial pressure at 952 bar (case D), the target density is 8 % less than in cases A-C. These results clearly show an inverse correlation between density and initial plasma pressure. However, there is a trade-off for increasing the liner inertia, i.e., a greater liner inertia may create a stronger shock wave in the target, which may increase thermal energy at the expense of compression energy, leading to lower target density.

Average target densities from CALE at peak compression are consistently lower than from HYDRAD by 3 - 4 gm/cm³. This density difference may be attributed to nonuniform compression in the 2-D simulation. Because of the cylindrical symmetry of the liner, the

radial compression wave converges earlier at the equator ($z = 0$) than the axial compression wave at the axis ($r = 0$). The compression of the target in CALE is more nearly cylindrical than spherical. This also explains why the target at peak compression appears prolate, as will be seen in Fig. 4. Therefore, the compression wave in CALE is less focused than in HYDRAD, giving rise to smaller average target densities.

Two-dimensional density profiles at peak compression from CALE are shown in Fig. 4. As seen, the lower the initial plasma pressure, the closer the liner gets to the target. This is especially true in cases B-D. The bubbles seen in B-D in the plasma near the equator are most likely caused by the local imbalance of plasma and magnetic pressure, less likely by an instability. Since the magnetic pressure is lowest at the equator ($z=0$), as Eq. (14) shows, the plasma pressure exceeds the magnetic pressure earlier in time than for regions closer to the pole. In case D, a large bubble has been formed in the liner due to early development of high pressure in the plasma. As seen by the contour lines, higher initial plasma pressure results in more nearly adiabatic and uniform target compression. The density gradients for case D are much smaller than those for cases A-C, and the contours are more spherical than cylindrical. Referring back to Fig. 3, the temperature for case D is low, indicating that target compression is more nearly adiabatic.

One-dimensional shock wave motion in the target can be seen in Fig. 5, which shows radial profiles of pressure, density and temperature at different times close to peak compression for case A. Initially, the magnitude of the shock pressure in the target is approximately 5 Mbar, about the same as the plasma pressure. The inertia of the target surface compresses the target interior, until the pressure gets up to 35 Mbar at the center and rebounds. Time histories of the average target pressure, density and temperature from HYDRAD for case A are shown in Fig. 6. The compression process takes about 1 μsec , and the dwell time for which the average target density is above 35 gm/cm^3 is about 500 nsec.

The plasma pressure at peak compression from HYDRAD ranges from 2.17 Mbar to 3.32 Mbar as shown in Table II. The temperature reaches above 100 eV for cases A and B; bremsstrahlung radiation from these hot dense plasmas may have significant influence on compression. For instance, the preheating of the target may reduce shock wave compression in the target. On the other hand, loss of plasma pressure at early times may increase maximum liner inertia, thus causing a high plasma pressure at peak compression. These two competing mechanisms can affect compression in either way.

Table III shows plasma conditions at peak compression from CALE. Plasma pressures are 2-4 Mbar, which are close to HYDRAD values. However, CALE's temperatures are about 1.2 - 1.5 times higher than HYDRAD's. Since thermal conduction is not included in either calculation, this behavior suggests that viscous heating in CALE's plasma is quite significant.

The distribution of energy at peak compression from HYDRAD for all cases is shown in Table IV. The internal energy in solids is defined as the sum of 1) degenerate electron energy (compression energy) 2) ionization energy, and 3) ion thermal energy. The total energy deposited in the system is ≈ 1.2 MJ and is consistent with Eq. (18). The target energy is $\approx 20\%$ of the total energy deposition. Most of the energy is deposited in the liner, and about 30% - 50% of the total energy is in solids in the form of thermal energy. Energy of ≈ 100 to 200 KJ is deposited in the target as degenerate electron energy which is the energy accounted for by compression. Therefore, about 4 % of the capacitor energy is delivered into the target in the form of compression work.

For comparison, the energy distribution in each component from CALE for case A is shown in Table V. The total energy input is around 1 MJ, and $\approx 20\%$ of the total energy input is deposited in the target. Again, this result agrees with HYDRAD.

Table VI lists HYDRAD and CALE results for case A (2 eV, 1×10^{19} cm⁻³ initial plasma conditions.) The time at peak compression is about 13 μ sec for both cases. CALE has a higher local pressure and density, although the average target pressure and density are higher in HYDRAD. The highest pressure in the CALE simulation usually occurs on the z axis, i.e., the center of the compression. CALE's steeper profiles may be due to the smaller radial grid size at the axis, which reveals more detailed structure of local quantities. Therefore, CALE's local pressure appears higher than HYDRAD's. Time histories of pressure, density and temperature from CALE for case A are shown in Fig. 7. The dwell time for the average target density above 35 gm/cm³ is about 400 nsec and consistent with HYDRAD.

B. With Radiation

Spatially averaged target quantities with radiation at peak compression from HYDRAD are shown in Fig. 8. For comparison, results without radiation from HYDRAD are also shown. The average target density increases as the initial plasma pressure decreases, which is similar to the trend seen without radiation. Therefore, a lower initial plasma pressure is more desirable.

The temperature in the target is generally higher with radiation than without radiation, as is the pressure. Target densities are lower in cases A-C and higher in D with radiation than without radiation. This shows that the role of radiation is complex. As discussed earlier, there are two competing mechanisms: 1) preheating of the target and 2) loss of pressure in the hydrogen plasma, affecting target compression. These two mechanisms may lead to changes in target density, in either positive or negative directions. The effect of preheating depends more upon thermal conduction inside the target, while pressure loss depends more upon heat transfer at the boundary surface of the plasma. As the radiation loss in the plasma increases and thermal conduction inside the target remains unchanged, effects from pressure loss in the plasma will dominate over effects from preheating. Since

the pressure loss leads to increased momentum in the liner, the target density is increased at peak compression. This explains why the average target density in case D increases, while the others decrease due to thermal radiation.

Plasma quantities at peak target compression are shown in Fig. 9. As seen, plasma temperatures in all cases are significantly lower with than without radiation. Correspondingly, plasma densities are higher with radiation than without radiation as a result of resisting the inward motion of the liner. Plasma densities in some cases are higher than solid density. However, since the Fermi energy at densities of $\approx 0.1 \text{ gm/cm}^3$ is around 5 eV, which is smaller than the plasma temperature ($\approx 20 \text{ eV}$), use of the Saha equation is well justified.

Figure 10 shows the time history of average target pressure, density and temperature for case A. The histories are similar to results without radiation, despite significant differences in plasma properties when radiation is included. The dwell time for average target density above 35 gm/cm^3 is still about 500 nsec. Because of radiation loss, the liner speed is faster with than without radiation. Peak compression times in all four cases are earlier by tens of nanoseconds due to radiation.

The energy distribution with radiation from HYDRAD is shown in Table VII. Comparing Table VII with Table III, all internal energies in the target are increased to $\approx 320 \text{ KJ}$. The increased energy raises the target temperature, instead of increasing the target density, in cases A-C. The total energy deposited in the system is around 1.25 MJ, which is close to that without radiation.

IV. Summary

In this study, the 1-D hydrodynamics code HYDRAD and the 2-D MHD code CALE are used to simulate compression of a hydrogen working fluid and target. We find that the

1-D and 2-D results without radiation are consistent. Assuming no instability occurs during the compression, 1-D results with radiation show the following:

- a) time for peak compression of a 27 gram gold target is 12.5 μ sec - 13 μ sec,
- b) the dwell time for peak compression is approximately 400 nsec,
- c) average target density (pressure) of about 42 gm/cm³ (12 Mbar), and a maximum local density (pressure) of 60-80 gm/cm³ (40-110 Mbar), can be achieved in the target using 5.3 MJ of energy from SHIVA STAR,
- d) energy of \approx 1 MJ is deposited in the liner, plasma and target, including 200 - 300 KJ in the target,
- e) the plasma temperature at peak compression is consistently around 20 eV,
- f) and to obtain a higher target density, a lower initial plasma pressure is more desirable.

REFERENCES

1. A. E. Sherwood, E. L. Cantvel, C. A. Ekdhal, I. Henins, H. W. Hoiday, T. R. Jarboe, P. L. Klinger, R. C. Malone, J. Marshall, and G. A. Sawyer, *Megagauss Physics and Technology*, edited by P. J. Turchi (Plenum Press, New York, 1980), p. 375.
2. P. J. Turchi, A. L. Cooper, R. D. Ford, D. J. Jenkins, and R. L. Burton, in *Megagauss Physics and Technology*, edited by P. J. Turchi (Plenum Press, New York, 1985), p. 375.
3. S. G. Alikhanov, V. P. Bakhtin, and D. A. Toporkov, in *Ultrahigh Magnetic Fields-Physics, Techniques, Applications*, edited by V. M. Totov and G.A. Shvetsov (Moscow Nauka, 1984), p. 213.
4. A. G. Eskov, M. I. Kitayev, and R. Kh. Kurtmullayev, in *Ultrahigh Magnetic Fields-Physics, Techniques, Applications, V.* edited by V. M. Totov and G.A. Shvetsov (Moscow Nauka, 1984), p. 204.
5. A. A. Petrukhin, N. P. Bidlyo, S. F. Garanin, V. M. Danov, V. V. Zmushko, A. I. Kuzyaev, V. N. Mokhov, E. S. Pavlovskii, V. A. Prokopov, V. K. Chernyshev, V. A. Shvetsov, and V. B. Yakubov, in *Ultrahigh Magnetic Fields-Physics, Techniques, Applications*, edited by V. M. Totov and G.A. Shvetsov (Moscow Nauka, 1984), p. 406.
6. J. H. Degnan, M. L. Alme, W. L. Baker, J. S. Buff, C. B. Boyer, C. J. Clouse, S. K. Coffey, D. W. Conley, D. Dietz, J. D. Graham, S. L. Gonzalez, K. E. Hackett, D. J. Hall, J. L. Holmes, E. A. Lopez, W. F. McCullough, D. W. Price, R. E. Reinovsky, N. F. Roderick, P. J. Turchi, and J. M. Welby, in *Megagauss*

- Technology and Pulsed Power Applications*, edited by C. M. Fowler, R. S. Caird, and E. J. Erickson (Plenum Press, New York, 1987), p. 699-706.
7. J. H. Degnan, W. L. Baker, J. D. Beason, C. J. Clouse, D. Dietz, D. J. Hall, J. L. Holmes, D. W. Price, and C. R. Sovinec, in *Megagauss Technology and Pulsed Power Applications*, edited by V. M. Titov and C. A. Shvetsov (Plenum Press, New York, 1990), p. 623-630.
 8. N. A. Krall and A. W. Trivelpiece, *Principles of Plasma Physics*, (McGraw Hill, New York, 1973).
 9. B. Chen, T. A. Armstrong, R. A. Lewis, R. Newton, G. A. Smith, J. P. Bocquet, F. Malek, H. Nifenecker, M. Maurel, E. Monnard, P. Perrin and C. Ristori, G. Ericsson, T. Johansson, G. Tibell, M. Rey-Campagnolle, S. Polikanov, T. Krogulski and J. Mougey, *Phys. Rev. C* **45**, 2332 (1992).
 10. E. D. Minor, T. A. Armstrong, R. Bishop, V. Harris, R. A. Lewis, G. A. Smith, *Z. Phys. A* **336**, 461 (1990).
 11. R. A. Lewis, G. A. Smith, R. J. Kanzleiter, K. I. Higman and R. Newton, *Fusion Tech.* **20**, No. 4, Part 2, 1046 (1991).
 12. R. A. Lewis, R. Newton, G. A. Smith and R. J. Kanzleiter, *Nuc. Sci. Eng.* **109**, 411(1991).
 13. P-R. Chiang, 'HYDRAD - One-Dimensional Radiative Hydrodynamics Code,' Laboratory for Elementary Particle Science, The Pennsylvania State University, 1993 (unpublished).
 14. CALE users manual, July 1, 1991, R. Tipton, LLNL, Mail Stop L-35, P.O. Box 808 Livermore, LA 94550.

15. F. M. Lehr, A. Alaniz, J. D. Beason, L. C. Carswell, J. H. Degnan, J. F. Crawford, S. E. Englert, T. J. Englert, J. M. Gahl, J. H. Holmes, T. W. Hussey, G. F. Kiuttu, B. W. Mullins, R. E. Peterkin, Jr., N. F. Roderick, P. J. Turchi, and J. D. Graham, ' Formation of Plasma Working Fluid for Compression by Liner Implosions, ' submitted to *Journal of Applied Physics*.
16. F. M. Lehr, J. H. Degnan, D. Dietz, S. E. Englert, T. J. Englert, T. W. Hussey, G. F. Kiuttu, J. M. Messerschmitt, B. W. Mullins, C. A. Outten, R. E. Peterkin, Jr., N. F. Roderick, P. J. Turchi, and J. D. Graham, 9-th IEEE Pulsed Power Conference, June 6-10, 1993.
17. Ya. B. Zeldovich and Yu. P. Raizer, *Physics of Shock Waves and Temperature Hydrodynamic Phenomenon* (Academic Press, New York, 1966).
18. P. Collela and P. R. Woodard, *J. Comp. Phys.* **54**, 174 (1984).
19. P. R. Woodard and P. Collela, *J. Comp. Phys.* **54**, 115 (1984).
20. T. Tajima, *Computational Plasma Physics: With Applications to Fusion and Astrophysics* (Addison-Wesley, New York, 1989).
21. N. A. Tahir and K. A. Long, *Laser and Particle Beams* **4**, 287 (1986).
22. J. P. Christiansen, D. E. T. F. Ashby and K. V. Roberts, *Comp. Phys. Comm.* **7**, 271 (1974).
23. S. P. Lyon and J. D. Johnson, LA-UR-92-3407 (1992).
24. J. A. Bittencourt, *Fundamentals of Plasma Physics*, (Pergamon Press, New York, 1988).

Table I. Initial plasma conditions for simulations. All cases have a 27 gram gold target at the center, and the liner and target are initially at room temperature.

Case	Density	Temperature (eV)	Pressure (bar)
A	10^{19} cm^{-3} ($1.67 \times 10^{-5} \text{ g/cm}^3$)	2	71
B	10^{19} cm^{-3} ($1.67 \times 10^{-5} \text{ g/cm}^3$)	5	161
C	$6 \times 10^{19} \text{ cm}^{-3}$ ($1 \times 10^{-4} \text{ g/cm}^3$)	2	256
D	$6 \times 10^{19} \text{ cm}^{-3}$ ($1 \times 10^{-4} \text{ g/cm}^3$)	5	952

Table II. Plasma conditions at peak compression from HYDRAD without radiation.

Case	Plasma pressure (Mbar)	Plasma temperature (eV)	Plasma density (gm/cm³)
A	3.32	138	0.0125
B	3.11	263	0.00613
C	2.91	57	0.0266
D	2.17	110	0.0102

Table III. Plasma conditions at peak compression from CALE.

Case	Plasma pressure (Mbar)	Plasma temperature (eV)	Plasma density (gm/cm ³)
A	3.7	220	0.009
B	2.7	350	0.0040
C	2.4	76	0.0332
D	1.4	128	0.0057

Table IV. Energy distribution in the system at peak compression from HYDRAD without radiation.

	Case A	Case B	Case C	Case D
Internal energy in target	290 KJ	248 KJ	222 KJ	121 KJ
Internal energy in plasma	124 KJ	238 KJ	306 KJ	597 KJ
Internal energy in liner	780 KJ	709 KJ	657 KJ	399 KJ
Kinetic energy in target	3 KJ	3 KJ	2 KJ	1 KJ
Kinetic energy in plasma	≈0.04 J	0.2 J	24 J	9 J
Kinetic energy in liner	51 KJ	56 KJ	66 KJ	100 KJ
Total energy	1.25 MJ	1.25 MJ	1.25 MJ	1.22 MJ

Table V. Energy distribution in the system at peak compression from CALE.

	Case A	Case B	Case C	Case D
Internal energy in target*	221 KJ	192 KJ	206 KJ	89 KJ
Internal energy in plasma	114 KJ	243 KJ	149 KJ	368 KJ
Internal energy in liner*	616 KJ	486 KJ	591 KJ	358 KJ
Kinetic energy in target	13 KJ	2 KJ	11 KJ	1 KJ
Kinetic energy in plasma	2 J	3 J	11 J	300 J
Kinetic energy in liner	38 KJ	35 KJ	50 KJ	79 KJ
Total energy	1002 KJ	958 KJ	1017 KJ	895 KJ

* The energy of degenerate electrons has been estimated by using the cold-temperature EOS from the TFC model and included in the internal energy.

Table VI. Comparison between HYDRAD and CALE'compression for case A.

Parameters	HYDRAD	CALE
Initial plasma conditions	2 eV, $1 \times 10^{19} \text{ cm}^{-3}$	2 eV, $1 \times 10^{19} \text{ cm}^{-3}$
Target	27 gm Au	27 gm Au
Initial target radius	0.783 cm	0.682 cm
Maximum current	= 16 MA	= 16 MA
Peak compression time	12.81 μsec	12.99 μsec
Plasma P at peak	= 3.3 Mbar	= 3.6 Mbar
Plasma T at peak	= 135 eV	= 221 eV
Maximum target P at peak	= 34 Mbar	= 147 Mbar
Maximum target ρ at peak	= 60 gm/cm^3	= 94 gm/cm^3
Maximum target T at peak	= 4.8 eV	= 11.8 eV
Average target P at peak	= 11.3 Mbar	= 10 Mbar
Average target ρ at peak	= 43 gm/cm^3	= 40 gm/cm^3
Average target T at peak	= 2.2 eV	= 1.7 eV
Average liner ρ at peak	= 6.0 gm/cm^3	= 4.2 gm/cm^3
Average liner T at peak	= 0.3 eV	< 1 eV

Table VII. Energy distribution in the system at peak compression from HYDRAD with radiation.

	Case A	Case B	Case C	Case D
Internal energy in target	344 KJ	342 KJ	322 KJ	320 KJ
Internal energy in plasma	18 KJ	18 KJ	144 KJ	147 KJ
Internal energy in liner	834 KJ	841 KJ	730 KJ	726 KJ
Kinetic energy in target	4 KJ	4 KJ	3 KJ	2 KJ
Kinetic energy in plasma	-0.005 J	0.02 J	0.32 J	42 J
Kinetic energy in liner	49 KJ	46 KJ	54 KJ	63 KJ
Total energy	1.25 MJ	1.25 MJ	1.25 MJ	1.26 MJ

LIST OF FIGURES

- Fig. 1. Schematic of spherical solid liner at Shiva Star.
- Fig. 2. Schematic of system geometry in one dimensional simulation of compression.
- Fig. 3. Average target pressure, density and temperature at peak compression vs. initial plasma pressure from HYDRAD.
- Fig. 4. System geometries and density contours in the target at peak compression for cases A-D (see Table I) from CALE.
- Fig. 5. Radial profiles of pressure, density, and temperature at different times close to the peak compression from HYDRAD for case A.
- Fig. 6. Time history of average pressure, density, and temperature in the target from HYDRAD without radiation for case A.
- Fig. 7. Time history of average pressure, density, and temperature in the target from CALE without radiation for case A.
- Fig. 8. Average target pressure, density and temperature at peak compression vs. initial plasma pressure from HYDRAD with and without radiation.
- Fig. 9. Average plasma pressure, density and temperature at peak compression vs. initial plasma pressure from HYDRAD with and without radiation.
- Fig. 10. Time history of average pressure, density, and temperature in the target from HYDRAD with radiation for case A.

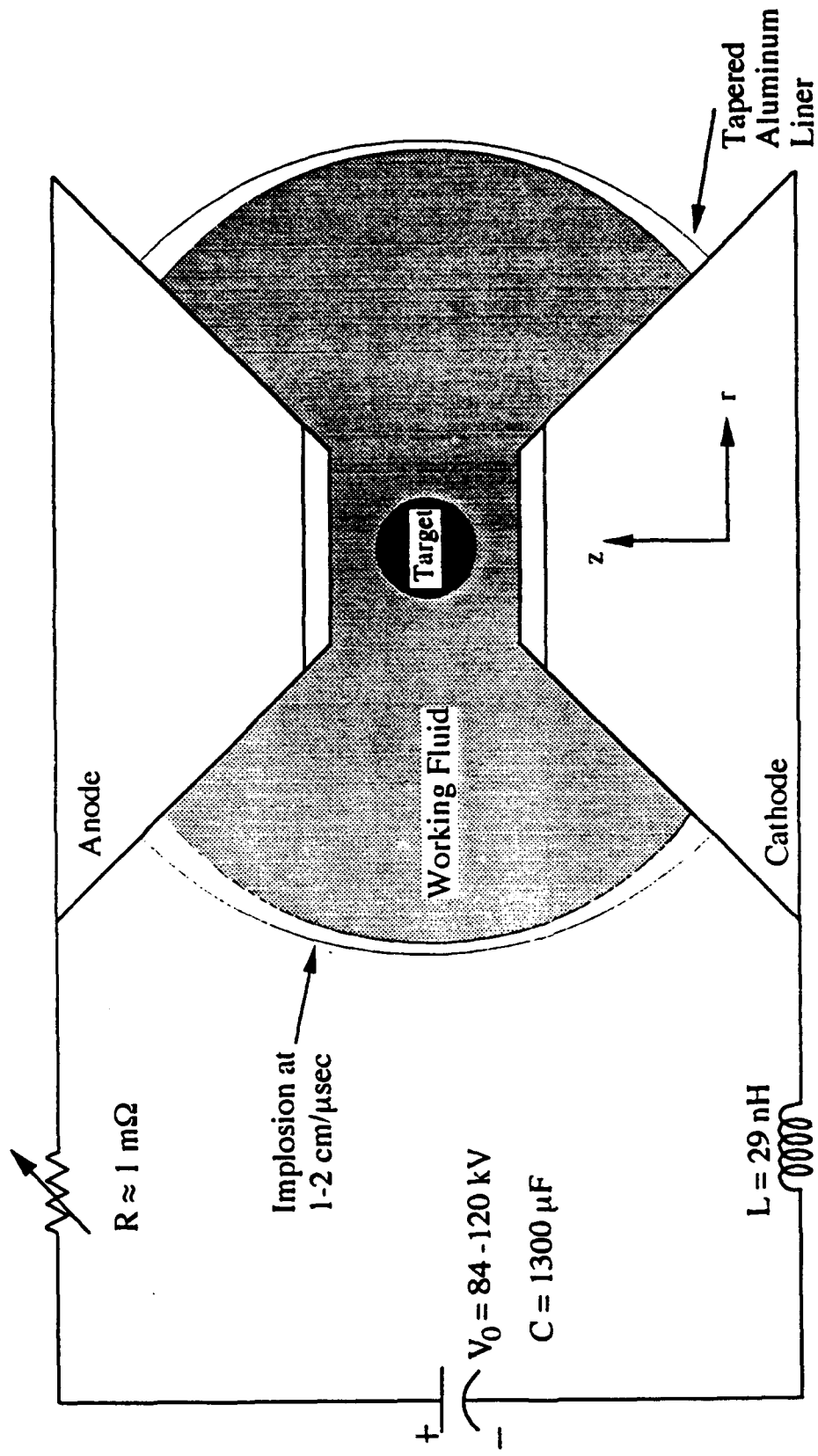


Fig. 1.

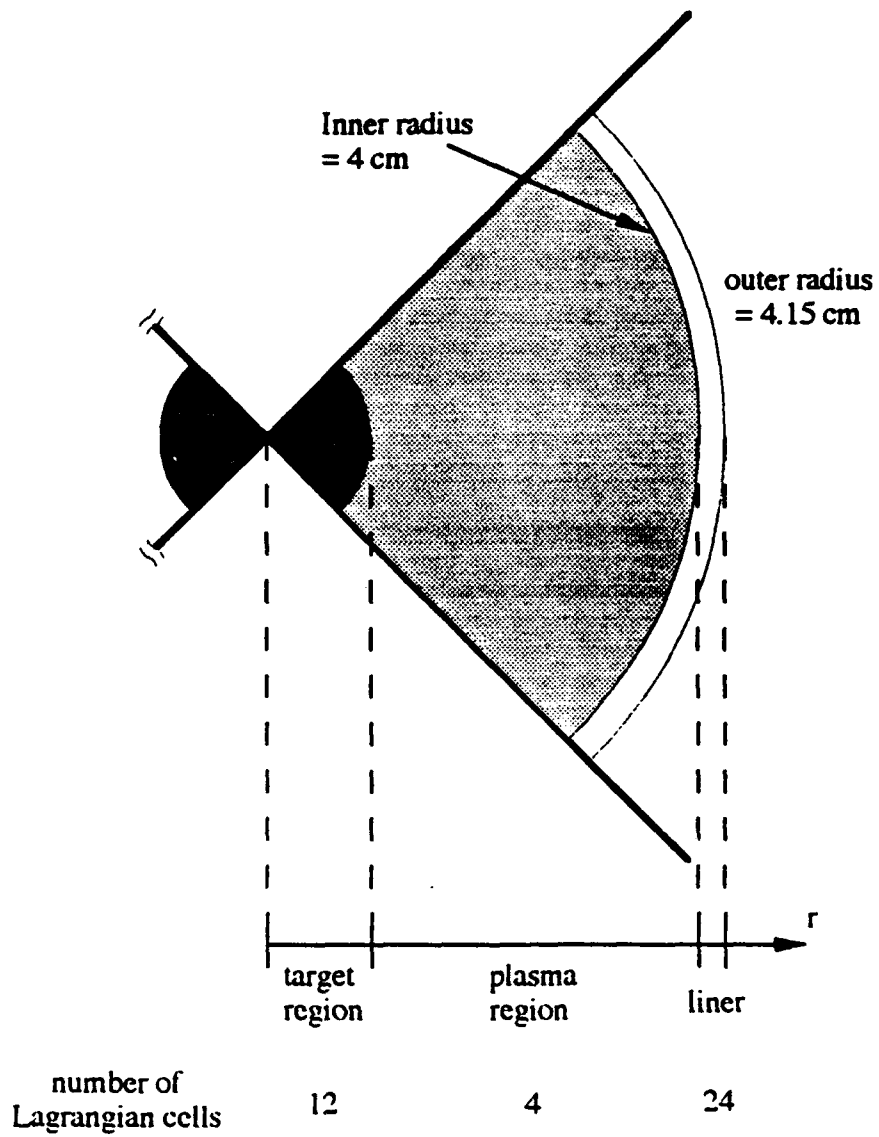


Fig. 2.

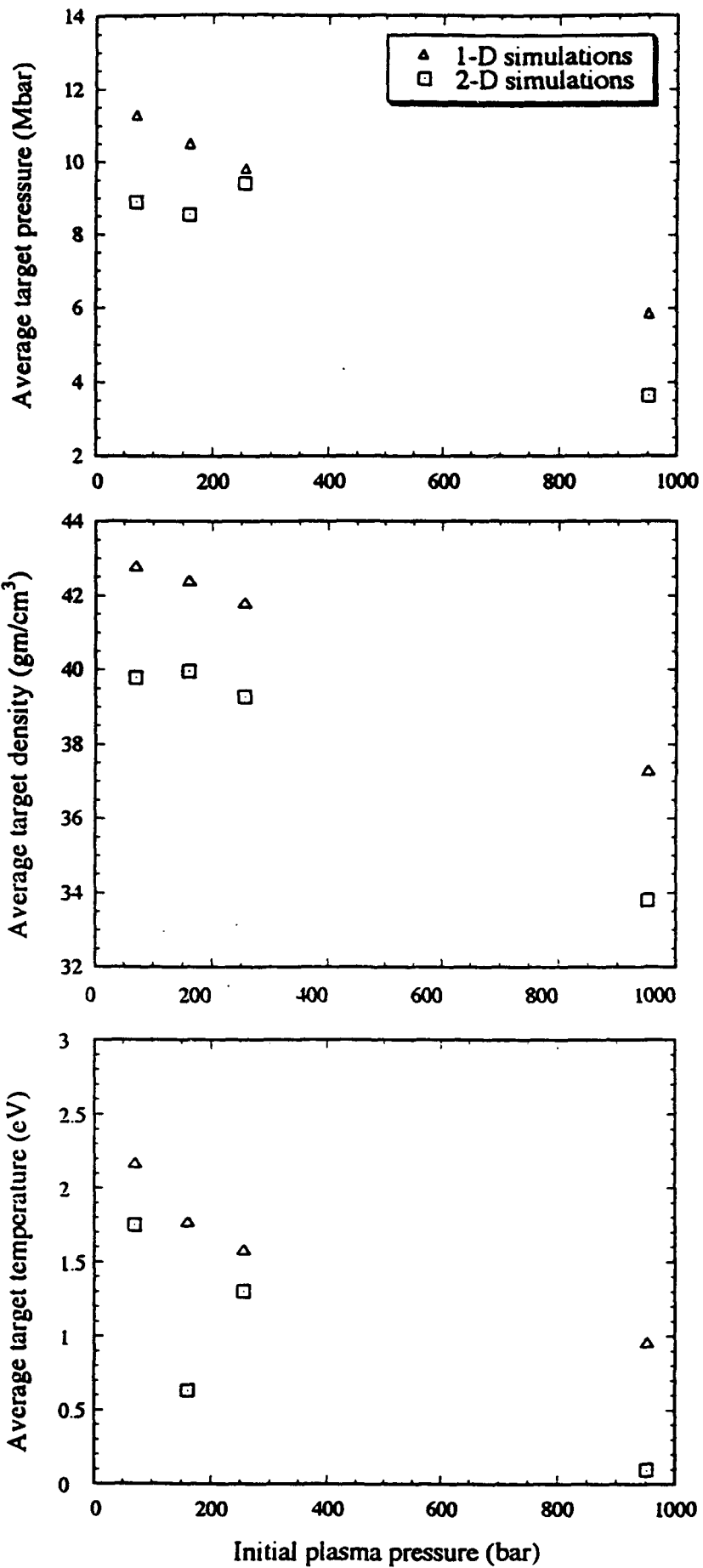
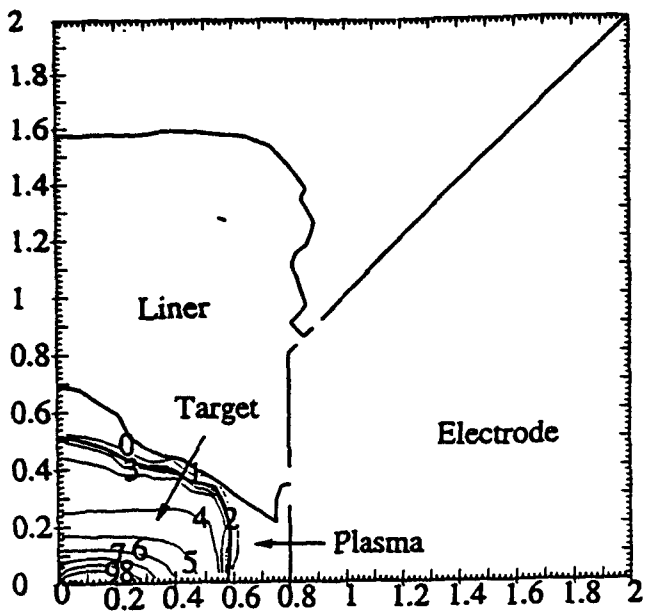
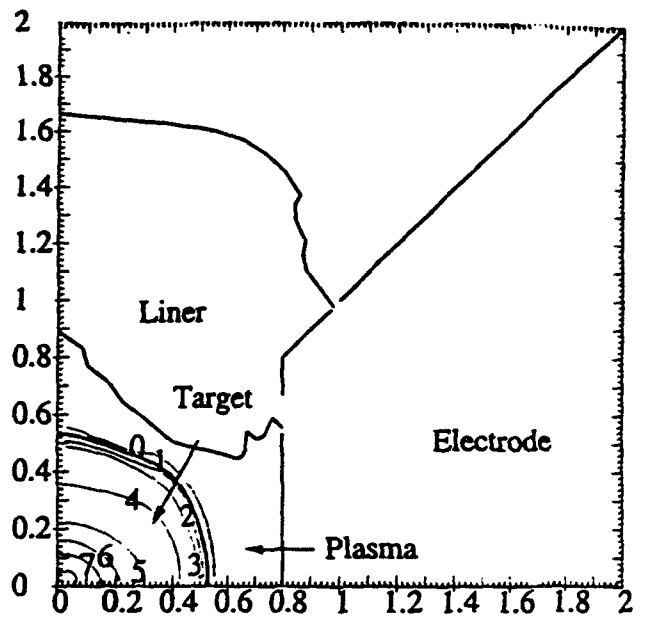


Fig. 3

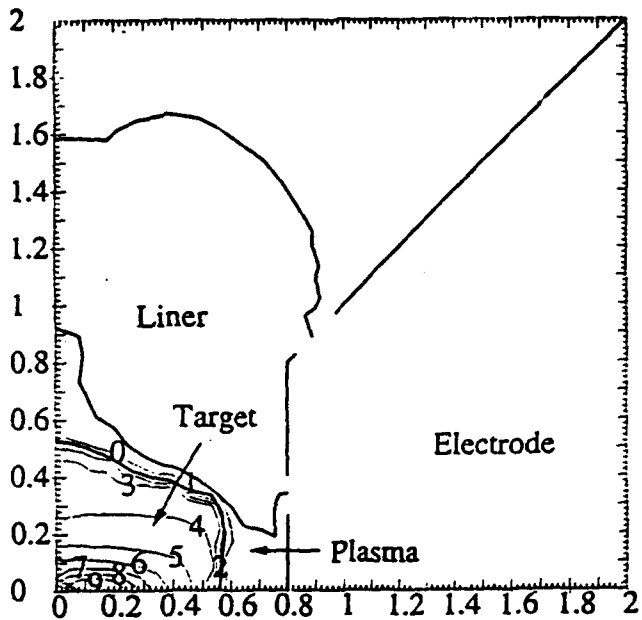
Case A



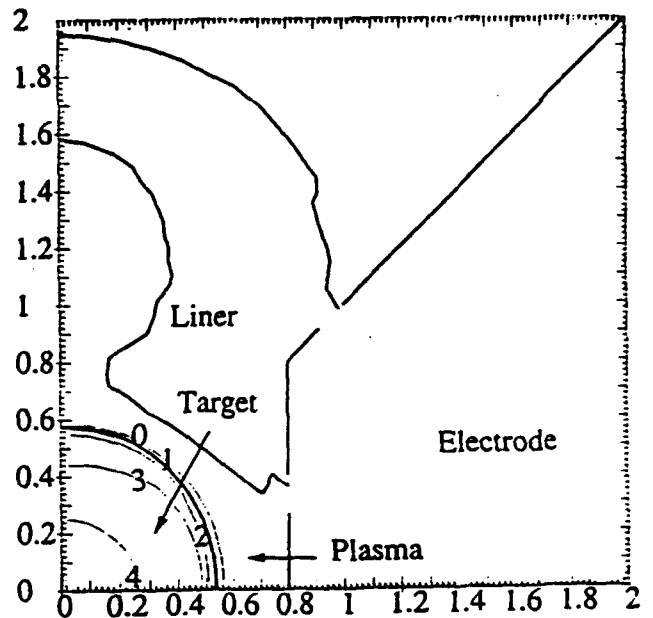
Case C



Case B



Case D



r (cm)
 z (cm)

Contour	Density (gm/cm^3)
0	8.0
1	16.0
2	24.0
3	32.0
4	40.0
5	48.0
6	56.0
7	64.0
8	72.0
9	80.0

Fig. 4

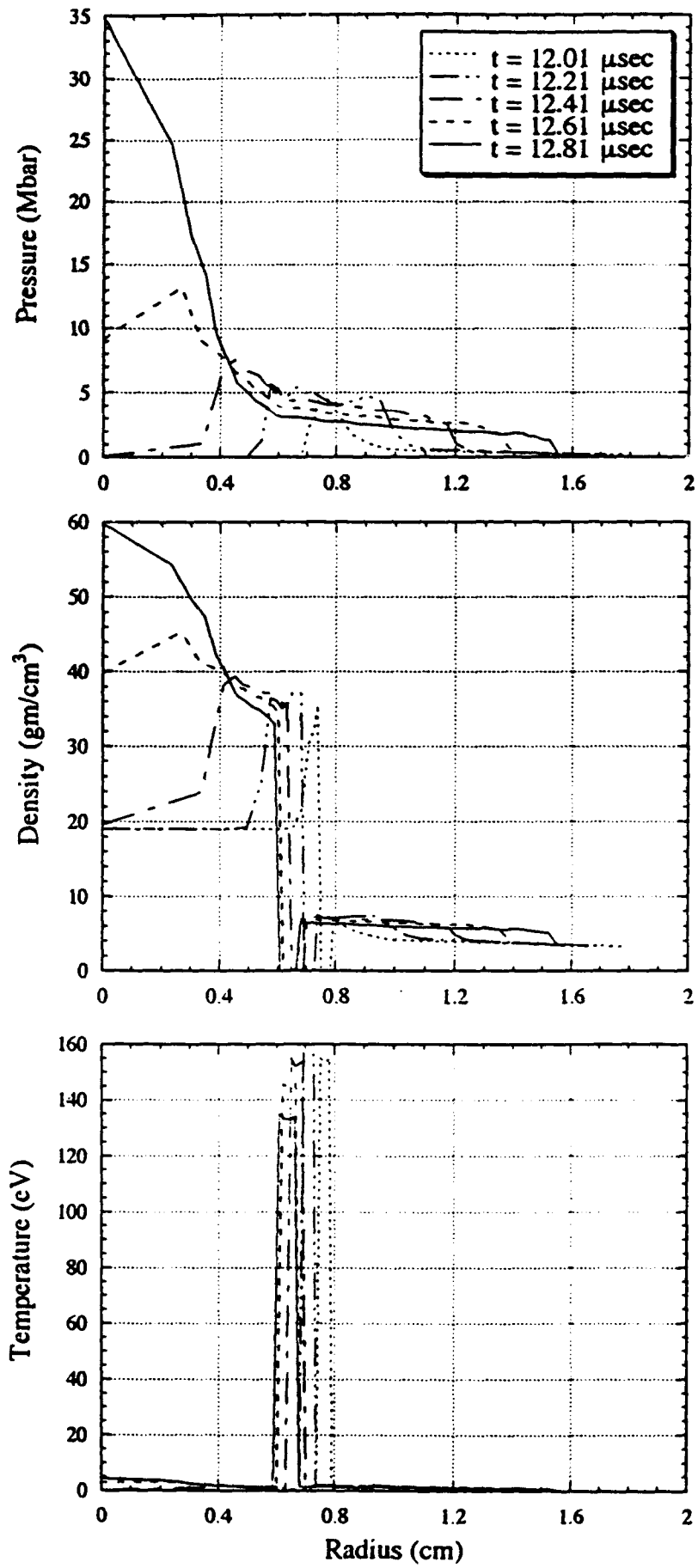
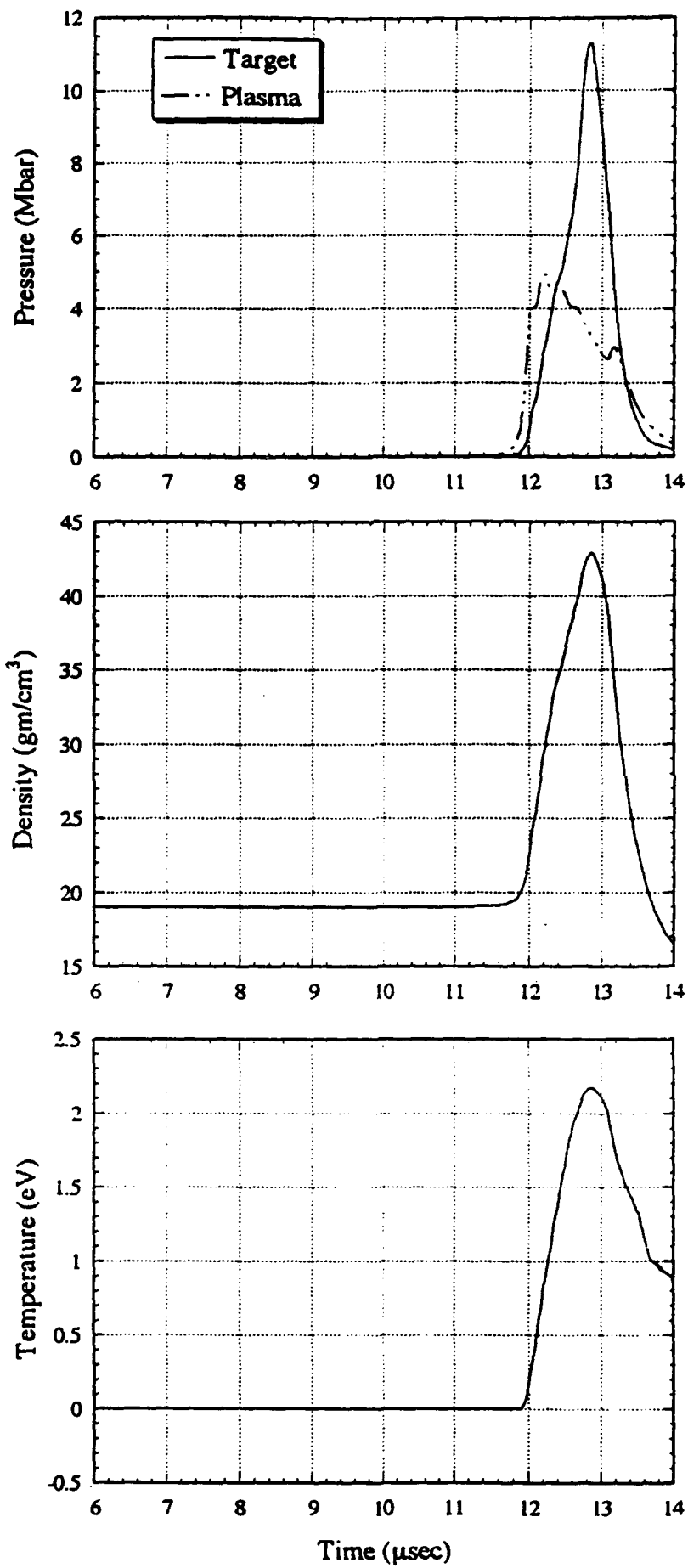


Fig. 5



Time (μsec)

Fig. 6

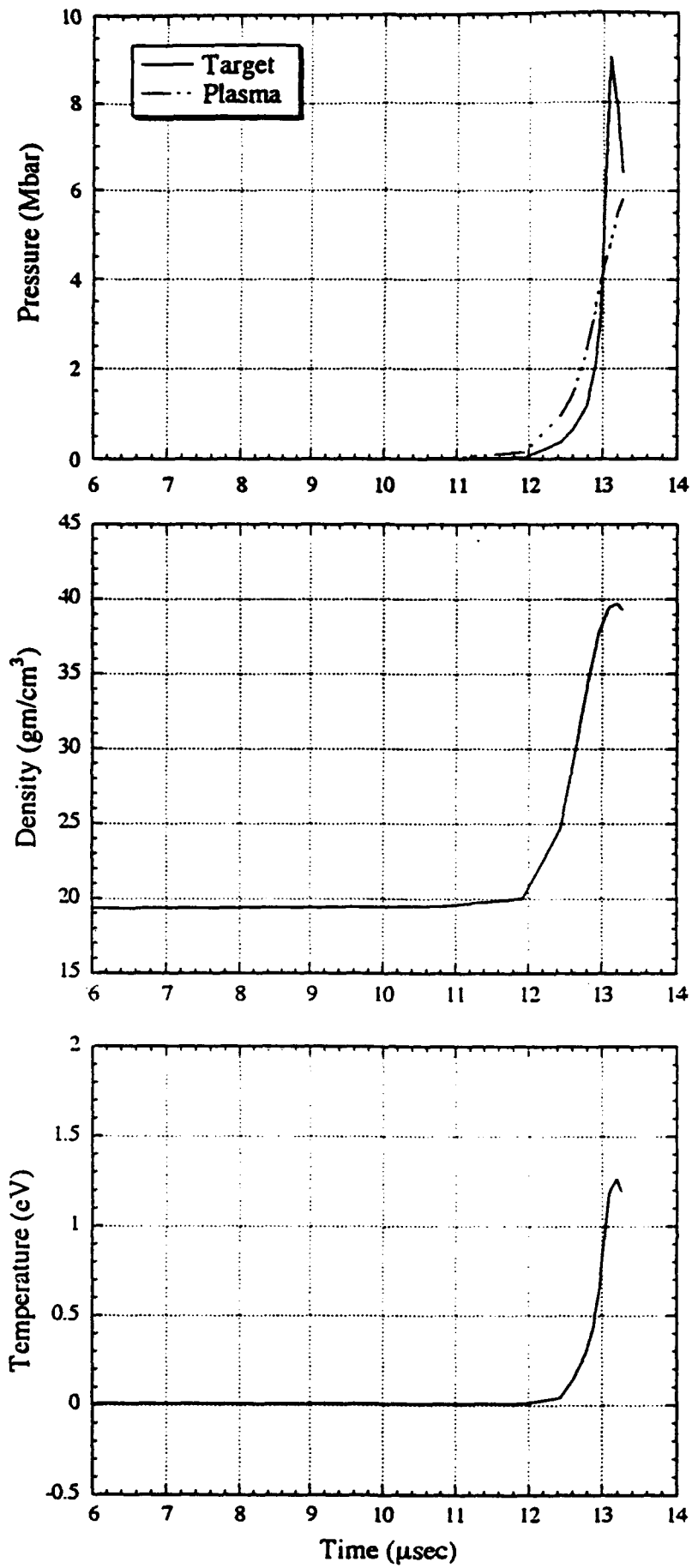


Fig. 7

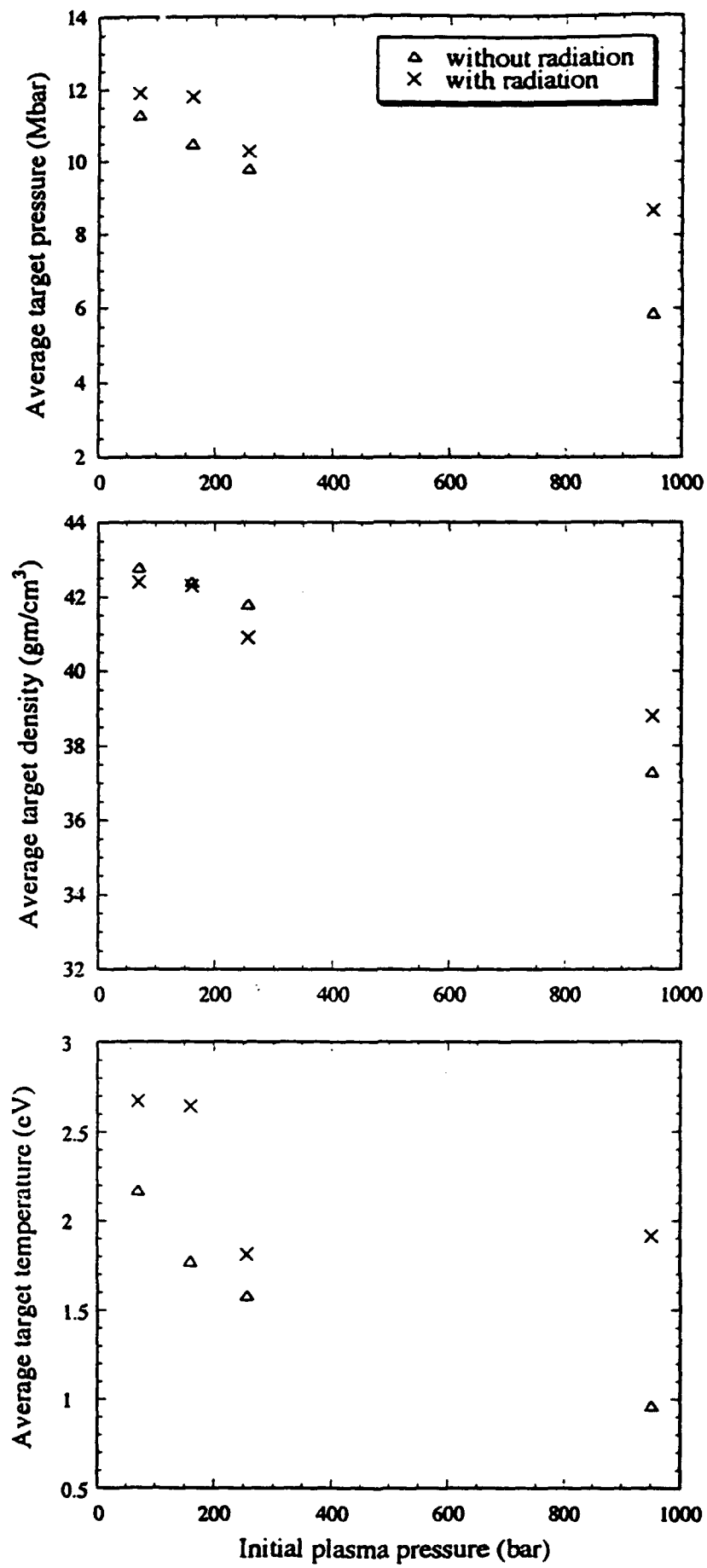


Fig. 8

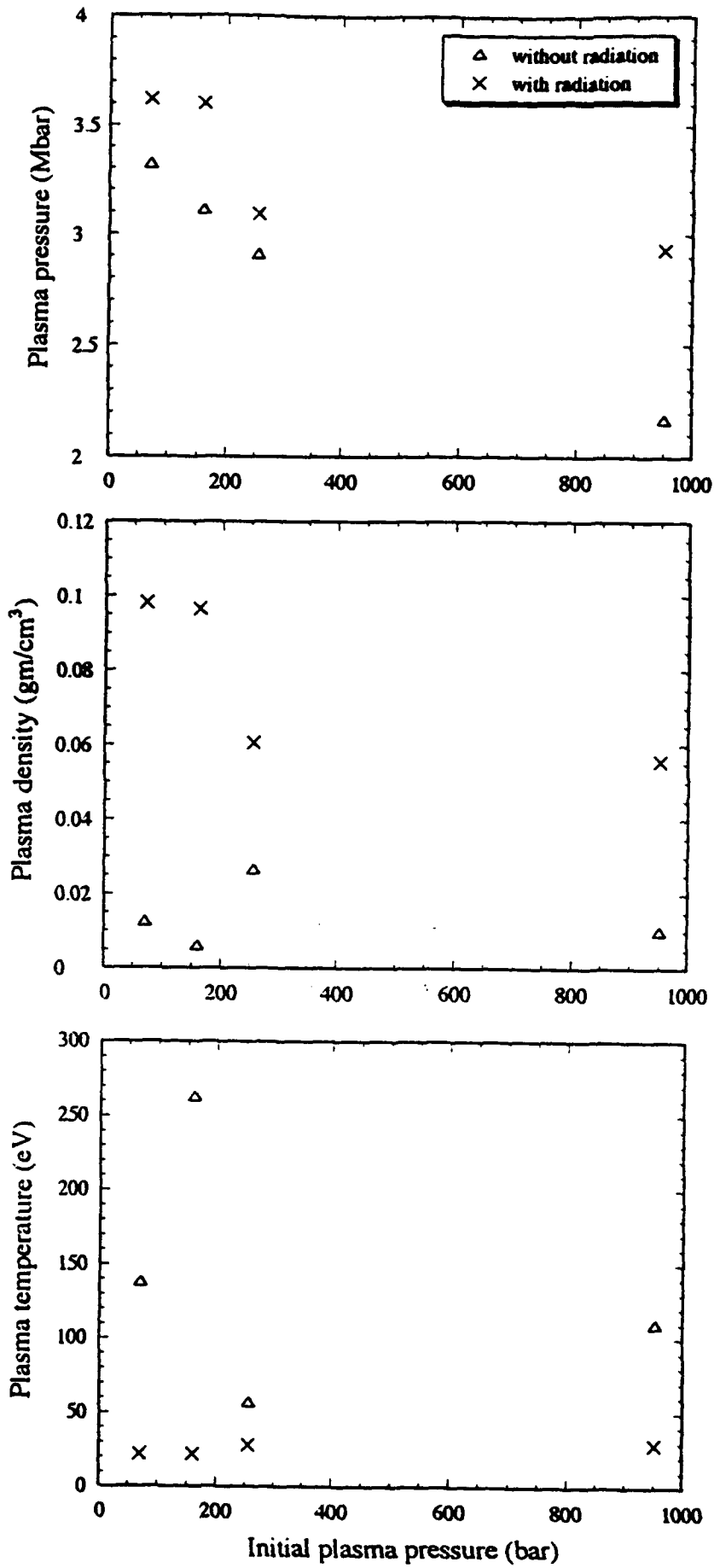


Fig. 9

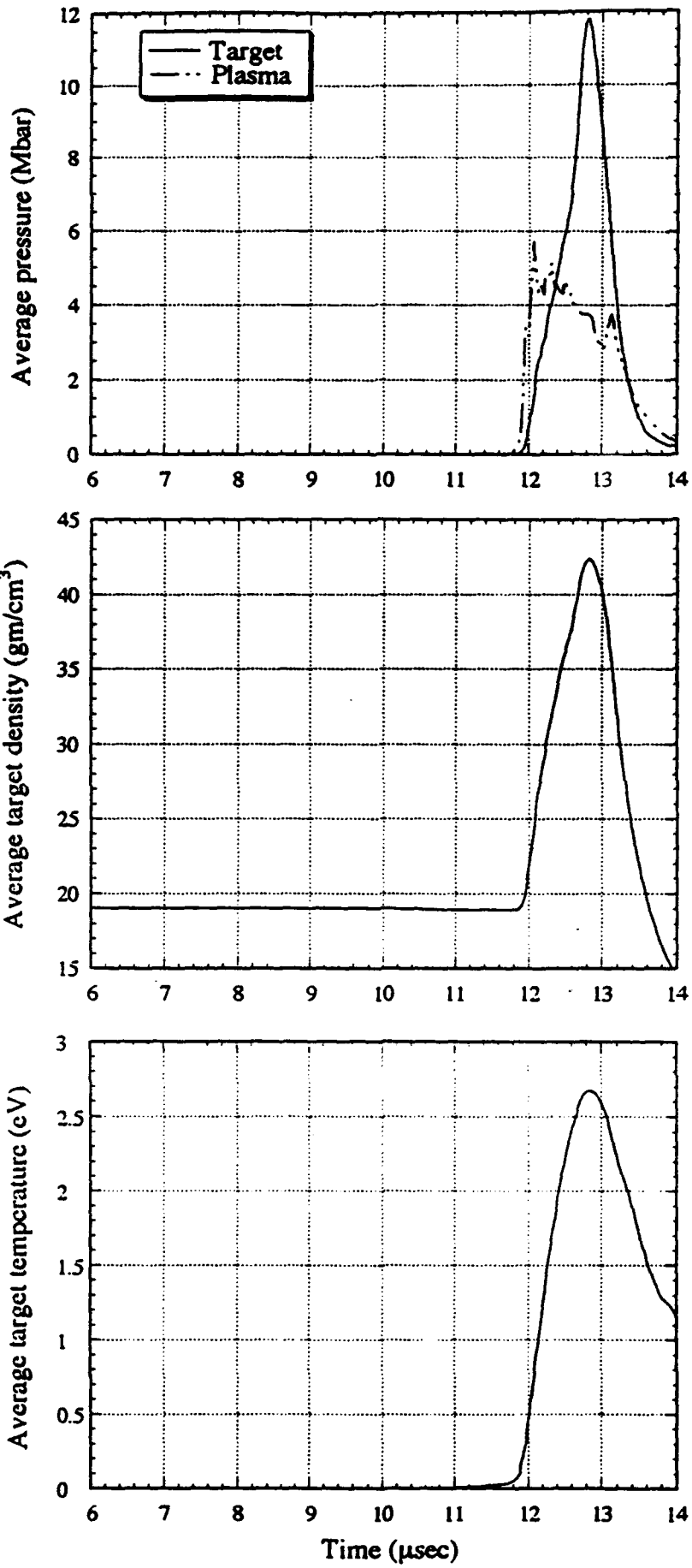


Fig. 10

APPENDIX V



High energy density
imploding liner
experiments



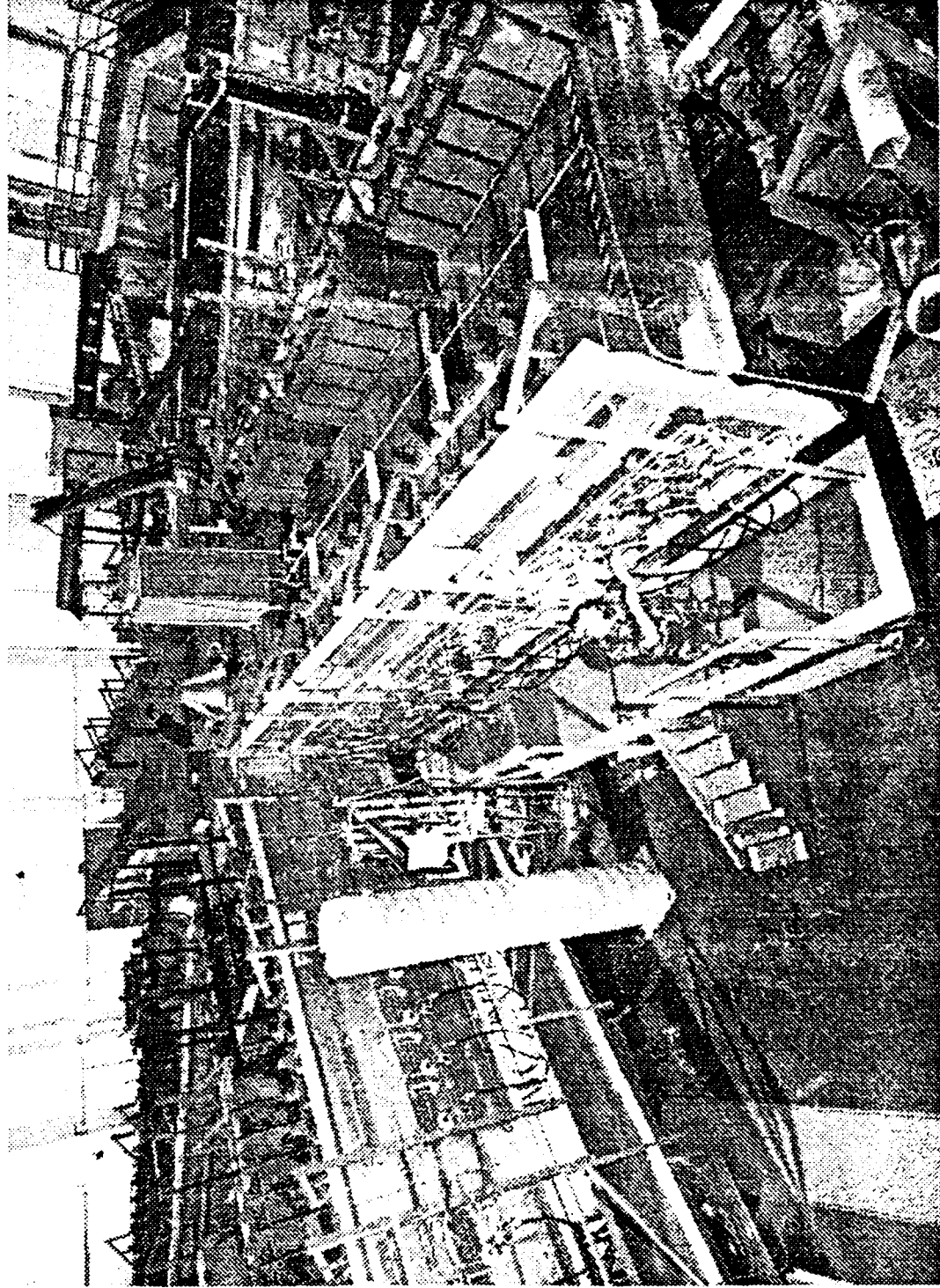
ADVANCED WEAPONS CONCEPTS FOR THE 21ST CENTURY

- Counter-orbital velocity projectiles
- Antiproton-catalyzed microfission
- Magnetized target fusion
- Advanced materials and manufacturing

For more information contact:
Phillips Laboratory, High Energy Plasma Division
(505) 846-5073 DSN 246-5073



Shiva Star Fast Capacitor Bank Delivers 3 Trillion Watts of Power

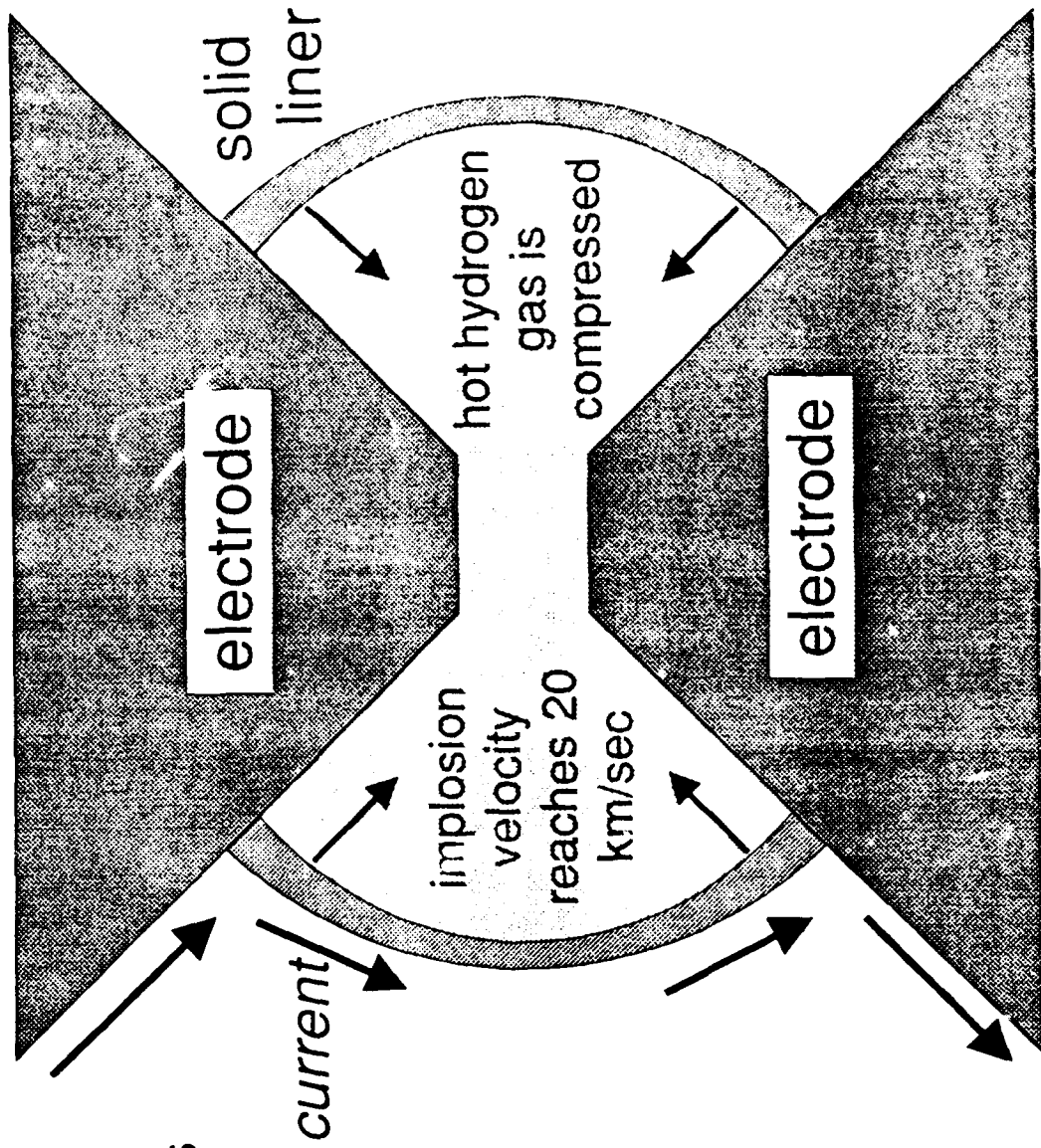




The electrical discharge from Shiva Star implodes the liner.

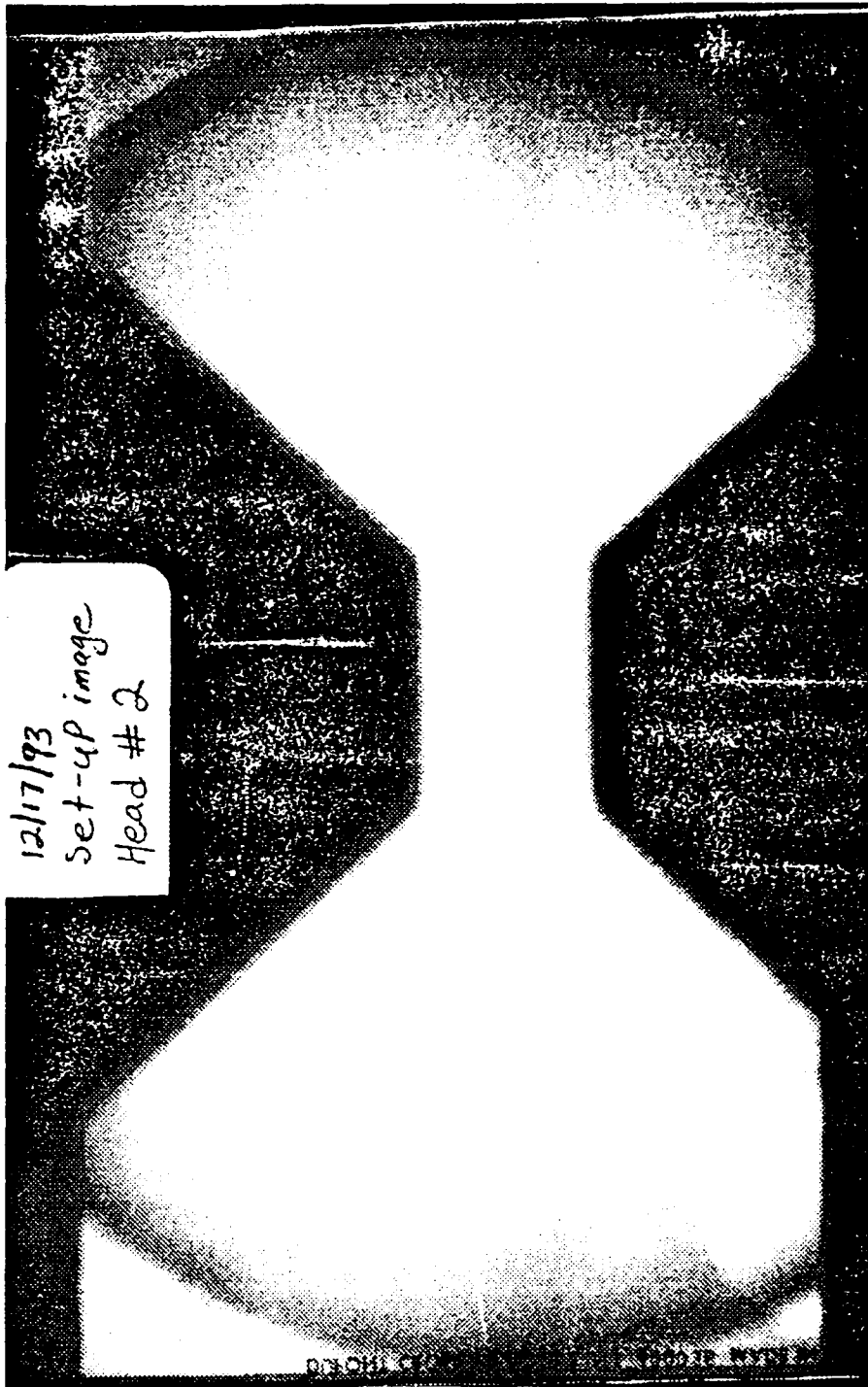
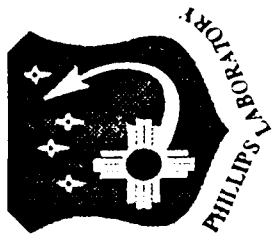


- 14 million Amperes of current flows through the liner for 10 millionths of a second.
- This is the electrical equivalent of two pounds of TNT!
- The inner surface of the imploding sphere reaches 20 km/sec.
- The pressure inside the sphere briefly exceeds 10 million atmospheres.

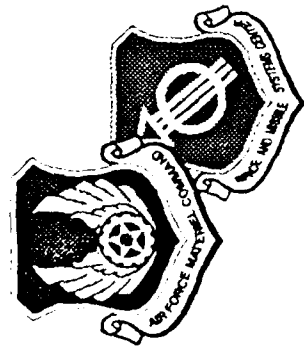




Quasi-Spherical Solid Liner Implosion X-ray Radiograph



Setup picture shows enlargement of liner mounted between electrodes.



Quasi-Spherical Solid Liner Implosion X-ray Radiograph



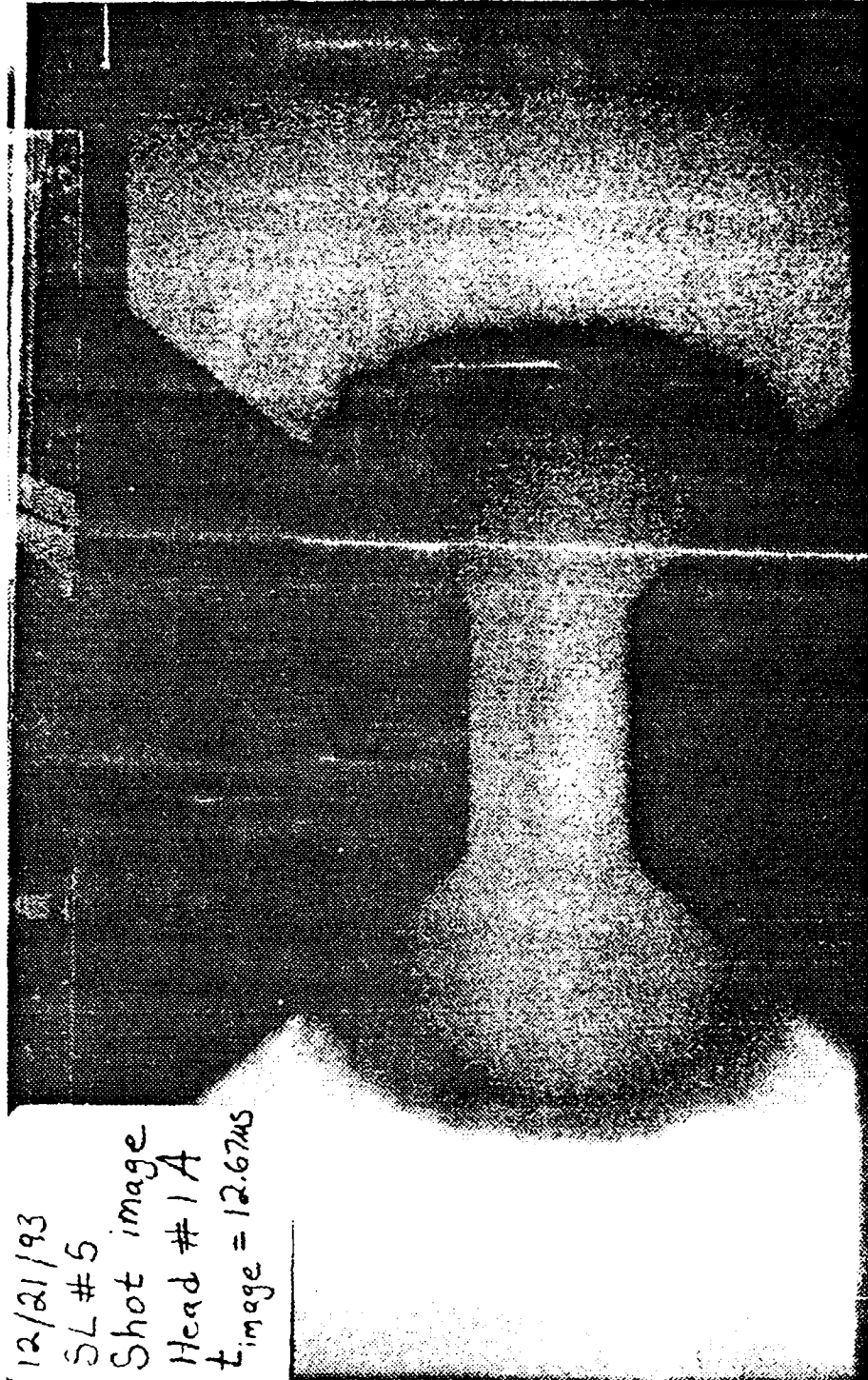
12/21/93

SL # 5

Shot image

Head # 1 A

$t_{\text{image}} = 12.67 \mu\text{s}$



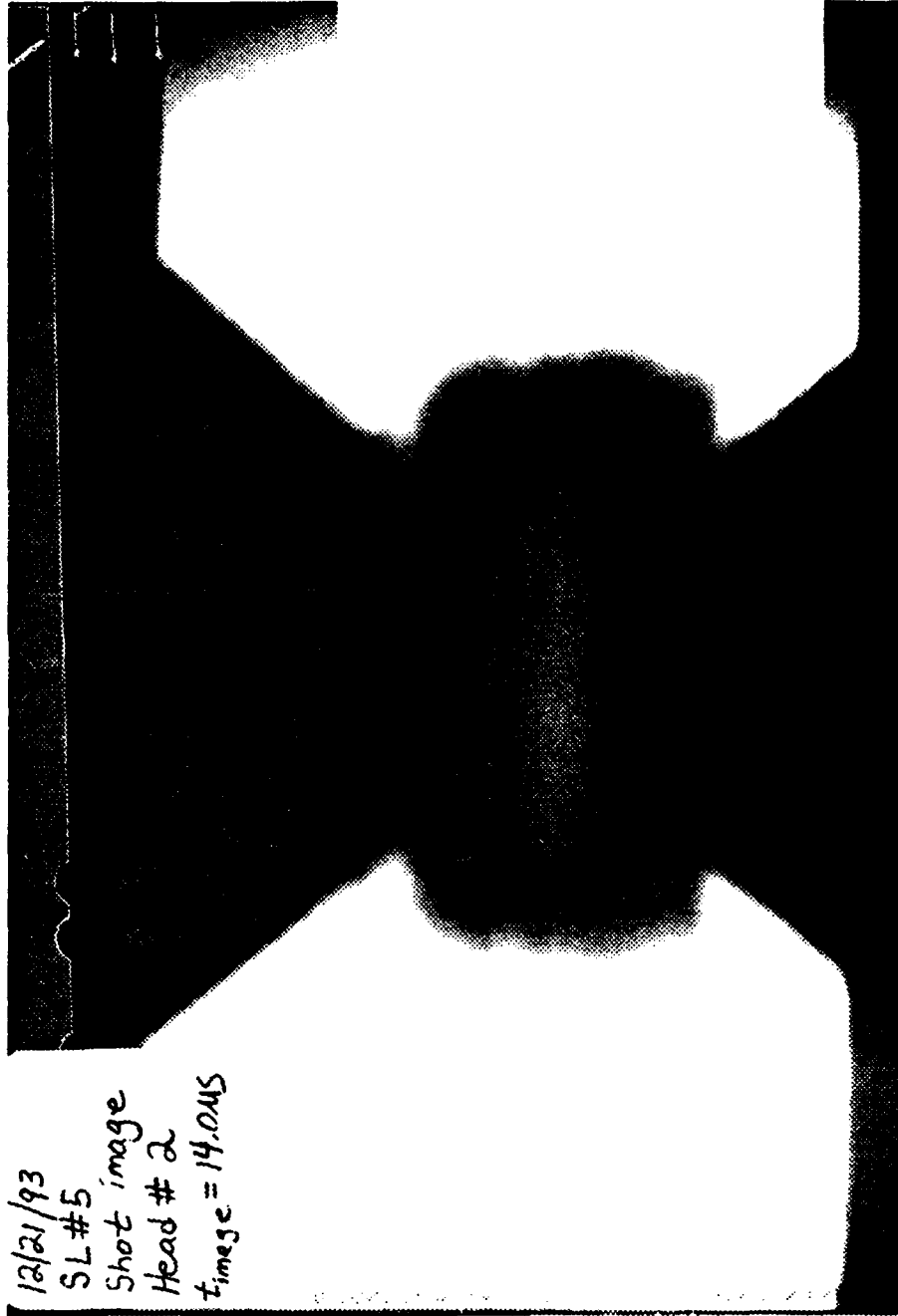
Picture at 12.7 microseconds showing nearly perfect symmetry in the implosion.



Quasi-Spherical Solid Liner Implosion X-ray Radiograph



12/21/93
SL#5
Shot image
Head # 2
time = 14.045



Picture at 14.0 microseconds showing good symmetry at high compression.

APPENDIX VI



October 15, 1993

Accelerator Technology

Dr. Gerald Smith
Pennsylvania State University
303 Osmond Laboratory
University Park, PA 16802-6310

Dear Gerry,

Enclosed is the summary report for the RFQ TEST, Penn State University contract number 146822D. I apologize for not sending the updated report to you any earlier. I think we have cleared up the issues raised during the review meeting held on August 30, 1993 here in San Diego.

I have included an IBM formatted disk which contains the actual emittance data converted to a text format. I have also taken these same files and converted them to WordPerfect files and given them extensions of "wp" if the text files do not work for you. These contain the same data the binary files that you received while you were here for the review meeting. I have attached an explanation of the structure of these data files. If you have any questions please call me.

I have given you copies of all of the drawings created for this project and the previous project, RFQ preparation. I have looked at the list of drawings you already have at the Phillips laboratory and found no additional drawings here at SAIC. I am going to assume that the shipment of any hardware will be worked out along with the shipment of other "AFWL" equipment presently at SAIC.

I am not aware of any outstanding requirements of this contract and believe that it is complete. Thank You for the opportunity to support your program. If we can be of further assistance please let us know. Sincerely,

SCIENCE APPLICATIONS
INTERNATIONAL CORPORATION

Steven J. Ringler
Mechanical Engineer
Principal Investigator

encl.: 1. Summary Report
2. E-scanner data reference
3. Floppy disk

cc: Phil Young: SAIC; w/ encl. 1., 2.
Michael Flumian: SAIC; w/ encl. 1., 2.

**Science Application International Corporation
Accelerator Technology Division**

Emittance Scanner Reference Information

Steven J. Ringler 10/93

The SAIC emittance scanner is a slit and collector emittance scanner. The scanner assembly consists of a small horizontal slit at the front with 32 horizontal collector wires approximately 6 inches behind the slit. The scanner assembly is stepped through the beam (51 steps) and data is obtained which indicates the relative magnitude of the current passing through the slit as well as the angular spread of the beam. The data is arranged in a 51 X 51 array. Each cell in the array contains three values; DATA, X-VALUE, and Y-VALUE. A data conversion program was used to take this binary data and write it to an ASCII file for use with data manipulation routines. The following information describes the physical meaning of each data value of the ASCII files.

- DATA** The relative current that is collected on a wire. It is useful only for comparison to the other values. In other words, the data value is not a calibrated measurement and the number represents a magnitude of current relative to the other DATA values.
- X-VALUE** The position of the scanner (in inches) at the time the DATA value is collected. The difference between two adjacent X-VALUE's represents the step size of each of the 51 steps taken during the run.
- Y-VALUE** The angle (mrad) that the DATA value is registered. This identifies the wire that the beam is collected on. The angle has been computed by the conversion program based on the physical dimensions of the collector assembly.
- IX** The column number of the array where the data resides. This represents the position of the emittance scanner for a collection cycle. Each emittance scanner run consists of 51 steps or collection cycles
- IY** The row number of the array where the data resides. This represents the angle(s) of the beam for the portion of the beam passing through the slit at position IX. Note that since there are only 32 collector wires on the scanner assembly the 51 x 51 array is not completely filled.

Penn State University Contract Number 146822D

**Radio Frequency
Quadrupole Test
Summary Report**

October 12, 1993

Prepared by:

SCIENCE APPLICATIONS INTERNATIONAL CORPORATION
Accelerator Technology Division

Steven J. Ringler
Wayne D. Cornelius

Approved by:


Division Manager

Submitted to:

PENNSYLVANIA STATE UNIVERSITY
Dr. Gerald A. Smith
303 Osmond Laboratory
University Park PA 16802-6310

TABLE OF CONTENTS

Abstract.....	1
1. RF Power System Preparation.....	2
1.1 RF Power System Preparation.....	2
2. Installation.....	3
2.1 RFQ installation.....	3
2.2 RFQ Conditioning.....	4
3. Test.....	5
3.1 RFQ Test.....	5
3.1.1 Beam Current and Transmission.....	5
3.1.2 Beam Energy.....	8
3.1.3 Output Beam Emittance.....	10
4.0 Suggestions & Considerations.....	16

Abstract

This report is a summary of the work done for Pennsylvania State University contract number 146822D.

For this contract a 425 MHz RF power system from another SAIC project was modified and the 425 MHz RFQ owned by the Air Force was installed on the beam line test stand and tested. The RFQ was previously prepared for testing under Pennsylvania State University contract number 361148D.

The RF power system modification consisted of changing of the coaxial waveguide from the final power amplifiers to the RFQ so that it could reach the installed position of the RFQ and that the electrical length of the waveguide was satisfactory.

The RFQ was installed on the beam line test stand with the output of the RFQ connected to appropriate diagnostic equipment enabling characterization of the RFQ operational parameters. The RFQ was powered and RF conditioned in preparation for operational testing. The RFQ was operated and various test data was collected for analysis. The details of tests conducted and the results of the analyses performed are discussed in section 3.1.

We have been successful in meeting the requirements of this contract.

1. RF Power System Preparation

1.1 RF Power System Preparation

The 425 MHz rf power system from another project was modified to power this RFQ. The coaxial waveguide connecting the final power amplifiers to the drive loop of the RFQ was changed to meet the physical requirements of this RFQ installation. The electrical length of the waveguide was carefully considered for proper matching to the RF power system.

It is important to properly match the electrical length of the high power coaxial cable. This necessity derives from the characteristics of the two resonant cavities at each end of the power cable (Final Power Amplifier and RFQ). During the fill time of the RFQ, the RFQ load appears as a short circuit across the drive loop. A short circuit will cause the incident power to be reflected back to the rf amplifier. If the line length is wrong, the standing wave set up by the superposition of the incident and the reflected waves will cause twice the voltage to appear at the anode of the power amplifier tube. This high voltage can cause the power tube to spark and break down. Hence, one sets the line length to be close to $n\lambda / 2$ long where n is an integer multiple and λ is the wave length. The proper line length will cause a voltage minimum to appear at the power tube during the fill of the cavity or an RFQ cavity conditioning spark.

2. Installation

2.1 RFQ Installation

The RFQ was connected to the rf power amplifier and the vacuum system and then powered. The resonant frequency under vacuum was 425.005 MHz. The pressure in the RFQ prior to powering the cavity was approximately 3×10^{-7} torr. During operation of the RFQ with beam the pressure in the RFQ increased to approximately 4×10^{-6} torr. This pressure increase was due to the additional gas load into the RFQ created by the ion source gas passing from the ion source chamber and into the RFQ through the RFQ end wall aperture. This operating pressure is acceptable for operation of the RFQ. SAIC has operated other RFQ's at pressures as high as 5×10^{-5} torr, although operation at these pressures can be less stable due to an increase in potential for high voltage sparks within the cavity. The coupling factors of the two rf monitor loops were calibrated and the coupling of the drive loop was adjusted. The output beam line of the RFQ was connected to a pair of diagnostic devices as shown in Figure 1. The first diagnostic actuator contained a scintillating beam viewer. A slit-and-collector emittance scanner was attached to the second diagnostic actuator. A rotational adapter located between the two diagnostic devices allowed measurement of both emittance planes without breaking vacuum. A Faraday cup to measure the accelerated beam current was installed at the end of the output beam line.

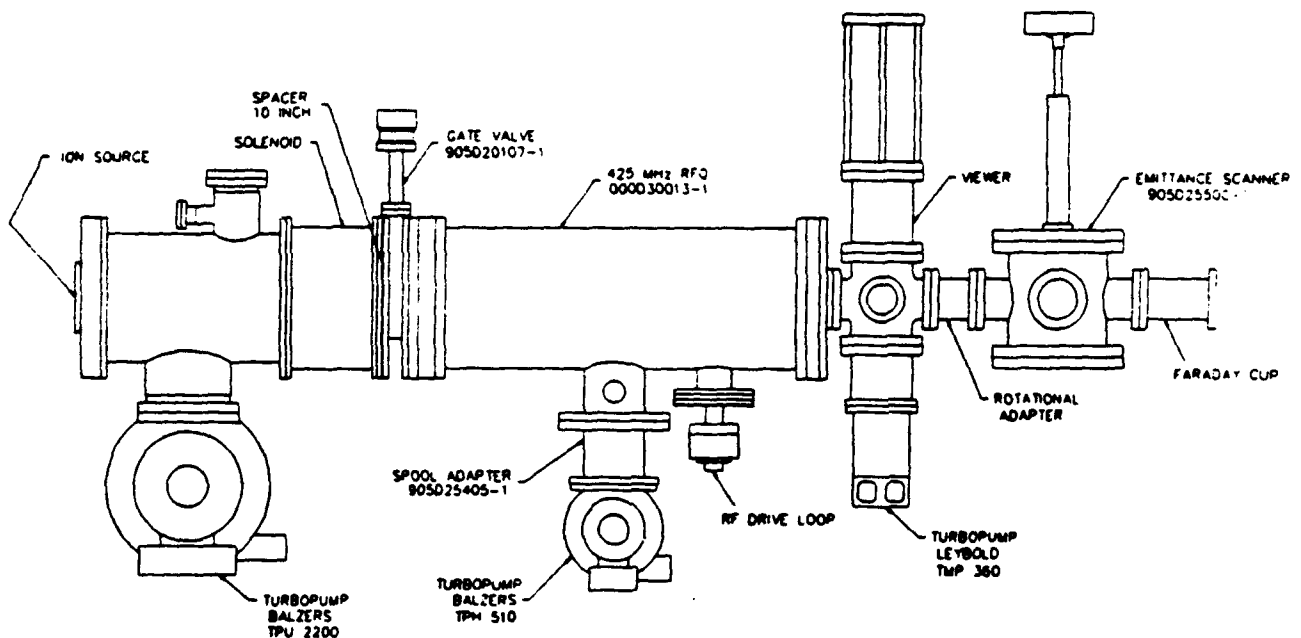


Figure 1. Experimental arrangement for testing the Phillips' RFQ. The ion source was coupled to the RFQ through a solenoid magnet and a vacuum isolation valve. The output beam of the RFQ was directed through a pair of diagnostic stations and into a Faraday cup.

2.2 RFQ Conditioning

The RFQ was operated at 20 Hz with a 60 μ sec rf pulse for a period of time before attempting to accelerate beam. This serves to stabilize the operating conditions. Beam was accelerated in the RFQ after only 4 hours of this rf conditioning. The initial operation achieved 10 mA of accelerated protons. After further rf and ion source conditioning and improvement of the input power match, 14 mA or more of accelerated beam were typically produced.

3. Test

3.1 RFQ Test

3.1.1 Beam Current and Transmission

To achieve good stability of the ion source it was necessary to operate the ion source with 120 μsec pulses at 60 Hz. The RFQ was operated with 60 μsec pulses at 20 Hz. The rf pulse was initiated approximately 50 μsec after the start of every third ion source pulse. This timing scenario insured that any space-charge neutralization of the ion source beam was well-established and the RFQ input beam characteristics were stable before the rf power was turned on.

Figure 2 shows a plot of the beam current measured in the Faraday cup for a typical beam pulse. The current was determined from the voltage induced in a 1 k Ω resistor connecting the Faraday cup to ground (a 1 k Ω resistor produces 1 volt per milliamp of current). Secondary emission from the Faraday cup was suppressed with permanent magnets surrounding the entrance of the cup. The rise- and fall-time of the current pulse is due to the rise- and fall-time of the rf fields in the RFQ and the capacitance of the Faraday cup. This pulse shape is characteristic of this particular operational scenario. A discussion of the suggested operational scenario for antiproton acceleration is discussed in section 4.0.

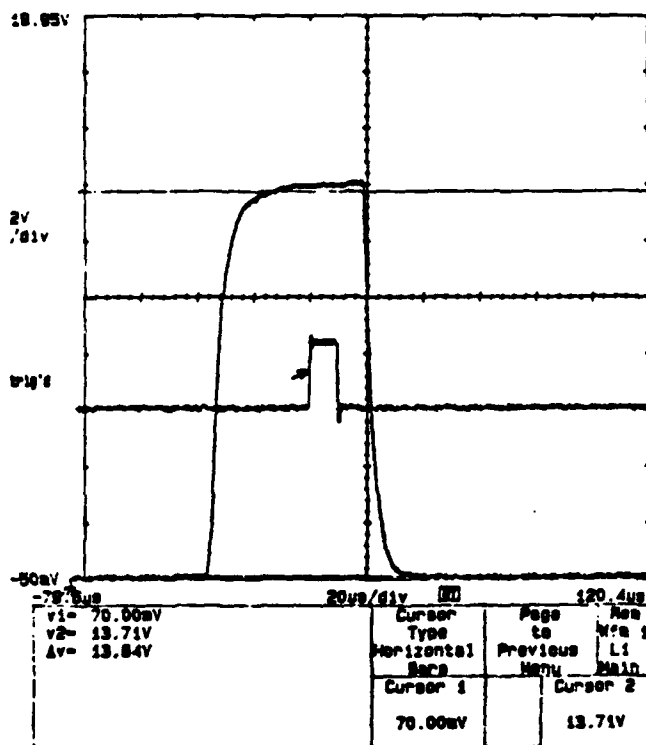


Figure 2. Faraday cup voltage signal typical of the operation of the RFQ. The large pulse indicates a typical output beam pulse. The leading and trailing edges are characteristic of the RFQ cavity rise and fall time. The small trace denoted with the arrow shows the diagnostic trigger.

The ion current illustrated in Figure 2 is more than 13.64 mA (as determined from the difference between the cursor readings v1 and v2 shown at the bottom left of the figure). The smaller pulse near the center of the figure is the sample gate for the data acquisition system (input ADCs are latched on the falling edge of the gate). Hence the beam parameters were measured approximately three-quarters of the way through the beam pulse.

The ion source characterization studies described in a previous report for Pennsylvania State University (contract number 361148D) determined the proper ion source settings for production of an ion beam with 70% proton fraction. Operating the ion source at these settings and correcting the measured 25 mA ion current in the low energy transport line for the proton fraction, yields an RFQ input proton current of 17.5 mA. The 14 mA of accelerated beam current yields 80% transmission through the RFQ.

Figure 3 shows two measurements of the relative beam current in the Faraday cup as a function of rf power in the RFQ.¹ The data points without the line show total Faraday cup current. The data points connected by the solid line show only accelerated beam current.

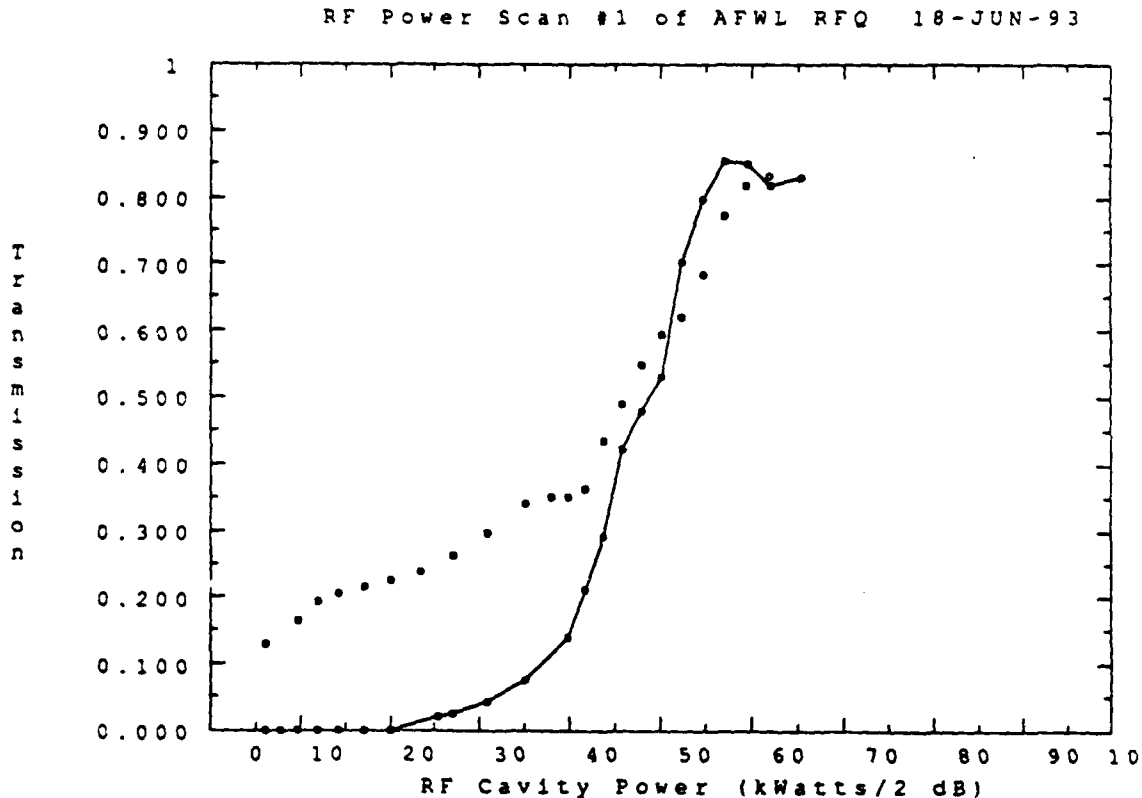


Figure 3. Plot of beam transmission as a function of rf power in the RFQ. The data points indicate the total beam transmission on the Faraday cup and the points connected by the line indicate only the 1.2 MeV component.

¹Note however that the rf power scale was adjusted downward by 2 dB. The absolute calibration of rf cavity power levels is difficult to extrapolate from measurements made at low power and field uncertainties of 3 dB are common.

It is characteristic of RFQ accelerators that the reduced-power rf fields can focus and transport the beam ions without accelerating them. Hence the total beam current in the Faraday cup increases because additional ions are transported, but not accelerated, by the "quadrupole focusing channel". Acceleration of these ions at higher rf power levels does not change the measured current because these ions are already collected in the Faraday cup. Installation of a dipole magnetic field at the exit of the RFQ displaced the unaccelerated ions so that they would not be intercepted by the Faraday cup. These data are indicated in figure 3 by the data points connected by the solid line. A calorimetric measurement of energy deposited in the Faraday cup would also differentiate between accelerated and unaccelerated beam components.

Figure 4 shows a comparison of PARMTEQ calculations with the measured transmission of the accelerated beam current. The PARMTEQ values shown by the solid line have $\pm 2.5\%$ uncertainty and were derived by assuming an input emittance of 90π mm-mrad² (the RFQ was designed for an input emittance of 50π mm-mrad). The theoretical transmission of the RFQ is a sensitive function of the input emittance and goes from 90% to 60% as the emittance increases from 50π to 120π mm-mrad. The 90π emittance used in the PARMTEQ calculations was not measured, but rather was inferred by comparing the measured transmission with the theoretical result and choosing the best fit.

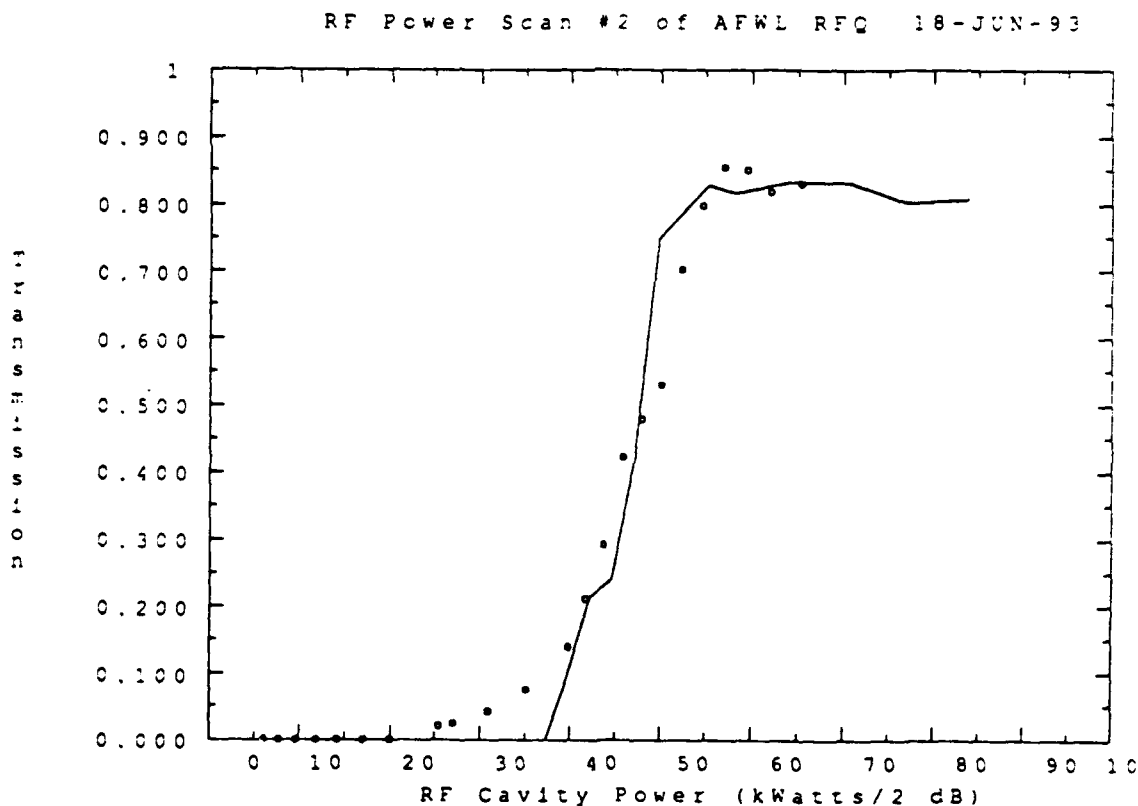


Figure 4. Comparison of the measured beam transmission as a function of rf power (dots) and the theoretical value (solid line).

²This emittance value is not too different from that expected from scaling the ³He beam emittance.

3.1.2 Beam Energy

The output beam energy was crudely determined by measuring the off-axis deflection of the beam produced by a permanent magnet (PM) dipole. The beam was measured prior to introducing the magnetic field and subsequently while bending the beam both up and down. The deflection distance was determined from the differences between centroids of Gaussian fits of the beam profiles measured with the emittance scanner. The fit procedure reduces the sensitivity to noise and improves the quality of the result because the deflection distance is small compared to the size of the beam. Additionally the deflection angles can be directly measured from the centroid shift of the emittance profile projected onto the angle axis. Figures 5a through 5c illustrate the profile data and the resulting fits. The Gaussian fit parameters are summarized in Table I.

Condition	ID	A	b (cm ⁻¹)	Y ₀ (cm)
Bend "UP"	Y	589.8±16.2	0.7061±0.0226	0.7172±0.0317
No Bend	Y	577.4±10.4	0.7149±0.0149	0.2642±0.0206
Bend "DOWN"	Y	551.9±16.1	0.7133±0.0240	-0.3344±0.0333
Condition	ID	A	b (mrad ⁻¹)	Y' ₀ (mrad)
Bend "UP"	Y'	916.7±17.5	0.0381±0.0009	-50.5170±0.4078
No Bend	Y'	898.8±10.6	0.0388±0.0005	-39.6822±0.2477
Bend "DOWN"	Y'	863.6±10.6	0.0391±0.0006	-26.3865±0.2565

Table I. Fit parameters for Gaussian fits to the emittance projections illustrated in figures 5a through 5c. The fit is shown for position (Y) and angular (Y') emittance data. The shift in the centroids (Y₀, Y'₀) indicate the deflection distances due to the magnetic field. The form of the Gaussian function used is:

$$F(y) = Ae^{-b^2(y-y_0)^2}$$

The field integral of the PM dipole was calibrated by turning off the rf power in the RFQ and measuring the deflection of the known 21kV ion source beam. The output beam energy was then determined from the square of the ratio of deflection angles. Note that the "UP" deflection data runs off of the bottom end of the angle scale (figure 5a). This loss of data apparently reduced the effective deflection angle and rendered this data unreliable. The result of the "DOWN" measurements (for beam position and angle change) are 1.57±0.29 and 1.35±0.06 MeV.³ Although somewhat high, these values are in reasonable agreement with the 1.2 MeV design energy. Actually an RFQ is a resonant device that is virtually incapable of producing anything except 1.2 MeV except over a small interval of rf power between no acceleration and full acceleration⁴. Hence measuring a significant change in the beam energy is equivalent to measuring full acceleration.

³ The Uncertainties only reflect the uncertainties in the position measurements and do not account for systematic uncertainties.

⁴LANL Accelerator Theory Note, AT-6:ATN-84-10

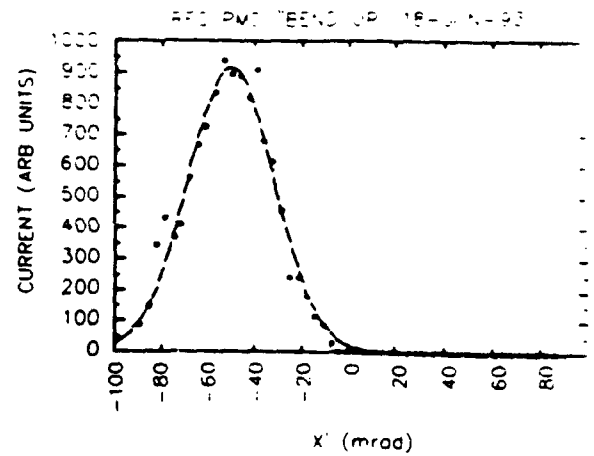
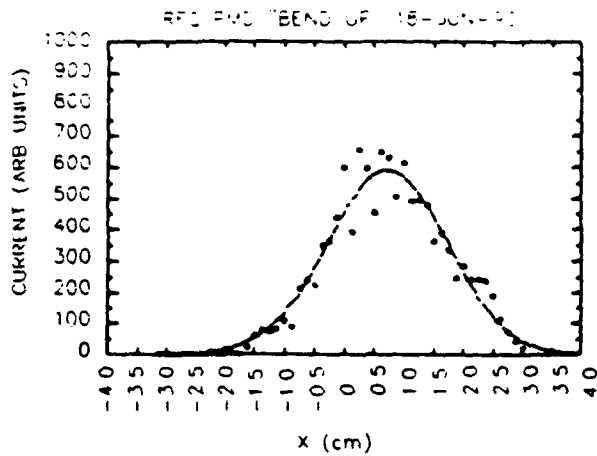


Figure 5a. Plots showing a shift upward of the profiles in figure 5b due to the addition of a permanent magnet dipole upstream of the emittance scanner. The centroids and fit parameters are given in Table I.

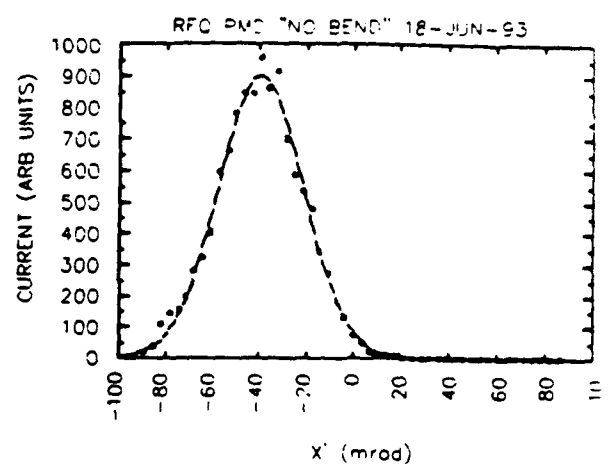
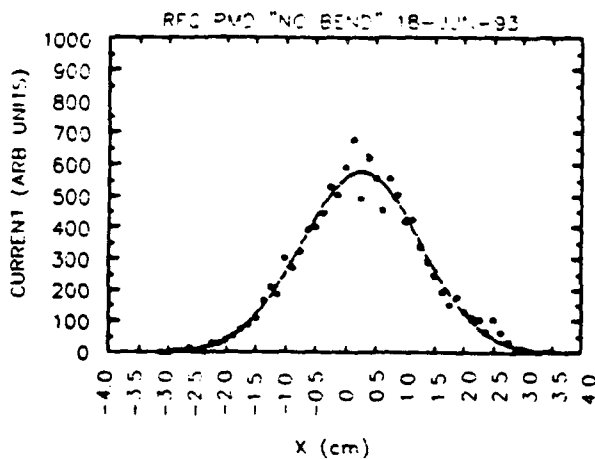


Figure 5b. Gaussian fits of Y plane beam emittance profiles projected onto the position (Y) and angle (Y') axes. The centroids and fit parameters are given in Table I.

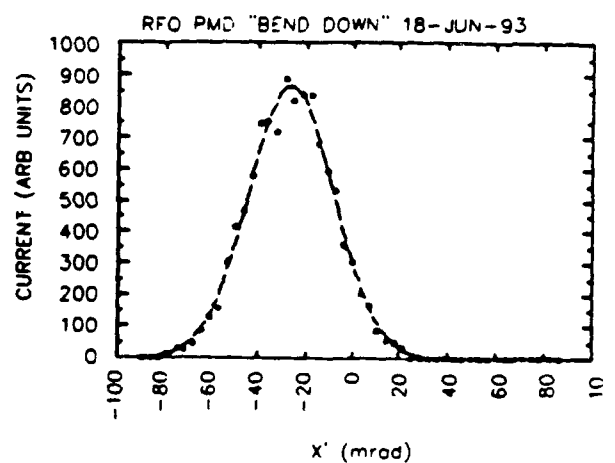
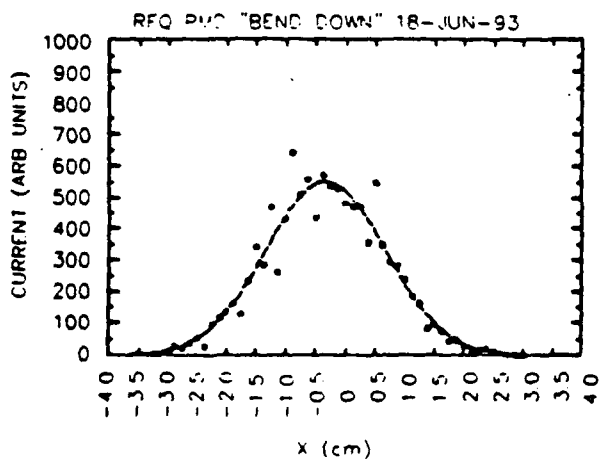


Figure 5c. Plots showing a shift downward of the profiles in figure 5b due to the addition of a permanent magnet dipole upstream of the emittance scanner. The centroids and fit parameters are given in Table I.

3.1.3 Output Beam Emittance

The output beam emittance was measured with a slit and collector emittance scanner located approximately 560 mm downstream of the RFQ. The angular resolution of the wire collector was limited to 3.5 mrad. It was noted during acquisition of the data that the angular spread of the beam was entirely collected on a single wire for approximately three position steps. This indicates that the angular spread was approximately one-third of the wire resolution. Hence the emittance values derived are about three times the actual beam emittance.

Figure 6 shows the 4, 5, and 6-RMS contour plots derived from the emittance data for both transverse emittance planes. Table II summarizes the results of the emittance measurements. The values in the table are the 4-RMS values typically quoted in the literature. Note however that it is expected that these emittance areas are approximately a factor of three larger than the actual emittance values because of the limited angular resolution of the emittance scanner. Figure 7 shows the comparison of the experimental data with the theoretical results from PARMTEQ⁵. Note that the extents of the 6-RMS ellipses shown in figure 7 are smaller than the extents of the 6-RMS ellipses shown in figure 6. This difference exists because the 6-RMS contours of figure 6 consider all of the raw emittance data and are subject to noise thereby exaggerating the full extents of the beam. For this reason the 4-RMS values were multiplied by 6/4 for comparison to theoretical results from PARMTEQ in figure 7. Figures 8a and 8b show isometric plots of the emittance data from two different relative perspective locations.

Emittance Plane	4-RMS Emittance (mm-mrad)	α	β (mm/mrad)
X	38.13	-10.115	5.778
Y	32.77	-10.545	5.625

Table II. Summary of measured RFQ output emittances. The 4-RMS values are given along with the Twiss parameters.

Since we are interested in the beam parameters at the exit of the RFQ and the emittance scanner was located 560 mm downstream, the phase space and orientation of the beam exiting the RFQ was found by tracing the experimental data back to that point. The tracing program TRACE3D was used for this purpose. Space charge was included although its effect is minor. The physical location and the beam parameters are shown in figure 9. The beam optics for the transport should be located from this point.

⁵ G.P. Biocourt, et. al., Comparison of Simulation with Experiment in an RFQ, IEEE Trans. on Nucl. Science NS-32, 5, 10/85

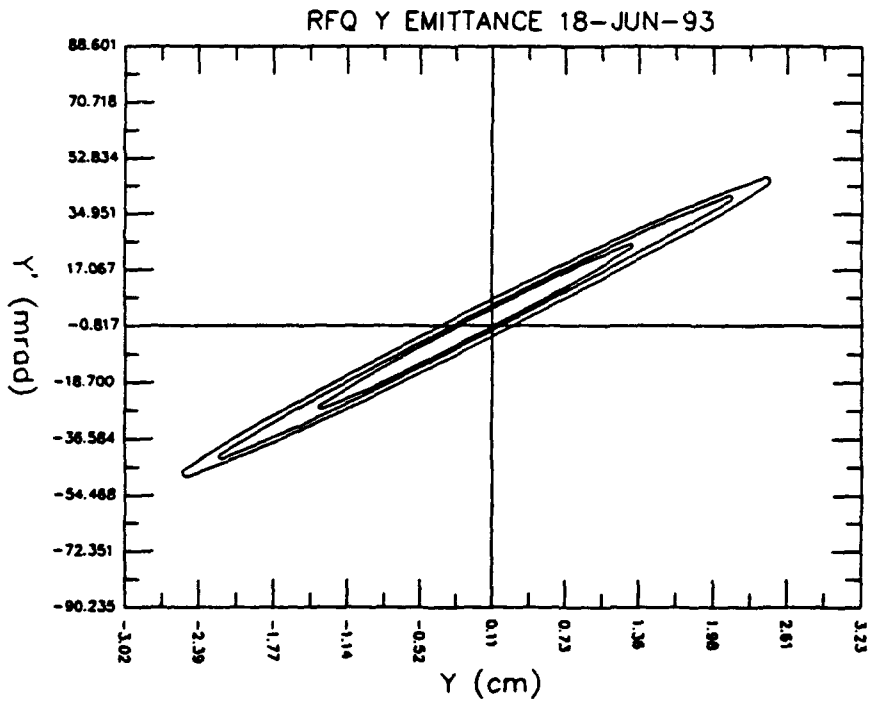
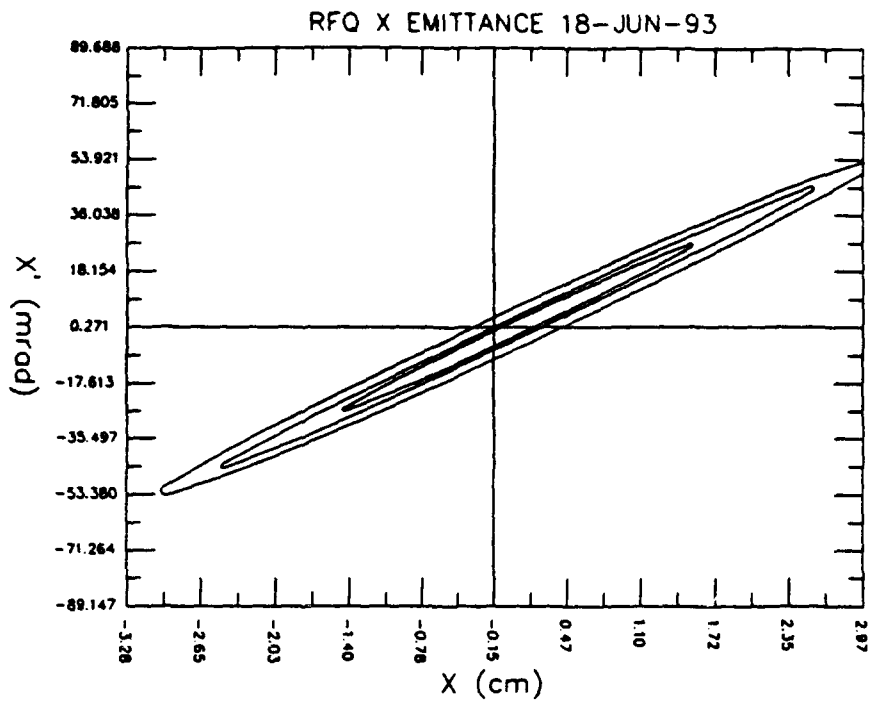


Figure 6. Contour plots of the X and Y emittance data taken 560 mm downstream of the RFQ. The 4, 5 and 6 RMS contours are shown.

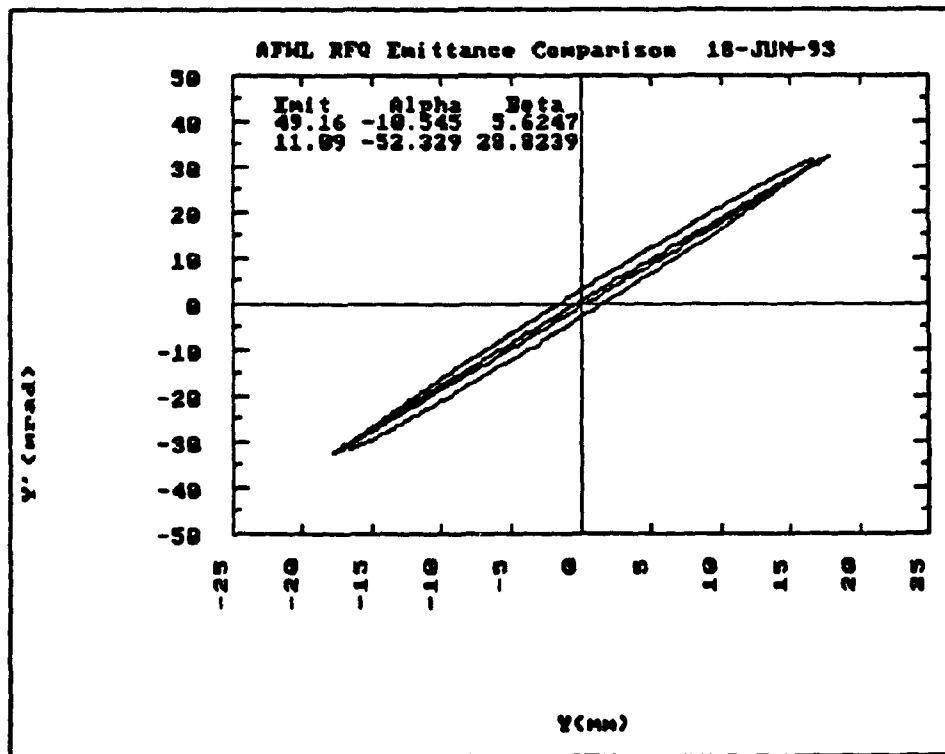
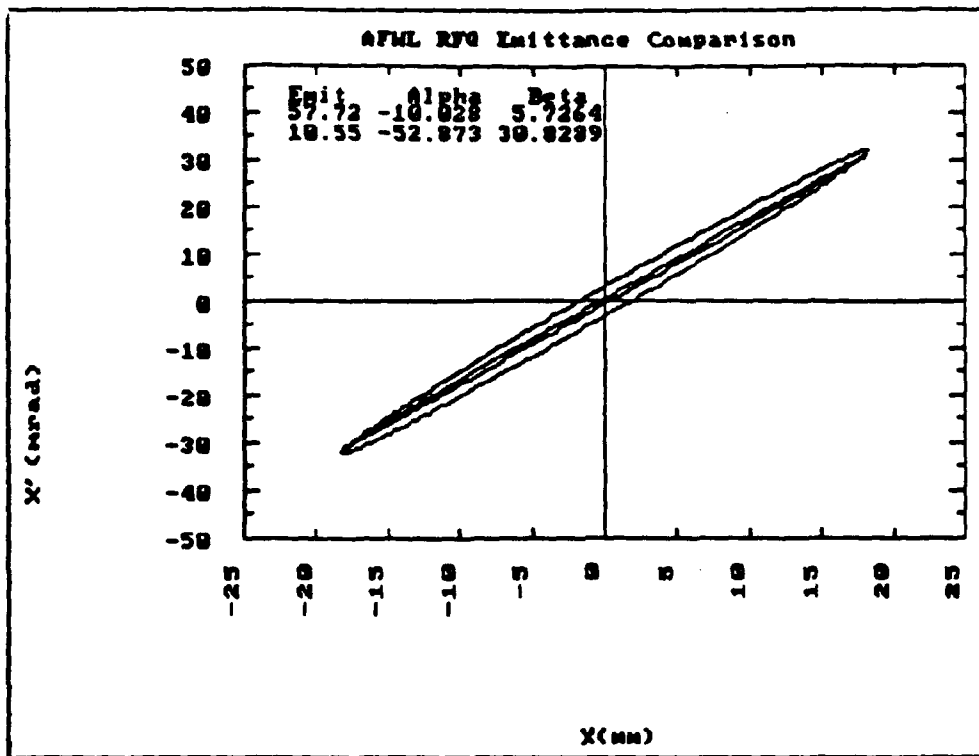


Figure 7. Comparison of experimental x and y-plane emittance (outer envelope) with the 6-RMS theoretical results from PARMTEQ (inner envelope). The first row of numbers in each graph shows experimental results and the second row are the results from PARMTEQ. Both the experimental data and the theoretical results from PARMTEQ are taken at a point 560 mm downstream of the RFQ.

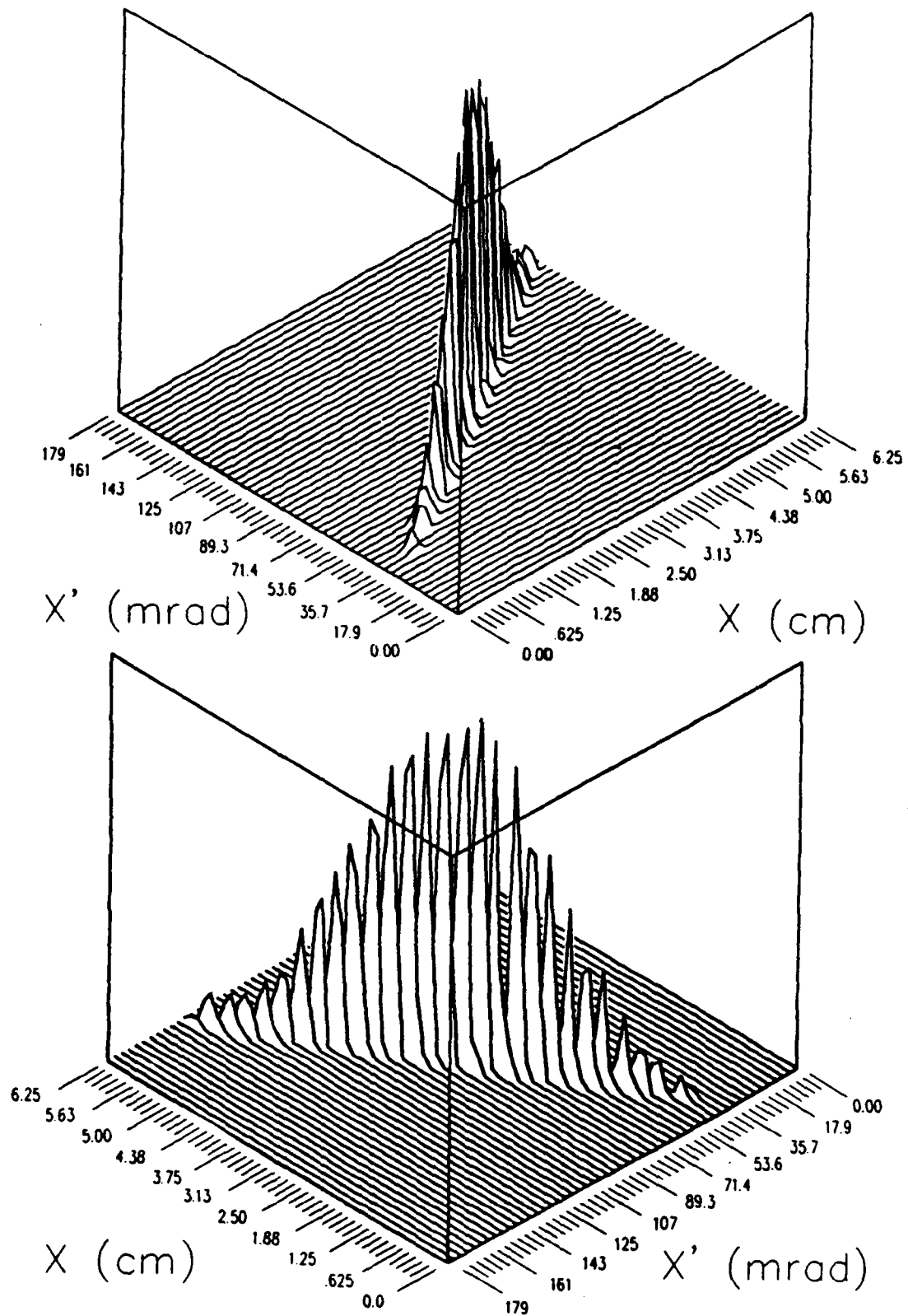


Figure 8a. Isometric plots of X-plane emittance data shown from two different relative perspective locations. The data shown was taken 560 mm downstream of the RFQ.

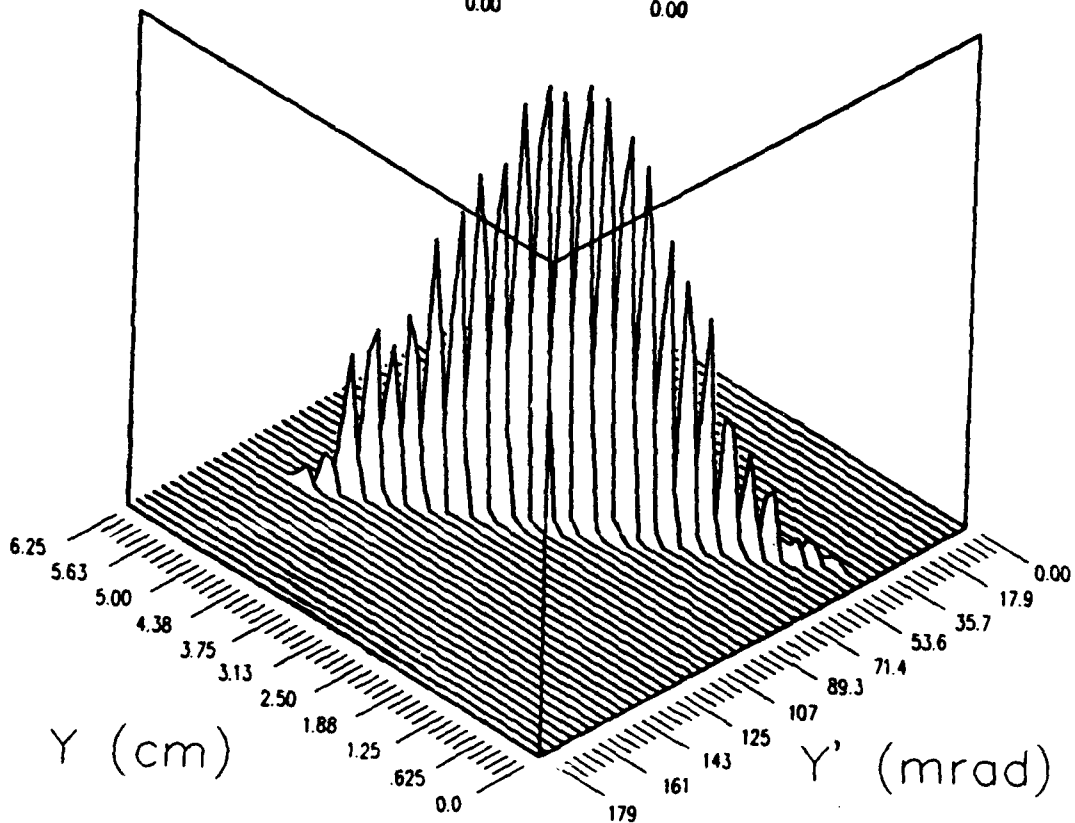
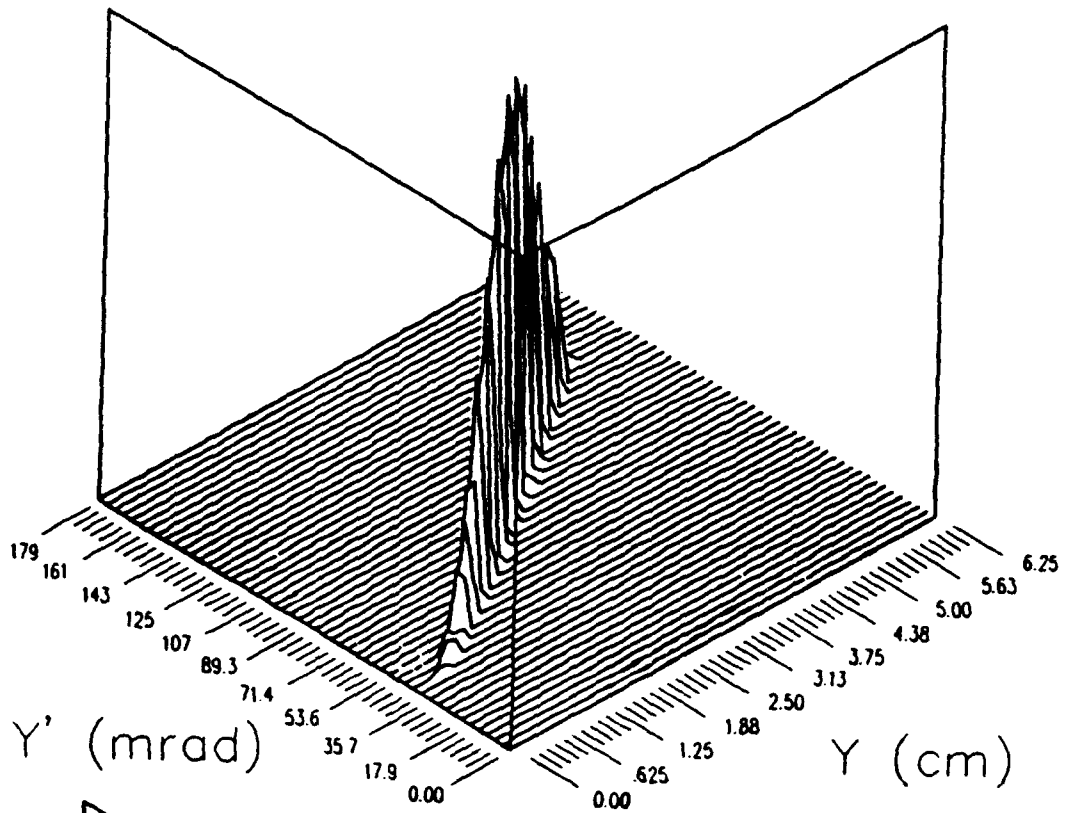


Figure 8b. Isometric plots of Y-plane emittance data shown from two different relative perspective locations. The data shown was taken 560 mm downstream of the RFQ.

4.0 Suggestions & Considerations

We suggest that the scenario for antiproton acceleration is to operate the RFQ with 10-100 μ s pulses at 10 Hz. Because only one beam pulse will be available from the antiproton trap, it is essential to stabilize the operation of and verify the performance of the RFQ before injecting the antiprotons.

As discussed above, the operating scenario for the RFQ tests at SAIC consisted of operating the ion source at 60 Hz and the RFQ at 20 Hz. The rf pulse was turned on approximately 50 μ s after the ion source pulse. This mode of operation is used whenever it is impractical or undesirable to turn on the rf before the ion beam. In other instances, it is desirable to turn on the rf before introducing the beam into the RFQ. In this case, the rf amplitude controller sees a decrease in the RFQ cavity field when the beam begins to remove energy from that field. The closed-loop amplitude controller compensates for that droop by increasing the rf drive. The "capture time" of the controller is limited by a combination of the bandwidth of the controller and the round-trip time of the rf signal through the power amplifier, through the RFQ, and back into the error-signal input to the amplitude controller. Typical closed-loop capture times are on the order of 1-2 μ s. The round-trip time of the amplitude control signal far exceeds the 50 ns beam pulse width.

The RFQ was designed for an input current of 20 mA. If the antiproton trap contains 10^{10} ions, then the trap cannot be emptied in less than 80 ns without exceeding the design current of the RFQ. It is also important to note that the rf power required to accelerate the beam is 1.2 kW per mA. If a 20 mA antiproton beam is simply injected into the RFQ without simultaneously increasing the rf drive, the beam will deplete the rf energy in the RFQ and the electric fields will droop below the level required to maintain acceleration. The time scale of this process is substantially less than the reaction time of the amplitude control circuits described above. Hence it will be necessary to anticipate the injection of the antiproton beam and increase the rf drive to accommodate it. Such a feature has been implemented in our standard rf system as the "feed-forward" feature. The rf output power is increased by the amplitude of the feed-forward pulse and lasts for the duration of that pulse. One will need to take care to condition the RFQ cavity to these higher levels before operation with the beam. Failure to do this may cause unpredictable conditioning sparks (collapse of fields) during operation.

In summary, the suggested operating mode for the Phillips' RFQ is to run the RFQ with 10-100 μ s pulses at 10 Hz to stabilize the operation of the RFQ. This small duty factor will keep the RFQ from heating and the resonant frequency from changing. The resonant frequency in this application is not critical and can be set to minimize the reflected power. The antiproton beam pulse can be injected at any time (and at any rf phase) during a particular rf pulse. However, the rf drive should be simultaneously increased by an appropriate amount to accommodate beam loading. Although the relative timing and sequencing is straight forward, the operation should be debugged using trapped protons before attempting to accelerate antiprotons.